Studies of the Local Atomic Ordering in Nanostructured Amorphous Materials Using Advanced Scanning Transmission Electron Microscopy Techniques

Alastair Kelway Doye

Department of Physics and Astronomy
University of Glasgow
23/04/22

Presented as a thesis for the degree of Ph.D in the University of Glasgow, University Avenue, Glasgow, G12 8QQ

Abstract

In this thesis, the short and medium range order of a range of glasses are investigated using scanning transmission electron microscopy.

One of the most powerful tools for achieving this is fluctuation microscopy, where a set of diffraction patterns are recorded using a small, but fairly parallel electron probe that is scanned over the sample using a small step size. Calculation of the normalised variance between diffraction patterns allows the determination of the range over which the medium range order persists.

A new direct electron detector was used, and a balance between exposure times that are long enough to not be dominated by shot nose and those short enough to allow rapid data acquisition was struck.

This technique was applied to the study of short range order and medium range order in two different classes of materials - amorphous metal silicides ($MoSi_x$, $NbSi_x$ and WSi_x), and amorphous oxides (TiO_2 doped Ta_2O_5 and SiO_2).

In each case, short range order in the amorphous metal silicides was found to be A15 like, with atom spacing that varied with atomic number, as expected. Medium range order was found to be typically around 1 nm or below, but in a few regions it extended over a few nm. Electron energy loss spectroscopy results found that the chemistry of the materials was consistent with A15 structures.

Time stability of each glass was investigated by using a static electron beam and recording a sequence of diffraction patterns at short exposure times, then analysing the variations in these. Intensity of diffraction spots was tracked as a function of time, electron correlation microscopy was used, where $g_2(t)$ was calculated allowing for the calculation of a characteristic decay time τ and stretching parameter β describing how long the diffraction pattern remains stable. In all of the glasses observed the structure seems to vary with time, but the timescale varies in each of them, τ values were estimated to be around 80-150 ms in SiO_2, around 800 ms in $NbSi_x$, and 2400 ms in TiO_2 doped Ta_2O_5.

A lack of time stability makes fluctuation microscopy of materials more problematic, and means that consideration is necessary to ensure that apparent spatial variances are correctly interpreted. In the case of SiO_2 an exposure time of 100 ms per diffraction pattern would mean that any spatial variance measurements would actually contain very little spatial information. As the metal silicides and TiO_2 doped Ta_2O_5 have a much higher τ, time stability is enough to that spatial variances are meaningful. Time variance in glasses needs further research and understanding it is essential to understanding spatial variance correctly.

Contents

1 Introduction **1**

1.1 The Origins of Materials Research 1

1.2 Materials by Design 3

1.3 Amorphous Materials 4

1.4 Uses of Amorphous Materials or Glasses 4

1.5 Structural Properties of Amorphous Materials 6

1.6 Conclusions 7

2 Investigating the Atomic Structure of Amorphous Materials **8**

2.1 Introduction 8

2.2 Describing Atomic Structure in Amorphous Materials 9

2.3 EXAFS 10

2.4 X-Ray PDF 13

2.5 Neutron Diffraction 13

2.6 Electron Microscopy 14

2.6.1 Electron Interactions with Matter 16

2.6.1.1 Elastic Scattering 16

2.6.1.2 Inelastic Scattering 18

2.6.2 Electron Microscopy Based Analysis of the Structure of Amorphous Materials 19

2.6.3 Electron Diffraction RDF Measurements 19

2.6.4 Scanned Diffraction / 4DSTEM and Fluctuation Electron Microscopy 20

2.6.4.1 Fluctuation Electron Microscopy 20
2.6.4.2 Virtual Dark Field Imaging (VDFI) 22
2.7 Electron Energy Loss Spectroscopy (EELS) 22
2.8 Discussion & Summary 24

3 Principles, Instrumentation and Practice for the Structural Characterisation of Thin Amorphous Films 26

3.1 Introduction 26
3.2 Samples 27
3.2.1 Sample Preparation Procedures 27
3.2.1.1 Focussed Ion Beam 27
3.2.1.2 FIB Sample Preparation 28
3.3 TEM and STEM 30
3.3.1 Electron Sources 32
3.3.2 Components in the STEM column 34
3.3.3 Aberrations in TEM/STEM 35
3.3.4 Detectors 36
3.3.4.1 Gatan Orius SC1000A 38
3.3.4.2 Medipix III – Merlin for EM 39
3.3.4.3 Gatan 965 Quantum ER Spectrometer 40
3.4 Electron Energy Loss Spectroscopy 40
3.4.1 Dual EELS 44
3.4.2 EELS Data Processing 44
3.5 Diffraction and Resolution in STEM Mode 46
3.5.1 Topspin Software 51
3.6 Virtual Dark Field Imaging 51
3.7 Fluctuation Electron Microscopy 53
3.7.1 Kinematical Electron Scattering Theory for Fluctuation Electron Microscopy 56
3.8 Summary 65

4 Characterisation of the Atomic Structure and Composition of Materials for Superconducting Nanowire Single Photon Detectors 67

4.1 Introduction . . . 67

4.1.1 Superconductivity . . . 68

4.1.2 Superconducting Nanowire Single Photon Detectors . . . 69

4.1.3 Materials for SNSPDs . . . 70

4.2 Experimental Setup . . . 74

4.2.1 Deposition Procedures and Sample Preparation . . . 74

4.2.2 FEM Microscope Setup . . . 74

4.2.2.1 Co-Sputtered $MoSi_x$ FEM Microscope Settings . . . 75

4.2.2.2 Alloy $MoSi_x$ FEM Microscope Settings . . . 75

4.2.2.3 Co-Sputtered $NbSi_x$ FEM Microscope Settings . . . 75

4.2.2.4 Co-Sputtered WSi_x FEM Microscope Settings . . . 77

4.2.3 FEM Data Processing . . . 77

4.2.4 EELS Microscope Setup . . . 78

4.3 Experimental Results . . . 78

4.3.1 Effect of Exposure Time on Variance . . . 78

4.3.2 FEM and VDF imaging . . . 81

4.3.2.1 Co-Sputtered $MoSi_x$ . . . 81

4.3.2.2 Alloy Sputtered $MoSi_x$ . . . 86

4.3.2.3 VDF Images . . . 88

4.3.2.4 Co-Sputtered $NbSi_x$ . . . 98

4.3.2.5 VDF Images . . . 98

4.3.2.6 Co-Sputtered WSi_x . . . 108

4.3.2.7 VDF Images . . . 108

4.3.3 EELS . . . 116

4.3.3.1 Co-Sputtered $MoSi_x$ . . . 116

4.3.3.2 Alloy Sputtered $MoSi_x$ . . . 121

4.3.3.3 Co-Sputtered $NbSi_x$ . . . 124

4.3.3.4 Co-Sputtered WSi_x . . . 124
4.4 Discussion . . . 128

5 Investigations of the Fluctuation of Glass Structures as a Function of Time 132

5.1 Introduction . . . 132
5.2 LIGO Ta_2O_5/SiO_2 Multilayer Film . . . 134
5.3 Electron Correlation Microscopy . . . 135
5.4 Experimental Parameters . . . 136
5.4.1 Possible sources of error . . . 138
5.5 Time Variation Using 1 ms Exposure Time . . . 140
5.5.1 $NbSi_x$ 1 ms Exposure . . . 140
5.5.2 SiO_2 Substrate 1 ms Exposure . . . 148
5.6 Time Variation Using 21.6 ms Exposure Time . . . 157
5.6.1 $NbSi_x$ 21.6 ms Exposure . . . 157
5.6.2 Ti:Ta_2O_5 21.6 ms Exposure . . . 166
5.6.3 SiO_2 Substrate 21.6 ms Exposure . . . 174
5.6.4 SiO_2 Multilayer Film 21.6 ms Exposure . . . 184
5.7 Discussion . . . 193

6 Conclusions 196

6.1 Superconducting Nanowire Single Photon Detectors . . . 196
6.2 Temporal Fluctuations in the Diffraction Pattern . . . 199
6.3 Final Conclusions . . . 201
6.4 Future Work . . . 202

Appendix A 216

A.1 Convert APP5 file to HDF5 . . . 216
A.2 FEM calculations . . . 216
A.3 VDF calculations . . . 223

Appendix B **229**

B.1 Convert binary files to HDF5 229

B.2 Import packages and apply mask to central beam 229

B.3 Create figures showing diffraction patterns 232

B.4 Tracking intensity of selected spots with time 238

B.5 Calculate the similarity of diffraction patterns 242

List of Figures

2.1 a) Diffraction pattern of amorphous Ti doped Ta_2O_5. b) Diffraction pattern from a) masked to enable radial averaging. c) Radial average intensity of diffraction pattern shown in b). d) Reduced density function (RDF) obtained from the diffraction data. 11

2.2 Different kinds of signals that can be observed in a TEM. 16

2.3 Different ways that an electron can be scattered by interactions with an atom. Redrawn from[70]. 17

2.4 Examples of speckle patterns from; a) thin layer of amorphous silicon, b) protective layer of platinum deposited on top of sample and c) amorphous $MoSi_x$ thin film. 21

3.1 Diagram showing the FIB lift-out procedure 29

3.2 Basic diagram of the general components of a TEM. 31

3.3 Diagram of a FEG electron source. 34

3.4 Imaging detectors in the STEM, high angle annular dark field (HAADF), annular dark field (ADF) and bright field (BF). 37

3.5 Basic diagram of how an EELS spectrometer works. 41

3.6 Features of an EELS spectrum, showing; a) the zero loss peak and plasmon peak; b) core loss edges from tungsten and molybdenum. . . . 43

3.7 EELS spectrum showing a Nb $L_{2,3}$edge. A box is used to calculate the background and then the edge signal is extracted. 46

3.8 Illumination modes, a) shows a setup for parallel illumination, b) shows a setup for nanobeam diffraction and c) shows the lens setup for convergent illumination. 48

3.9 Angles that are important in STEM. 49

3.10 Diagram of the paths of electron rays, showing the incoming beam, sample and back focal plane. 50

3.11 This diagram shows how a diffraction dataset has an annular mask applied to it, creating a virtual dark field image showing diffraction intensity differences at the diffraction angle of the mask. 52

3.12 a) fcc diffraction pattern, along the [100] direction, b) mask of the four major diffraction spots (200), c) mask of the four minor diffraction spots(220). 53

3.13 Diagram of the FEM process in the STEM. The scanning probe is rastered across the sample and DPs are collected at set intervals in the sample. After that, the mean and variance of the diffraction patterns is calculated. Redrawn from [150]. 55

3.14 Imaging geometry of a scanned probe. Probe forming lenses (condenser lenses) and an aperture (condenser aperture) focus the radiation onto the scatterer, from which the scattering is collected by a detector/detectors. Redrawn from [150]. 57

3.15 FEM variance of a diamond-like carbon film doped with W and Mo. . . 65

4.1 Diagram showing on the left an SNSPD deposited on a substrate and on the right an example cross section of an SNSPD device. 69

4.2 A15 crystal structure diagram created using CrystalMaker (CrystalMaker Software Ltd., Oxon, UK) for a system with Si atoms (yellow) in the centre and corner sites, while metal atoms (blue-grey) occupy the other sites. 71

4.3 A section of the phase diagram of Nb-Al centred on Nb_3Al reproduced from Jorda et al. showing at which temperature and stoichiometries the A15 phase occurs. Open circles indicate single phase, while a half shaded circle indicates there are two phases present.[180] 72

4.4 Images of a) focussed probe while using a condenser aperture of 10 μm, used for calculating probe size, b) crystalline silicon diffraction pattern, obtained under the same microscope parameters for calculating convergence angle. 76

4.5 Normalised variance of the co-sputtered $NbSi_x$ at various exposure times at two different illumination conditions. a) shows results from an 2 nm probe diameter and b) from a 1 nm probe diameter. 79

4.6 Example diffraction patterns from the 2 nm probe size used on this co-sputtered $MoSi_x$ sample. The pairs of diffraction patterns shows images of the same diffraction patterns with different maximum pixel intensity in order to show the inner (upper) and the outer (lower) diffraction peak more clearly. 81

4.7 Normalised variance of the co-sputtered $MoSi_x$ film. Peak positions and relative heights of x-ray diffractogram peaks in A15 Mo_3Si are overlaid on the graph.[192] 82

4.8 BF and VDF images from the co-sputtered $MoSi_x$ film (each image is on a different color scale). The first image shows the bright field image, the next four images are annular VDF images taken in the range; k = 4.3 - 4.5 nm^{-1}, k = 6.75 - 6.95 nm^{-1}, k = 7.5 - 7.7 nm^{-1} and k = 10.4 - 10.6 nm^{-1} respectively. 83

4.9 Annular variance images from the co-sputtered $MoSi_x$ film (each image is on a different color scale). The images are calculated from the annular ranges; k = 4.3 - 4.5 nm^{-1}, k = 6.75 - 6.95 nm^{-1}, k = 7.5 - 7.7 nm^{-1} and k = 10.4 - 10.6 nm^{-1} respectively. 83

4.10 a) DP from the co-sputtered $MoSi_x$ film. Then using four circular apertures of diameter 1 nm^{-1} positioned on the diffraction pattern for variance peaks at b)4.5 nm^{-1}, c) 6.85 nm^{-1} and d) 7.6 nm^{-1}. 84

4.11 VDF images of the co-sputtered $MoSi_x$ film, taken using four different circular apertures of diameter 1 nm^{-1} positioned on the diffraction pattern for variance peaks at a)4.5 nm^{-1}, b) 6.85 nm^{-1} and c) 7.6 nm^{-1}. Each set of four images are on different color scales. 85

4.12 Example diffraction patterns from each of the probe sizes used on this alloy $MoSi_x$ sample. Each pair of diffraction patterns shows images of the same diffraction patterns with different maximum pixel intensity in order to show the inner (upper) and the outer (lower) diffraction peak more clearly. 87

4.13 FEM variance curves from the alloy $MoSi_x$ sample at three different probe sizes. 89

4.14 BF and annular VDF images from the alloy $MoSi_x$ film (each image is on a different color scale). Each column shows images from the three different probe sizes used, while the rows show the results of the different apertures. 91

4.15 Radial variance images from the alloy $MoSi_x$ film (each image is on a different color scale). Each column shows images from the three different probe sizes used, while the rows show the results of the different apertures. 91

4.16 VDF images of the alloy $MoSi_x$ film, generated from dataset with 2.2 nm probe size. Images formed using circular apertures placed on the DP at the position of the variance peaks at k values of a) 4.55 nm^{-1}, b) 7.4 nm^{-1} and c) 9.0 nm^{-1}. Each set of four images is on a different color scale. 94

4.17 VDF images of the alloy $MoSi_x$ film, generated from dataset with 2 nm probe size. Images formed using circular apertures placed on the DP at the position of the variance peaks at k values of a) 4.55 nm^{-1}, b) 7.4 nm^{-1} and c) 9.0 nm^{-1}. Each set of four images is on a different color scale. 95

4.18 VDF images of the alloy $MoSi_x$ film, generated from dataset with 1 nm probe size. Images formed using circular apertures placed on the DP at the position of the variance peaks at k values of a) 4.55 nm^{-1}, b) 7.4 nm^{-1} and c) 9.0 nm^{-1}. Each set of four images is on a different color scale. 96

4.19 Example diffraction patterns from each of the probe sizes used on this $NbSi_x$ sample. Each pair of diffraction patterns shows images of the same diffraction patterns with different maximum pixel intensity in order to show the inner (upper) and the outer (lower) diffraction peak more clearly. 97

4.20 FEM variance curves from the co-sputtered $NbSi_x$ sample at three different probe sizes. 99

4.21 BF and annular dark field images from the co-sputtered $NbSi_x$ film (each image is on a different color scale). Columns show images obtained at the different probe sizes. Rows show the images obtained from the different virtual annular apertures used. 101

4.22 Radial variance images from the co-sputtered $NbSi_x$ film (each image is on a different color scale). Each column shows results from a different probe size. Rows show images obtained over different annular regions. . 102

4.23 VDF images of the co-sputtered $NbSi_x$ film, generated from a dataset with 3 nm probe size. Images formed using circular apertures placed on the DP at the position of the variance peaks at k values of a) 4.25 nm^{-1}, b) 7.0 nm^{-1} and c) 8.45 nm^{-1}. Each set of four images is on a different color scale. 105

4.24 VDF images of the co-sputtered $NbSi_x$ film, generated from a dataset with 2.6 nm probe size. Images formed using circular apertures placed on the DP at the position of the variance peaks at k values of a) 4.25 nm^{-1}, b) 7.0 nm^{-1} and c) 8.45 nm^{-1}. Each set of four images is on a different color scale. 106

4.25 VDF images of the co-sputtered $NbSi_x$ film, generated from a dataset with 1.2 nm probe size. Images formed using circular apertures placed on the DP at the position of the variance peaks at k values of a) 4.25 nm^{-1}, b) 7.0 nm^{-1} and c) 8.45 nm^{-1}. Each set of four images is on a different color scale. 107

4.26 Example diffraction patterns from each of the probe sizes used on this WSi_x sample. Each pair of diffraction patterns shows images of the same diffraction patterns with different maximum pixel intensity in order to show the inner (upper) and the outer (lower) diffraction peak more clearly. 109

4.27 FEM variance curves from the co-sputtered WSi_x sample at three different probe sizes. 110

4.28 BF and annular dark field images from the co-sputtered WSi_x film (each image is on a different color scale). Each column shows images obtained at the three different probe sizes used, while the rows show images obtained using a set of annular masks. 111

4.29 Radial variance images from the co-sputtered WSi_x film (each image is on a different color scale). Columns show images from the different probe sizes used. Rows show images obtained from different annular regions. 112

4.30 VDF images of the co-sputtered WSi_x film, generated from a dataset with 2.5 nm probe size. Images formed using circular apertures placed on the DP at the position of the variance peaks at k values of a) 4.5 nm^{-1}, b) 7.25 nm^{-1} and c) 8.75 nm^{-1}. Each set of four images is on a different color scale. 113

4.31 VDF images of the co-sputtered WSi_x film, generated from a dataset with 2.3 nm probe size. Images formed using circular apertures placed on the DP at the position of the variance peaks at k values of a) 4.5 nm^{-1}, b) 7.25 nm^{-1} and c) 8.75 nm^{-1}. Each set of four images is on a different color scale. 114

4.32 VDF images of the co-sputtered WSi_x film, generated from a dataset with 1.2 nm probe size. Images formed using circular apertures placed on the DP at the position of the variance peaks at k values of a) 4.5 nm^{-1}, b) 7.25 nm^{-1} and c) 8.75 nm^{-1}. Each set of four images is on a different color scale. 115

4.33 EELS-SI analysis of the co-sputtered $MoSi_x$ sample with Si cap (Sample A), showing; a) map of EELS background-subtracted signal from the Si-K edge over a 150 eV range starting from 1820 eV; b) map of background-subtracted signal from the Mo $L_2, 3$ edges over a 150 eV range starting from 2499 eV; c) low loss spectrum; d) full energy range view of the high loss spectrum from the $MoSi_x$ film; e) detail of the Si K edge; and f) detail of the Mo $L_2, 3$ edges. 117

4.34 EELS-SI analysis of the uncapped co-sputtered $MoSi_x$ sample (Sample B), showing; a) Map of EELS background-subtracted signal from the Si-K edge over a 150 eV range starting from 1821.4 eV;b) Map of background subtracted signal from the Mo $L_2, 3$ edges over a 150 eV range starting from 2498.4 eV;c) low loss spectrum, d) full energy range view of the high loss spectrum from the $MoSi_x$ film; e) detail of the Si K edge; and f) detail of the Mo $L_2, 3$ edges. 118

4.35 Background subtracted, Fourier deconvolved Mo $L_2, 3$ EELS edges from BCC Mo,[107] MoO_2,[84] co-sputtered $MoSi_x$ with capping layer, co-sputtered $MoSi_x$ without capping layer and $MoSi_x$ sputtered from an alloy target. Red, blue and yellow regions indicate areas of particular interest. 119

4.36 HAADF survey images of the areas scanned by EELS-SI of a) sample A (Si capped) and b) sample B (uncapped), with the green boxes indicating the scan areas. EELS-SI composition plots of the scanned areas, showing the concentration of Si and Mo in c) sample A and d) sample B. 120

4.37 EELS-SI analysis of the sputtered-alloy $MoSi_x$ sample, showing; a) map of EELS background subtracted signal from the Si-K edge over a 151 eV range starting from 1820 eV; b) map of background subtracted signal from the Mo $L_2, 3$ edges over a 151 eV range starting from 2048 eV; c) low loss spectrum; d) full energy range view of the high loss spectrum from the $MoSi_x$ film, e) detail of the Si K edge and f) detail of the Mo $L_2, 3$ edges. 122

4.38 Images showing a representation of a) Si percentage composition and b) Mo percentage composition. These are a result of EELS-SI analysis of the Si K absorption edge and the Mo L absorption edge.c) shows composition of alloy deposited $MoSi_x$, from EELS-SI analysis of the Si K edge and the Mo L edge. 123

4.39 EELS-SI analysis of the co-sputtered $NbSi_x$ sample (with end cap), showing; a) map of background-subtracted EELS signal from the Si-K edge over a 149 eV range starting from 1824 eV; b) map of background subtracted signal from the Nb $L_2, 3$ edges over a 149 eV range starting from 2357 eV; c) low loss spectrum; d) full energy range view of the high loss spectrum from the NbSix film; e) detail of the Si K edge; and f) detail of the Nb $L_2, 3$ edges. 125

4.40 HAADF survey image of spectrum image area for the cosputtered $NbSi_x$ sample, b) and c) show images giving a representation of b) the Si percentage composition and c) Nb percentage composition. These are a result of EELS-SI analysis of the Si K absorption edge and the Nb L absorption edge. d) Composition of co-sputtered $NbSi_x$, from EELS-SI analysis of the Si K edge and the Nb L edge. 126

4.41 EELS-SI analysis of the co-sputtered WSi_x sample, showing; a) image of low loss spectrum intensity, b) image of high loss spectrum intensity, c) low loss spectrum, d) full energy range view of the high loss spectrum from the WSi_x film; e) detail of the Si K edge and the overlapping W $M_{4,5}$ edge as well as the EELS atlas W $M_{4,5}$ edge f) background subtracted spectrum from e). 127

4.42 Maps of the WSi_x sample, showing the signal from the a) Si K edge and b) W $M_{4,5}$ edge as calculated by the Digital Micrograph elemental quantification plugin. Maps show the images generated from the EELS-SI dataset for background-subtracted energy loss windows of c) 98-102 eV (Si L edge), d) 1800-1824 eV (W M_5 edge), e) 1833-1869 eV (Si K edge, with W-M_5 contribution) and f) 2270-2295 eV (W M_3 edge). All maps have the same scale. 128

5.1 DPs obtained from the $NbSi_x$ film using an exposure time of 1 ms. This figure shows patterns taken from the dataset at regular 90 ms intervals. Arrows show some areas of the DP where diffraction spots are present in all DPs shown. 141

5.2 DPs obtained from the $NbSi_x$ film using an exposure time of 1 ms. This figure shows twelve consecutive patterns taken from the dataset. 142

5.3 Normalised variance obtained from the $NbSi_x$ diffraction patterns at 1 ms exposure time. Variance curves from the summed diffraction patterns over eleven different timeframes are shown. The top graph includes the spatial variance, to show how large the temporal variance is in comparison. 143

5.4 Sum of all 1000 DPs in the dataset obtained from the $NbSi_x$ film, showing selected diffraction spots. 144

5.5 Line plots of the summed intensity within each of the four spots as a function of time. Shown over the full time range of the experiment . . 144

5.6 Plots of the summed intensity for the first 200 ms of the dataset within each of the four spots. A rolling average and standard deviation from a window 11 patterns wide are overlaid. 145

5.7 This figure shows five DPs obtained with an exposure time of 1 ms from the $NbSi_x$ layer. These are spread at 175 ms intervals through the dataset. The top row shows the DPs, while the bottom row shows the absolute difference in intensity (detector counts) between the central DP in the top row and the DP directly above it. 146

5.8 This figure shows five consecutive DPs obtained with an exposure time of 1 ms from the $NbSi_x$ layer. The top row shows the DPs, while the bottom row shows the absolute difference in intensity (detector counts) between the central DP in the top row and the DP directly above it. . 147

5.9 DPs obtained from the SiO_2 substrate of the $NbSi_x$ film using an exposure time of 1 ms. This figure shows patterns taken from the dataset at regular 90 ms intervals. Arrows show some features of interest present in the patterns shown. 149

5.10 DPs obtained from the SiO_2 substrate of the $NbSi_x$ film using an exposure time of 1 ms. This figure shows twelve consecutive patterns taken from the dataset. Arrows show some features of interest present in the patterns shown. 150

5.11 Normalised variance obtained from diffraction patterns at the SiO_2 substrate using 1 ms exposure time. Variance curves from the summed diffraction patterns over eleven different timeframes are shown. 151

5.12 Sum of all 1000 DPs from the SiO_2 substrate of the $NbSi_x$ film, showing selected diffraction spots. 151

5.13 Line plots of the summed intensity within each of the four spots as a function of time. 153

5.14 Plots of the summed intensity for the first 200 ms of the dataset within each of the four spots. A rolling average and standard deviation from a window 11 patterns wide are overlaid. 153

5.15 This figure shows five DPs obtained with an exposure time of 1 ms from the SiO_2 substrate of the $NbSi_x$ layer. These are spread at 175 ms intervals through the dataset. The top row shows the DPs, while the bottom row shows the absolute difference in intensity (detector counts) between the central DP in the top row and the DP directly above it. . 154

5.16 This figure shows five consecutive DPs obtained with an exposure time of 1 ms from the SiO_2 substrate of the $NbSi_x$ layer. The top row shows the DPs, while the bottom row shows the absolute difference in intensity (detector counts) between the central DP in the top row and the DP directly above it. 154

5.17 DPs obtained from the SiO_2 substrate of the $NbSi_x$ film using an exposure time of 1 ms. This figure shows twelve consecutive patterns taken from the dataset. Arrows show some features that are present to some extent in the all of the patterns shown. 155

5.18 This figure shows five consecutive DPs obtained with an exposure time of 1 ms from the SiO_2 substrate of the $NbSi_x$ layer. The top row shows the DPs, while the bottom row shows the absolute difference in intensity (detector counts) between the central DP in the top row and the DP directly above it. 156

5.19 DPs obtained from the $NbSi_x$ film using an exposure time of 21.6 ms. This figure shows patterns taken from the dataset at regular 971.1 ms intervals. Arrows are pointing to features that are present in each of the DPs shown. 158

5.20 DPs obtained from the $NbSi_x$ film using an exposure time of 21.6 ms. This figure shows twelve consecutive patterns taken from the dataset. . 159

5.21 Normalised variance obtained from the $NbSi_x$ diffraction patterns at 21.6 ms exposure time. Variance curves from the summed diffraction patterns over ten different timeframes are shown. 160

5.22 Sum of all 500 DPs from the $NbSi_x$ film, showing selected diffraction spots. 161

5.23 Line plots of the summed intensity within each of the four spots as a function of time. 162

5.24 Plots of the summed intensity for the first 2000 ms of the dataset within each of the four spots. A rolling average and standard deviation from a window 5 patterns wide are overlaid. 162

5.25 This figure shows five DPs obtained with an exposure time of 21.6 ms from the $NbSi_x$ layer. These are spread at 2158 ms intervals through the dataset. The top row shows the DPs, while the bottom row shows the absolute difference in intensity (detector counts) between the central DP in the top row and the DP directly above it. 163

5.26 This figure shows five consecutive DPs obtained with an exposure time of 21.6 ms from the $NbSi_x$ layer. The top row shows the DPs, while the bottom row shows the absolute difference in intensity (detector counts) between the central DP in the top row and the DP directly above it. . 163

5.27 Images of the masked version of the first $NbSi_x$ diffraction pattern in the dataset, along with the τ and β values calculated from each pixel. Two different images of τ are shown, with both the full range as well as the detail at the lower end (0-2000 ms) of the τ range. 164

5.28 a), b) and c) show examples of non-linear least squares KWW fitting to $g_2(t)$ from pixels in the $NbSi_x$ diffraction patterns. d) shows a histogram of the wide distribution of τ values calculated from all of the pixels in the masked pattern. Results from the annular masked region are shown in e) KWW fit to average of each pixels $g_2(t)$ and f) histograms of τ and β calculated from each pixel. 165

5.29 DPs obtained from the Ti:Ta_2O_5 film layer using an exposure time of 21.6 ms. This figure shows patterns taken from the dataset at regular 971.1 ms intervals. Arrows are pointing to features that are present to some extent in all of the patterns shown. 167

5.30 DPs obtained from the Ti:Ta_2O_5 film layer using an exposure time of 21.6 ms. This figure shows twelve consecutive patterns taken from the dataset. 168

5.31 Normalised variance obtained from the Ti:Ta_2O_5 diffraction patterns at 21.6 ms exposure time. Variance curves from the summed diffraction patterns over ten different timeframes are shown. 169

5.32 Sum of all 500 DPs from the Ti:Ta_2O_5 film, showing selected diffraction spots. 169

5.33 Line plots of the summed intensity within each of the four spots as a function of time. 170

5.34 Plots of the summed intensity for the first 2000 ms of the dataset within each of the four spots. A rolling average and standard deviation from a window 5 patterns wide are overlaid. 171

5.35 This figure shows five DPs obtained with an exposure time of 21.6 ms from the Ti:Ta_2O_5 film layer. These are spread at 2158 ms intervals through the dataset. The top row shows the DPs, while the bottom row shows the absolute difference in intensity (detector counts) between the central DP in the top row and the DP directly above it. 171

5.36 This figure shows five consecutive DPs obtained with an exposure time of 21.6 ms from the Ti:Ta_2O_5 film layer. The top row shows the DPs, while the bottom row shows the absolute difference in intensity (detector counts) between the central DP in the top row and the DP directly above it. 172

5.37 Images showing the masked version of the first Ta_2O_5 diffraction pattern in the dataset, along with the τ and β values calculated from each pixel. Two ranges of τ are shown, the full range as well as a smaller range so that more detail is visible in the 0-3000 ms range. 172

5.38 a), b) and c) show examples of non-linear least squares KWW fitting to $g_2(t)$ from pixels in the Ta_2O_5 diffraction patterns. d) shows a histogram of the wide distribution of τ values calculated from all of the pixels in the masked pattern. Results from the annular masked region are shown in e) KWW fit to average of each pixels $g_2(t)$ and f) histograms of τ and β calculated from each pixel. 173

5.39 DPs obtained from the SiO_2 substrate of the $NbSi_x$ film using an exposure time of 21.6 ms. This figure shows patterns taken from the dataset at regular 971.1 ms intervals. Arrows are pointing to features of interest. 175

5.40 DPs obtained from the SiO_2 substrate of the $NbSi_x$ film using an exposure time of 21.6 ms. This figure shows twelve consecutive patterns taken from the dataset. Arrows are pointing to features of interest. . . 176

5.41 Normalised variance obtained from diffraction patterns at the SiO_2 substrate using 21.6 ms exposure time. Variance curves from the summed diffraction patterns over ten different timeframes are shown. 177

5.42 Sum of all 500 DPs from the SiO_2 substrate of the $NbSi_x$ film, showing selected diffraction spots. 177

5.43 DPs obtained from the SiO_2 substrate of the $NbSi_x$ film using an exposure time of 21.6 ms. This figure shows twelve consecutive patterns taken from the dataset. Arrows are pointing to features of interest. . . 179

5.44 Line plots of the summed intensity within each of the four spots as a function of time. 180

5.45 Plots of the summed intensity for the first 2000 ms of the dataset within each of the four spots. A rolling average and standard deviation from a window 5 patterns wide are overlaid. 180

5.46 This figure shows five DPs obtained with an exposure time of 21.6 ms from the SiO_2 substrate of the $NbSi_x$ layer. These are spread at 2158 ms intervals through the dataset. The top row shows the DPs, while the bottom row shows the absolute difference in intensity (detector counts) between the central DP in the top row and the DP directly above it. . 181

5.47 This figure shows five consecutive DPs obtained with an exposure time of 21.6 ms from the SiO_2 substrate of the $NbSi_x$ layer. The top row shows the DPs, while the bottom row shows the absolute difference in intensity (detector counts) between the central DP in the top row and the DP directly above it. 181

5.48 Images from the SiO_2 substrate of the $NbSi_x$ film showing the masked version of the first SiO_2 diffraction pattern in the dataset, along with the τ and β values calculated from each pixel. 182

5.49 a), b) and c) show examples of non-linear least squares KWW fitting to $g_2(t)$ from pixels in the SiO_2 diffraction patterns from the substrate of the $NbSi_x$ film. d) shows a histogram of the distribution of τ values calculated from all of the pixels in the masked pattern. Results from the annular masked region are shown with e) a KWW fit to the average $g_2(t)$ of all the pixels and f) histograms of τ and β calculated from each pixel. 183

5.50 DPs obtained from the SiO_2 multilayer film layer using an exposure time of 21.6 ms. This figure shows patterns taken from the dataset at regular 971.1 ms intervals. Arrows are pointing to features of interest. 185

5.51 DPs obtained from the SiO_2 multilayer film layer using an exposure time of 21.6 ms. This figure shows twelve consecutive patterns taken from the dataset. Arrows are pointing to features of interest. 186

5.52 Normalised variance obtained from diffraction patterns in the SiO_2 layer using 21.6 ms exposure time. Variance curves from the summed diffraction patterns over ten different timeframes are shown. 187

5.53 Sum of all 500 DPs from the SiO_2 multilayer film layer, showing selected diffraction spots. 187

5.54 Line plots of the summed intensity within each of the four spots as a function of time. 188

5.55 Plots of the summed intensity for the first 2000 ms of the dataset within each of the four spots. A rolling average and standard deviation from a window 5 patterns wide are overlaid. 189

5.56 This figure shows five DPs obtained with an exposure time of 21.6 ms from the SiO_2 multilayer film layer. These are spread at 2158 ms intervals through the dataset. The top row shows the DPs, while the bottom row shows the absolute difference in intensity (detector counts) between the central DP in the top row and the DP directly above it. 189

5.57 This figure shows five consecutive DPs obtained with an exposure time of 21.6 ms from the SiO_2 multilayer film layer. The top row shows the DPs, while the bottom row shows the absolute difference in intensity (detector counts) between the central DP in the top row and the DP directly above it. 190

5.58 This image shows images from the SiO_2 layer of the Ta_2O_5 film, these are the masked version of the first diffraction pattern in the dataset, along with the τ and β values calculated from each pixel. 191

5.59 a), b) and c) show examples of non-linear least squares KWW fitting to $g_2(t)$ from pixels in the SiO_2 diffraction patterns from the multilayer Ta_2O_5/SiO_2 film. d) shows a histogram of the distribution of τ values calculated from all of the pixels in the masked pattern. Results from the annular masked region are shown with e) a KWW fit to the average $g_2(t)$ of all the pixels and f) histograms of τ and β calculated from each pixel. 192

List of Tables

4.1 Superconducting critical temperatures for the materials investigated in this chapter. . . . 73

4.2 Microscope settings used in FEM experiments on the $MoSi_x$ film deposited by co-sputtering Mo and Si. . . . 75

4.3 Microscope settings used in FEM experiments on the $MoSi_x$ film deposited from $MoSi_{.25}$ alloy. . . . 77

4.4 Microscope settings used in FEM experiments on the $NbSi_x$ film deposited by co-sputtering Nb and Si. . . . 77

4.5 Microscope settings used in FEM experiments on the WSi_x film deposited by co-sputtering W and Si. . . . 77

4.6 Interatomic distances from Mo atoms to neighbouring atoms in the A15 Mo_3Si structure. . . . 119

5.1 Illumination conditions for each of the datasets acquired in this chapter. 137

5.2 Analysis of the FWHM of intensity peaks from four spots in the DPs obtained from the SiO_2 substrate of the $NbSi_x$ film using a 1 ms exposure time. . . . 152

5.3 Analysis of the FWHM of intensity peaks from four spots in the DPs obtained from the centre $NbSi_x$ film using a 21.6 ms exposure time. . . . 160

5.4 Analysis of the FWHM of intensity peaks from four spots in the DPs obtained from the SiO_2 substrate of the $NbSi_x$ film using a 21.6 ms exposure time. . . . 178

5.5 Analysis of the FWHM of intensity peaks from four spots in the DPs obtained from the SiO_2 layer of the Ti:Ta_2O_5/SiO_2 multilayer film using a 21.6 ms exposure time. . . . 188

5.6 Structural relaxation times τ from annular region around principal diffraction peak . . . 194

6.1 Estimated composition of SNSPD films from EELS-SI analysis. . . . 199

List of Publications

The author has contributed to the following publications.

[1] *Sharp, J., Muller, I.C., Mandal, P., Abbas, A., Nord, M., Doye, A., Ehiasarian, A., Hovsepian, P., MacLaren, I., Rainforth, W.M.* Characterisation of a High-Power Impulse Magnetron Sputtered C/Mo/W wear resistant coating by transmission electron microscopy, *Surface and Coatings Technology*, (2019), **377**, *124853*

[2] *Lindgren, P., Hallis, L., Hage, F.S., Lee, M.R., Parnell, J., Plan, A., Doye, A., MacLaren, I.* A TEM and EELS study of carbon in a melt fragment from the Gardnos impact structure, *Meteorics and Planetary Science*, (2019), **1-12**, *13381*

[3] *Banerjee, A., Baker, L.J., Doye, A., Nord, M., Heath, R.M., Erotokritou, K., Bosworth, D., Barber, Z.H., MacLaren, I., Hadfield, R.H.* Characterisation of amorphous molybdenum silicide (MoSi) superconducting thin films and nanowires. *Superconductor Science and Technology*, (2017), **30**, 8

Acknowledgements

I would like to thank my supervisor Dr Ian MacLaren for his support, advice and constructive criticism throughout this work. I must also thank Professor Andrew Harvey, Professor Ian Underwood and everyone else involved in the Centre for Doctoral Training in Intelligent Sensing and Measurement for providing me the opportunity to do this research.

This work would not have been possible without the help of Ian MacLaren in driving the microscope for FEM measurements and collecting the EELS-SI datasets, Dr Martin Hart for getting me started and showing me how to conduct FEM measurements and Dr Gary Paterson for his assistance with writing code to resolve issues with diffraction patterns. I also appreciate the help of Dr Sam McFadzean, Colin How and William Smith for their technical help and advice in various different areas. I must also show appreciation to all my colleagues who were part of the CDT-ISM for their help throughout this project.

My friends have been a great source of support during these last few years so thank-you to Caleb, Emmanuel, Miikke and Kristoffer.

Thank you to Abby for all your help, including all the food and everything. It would have been much more difficult without you.

Finally, I thank my family for their support throughout this PhD and everything that lead up to it, especially my parents and grandparents.

School of Physics and Astronomy

Statement of Originality to Accompany Thesis Submission

Name: Alastair Kelway Doye

Registration Number:

I certify that the thesis presented here for examination for a PhD degree of the University of Glasgow is solely my own work other than where I have clearly indicated that it is the work of others (in which case the extent of any work carried out jointly by me and any other person is clearly identified in it) and that the thesis has not been edited by a third party beyond what is permitted by the University's PGR Code of Practice.

I declare that the thesis does not include work forming part of a thesis presented successfully for another degree.

I declare that this thesis has been produced in accordance with the University of Glasgow's Code of Good Practice in Research.

I acknowledge that if any issues are raised regarding good research practice based on review of the thesis, the examination may be postponed pending the outcome of any investigation of the issues.

Chapter 1

Introduction

Throughout history, human beings have striven to advance in knowledge and technology. Various inventions and discoveries have revolutionised how we interact with the world. The world we know today is vastly different to even 100 years ago. Since ancient times, the materials available to us have played crucial roles. They have been used for trading, making tools, constructing buildings, fashioning clothing and almost anything manufactured by humans. During the last century there have been major advances in our understanding of why materials behave in certain ways, as well as our knowledge of how their structure is connected to useful properties. Techniques for gaining insight into how materials function are becoming much more advanced. This enables a better grasp of what causes useful functions of a material, which allows for improved understanding of methods for optimising materials for a given application. This is critical to knowledge-led advances in materials, rather than simple trial and error or opportune discovery. Gaining an understanding of the properties of materials and how they could be used is vital as we look to the future.

1.1 The Origins of Materials Research

Alchemy was first recorded in ancient Egypt, where it was used in the mummification of dead bodies, this means that they had some chemical knowledge. When the Greeks conquered Egypt, their studies of how they viewed the four elements of nature (fire, earth, air and water) blended into the knowledge of the Egyptians. In the 8^{th} century, alchemy was brought by the Arabs to Spain, from where it spread across Europe. At

that time, alchemists strived to change metals into gold, by using a mythical substance called the Philosophers Stone. In Europe, alchemy lead to the discovery of amalgams, as well as advancing the knowledge in other chemistry and the apparatus required. In the 16^{th} century, there were two groups of alchemists; the first focussed on discovering new compounds and how they react, while the other took more interest in the metaphysical side. The first group led to what is known now as chemistry.

The Greek philosopher Democritus believed that if you cut an object into ever smaller chunks, eventually there would be a point at which you couldn't cut them into smaller pieces. These uncuttable pieces he called *atomos*, this is where the word *atom* comes from. Aristotle however disagreed with Democritus, so the idea of atoms was largely abandoned for 2000 years, until John Dalton, a British chemist rekindled the theory in around 1800. His theory is mostly accepted today, apart from the idea that atoms are the smallest particles. Dalton's model of the atom was that it was a solid ball, however when electrons were discovered, the Scottish scientist Thomson created the plum pudding model, where negatively charged electrons were embedded in a positively charged volume of the atom. Rutherford then made the discovery that atoms had a positively charged nucleus with electrons outside it.[1] Bohr then improved on Rutherford's model by including quantisation of energy levels based on a simple numerical formula.[2] The appearances of these energy levels was explained by quantum mechanics, based on the Schrödinger equation applied to an atom, combined with Pauli-Dirac statistics.

There are 118 elements in the periodic table, some of which were discovered in ancient times, such as; copper, sulphur, silver, tin, antimony, gold, mercury and lead. The first element that we know to have been scientifically discovered in the modern era was phosphorus in 1649. After this, the number being discovered increased rapidly in the 1700s, starting with cobalt, platinum and nickel. Most of the elements we know today were discovered in the 1800s and 1900s, with just a few super-heavy elements discovered in the 2000s.

As the number of known elements grew, patterns in their properties were observed, allowing them to be arranged into different classifications, particularly in the now well known periodic table of Mendeleev. They are now arranged into these categories: alkali metals, alkaline earth metals, lanthanoids, actinoids, transition metals, post-transition metals, metalloids, other non-metals and noble gases.

There are four states of matter that can be seen in our everyday lives: solid, liquid, gas and plasma, although there are other states that occur under sometimes extreme conditions. Solids are constructed of atoms that are tightly packed together and generally fit into two categories; crystalline or amorphous. Crystal structures were first experimentally determined in 1913 by W.H and W.L Bragg, when they determined the

crystal structure of diamond.[3] This was made possible by the discovery that X-rays are diffracted by crystals in 1912. X-ray diffraction, and diffraction of other forms of radiation have since revolutionised our ability to solve crystal structures.

1.2 Materials by Design

Is it possible to design materials so that they are able to fulfil certain requirements? Many different applications require materials which have very specific properties, whether those are optical, electrical, chemical, physical or anything else.

The structure and properties of a material are linked. For example, the type and strength of bonding could make a material either hard or soft, brittle or ductile. Distance, number and arrangement of the nearest neighbours can affect the electric, dielectric or magnetic properties – causing some materials to be insulators, while others are metals or semiconductors. Some materials have permanent magnetic orderings, or a paramagnetic response that is strong, while others do not. Some materials have a superconducting state at low temperatures, while most do not. All of these properties depend on atomic structure, so we must understand this in order to understand the properties of materials.

In order to optimise materials, it is vitally important that they are designed with the best properties for each specific application, an approach that can be called materials by design. The number of publications concerned with materials design has experienced almost exponential growth.[4] Some areas where materials by design is at the forefront of research are; discovery of thermoelectric materials,[5] perovskite photovoltaics,[6] organic semiconductors for PV and LEDs,[7] solid-state lighting,[8] catalysts for chemistry,[9] Li-ion batteries,[10] multifunctional metallic alloys,[11] transparent materials that are conducting,[12] and functional ceramics.[13]

The Materials Genome Initiative, which was created as a multi-agency enterprise, was initiated in an attempt to create infrastructure, resources and policy so that U.S. institutions are able to conduct research, manufacture and implement new materials.[14] It aims to do this at two times the speed of traditional methods, at a much lower cost. It has been involved in projects such as the redesign of the nickel coin, and is involved in projects over a wide range of applications, such as renewable energy generation, energy storage, national defence and supercomputing. It is estimated that the economic impact of having enhanced Materials Innovation Infrastructure would be somewhere between $123-$270 billion every year.[15]

Characterising atomic structure is a key part of understanding structure-function relationships, and is thus a key part of this agenda where a future in which materials and structures containing materials (e.g. thin film systems) are designed, not just discovered by trial and error.

1.3 Amorphous Materials

Amorphous materials differ in their atomic structure from crystalline materials. Atoms within crystalline materials follow regular arrangements with a periodicity that persists over a substantial number of atomic diameters, while each atom has set connections with lattice points in the crystal. There are usually symmetry elements in crystal structures, such as mirror planes, or rotation axes, which leave the crystal looking identical at different points in its rotation. This means that crystalline materials show both short range order (SRO) and long range order (LRO). Amorphous materials are different as their atomic structure does not repeat itself over more than a few atoms at a time. Because of this, amorphous materials possess SRO, but do not exhibit any LRO. Some examples of common materials that show SRO and no LRO would be liquids, waxes or glasses. Some materials could be crystalline/ordered in one state or phase, and disordered in another, for example SiO_2, which when cooled relatively quickly from the melt forms a glass, but when cooled slowly can form crystals such as quartz. These are two solid materials with the same chemistry, similar SRO, but different LRO.

Amorphous materials can occur naturally, such as when lava that has a high silicon content cools (e.g. pumice, obsidian), or in organic materials that have solidified, (e.g. amber). In most cases they are man-made, often by quenching/cooling a liquid phase very quickly or by depositing atoms in the vapour phase onto a relatively cool substrate.

1.4 Uses of Amorphous Materials or Glasses

There are many uses of amorphous solids. In fact, we see/use them all the time. As mentioned earlier, glass is an amorphous material, based on SiO_2. In addition to well-known devices such as glasses for your eyes, there are many different optical applications of amorphous materials. These include camera lenses and optical filters where a combination of layer thickness and refractive index in a multilayer coating is used to either enhance transmission and minimise reflection of certain wavelengths of light, or to exclude and reflect other wavelengths of light. Glasses are also used in high

speed data transfer in optical fibres, and some photonic semiconductor devices can be formed using amorphous silicon.

Amorphous silicon thin films can be used for various applications. They are widely used in solar cells, however these amorphous silicon thin film solar cells often have a low efficiency compared to other options.[16] The solar cells are widely used as a dependable source of power for devices such as clocks, calculators and watches.[17] Hydrogenated amorphous silicon thin films could also be used for flexible photovoltaic devices.[18] Amorphous silicon alloys also have many applications in photovoltaic solar cells, electronic devices such as diodes and transistors,[19] image sensors as well as other optoelectronic devices

The semiconductor industry has used SiO_2 glasses as the gate dielectric material for many years, and also uses SiO_2 to passivate the surfaces of devices and prevent extraneous conduction.[20–23] In recent years, further miniaturisation in CMOS technology has led to the replacement of SiO_2 with a higher dielectric constant HfO_2-based gate dielectric.

Metallic glasses, or amorphous metals, have different areas of application. Some show ferromagnetic properties. It is possible to pattern amorphous metals on very short length scales that could be as low as 13 nm, which means that they are useful in nanoimprint lithography.[24] In cases where they have a high electrical resistance, they can be used to make devices such as computer memory or sensors for magnetic resistance.[25]

Metallic glasses have interesting mechanical properties, including high mechanical strength and hardness, as well as good wear and corrosion resistance. This means that they could be applied in a wide range of areas such as sports equipment, aerospace, or naval applications.[26] High corrosion resistant metallic glasses can be used in surgical instruments or in biomaterials for prosthetics that can be implanted in the body.[27, 28]

Filters can be created for infrared radiation using multilayer optical coatings with alternating high and low refractive index. One example of their use is in capnography, where the carbon dioxide (CO_2) in breath is detected using the CO_2 absorption wavelength at 4.28 μm. Other gases such as N_2O have absorption wavelengths very close (4.50 μm), so will be filtered out.[29]

High precision interferometers such as those for gravitational wave detection require mirrors that are low noise and highly reflective at very specific wavelengths (currently 1064 nm for Advanced LIGO, although this may change in future detectors). These

can be created by depositing multilayer coatings formed with amorphous materials onto the mirror surface.[30]

The applications shown here are a small selection of the applications that amorphous materials have, in various areas. They can be found everywhere, from devices for everyday use to the cutting edge of science and technology.

1.5 Structural Properties of Amorphous Materials

Over the years there has been a lot of discussion over the atomic structure of amorphous materials like amorphous silicon (a-Si) and amorphous silica (a-SiO_2). Much of this debate has been speculation on whether Zachariasen's (continuous random network) model of an ideal glass [31] is compatible with their atomic structures, or if they retain some structural fragments that are present in their crystalline forms. Whilst at the time of Zachariasen (1930s) it was only possible to experiment on macroscopic properties. Conducting experiments on the short or medium range atomic structure using diffraction techniques was not possible until X-ray [32] and electron scattering [33–37] techniques arrived later.

Zachariasen's model for an oxide glass formed of element A and oxygen states that: an oxygen atom cannot be linked to more than two A atoms; there must only be a small number of oxygen atoms surrounding an atom A; polyhedra of oxygen must only share corners, not faces or edges; in a 3D network, at least three of the corners in every oxygen polyhedron should be shared.[31] Early models of amorphous materials based on Zachariasen's model were constructed using physical balls and sticks.[38]

In the 1960s, extra momentum was added to the investigation of the atomic arrangement of amorphous solids.[39–41] This led to two main areas of interest: firstly, the study of the packing of spheres and molecules; secondly, the simulation of atomic structure using molecular dynamics methods. There are two main groups of amorphous solids: non-crystallisable and crystallisable. Non-crystallisable materials would include solids formed from cross-linked polymers. Some metal oxides, metallic/metalloid glasses and amorphous solids where crystallinity can be increased by annealing are crystallisable.

There are four groups that amorphous materials can fit into. They are metallic glasses, inorganic glasses, organic glasses and amorphous thin films.

Most amorphous materials are formed of more than one element. A pair distribution function (PDF) describes the correlations between one atom and its neighbours. A PDF

from one particular element in the material can be obtained using X-ray or neutron scattering experiments. Combining PDFs with simulation of the atomic structure is one way to attempt the assesment of structure in the material.

Materials can be deposited or grown on a substrate in multiple ways, any of which can result in properties of the material being different, resulting from differences in the atomic structure caused by differences in the deposition.

There are various techniques that can be used to create amorphous thin films. These include: electron beam evaporation;[42] atomic layer deposition;[43] particle irradiation; sputtering;[44, 45] liquid quenching;[46] and ion mixing/implantation [47]. Each of these techniques will create films with different structures and properties. Moreover, variations in process parameters including the details of how the substance is deposited (e.g. magnetron power in sputtering, or gas pressure in atomic layer deposition), and in the substrate temperature can have a huge effect on the structure and properties of the film.

1.6 Conclusions

Materials are key to human progress, and history has shown that the discovery of new materials revolutionises how we live.

It is well established that the properties of materials are linked to their atomic structure. This means that understanding their atomic structure is key.

In the future, as experimental methods improve, so will our ability to observe the atomic structures of materials. This enables a materials by design approach in the future, where materials are created based on our understanding of how they behave.

There are many crucial materials that are amorphous (no LRO). Conventional methods of crystal structure solution do not work on these materials, so in order to apply a materials by design philosophy to amorphous materials, especially thin films, adapted techniques will be needed.

In the next chapter, we will discuss some of the methods that can be used to investigate the atomic structure of amorphous materials, both as bulk materials and as thin films.

Chapter 2

Investigating the Atomic Structure of Amorphous Materials

2.1 Introduction

The methods most commonly used to determine the atomic structure of materials are based on diffraction. An incident beam, which could be formed from electrons, neutrons or X-ray photons, is formed into a probe and focussed on the material. As it passes through, the beam is deflected through coherent elastic scattering, which creates diffraction patterns. Depending on the availability of experimental facilities and the material information you require, you can choose from any of these probe types.

These methods all appear to be similar, in that they all rely on the geometrical theory of diffraction [48], however they differ in some of their properties. The probe sizes used for each technique are different, while there are different ways that the beam can be manipulated for each type. One of the most fundamental differences between these techniques is in the way that their elastic and inelastic scattering cross sections differ. These cross sections are what describe how the beam probe interacts with the specimen material.[49] Electrons are scattered by the electrostatic potential (Coulomb force) of other charged particles, such as the atomic nuclei and electron shells [50], neutron scattering occurs from interactions with atomic nuclei by their delta function potential [51], X-ray scattering is a result of interactions with the electron shells of atoms, and is not affected by the atomic nuclei.[52] The cross sections for X-rays and electrons are

related, since the number of protons in the nucleus and number of electrons surrounding it are closely related and are both electromagnetic interactions. Neutron cross sections are totally unrelated to the X-ray and electron cross sections as they are a function of the nuclear structure and the interaction is governed by the strong nuclear force.

Coherent elastic scattering of electrons within the sample is stronger than that for both neutrons and X-rays, the ratios of coherent scattered intensity for X-rays, electrons and neutrons are $1 : 10^6 : 10^{-2}$.[49] It is possible to collect very large amounts of diffraction data very quickly using electron diffraction methods, much faster than for neutron or X-ray scattering, this provides an additional advantage to this technique.

The amorphous thin films studied in this thesis were fabricated using variations of the sputtering process. A basic sputtering process involves the substrate, target and gas (usually argon) in a plasma. When the gas atoms in the plasma lose electrons, they become ions with positive charge, these are accelerated onto the target (cathode), when they strike the target with a kinetic energy high enough to dislodge atoms, these dislodged atoms then cross the deposition chamber and hit the substrate (anode). As this process continues, a film composed of atoms from the target grows on the substrate.

The materials analysed in this thesis all are either very thin layers (around 30 nm or less) or have features within that are very small. This means that the experimental techniques required to analyse these materials must have both a small probe size and have the ability to move the probe in a controlled manner over small increments that can be as small as 1 nm.

2.2 Describing Atomic Structure in Amorphous Materials

All of the materials analysed in this thesis are amorphous, which comes from the Greek word "$\alpha\mu o\varrho\varphi o\varsigma$ ", meaning "without form" or "shapeless". Although these materials don't have long range structure as a crystal would, as summarised briefly in Chapter 1, they do have short range order. This short range order contains data concerning the structural properties of the material.[53] If diffraction patterns are taken from these materials over an adequate volume, such that they are an average over that volume, one sees diffuse rings of diffracted intensity distributed at different radii. There are no diffraction spots visible in these diffraction patterns, due to the amorphous nature of the atomic structure. If these diffraction patterns are azimuthally averaged, intensity profiles are acquired, the radius at which the peak appears is related to how the nearest neighbour atoms are arranged around an arbitrary atom. An example of this kind of

diffraction pattern and its intensity profile is shown in Figure 2.1.

Amorphous structures are generally described by using statistical functions that describe how pairs of atoms are distributed. These functions can be attained from different sources, such as from theory, experiment or models. The most common experimental sources of these are neutron or X-ray probes, but electron probes can also be used. Using electrons has advantages over the other experimental techniques, due to electrons having a smaller interaction potential and wavelength. The radial distribution function (RDF), or $J(r)$ is the most commonly used function, alongside the pair distribution function (PDF) $g(r)$. For information on the correlation functions that are often used to describe scattering see the paper by Keen.[54]

An RDF or PDF describes the short range order (SRO) of a material, over a length scale of around one or two atomic spacings. Some characteristic quantities of SRO would be the distribution of bond lengths to nearest-neighbours, average bond length and coordination number. Medium range order (MRO) describes the order of a material over a larger distance, between around 1-5 nm. While the SRO of a material can be easily investigated, it is more difficult to investigate the MRO of a material. If an amorphous material had a large amount of MRO, it is verging on nano-crystalline - in fact, drawing a hard and fast line between a well-ordered amorphous material and a very fine grained nano-crystalline material is impossible.

In the following sections some of the experimental methods that can be used to describe the atomic structure of materials through these statistical functions will be discussed.

2.3 EXAFS

X-ray absorption spectroscopy (XAS) is the overarching technique that is comprised of both X-ray absorption near edge structure (XANES) and extended X-ray absorption fine structure (EXAFS). These techniques use X-rays with a narrow energy resolution, which are focussed on the sample, both the incident and transmitted intensity of the X-rays is recorded as the X-ray energy incident on the sample is gradually increased. The transmitted intensity of the electrons is given by the equation

$$I_t = I_0 e^{-\mu x} \tag{2.1}$$

where I_t is the transmitted energy of the X-rays, I_0 is the incident energy of X-rays on the sample, μ is the absorption coefficient and x is the thickness of the sample. The

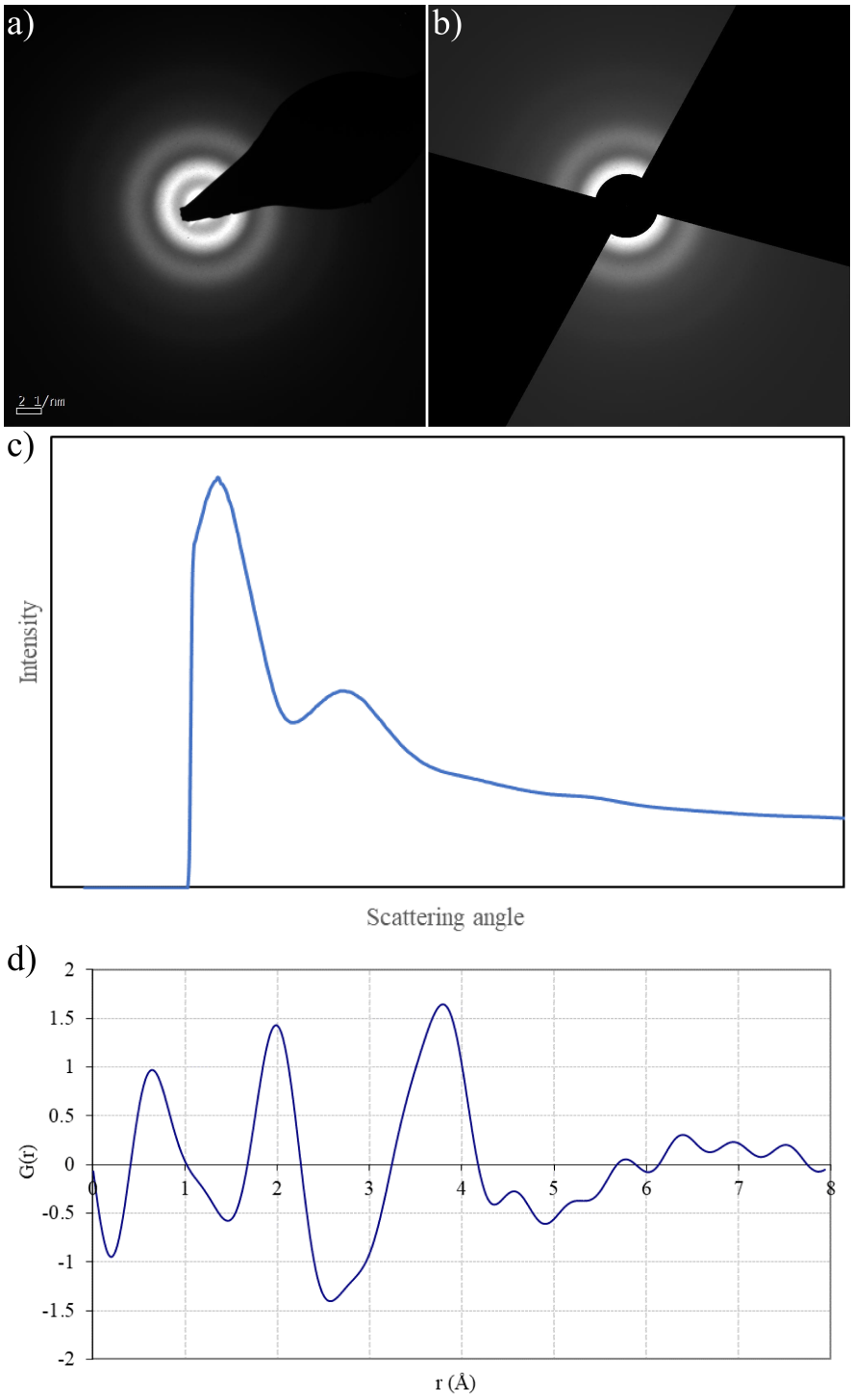

Figure 2.1: a) Diffraction pattern of amorphous Ti doped Ta_2O_5. b) Diffraction pattern from a) masked to enable radial averaging. c) Radial average intensity of diffraction pattern shown in b). d) Reduced density function (RDF) obtained from the diffraction data.

absorption coefficient is defined as;

$$\mu = \frac{-ln(I_t/I_0)}{x} \tag{2.2}$$

If the energy of the incident X-rays is equal to the binding energy of an electron within an atom in the sample, there will be a large increase in the number of X-ray photons absorbed within the sample, causing a drop in the X-ray intensity that is transmitted through the sample. This reduction in X-ray intensity is an absorption edge. Because each different element has a specific collection of electron binding energies, each has its own set of absorption edge energies. This means that it is possible to identify elements based on the X-ray absorption edges present from XAS.

Due to photoelectrons produced in the X-ray interactions with atoms, there is interference with the incident X-rays. This can be observed in the EXAFS spectra and can be used to find information on the chemical coordination of the material, as well as the local ordering.[55, 56] The probability of a photoelectron being produced at different energies is altered by interference between the different paths for photoelectron emission, such as the reflections from neighbouring atoms. This means that the distance to the nearest atoms, as well as their elemental identity affect the oscillations that occur after the edge. If these oscillations are Fourier Transformed into something like a $G(r)$ plot, there is information given on the nearest neighbours. Modelling this data can enable detailed information on the coordination and nearest neighbour distances to be determined.

Because EXAFS requires a bright X-ray source that has a tuneable wavelength, experiments are often carried out at synchrotrons. There are XAS machines that could fit into a lab, but they are expensive and have a lower X-ray flux than available at a synchrotron. Beamlines at a synchrotron can be tuned to a specific range of energy, so that specific absorption edges could be investigated.

It is possible to use this for films on substrates, as it is specific to one element at a time, so can work if film and substrate have different compositions. *Bassiri et. al.* effectively utilised EXAFS for amorphous Ta_2O_5 thin films, which were thicker ataround 500 nm and had a substrate material (SiO_2) that did not have absorption edges close to those resulting from the film itself (the Ta-L_3 edge).[57] This technique would not work very well with the films investigated in this thesis, due to the probe size being too large. Some of the films examined in this thesis are as thin as 10 nm and contain Si, while they also have Si substrates. Other films have clusters that are less than 10 nm in diameter and no perfect chemical distinction between clusters and matrix.

2.4 X-Ray PDF

Pair distribution function (PDF) analysis is a technique that has been around for a while, and is described in the textbook by Warren.[58] This technique expresses what the probability is that a pair of atoms would be found at a certain interatomic distance. It has mostly been used for the investigation of types of materials that do not appear to have long range order, such as glasses and liquids. In order to obtain the PDF experimentally, the first step is to obtain the normalised total structure factor $S(Q)$, which is simply the intensity measured by the detector that has been normalised to take into account the background, along with other factors such as multiple scattering, absorption and so on. Once $S(Q)$ has been obtained, it is Fourier transformed, where $Q = 4\pi(\sin\theta)/\lambda$. This leads to the calculation of the PDF.

While this technique can be used for thicker thin films, for example on sub-micron Ta_2O_5 films using grazing incidence X-rays[59], for films that are less than 10 nm thick it is not feasible, as some X-rays will always penetrate into the substrate. It does not provide any element-specific data, so it is vital that the X-ray beam only excites the material of interest.

2.5 Neutron Diffraction

This experimental method can be used to determine both the magnetic and atomic structure of materials. It was developed in the 1940s[60], and in 1994 Clifford Shull was awarded half of the Nobel prize for his role in its development.[61] A beam of either cold or thermal neutrons is produced and directed onto the sample, producing a diffraction pattern. While this technique is similar to X-ray diffraction, neutrons much have a lower interaction cross section, meaning that they can be used in the analysis of thicker samples (mm or cm in dimensions). While this technique is ideal for finding the crystal structure and properties of a material, and is sensitive to some things not seen or hardly seen by X-rays, including ^{1}H atoms and magnetic ordering, it is also useful for determining the SRO of amorphous materials.[62, 63]

One of the drawbacks of using neutrons is that it is necessary to use a nuclear reactor or other specialised large facility (e.g. spallation at a particle accelerator) as a source of neutrons. This can only happen at a large specialised facility of which there are rather few in the world.

An advantage of this technique is that it has the ability to distinguish between different isotopes of the same element. This is because the neutron interacts with the nucleus

of the atom, instead of the electrons surrounding it, and different isotopes of the same element have different nuclear structure and different scattering cross sections. This means that artificial isotope enrichment can be used to highlight the scattering from one specific atom in a structure.

Neutrons are not charged particles, however they do have a magnetic moment, this means that they can interact with other magnetic moments. Because of this, it is possible to use neutron diffraction to reveal the magnetic structure of a material on the microscopic scale.

While neutron diffraction would work for very thick samples, it would not be appropriate for this work, as the interaction cross section is extremely low, thus the interaction volume is measured in mm and is far too large for the few nm thin films considered here.

2.6 Electron Microscopy

In 1937, the Nobel Prize for Physics was awarded to George Paget Thompson and Clinton Joseph Davisson, for their independent observations of electron diffraction.[64] These observations brought confirmation of the theory that particles showed wave like behaviour, as the 1924 hypothesis of de Broglie stated.[65] Max Knoll and his team at the Technological University of Berlin conducted research on electron optics from the late 1920s, with projects on cathode ray oscilloscopes and components for electron optics, building on the original concept of a converging electron thin lens from Busch in 1926.[66] In 1931, Ernst Ruska working with Knoll was able to generate images of mesh grids that had been magnified by a system utilising two magnetic lenses. In 1932, they found out about de Broglie's hypothesis and realised due to the fact that electrons had wavelengths much smaller than that of light, it would be possible to image on the atomic scale using electrons. Ruska then designed a new form of electron microscope, where the samples were inserted into the microscope, as opposed to placing mesh grids over the anode aperture. This instrument was capable of diffraction of aluminium and normal imaging, but still didn't improve on light resolution microscopy. The first electron microscope to achieve a resolution greater than that available with visible light was built in 1933, when Ruska observed cotton fibres.[67] Ruska belatedly won the Nobel Prize for Physics in 1986 for this discovery.[68]

The discovery of electron microscopy was of great importance, because it gives a greater resolution than that which is available from optical microscopes. Optical microscopy is limited by the Rayleigh Criterion, which states that,

$$r = \frac{0.61\lambda}{nsin(\theta)} \tag{2.3}$$

where r is the smallest distance or minimum resolvable distance between two points, λ is the wavelength of the light, n is the refractive index and θ is the semi-angle of the magnified light collected. Because of the Rayleigh Criterion, the best achievable resolution with optical microscopy is around 300 nm.

de Broglie's equations for the wavelength of a non-relativistic electron relates it to its momentum,

$$\lambda_e = \frac{h}{p} = \frac{h}{\sqrt{2m_0eV}} \tag{2.4}$$

where λ_e is the wavelength of the electron, h is Planck's constant, p is the momentum of the electron, m_0 is the rest mass of the electron, e is the charge of the electron and V is the potential difference that the electrons are accelerated through. Most transmission electron microscopes (TEMs) operate with an accelerating potential difference of 60-300 keV, this means that the electrons are accelerated to a velocity at which it is necessary to apply relativistic corrections to Equation 2.4.

$$\lambda_{e,rel} = \frac{h}{\sqrt{2m_0eV(1 + \frac{eV}{2m_0c^2})}} \tag{2.5}$$

Where $\lambda_{e,rel}$, is the wavelength corrected for relativity and c is the speed of light. When a TEM is operating with an accelerating potential difference of 200 keV, this would produce a wavelength of 2.51 pm, which would produce a resolution that would theoretically be better than atomic resolution. There are however factors that limit this resolution, such as electrical and mechanical instabilities, which stop development of better correctors. Because of this, the principal reason for not reaching this resolution is the lens aberrations. It is now possible to obtain resolutions of less than an Angstrom, due to developments in the aberration correction of TEMs, it is also possible to locate atomic positions to a precision of less than a picometer.[69] Currently the main focus of developments is how to use enhanced beam current or resolution with a small probe, most modern TEMs have a resolution of less than 1 Å.

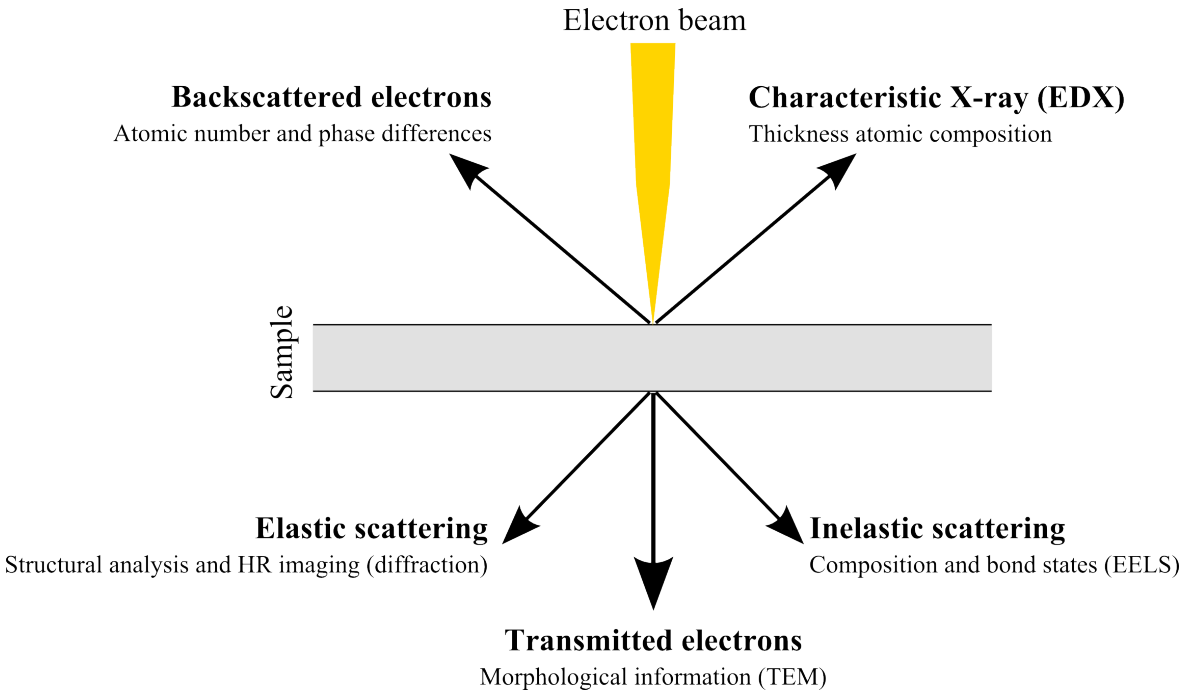

Figure 2.2: Different kinds of signals that can be observed in a TEM.

2.6.1 Electron Interactions with Matter

Electrons interact with matter electrostatically, they are negatively charged and have a low mass, this means that they can easily be deflected by travelling near to either a positively charged atomic nucleus or other electrons. All electron microscopy is dependent on these electrostatic reactions, as they are the cause of electron scattering. There are numerous ways that electrons interact with matter in an electron microscope, due to their high energy (keV), these different interactions are reviewed in Figure 2.2.

Analytical electron microscopy (AEM) utilises several of these effects to give information on factors such as the chemical and/or atomic composition of the sample under investigation. There are two main processes that produce these interactions, inelastic and elastic scattering.

2.6.1.1 Elastic Scattering

An elastic scattering process involves an interaction where total kinetic energy is conserved. Rutherford scattering is when the interaction is between charged particles, due to the Coulomb interaction. There are two ways in which electron scattering happens, either as a result of an interaction with the cloud of electrons surrounding a nucleus, or as a result of interaction with the nucleus. The former of these produces a small deviation in the angle that the electron is travelling, while the latter can produce much

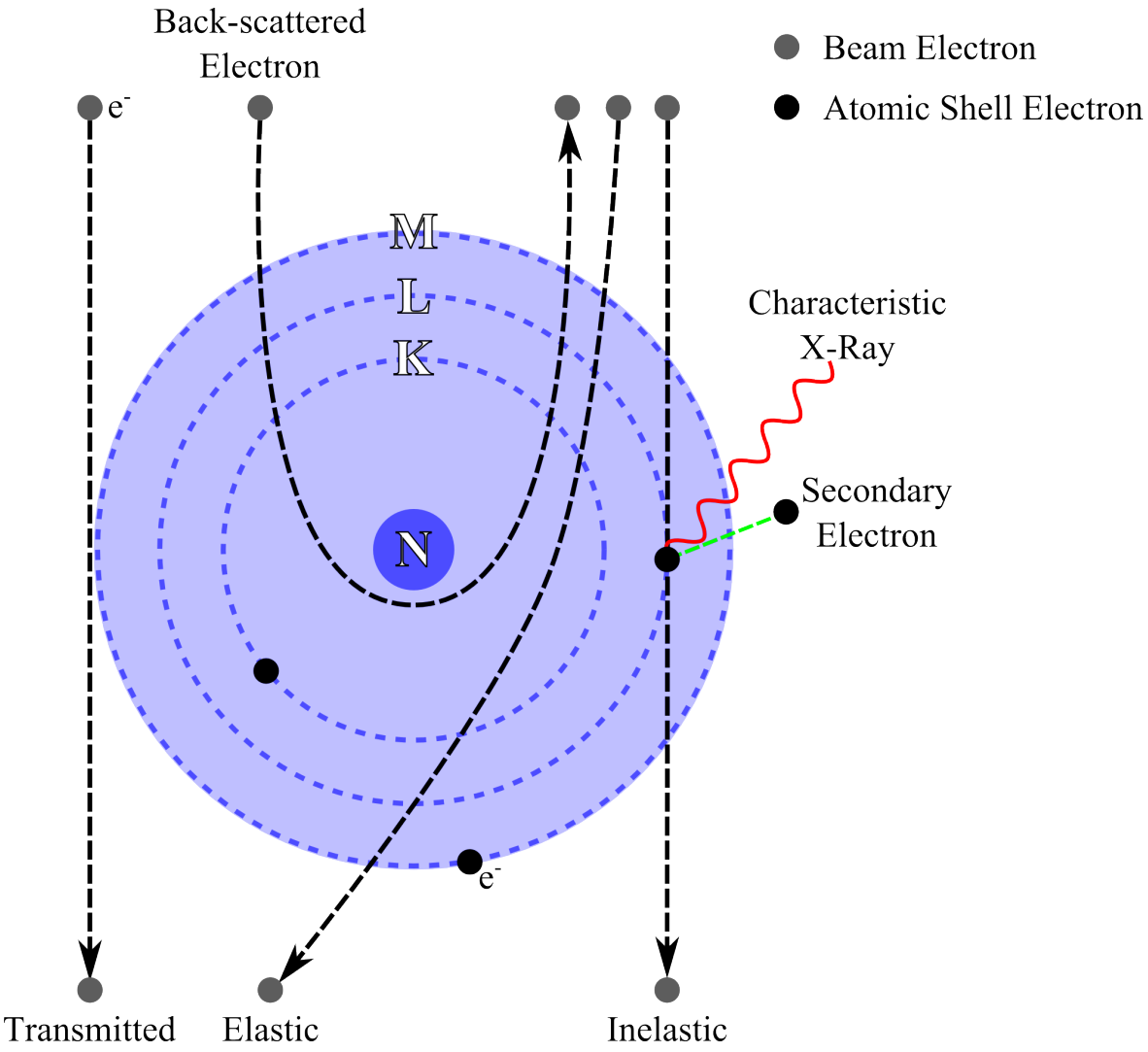

Figure 2.3: Different ways that an electron can be scattered by interactions with an atom. Redrawn from[70].

larger deviations or can even cause the electrons to be backscattered, due to the larger Coulomb force between the nucleus and electron. A summary of ways that electrons interact with atoms is shown in Figure 2.3.

Due to the fact that amorphous materials do not have regular crystallographic planes, it is necessary to conduct a statistical investigation of experimental data in order to find information on the real space ordering of the material.[71] The scattering patterns obtained from amorphous materials do show structures that are distinct to the short range order of the material. A useful handbook to elastic scattering, specifically in the context of TEM can be found in the textbook by Williams and Carter.[72]

2.6.1.2 Inelastic Scattering

Inelastic scattering occurs when there is a collision that does not conserve total kinetic energy, some of the kinetic energy is changed into another type of energy. For example a photon could be produced. There are several ways that inelastic scattering can happen, that lead to different kinds of signals, such as; Bremsstrahlung, phonons, plasmons, inner shell ionisations and secondary electrons. There are various techniques that can be used to observe these effects, as well as measuring the energy loss of electrons using electron energy loss spectroscopy (EELS) which form the basis of analytical electron microscopy.

Bremsstrahlung, or braking radiation, is X-ray radiation that is caused by a charged particle decelerating when it is deflected by another charged particle, most often due to the Coulomb force of an electron being slowed by the nucleus of an atom. As the electron's kinetic energy decreases, this energy is converted into X-ray photons. These photons can have any energy up to the limit of that of the incident electron.

Because each atom in a material is bonded to other atoms, they cannot vibrate independently, however it is possible for collective modes to move through the material, these are called phonons. These can be thought of as sound waves, and travel through the material at the speed of sound in that specific material. Phonons can be started by the electrons transferring energy to the atoms upon impact, and heat the sample. In an amorphous material, phonons are not as well defined as in crystals, because they do not have a periodic structure.

Plasmons occur in the electron cloud when incident electrons transfer energy to the free or weakly bound electrons in the sample material, this results in collective oscillations in the electron cloud of the sample.

When an incident electron travels through an atom's electron cloud, some of its energy can be transferred to an electron somewhere in that cloud. This can cause an electron to be promoted into an unoccupied energy level in either the conduction or valence band, or alternatively expelled into the vacuum, if a large enough quantity of energy is transferred. If any of these instances occur, an electron from a higher energy will then drop down to the vacancy in the inner shell, so that the most energetically favourable ground state is attained. The difference in energy between the two levels causes either an X-ray to be produced, or a secondary electron to be emitted (also called Auger electron). These X-rays are characteristic of the element/elements that make up the sample, due to each element having a discrete set of energy levels, causing the X-rays emitted to have a frequency typical of that element. Sometimes, instead of an X-ray being emitted, the excess energy can be moved to another electron, which would then

be emitted from the atom, called an Auger electron.

Another way that secondary electrons can be emitted is when an electron that is in either the conduction or valence band requires only a small energy transfer in order to overcome the material's work function, causing the electron to be emitted into the vacuum. This process causes the emission of what are called slow secondary electrons.

2.6.2 Electron Microscopy Based Analysis of the Structure of Amorphous Materials

In principle, it should be possible to use electron microscopy to study the structure of glasses. The majority of the work to date has focussed on diffraction based methods, although an absorption spectroscopy based method is also possible, in principle. These will be reviewed in the sections below.

2.6.3 Electron Diffraction RDF Measurements

The reduced radial density function or reduced density function (RDF) $G(r)$ is a statistical function that describes an atomic position in relation to a central atom. It was developed from the radial distribution function $J(r)$ and is obtained from a Fourier transform of diffraction data. Both $J(r)$ and $g(r)$ the pair distribution function can be calculated from $G(r)$. A mathematical description of the process is given by Cockayne.[73] In order to obtain a precise $G(r)$ it is vital that diffraction is collected over as large a q range as possible, as the resolution depends directly on q_{max}.

Figure 2.1 shows some of the steps taken to obtain an RDF. A diffraction pattern is obtained from the TEM, which is then masked and radially averaged, creating an intensity distribution $I(q)$. From this, the reduced intensity function $\varphi(q)$ is calculated allowing the calculation of $G(r) = \int_0^\infty \varphi(q) sin(qr) dq$, which is shown in Figure 2.1d.

Previous work at the university of Glasgow has focussed on the effects of heat treatment and doping on the mechanical loss of amorphous Ta_2O_5 mirror coatings using electron PDFs.[74–76]

Bassiri investigated how heat-treatment between 300° C and 800° C and Ti doping affected the atomic structure and composition of Ta_2O_5 films using diffraction and EELS in the TEM to calculate RDFs and atomic composition.[74] Evans carried out similar diffraction experiments on Ti doped Ta_2O_5, while he also examined the effect of heat treatment on the Ti doped films; RDFs from his data was used in RMC and

DFT simulations to predict the atomic structure of these films.[75] Hart investigated the effect of annealing in pure Ta2O5, as well as 14 % and 52 % Ti doped Ta_2O_5 in both annealed and non-annealed samples.[76]

At high scattering angles, there were issues with distortions from the lens systems that affected the quality of the calculated RDF and resulted in a Fourier Transformed $G(r)$ plot. This affected all three students. In addition to this, it would be difficult to generate a small enough electron beam that would work with these measurements for films that are only a few nm thick.

2.6.4 Scanned Diffraction / 4DSTEM and Fluctuation Electron Microscopy

In a STEM, imaging, diffraction or spectroscopy can be performed while the beam is scanned over the sample. Recently, due to advances in detector technology, it is possible to scan the probe over a large number of discrete steps, recording a diffraction pattern at each probe position, and thereby building up a 4D dataset of from each probe position, this is often known as 4DSTEM.[77] There are many different applications of this technique, such as; virtual diffraction imaging, mapping strain or phase, measuring medium-range order, measuring the thickness of samples, and various phase contrast imaging techniques.[77–79]

Ordered areas of a material will diffract coherently, regardless of how small they are. This means that even SRO will result in coherent diffraction spots or speckles. A diffraction pattern that is obtained over an area of tens of nm will average these speckles out so that diffuse rings are visible, such as those used in RDF measurement. If a small enough sample diffracted volume is used, it is possible to see individual diffraction speckles. Examples of these are shown in Figure 2.4.

2.6.4.1 Fluctuation Electron Microscopy

Fluctuation electron microscopy (FEM) looks at how atoms or nano-particles are arranged and how they scatter incident radiation coherently. FEM investigates any variations in the scattered incident radiation by the sample. It is possible to use various types of incident radiation in FEM, such as x-ray photons, visible light photons or electrons.

SRO describes the atomic structure of a material over a size region of around the nearest neighbour bonds. MRO is on a larger length scale of 1-5 nm. This range has

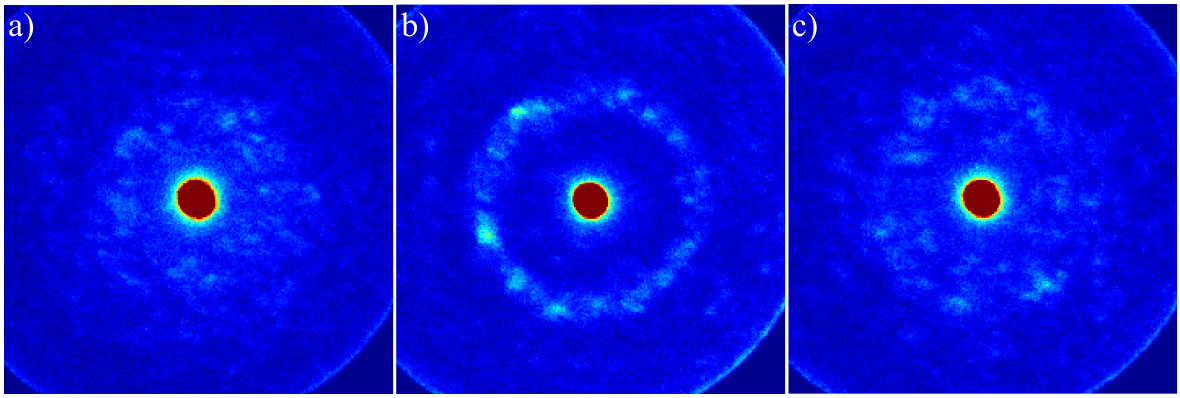

Figure 2.4: Examples of speckle patterns from; a) thin layer of amorphous silicon, b) protective layer of platinum deposited on top of sample and c) amorphous $MoSi_x$ thin film.

historically been difficult to explore, because the signal from conventional diffraction PDF or EXAFS methods is faint, but using STEM fluctuation microscopy techniques with modern direct electron detectors it has become easier.

FEM uses the azimuthally averaged intensity of a set of diffraction patterns and calculates their variance. There are two ways to do this. Firstly, by imaging in DF using a small aperture, while moving the DF tilts to change the radial and azimuthal angles, collecting a series of DF images.[80] These images will show small bright regions that are related to particular speckles and can show directly the size of the ordered regions. Secondly, a small probe can be scanned across the sample, recording a diffraction pattern at each point, then looking at the way that the diffraction pattern changes with position on the sample.[81]

FEM is sensitive to MRO because it measures the diffracted intensity from small volumes of the sample shorter than the length scale of the MRO and measures the fluctuations in that intensity, both as a total variance over all areas, and as a spatial variability in virtual dark field images (VDFI).

The equation that quantifies the diffracted intensities' normalised variance is,

$$V(\mathbf{r}, k, Q) = \frac{\langle I^2(\mathbf{r}, k, Q\rangle}{\langle I(\mathbf{r}, k, Q\rangle^2} - 1 \tag{2.6}$$

where V is the magnitude of the normalised variance, $\mathbf{r}$ is the position on the sample, k is the scattering vector, Q is a variable proportional to one divided by the real space resolution and $I(\mathbf{r}, k, Q)$ is the intensity being measured. The brackets $\langle ... \rangle$ show that this is averaged over all sample positions used in the dataset (or portion thereof) analysed.

Variable coherence microscopy, where one measures $V(k)$ while keeping Q constant, was first done by Gibson and Treacy.[80] This method can give evidence of how much MRO is present, by analysing the peak heights and can also show some evidence of ordered regions by examining the positions of the peaks. Variable resolution microscopy, where $V(Q)$ is measured while keeping k constant, is a useful technique in finding the MRO length scale characteristic for a specific sample. Measuring $V(k, Q)$ where both k and Q are variables gives the greatest possible total information, although this would require a large volume of data and be very time consuming.

When the probe size of the electron beam is on a similar length scale to that of the MRO order in the sample, the fluctuations in intensity are most sensitive. The way that MRO is quantified is by the scale of the variance in the intensity of the diffraction, as a function of the scattering vector on a scale of length that is controlled by the probe size used.

2.6.4.2 Virtual Dark Field Imaging (VDFI)

Typically, a dark field image is produced from certain electrons that have been scattered by the sample, and not including the central electron beam. An aperture is inserted into the back focal plane from the objective lens, causing only electrons that have been diffracted through an angle corresponding to the position of the aperture to be transmitted. Most of the diffraction pattern is masked in this way. Dark field imaging can be done in discrete steps, however a different image has to be taken for each diffraction angle. Virtual dark field imaging (VDFI), using the technique of Rauch and Veron [82] can be used to create VDF images that are instead formed from a diffraction dataset, where virtual apertures are formed and applied to the dataset. This means that it is possible to look for features in the dataset by creating masks that correspond to these features. These diffraction datasets can be obtained using nanometre size probes in the STEM.

2.7 Electron Energy Loss Spectroscopy (EELS)

Unlike other techniques in this chapter, EELS is not an experimental technique that directly measures the atomic structure of a material. However, it is necessary to obtain information on which types of atoms are present in the samples, so that diffraction data can be correctly interpreted. This can be achieved by using either EELS or X-ray spectroscopy in the electron microscope. EELS is used in this thesis.

EELS is an experimental technique that was first developed in the 1940s [83], that utilises the effects of inelastic scattering of electrons. It did not have widespread use until the 1990s, because of the development of better microscopes and improved spectrometers (early parallel recording spectrometers were available from the late 1980s). A sample material will be exposed to an electron beam that is almost monochromatic (except for the slight energy width of the beam from the characteristics of the electron gun, see Chapter 3). If any of the atoms in the sample inelastically scatter electrons, those electrons will lose some of their kinetic energy, in addition to their paths being slightly altered. An electron energy loss spectrometer can be used to measure the energy loss of the electrons, these energy losses can then be translated into their causes. Some of the properties of a material that can be observed from EELS spectra are; sample thickness (from the intensity of the spectrum and the zero loss peak), conduction/valence electron density (plasmon peaks), band structure (features that appear near the zero loss peak), composition of elements (from the core-loss edges), oxidation and bonding states (ELNES - near edge fine structure) and how the nearest neighbour atoms are distributed (EXELFS – extended energy loss fine structure). There are various different inelastic scattering processes that can take place within the sample, one of which is inner shell ionisations. These inner shell ionisations cause the electron interacting with that atom to lose an amount of energy corresponding to the energy that is necessary to remove an inner shell electron from that atom, the energy loss shown on the spectrometer for these events (core-loss edges) can then show which elements are present in the sample. With the aid of calculated cross sections or experimental standards, intensities in core-loss edges can be converted to quantities of elements. It is possible in this way to calculate the number of atoms of each type present in the sample, if an appropriate energy loss range is investigated.

It is, in principle, possible to use EXELFS to perform similar measurements to EXAFS of the nearest neighbour distributions around specific atoms.[84] This has an advantage over EXAFS of much improved spatial resolution measured in nanometres, but data analysis is not straightforward, and suitable absorption edges in a suitable energy range are not present for many elements. Thus, this has been little used for glass structure analysis to date.

EELS requires very thin samples, as the sample thickness increases, there is more chance that the electrons could go through multiple events that cause energy loss, this can cause a reduction in the ratio of signal to background in the edges. It is possible to use this technique with very small probe sizes of the order of nanometres, this means that is a useful tool for investigating how the atomic composition of a sample can fluctuate over small distances.

A technical description of the EELS techniques used in this chapter is given in the next Chapter.

2.8 Discussion & Summary

Decisions made on which experimental techniques to use in this thesis were based on the positive and negative aspects of them for the materials being investigated.

While EXAFS gives information on the elemental identification, chemical coordination and local ordering of a material, it requires X-ray sources with tunable wavelength that are not readily available, although the biggest factor is that it has a probe size too large for the films being investigated here.

X-ray scattering experiments in order to calculate a PDF are useful for finding the SRO in a material, however they require probe sizes far higher than those we require for investigating structure of nm scale regions within a film.

Neutron diffraction is very useful for the investigation of thick samples, due to its low interaction cross section, it is also ideal for finding information on the crystal structure of a material. This technique would not work in this case, due to the interaction volume being too large.

Electron diffraction for PDF analysis has previously been carried out here at the University of Glasgow and is useful for showing the SRO in a material. However this technique has encountered difficulties obtaining data to high scattering angles using the equipment available here due to distortions in the diffraction pattern at high scattering angle q. It is difficult to conduct analysis with probe sizes small enough for the few nm thick films here.

In this thesis, 4D-STEM techniques are used. There are various advantages to this technique. Probes of less than 1 nm diameter can be formed and scanned over a sample creating large datasets including a lot of structural information. It enables the use of FEM and VDFI to find differences in short range order between nano-volumes (regions with a diameter in the order of a few nanometres) of a material, while it is still possible to determine differences in short range order occuring in the local atomic structure. EELS-SI is also used, which enables the creation of quantitative elemental maps of the films with pixel sizes on the nm scale.

In the following chapter the principles and practice of these techniques will be more practically explained, especially as regards how they were implemented on the micro-

scopes available in Glasgow with the samples investigated in this work.

Chapter 3

Principles, Instrumentation and Practice for the Structural Characterisation of Thin Amorphous Films

3.1 Introduction

The previous chapter reviewed the methods available for the study of amorphous structure in materials, and considered the particular difficulty of doing so in thin films that are only a few nm thick. To achieve this, it was shown that the only feasible method is to use FEM. In order to do this, a STEM is required with a setup than enables the collection of datasets suitable for FEM, i.e. scanned datasets with a diffraction pattern recorded at each point. In addition to this, chemical data, specifically quantification of the proportions of elements, is necessary, and this can easily be obtained through EELS-SI in the STEM.

This chapter covers in more detail the principles of the instrumentation used, the practical details of the precise instruments used, and the procedures used in both using these instruments and the processing of the resulting data. This includes consideration of sample preparation to produce thin samples suitable for STEM analysis, STEM construction and operating principles, FEM data collection, data processing and visu-

alisation, and the principles and practice of EELS, EELS-SI, and its practice and data processing.

3.2 Samples

In order to analyse materials properly in the STEM, it is necessary to prepare samples that are suitably thin. A sample that is too thick can cause various issues such as plural scattering and incoherent inelastic scattering. This incoherent inelastic scattering can confuse the interpretation of any elastic scattering processes at low diffraction angles, as it adds a diffuse background. This could cause there to be too little variance in FEM as the volume of material being probed will be too high, especially with materials containing sub-nm ordered clusters. In addition to this, plural scattering will affect both FEM/diffractive imaging and EELS causing the data to be difficult to interpret. A sample that is too thin may result in surface damage from sample preparation causing artefacts in the signal, however with careful sample preparation this can be avoided. This means that the ideal sample is as thin as possible, while avoiding any significant amount of damage to the surface as a result of the preparation process. In this work this is achieved using focussed ion beam (FIB) techniques, in particular FIB lift out.

3.2.1 Sample Preparation Procedures

Materials examined in this thesis were all thin films deposited on silicon, amorphous silica, or steel substrates, this means that the best two options for creating STEM samples were using a focussed ion beam (FIB) or by manual preparation. The manual preparation procedure available was the conventional sandwich method, where films are first glued face to face, then cross sections are sawn off. These cross sections are then thinned/polished until they are only a few microns thick, finally ion beam milling is used to thin them to electron transparency. Due to difficulties experienced using the manual preparation method to prepare samples, only FIB techniques were used on the materials in this thesis. The FIB technique is discussed below.

3.2.1.1 Focussed Ion Beam

FIB devices have been revolutionary in preparing site-specific samples for TEM, especially those that combine FIB and SEM in one instrument, as it is possible to choose specific areas of a sample that you would like to make a specimen from, as well as being able to prepare cross-sectional samples from many different materials.[85]

A FIB machine is formed from an ion source, ion column, vacuum chamber and a stage that can be moved, which the sample is attached to. An array of detectors for various purposes are also present. If an additional SEM column is present, the two columns are placed at an angle to one another such that the beams from each of them are focussed on the point at which the sample is placed.

There are different ion sources that can be used in these instruments, with gallium most commonly used,[86] although in recent times other sources from noble gases like xenon have been widely introduced.[87, 88] The majority of FIB instruments will utilise ion beam energies that could be up to 30 keV and down to 2 kV or less.

There are certain disadvantages to using gallium as a FIB source. Gallium atoms can be implanted into the surface of a sample that is being milled, thus changing the structure and shape of the sample.[89, 90] Using gallium can also cause changes in the samples electrical behaviour.[91] Xenon plasma FIBs are not as affected by these issues, due to xenon's inertness as a noble gas.[92] Xenon plasma FIBs are less likely to suffer from amorphisation of the sample.[93] It is possible to mill at a faster rate using a xenon beam as it has a higher maximum current, improving the speed of sample preparation. [94]

Samples used in this thesis were prepared using a gallium FIB, this is because at the time they were prepared this was the equipment available.

Milling is the process where the ion beam sputters atoms away from the surface of a sample. Ions are much more massive than electrons, this means that when an ion beam is focussed on the surface of a material, it is sputtered away. The energy and intensity of the ion beam can be controlled so that the material is milled away at the rate required.

3.2.1.2 FIB Sample Preparation

In order to create a cross-sectional sample in the FIB, a variety of milling patterns, beam currents and sample tilt angles are used. A diagram showing the basic process is shown in Figure 3.1.

Before the sample is placed in the FIB, a gold layer is sputtered onto the sample. Typically, this is done at a current of 100 mA, with a deposition rate of approximately 20 nm every 15 seconds. This gives a sharp contrast between the original surface of the sample and the gold, meaning that the location and structure of that surface can be found more easily. The next step of the process is to place the sample into the FIB and choose the area of the material that a specimen will be taken from. Following this,

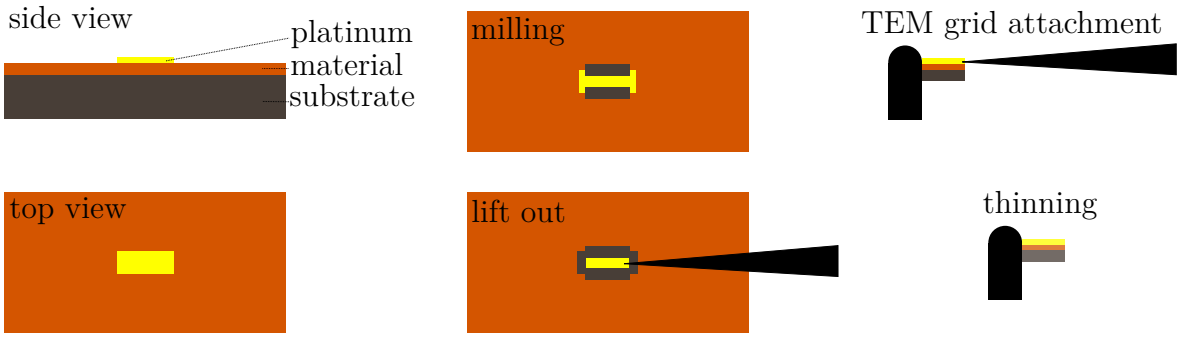

Figure 3.1: Diagram showing the FIB lift-out procedure

a thin protective layer formed from platinum or carbon is deposited onto the material, this is achieved by venting an organometallic precursor gas through a needle into an area close to the specimen, which is then decomposed using either the electron beam or ion beam, creating a nano-crystalline deposit of Pt or C. Firstly a layer with a thickness of around 500 nm is deposited using the electron beam, after which a thicker protective layer of up to 3 μm is deposited with the ion beam. Platinum deposited on the surface via an electron beam doesn't damage the surface, as it is deposited gently, the electron beam also doesn't damage the surface, this also applies to the gold evaporation on the surface. If platinum was deposited from an ion-beam straight onto the surface, the ion beam would implant into the surface during deposition. Once the platinum layer has been deposited by the electron beam, the subsequent ion-beam deposition only damages the platinum layer deposited using the electron beam.

After the protective layer has been deposited, trenches are milled away on each side of the desired region using a high ion beam energy of around 30 keV and high current in the nA range. Following this, a third side of the rectangle is milled away in a partial cut. Once these have been completed and a thin piece is left in the centre ready to be removed, a micromanipulator tip is attached to this lamella by depositing a blob of platinum between the two. The cut around the base of the sample is then completed allowing it to be lifted out freely.

When the piece of material has been removed it is mounted onto a copper support grid with Pt deposition, and is then thinned down to electron transparency. This normally occurs using lower ion beam energies (2-5 keV) and current (down to pA) than are used in the previous step, as the likelihood of surface damage affecting the area of interest is much larger during this step. The sample can be rotated to different angles so that it is thinned from both sides, and the beam currents get lower as the thickness of the sample decreases.[95] As mentioned earlier, milling with ion beams can cause the surface of the sample to amorphise or cause ion implantation into the sample, this is particularly true of FIBs that utilise gallium ion beams.[96] For this reason, the final

step is a very low energy and current beam used to polish the specimen and ensure that it is as smooth/flat as possible, since the lower energy ions will both implant less (and for shorter distances) and cause less structural damage to the surface.

3.3 TEM and STEM

A compound light microscope is formed from a light source, condenser lens to focus the light rays, a sample thin enough for transmission of light, objective lens and further lenses that form an image that can be magnified onto an eyepiece or detector.

A TEM follows a similar process, but with electrons instead of light. There are three main sections that describe how a TEM works, these are; illumination system, objective lens/stage and imaging system. A diagram showing the general structure of a TEM is shown in Figure 3.2. The electron gun and condenser lenses and apertures are the components of the illumination system, whose job is to transfer the electrons to the sample, from the source. There are two main ways that the illumination system is utilised; convergent beam and near-parallel beam. Convergent beam is mostly used for applications such as STEM imaging, convergent beam electron diffraction (CBED) and electron or X-ray spectrometry. Near-parallel beam is primarily used in selected area diffraction (SAD) and TEM imaging. There are some TEMs that have a mode called nanobeam electron diffraction (NBED), this mode plugs a hole in the region between CBED and SAD, where a beam that is almost parallel with a small convergence angle is formed.

The main section of the TEM is the objective lens and stage. Here is where the interactions between the beam and sample happen, and the images and diffraction patterns are created, before being magnified. The most important lens in a TEM is the objective lens, the standard of this lens is the determining factor in how good the information about our sample is. Modern TEMs/STEMs often have an aberration correction system to correct for lower order geometric aberrations present in the objective lens.[97–100]

There are several lenses in the imaging system that are used for magnification of the diffraction patterns or images obtained from the objective lens. After this magnification, lenses focus the diffraction patterns or images onto either a viewing screen or onto a detector, where the signal is often displayed on a computer.

A STEM is largely similar to a TEM, although it has the added ability to scan the electron beam over a sample. In a STEM, the beam is focussed into a small spot in

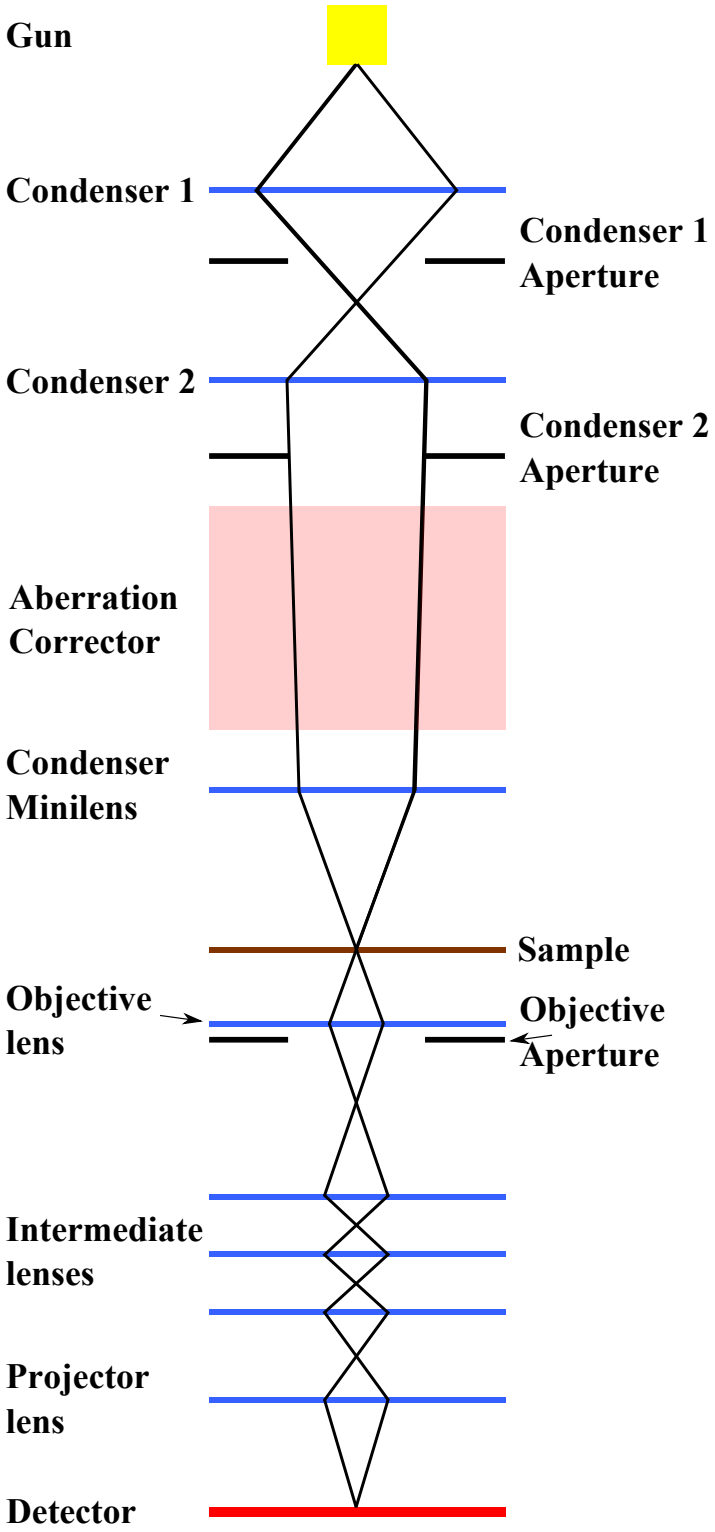

Figure 3.2: Basic diagram of the general components of a TEM.

the order of an Angstrom in diameter. An extra set of scan coils is used before the specimen, so that the convergent electron beam stays parallel to the optic axis as it is scanned over the surface of the specimen. In this way it is possible to generate images in a raster method, similar to that used in cathode ray tube televisions.

Because the beam is rastered across the sample, different types of detectors can be used. Bright field detectors collect the directly transmitted electron beam, and are used to form bright-field images. Annular dark field detectors collect electrons that are scattered by the sample through a certain scattering angle range onto an annular detector, which is positioned outside the path of the directly transmitted electron beam. ADF detectors, when positioned at high diffraction angles are commonly called high angle annular dark field (HAADF) detectors, these can form images with high contrast due to atomic number (Z-contrast). Universal detectors collect the complete diffraction pattern, creating a 4 dimensional dataset of the 2D set of scan positions and the 2D diffraction pattern collected at each scan position. X-ray spectrometers collect characteristic x-rays emitted from atoms within a sample when they are ionised by the electron beam. Electron energy loss spectrometers collect electrons that are transmitted through the sample and measure the energy they have lost as they pass through the sample. Some of these are discussed in more detail below.

3.3.1 Electron Sources

There are many different types of sources of electrons, however in order to get the best possible data from a STEM, there are strict requirements on which type of source is used. The most commonly used electron sources are; thermionic (heating) and field emission. Tungsten filaments or lanthanum hexaboride crystals are typically used in thermionic sources, while tungsten needles are used in field emission sources.

Electron sources that utilise field emission are normally called FEGs (field emission guns).[101] These operate differently to thermionic sources, utilising the fact that electric field strength at the sharpened tip is given by,

$$E = \frac{V}{r} \tag{3.1}$$

where E is the electric field strength, V is the voltage applied to a spherical point with a radius r. In order for this technique to work, it is necessary to be able to produce a very small needle point. It is possible to obtain a tip radius of less than 0.1 μm using tungsten wire. When a high enough potential is applied to the wire, the barrier of the work function decreases, allowing electrons to tunnel out. Because

of the high electric field on the tip, there is a lot of stress, so materials used for this purpose must have a high mechanical strength. One of the conditions of FEGs is that they must be operated in an ultra-high vacuum (UHV), because it is important to minimise contaminants on the surface which change the work function and suppress field emission. If the source is operated at normal temperatures, it is called a cold FEG. Alternatively, it is also possible to heat the tip somewhat in order to remove contaminants by thermal excitation in operation. These devices are called a Schottky gun or thermal FEG. Figure 3.3 shows a diagram of a FEG source.

In this microscope, the electron emitter operates at ambient temperature around 300 K and is called a cold FEG. Cold field emission can be described using Fowler-Nordheim theory, where you have a field induced wave mechanical tunneling of an electron through an exact or triangular barrier. Cold field emission can be characterised by local current density at the tip of the emitter, which in a generalised form is given by J_K^{GB}, the kernel current density, applicable to any barrier model chosen.

$$J_K^{GB} = \frac{aFc^2}{\phi} e^{\frac{-v_F^{GB} b\phi^{3/2}}{F_C}} \tag{3.2}$$

where the first Fowler-Nordheim constant $a = e^3/8\pi h_p$, the second $b = (8\pi/3)(2m_e)^{1/2}/eh_p$, then ϕ is the local work function, F_C is the barrier field found at the tip of the emitter and finally v_F^{GB} is a form correction factor for the model barrier of choice.

The system works by positively charging the 1st anode with respect to the tip, delivering the extraction voltage that is needed for the electrons to tunnel out from the tip so that the electrons are emitted from a region around 10 nm in diameter. After the electrons have been extracted, the 2nd anode acts as an electrostatic lens to form a first crossover. FEG sources are the most coherent and brightest sources of electrons for TEM. In addition to this, due to cold FEGs having the source size that is smallest compared to other types, they give an electron beam with the best possible spatial coherence, their energy spread is the least obtainable without using monochromation.[102] After the electrons have passed the 2nd anode, they then pass through an accelerator stack that accelerates the beam to the full beam energy.

The emission and lifetime of a CFEG source is strongly affected by gas adsorption and ion damage, which lead to a decrease in emission current and unstable emission current. A pulsed heating current is applied to the tip do desorb gas molecules and anneal out damage from ion collisions, this process is called flashing. After the source has been flashed, emission current will rapidly decrease before stabilising. Depending on the microscope parameters, a stable emission current can last for a few hours or

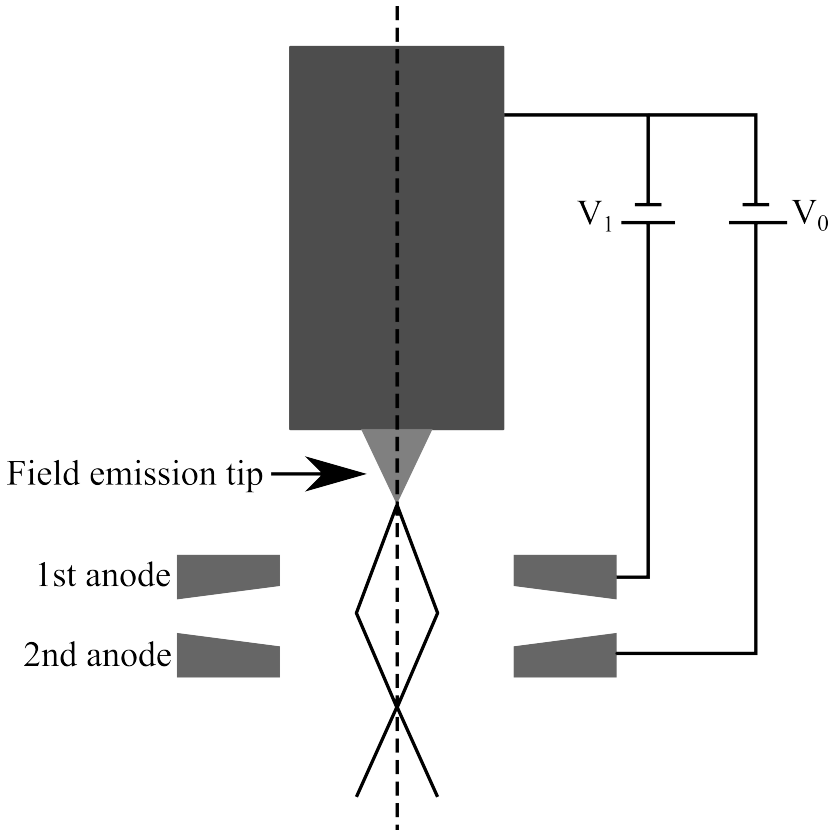

Figure 3.3: Diagram of a FEG electron source.

many hours, although there is flicker noise due to the gas adsorption, this means that over shorter timescales (milliseconds) the emission current fluctuates.[103, 104]

3.3.2 Components in the STEM column

The STEM column is comprised of several components. A basic outline of the components of a STEM column is shown in Figure 3.2. There are several sets of electromagnetic coils, apertures and electromagnetic lenses. The electromagnetic coils can be used to tilt and deflect the beam, and are used to make sure that the electron beam is centred on the optic axis, as it passes through the column.[105][p141-171]

Coils of copper wire inside cylindrically symmetric pole pieces of iron form the electromagnetic lenses. When a current passes through the coil, a magnetic field is formed along the beam direction which converges the electron beam as a consequence of the Lorentz force on rays passing the lens at an angle to the optic axis.[66] The magnetic field is stronger further from the optic axis. This can be used in the same way as a converging (convex) lens for light, and combinations can be used to magnify images, or focus to a spot, just as in a compound light microscope.

There are retractable or interchangeable apertures inserted in the condenser lens as-

semblies, which are often made out of molybdenum or platinum foil, and which are principally used to define the electron beam convergence angle in the probe.

3.3.3 Aberrations in TEM/STEM

Electron beams undergo both chromatic and geometric aberrations. Chromatic aberration occurs where the lenses have a focusing power that depends on electron beam energy and the electron beam has a significant energy spread. In the work in this thesis, the beam energy was 200 kV and the energy spread was less than 1 eV, and chromatic aberration had no significant effect on the imaging performed herein (although it had a slight effect on setups for EELS). Setting up camera length programs for optimum transfer of electrons having lost large amounts of energy is a separate topic and not the focus of this thesis, but such a program was used for the collection of the Mo-$L_{2,3}$ edge data in Chapter 5. More details of such lens programs are available elsewhere.[84, 106, 107]

When chromatic aberrations are not the limitation, such as at high beam energies, geometric aberrations become the limiting factor and affect the electron beam. Some examples of geometric aberrations are; defocus, coma, astigmatism and spherical aberration.

When the beam is not focussed, changing the current through the lens will change the strength of the lens to focus the beam. So, defocus is simply corrected.

When the electron beam is not aligned exactly along the optic axis, the coma aberration is visible. There are beam coils that can be used to tilt and shift the electron beam so that it is aligned along the optic axis, this eliminating coma. This is a standard part of microscope alignment.

Astigmatism is an effect that happens when the electrons move through a magnetic field that is not uniform as they circle around the optic axis. This effect can be corrected using stigmators, which are either quadrupole or octupole lenses that have independent wiring for different poles.

Spherical aberrations occur when a lens does not act in the same way for off-axis electrons. In the electromagnetic lenses used in a STEM, electrons that are at larger angles to the optic axis will be bent more strongly back in the direction of the optic axis, and this effect is intrinsic to all cylindrically symmetric electron lenses [Scherzer 1936] and cannot merely be avoided by improved lens design or construction. This means that a point object will be imaged as a disk that has a finite size. This kind of

aberration can be corrected, at least up to a certain angle, using aberration correctors, formed of a combination of quadrupole, sextupole, octupole or higher multipole lenses. See references for a full description of this effect.[105, 108] In the work described in this thesis, aberration correction was not critical to achieving the results that were obtained and similar results could have been obtained on an uncorrected microscope, although all modes used on the microscope did benefit from an appropriate setting of the aberration corrector.

3.3.4 Detectors

Most conventional TEMs and TEM/STEM instruments have a detector that is universal, which is the viewing screen. Doped zinc sulphide (ZnS) is normally used to coat the screen so that it will fluoresce at a wavelength of around 550 nm. Because this is in the centre of the spectrum of visible light, this wavelength is not overly taxing for the eyes.

In a STEM, it is necessary to collect electronic signals synchronously with the scanning of the electron beam. Electrons that are transmitted through the sample can be collected by annular integrating detectors. There are three types that are regularly used to create images, these are shown in Figure 3.4. The first is the bright field detector, which is positioned on the optic axis to collect electrons that pass straight through the sample and is used to form bright field images. Secondly there is the annular dark field detector which detects electrons that were scattered by the sample to medium or small angles, this is used to form dark field images. Finally there is the high angle annular dark field detector which detects electrons that were scattered to high angles, allowing the formation of high angle annular dark field images. This detector is useful because atoms that are heavier appear brighter using this method as they tend to scatter more to higher angles.[109] Because of this, most of the contrast using this method is in atomic number Z,[110] while other effects also influence it.[111]

However, these detectors miss much of the subtlety of information available in the diffraction pattern and detectors that record the full diffraction pattern can also be used. Until recently, much of the recording of images and diffraction patterns in the TEM or TEM/STEM has been done with charge coupled devices (CCDs), these can be positioned either below or above the viewing screen. CCDs use pixels that are capacitors made from metal oxide semiconductors (MOS), which convert photons into electrons at the interface between the semiconductor and oxide, after this the CCD then gives the charge in each capacitor. The amount of charge stored in each capacitor is dependent on the intensity of the radiation that is incident on it. In order to detect

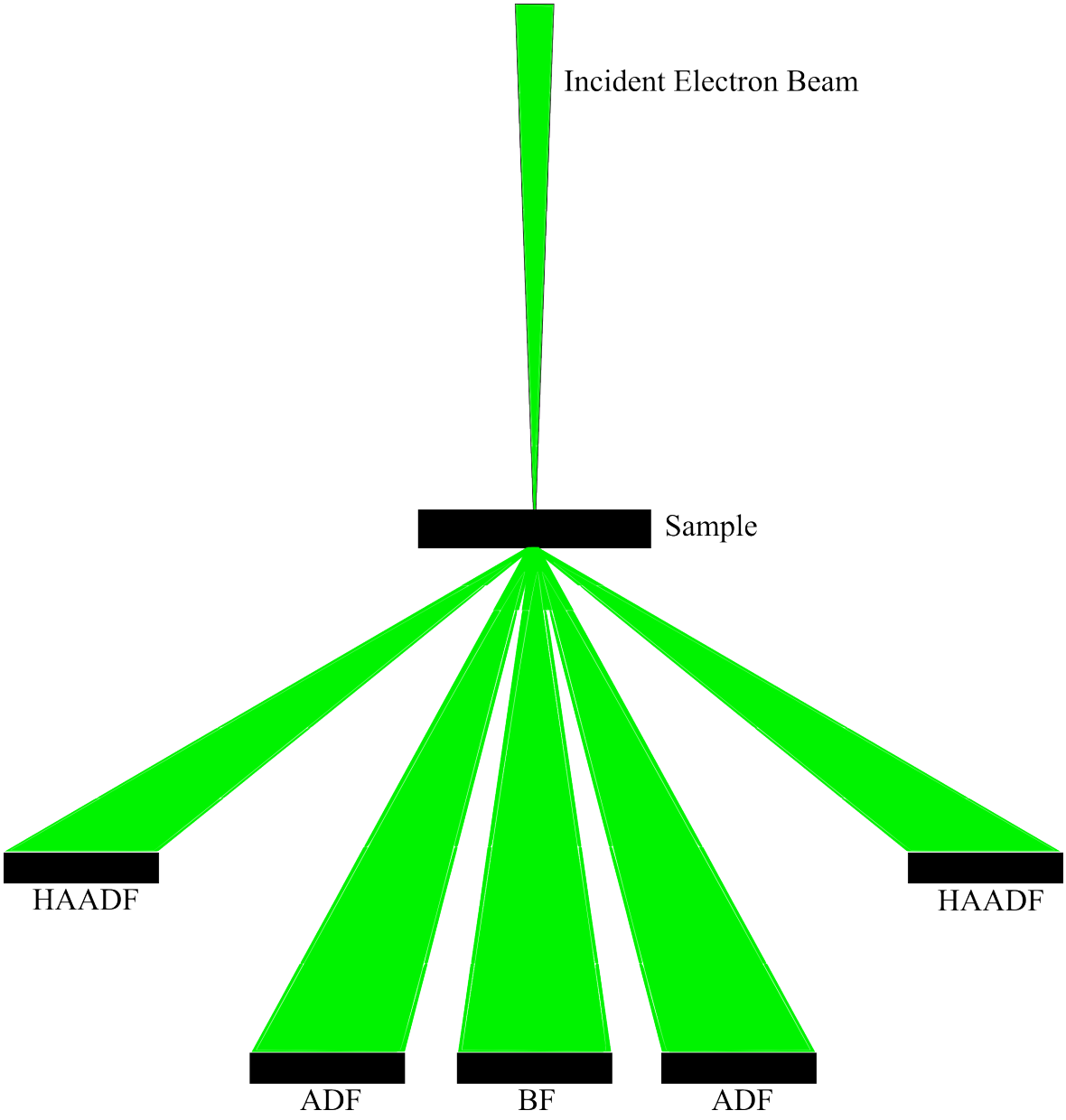

Figure 3.4: Imaging detectors in the STEM, high angle annular dark field (HAADF), annular dark field (ADF) and bright field (BF).

electrons, a scintillator plate is used to cover the CCD, this converts the incident electrons into photons, which is then detected in the CCD as charge, which is then digitised on readout. Typical CCD acquisition rates are of the order of 10 fps, this means that CCD detectors are not ideal for STEM imaging as they are too slow.

Recently, a new class of detectors that count electrons directly has become available, these have readout speeds much faster than those in CCDs, with acquisition rates of the order of 1000 fps. These detectors work by converting high-energy electrons directly into electron-hole pairs. These can then be either integrated as charge and then digitised or counted as individual pulses. This type of detector is faster, has less noise and has a smaller point spread on the detector, as the indirect detection via a scintillator does not occur. They can collect data from the back focal plane, which means that it is possible to carry out scanning diffraction experiments using them, which previously had been carried out using a fast video-rate CCD.[82] Some examples of these detectors are; EMPAD,[112] MerlinEM Medipix,[78] and the pnDetectors-pnCCD for (S)TEM.[113, 114]

Energy loss spectrometers can be integrated into a (S)TEM, allowing the capability of forming energy loss spectra from any samples that are being inspected. There are two different ways that an EELS system can be integrated into a (S)TEM, these are either before the final stage of image magnification or after it. This is discussed later in Section 3.4

There are three main detectors that were used in this work on the JEOL ARM200cF at the University of Glasgow, these are the Gatan Orius SC1000A, Medipix III – Merlin for EM and Gatan 965 Quantum ER Spectrometer.

3.3.4.1 Gatan Orius SC1000A

The Gatan Orius SC1000A is a fibre-optically coupled CCD camera. One of the main features of this camera is its anti-blooming abilities. Blooming is the process whereby an overflow of charge from once CCD pixel to it's neighbours occurs. This happens because higher intensity diffraction spots can saturate pixels. Normally the blooming problem requires usage of a beam stop so that the direct electron beam is blocked, however this is not necessary using this camera. This camera is an appropriate candidate for diffraction experiments, because of these anti-blooming abilities. It should be noted that anti-blooming is not perfect and charge still spills over into neighbouring pixels in bright parts of the image, while this issue is maybe improved in comparison with earlier CCDs.

This camera has a resolution of 11 megapixels, along with a maximum frame rate of 14 frames per second. The sensor has a surface area of 36 by 24 mm and has 14 bit dynamic range, over its 4008 by 2672 pixels, each of which are formed of 9 micron squares. If acquisition speed is prioritised over resolution, or if there are restrictions on data storage availability, it is possible to record using binning of up to 4 times. Binning is the process whereby the pixels in the detector are grouped together, forming an image with a lower resolution, but providing faster readout.

3.3.4.2 Medipix III – Merlin for EM

The Medipix III detector [115] was originally designed to be an X-ray photon detector. It is used for applications that require continuous readout of data and has circuitry designed to avoid charge sharing. Because of its design, each of its pixels have the ability to detect single electrons at 200 keV.

This detector is formed of two major parts, which are the absorbing layer and then the amplification and counting electronics. The absorber is an undoped semiconductor that is under an electric field. If there were high energy electrons that penetrated through the absorbing layer and got through to the electronics behind it, then they would be damaged and the chip would fail. This means that the front-end absorbing layer must absorb the incident electrons and convert them into a pulse of charge that is detected by the electronics. The thickness or material used in the absorbing layer can be altered to suit the energy of the incident electrons. If incident electrons had a higher energy than 200 kV, the absorbing layer could be changed to either a thicker layer, or one with a a higher atomic number Z which would stop electrons more quickly.[116] This may lead to a worse MTF, because when energy increases, electron dispersion does too and pixels further from the initial incidence can be triggered.[117]

This device has a 256 by 256 pixel sensor, which is a hybrid pixel detector that is silicon based. It has a CMOS architecture for readout, where each of the 55 μm pixels has circuitry for amplification and digitisation in it. This allows determination of whether the energy given by electrons is within a user defined range. When the energy is within this range, it is digitally counted. Theoretically this device could operate at a frame rate of 3000 frames per second, recording the full back focal plane, however this is dependent on bit depth, operating mode and the readout system being used, so in practice is limited to around 1000 frames per second. The sensor has a very high quantum efficiency and it's dynamic range is up to 24 bits.[115, 117] FEM and VDFI datasets were recorded using this detector.

Acquisition parameters on the detector were the same for all datasets. The detector

was in single pixel mode (SPM), with 24-bit depth the DACs Threshold_0 was set to 5 keV and Threshold_1 was set to 100 keV. The high voltage bias was set to 110 V.

3.3.4.3 Gatan 965 Quantum ER Spectrometer

This spectrometer is used for EELS or EELS-SI, it can be used with a high speed option that allows you to obtain microanalysis over a wide area quickly. The detector is able to operate in DualEELS mode, which means that it can obtain both the low loss and the core loss spectra for each pixel almost simultaneously.[118]

This detector utilises a post-column filter in order to carry out both energy filtering and spectroscopy. A magnetic prism bends the electron path through an angle of 90°, which disperses the electrons onto a vertical line determined by their energy. The highest energy electrons, such as those found in the zero loss peak are found at the bottom of the line, having been bent the least, while core loss electrons appear at the top, as they lose the most energy.

Using DualEELS, it is possible to simultaneously obtain the low-loss and high-loss spectra for each pixel in a spectrum image. There is a fast electrostatic shutter, which has a microsecond response time that is integrated into the spectrometer.[118] Firstly, the higher intensity low loss spectrum is acquired, then the electrostatic shutter deflects the beam onto a different part of the CCD, allowing the high-loss spectrum to be acquired. This process is carried out at each pixel in the spectrum image. Each of these spectra is recorded using the same optical conditions, while the high-loss spectrum has a longer exposure time as it is much lower in intensity. This approach means that the dynamic range of the detector, which is a limiting factor on the intensity range that can be acquired in the detector to be overcome.

This detector has a 2 kV field of view when operated at an accelerating voltage of 200 kV and is capable of an acquisition rate of 1000 spectra per second. It allows a separation of up to 2 kV between the low-loss and high-loss spectra.[119] There are two apertures which can be used, at 2.5 mm and 5 mm. The 2.5 mm aperture gives a spectrometer acceptance angle of 36 mrad.

3.4 Electron Energy Loss Spectroscopy

An electron energy loss spectrometer records the spectrum of the loss of kinetic energy from an electron beam that was initially almost monochromatic, once it has passed through a sample. When the beam of electrons undergoes interactions with an electron

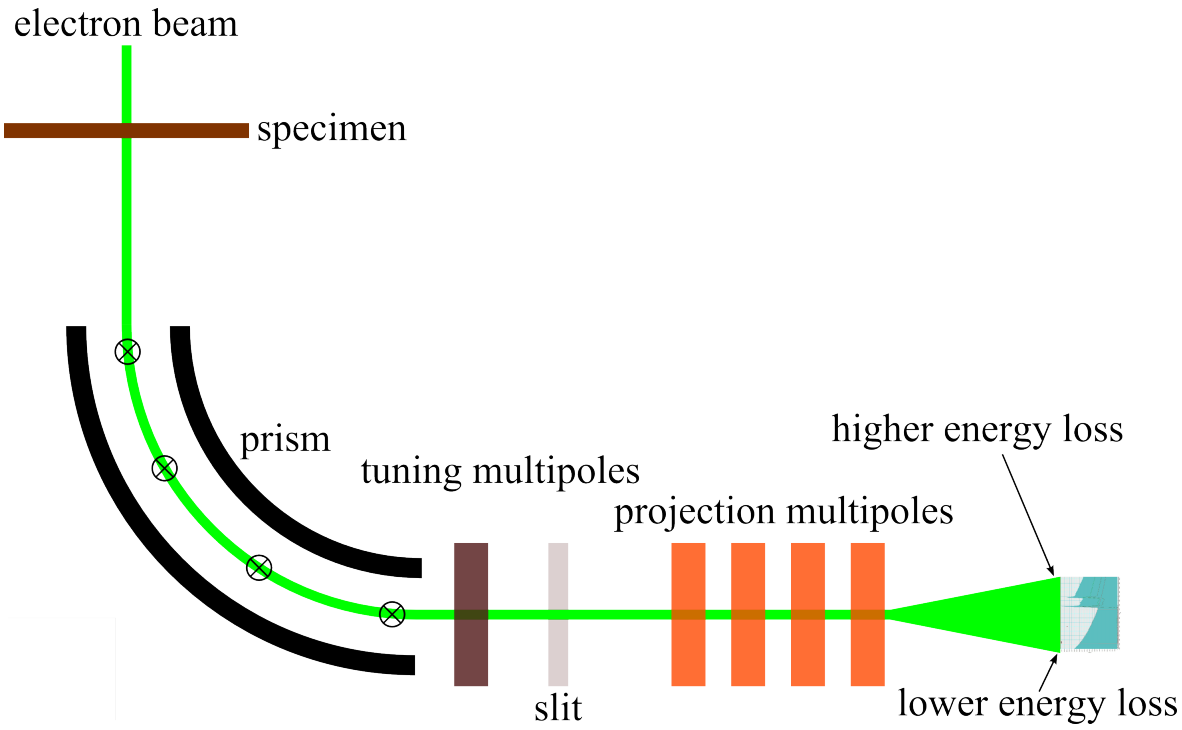

Figure 3.5: Basic diagram of how an EELS spectrometer works.

in the inner shell of an atom, it loses energy, this energy is absorbed by the inner shell electron. The electron that was initially in the inner shell moves to a state that is unoccupied above the materials Fermi level. The initial electron loses kinetic energy equal to the energy gained by the electron that was initially in the inner shell. As the amount of energy lost is a property characteristic to different elements, this process can be used to identify information on the composition of a material.

Figure 3.5 shows a simplified diagram of an EELS spectrometer. The principal component in the spectrometer is the magnetic prism that separates electrons by their kinetic energies. An electrons radius of curvature is given by;

$$R = \frac{\gamma m}{eB} v \tag{3.3}$$

where R is the radius of curvature, γ is the Lorentz factor, m is an electron rest mass, e is an electron charge, B is the magnetic field in the y direction and v is the speed the electron is travelling at in the z direction. γ is given by;

$$\gamma = \frac{1}{\sqrt{1 - \frac{v^2}{c^2}}} \tag{3.4}$$

where c is the speed of light. Thus, the electrons will be deflected by different amounts

depending on their velocity. If there were two electrons moving through a magnetic field initially on the same trajectory, the electron with a lower kinetic energy would be deflected by a larger amount. The Gatan Imaging Filter (GIF) used here bends electrons through an angle of 90°, the highest energy electrons appear at the bottom of the spectrum, while electrons that have interacted with core shells having lost more energy will appear towards the top. These are then detected by the EELS sensor which records the spectrum. Usually a CCD is used as the sensor, and the signal is integrated from a 2D image of the spectrum into a 1D line plot.

There are various different features in an EELS spectrum, the major ones are; the zero loss peak, plasmon peaks and core loss edges. These are shown in Figure 3.6. As its name implies, the zero loss peak is where electrons have passed through the sample without undergoing any inelastic scattering. The zero loss peak is the most intense feature in an EELS spectrum as shown in Figure 3.6a. it includes electrons that have undergone energy losses smaller than the spectrometers resolution limit, as well as from the electron sources energy spread. Plasmon peaks are a result of the inelastic scattering that occurs between the incident electron and an outer-shell electron. Core loss edges are a result of electrons being knocked out from core (inner K, L, M, …) shells of an atom. For this to happen, the core electron must receive a quantity of energy that is either equal or greater than the critical ionisation energy. The critical ionisation is a property that is dependent on the specific atom and electron shell. This means that different elements will have characteristic peaks on the EELS spectrum, allowing identification of specific elements.

Each EELS transition is named from the initial state the core electron was in. For example, the K edge is a result of a transition from an initial state of $1s^{1/2}$ or an L_1 edge from $2s^{1/2}$. As the electrons in the K shell are those that are closest to the nucleus of the atom, they require the largest amount of energy to be expelled from the atom, this means that the K edge will be the highest energy loss edge for any given element. In addition to this, as atoms get heavier, the K edge is shifted to increasing energy losses. Figure 3.6b shows edges from tungsten and molybdenum, the initial sharp rise in intensity is as a result of the ionisation threshold being reached, while as the energy loss increases, the peak then continues at decreasing intensity. An edge can also show what is known as fine structure, there are variations in the structure of an edge after its onset, these are due to bonding.

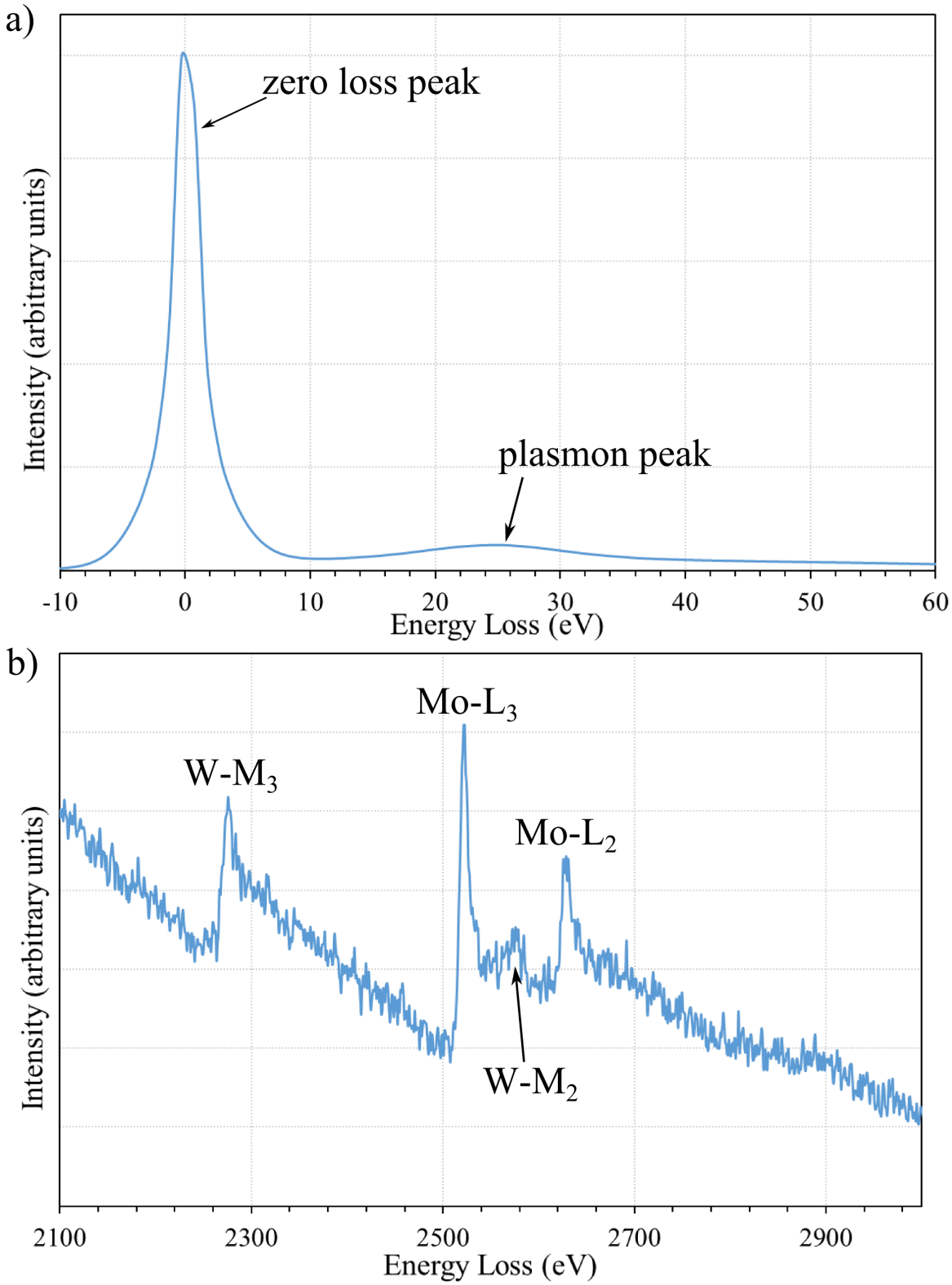

Figure 3.6: Features of an EELS spectrum, showing; a) the zero loss peak and plasmon peak; b) core loss edges from tungsten and molybdenum.

3.4.1 Dual EELS

Dual EELS is a process whereby a low-loss and high-loss spectrum are obtained almost simultaneously for every pixel in a spectrum image. The low-loss spectrum, which is more intense is collected first, then an electrostatic shutter is used to deflect the beam so that the high-loss spectrum can be collected. This approach is a way to get around the restricted dynamic range of the detector, which is a limiting factor in the intensity range that can be imaged.[118][119]

Obtaining the low-loss and high-loss spectra in the same conditions is important in obtaining accurate quantifications. Core-loss edges can be normalised by the zero loss peak, while plural scattering can be removed from the spectrum due to the low-loss spectrum being obtained.

3.4.2 EELS Data Processing

EELS spectra recorded on the spectrometer are not always perfectly aligned. Sometimes there is a small offset between the position of the zero loss peak and zero on the energy scale. This can be fixed during processing by moving the spectrum so that the zero loss peak is aligned to zero on the energy scale. To do this, the function "Align SI by peak" in Digital Micrograph^{TM} can be used to centre the zero loss peak for each pixel.

The next step is to exclude certain channels from each end of the spectrum, this is done with the "Volume-Extract volume" tool in Digital Micrograph^{TM}. This is because there is lower detection efficiency at each end of the spectrum.

X-rays can sometimes hit the detector as a result of electrons impacting on parts of the spectrometer and exciting X-rays which then reach the detector, causing spikes in intensity in the pixels they impact. These are removed with "Volume-Remove X-rays" function in Digital Micrograph^{TM}.

A large amount of noise is removed from the spectrum by using principal component analysis (PCA). To do this, a Digital Micrograph^{TM} plug-in called Multivariate Statistical Analysis (MSA) created by Lucas et al. was used.[120] This separates the complex 3D dataset into a number of spectral components (typically 80-100), each weighted by maps of the strength of that component in each pixel. It is important that enough PCA components are utilised, as if too few are used some of the weaker features in the spectrum can be missed.[121][122]

Plural scattering happens when there is a substantial portion of the incident electrons passing through the sample that are inelastically scattered multiple times. This can cause artefacts in the EELS spectrum that affect the fine structure of the edges, as well as making the background depart from the power law background model. To deconvolute the spectrum and remove these effects, it is possible to use a Fourier-ratio deconvolution.[123] In order to do this, the low loss and high loss spectra must be recorded under the same microscope conditions, then the background intensity is subtracted from the edge being investigated. Once that has been completed, both the low-loss spectrum and the core-loss edge that has had the background subtracted are Fourier-transformed. The Fourier transform of the core-loss spectrum is then divided by the Fourier transform of the low-loss spectrum. Finally, the Fourier transform is inverted, giving the deconvolved spectrum.

The likelihood that a scattering interaction happens between an incident electron and an atom in the sample is given by σ, the interaction cross section. This is dependent on the electron beam energy, all of the different possible interactions have specific cross sections which are proportional to the interaction probability. When looking at EELS edges, the following equation is used

$$I = I_0 N \sigma \tag{3.5}$$

where we have I the edge intensity, I_0 the ZLP intensity and N is the number of atoms per unit volume.

In order to extract the intensity of a core-loss edge from background, it is necessary to carry out a background subtraction. Figure 3.7 shows an example of the background subtraction of a Nb $L_{2,3}$ edges To achieve this, it is required that a background model is fitted, extrapolated, then subtracted to give the background subtracted intensity. A region on the low-energy side of the edge is identified to allow the determination of fit parameters. The fit resulting from this is extrapolated so that the background intensity underlying the edge signal is estimated. Background subtractions in this thesis are carried out using a power law background model with least squares fitting using Digital Micrograph^{TM}.[123]

In order to quantify the percentage composition of the materials investigated in this thesis, the "EELS Elemental Quantification" plug-in in using Digital Micrograph^{TM} can be used. The background and edge itself is regarded as a single function, where the background follows a power law and the edges are modelled using theoretical cross sections. This approach is useful as it allows edges that overlap to be treated automatically. Hartree-Slater cross sections are used to quantify the ratio between the different

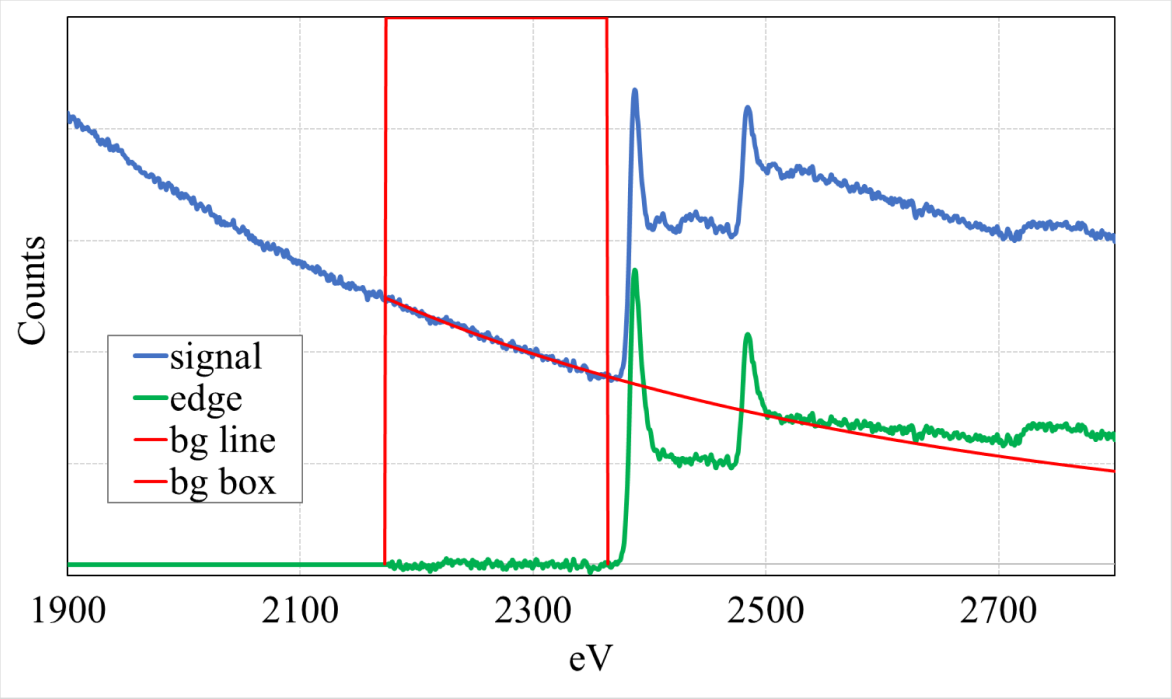

Figure 3.7: EELS spectrum showing a Nb $L_{2,3}$edge. A box is used to calculate the background and then the edge signal is extracted.

elements within the sample material.[124][125] Elemental maps can be created of the atomic composition from each pixel of the spectrum image.

3.5 Diffraction and Resolution in STEM Mode

The de Broglie wavelength of a particle/object with mass m and velocity v is given by

$$\lambda = \frac{h}{mv}, \tag{3.6}$$

where h is Planck's constant. This means that an electron that had been accelerated through a voltage of 100 kV would have a wavelength of 3.7014 pm and one that had been accelerated through 200 kV would have a wavelength of 2.5079 pm.

Elastically scattered electrons are typically deflected from the main electron beam by an angle less than 10°. The scattering angles from crystalline samples can be calculated using the Bragg equation,

$$2dsin(\theta) = n\lambda \tag{3.7}$$

where d for a cubic crystal is given by

$$d = \frac{a}{\sqrt{h^2 + k^2 + l^2}} \tag{3.8}$$

where a is the lattice parameter, h, k and l are the Miller indices. This allows the identification of diffraction spots on a diffraction pattern, as well as enabling the calibration of the detector in terms of scattering angle per pixel.

There are different illumination modes that can be used in the STEM, parallel beam, nanobeam and convergent beam (CBED). In this thesis, nanobeam and CBED were used.

We can see diagrams of these modes in Figure 3.8. In the TEM, the traditional mode is parallel illumination (Figure 3.8a)).

For parallel illumination, a demagnified image of the electron source (Gun) is formed by the first condenser lens (Condenser 1), the second condenser lens (Condenser 2) is then used to form an image of the Condenser 1 crossover in the front focal plane of the Condenser Minilens. The Condenser Minilens is then used to create a parallel beam.

When parallel illumination is used, practically Condenser 2 is under focussed so that the viewing screen is filled by the illuminated area on the specimen. When the magnification is increased, Condenser 2 has to be strengthened so that the illuminated area of the specimen continues to fill the viewing screen, this will make the beam less parallel.

In order to form small probes that have lower convergence angles, an aperture is introduced at the second condenser lens. This is seen in Figure3.8b). The strength of Condenser 2 is reduced and the Condenser Minilens focusses the beam onto the sample.

In order to form the smallest possible probe, convergent beam illumination is used (Figure 3.8c). This is achieved by using the final condenser lens to form an image of the Condenser 1 crossover at the specimen, practically this means that the Condenser Minilens is the final condenser lens and Condenser 2 is not used.

A key difference that CBED has from conventional electron diffraction is that the patterns obtained from this technique result in disks, not spots. This is becuase small probe sizes and large convergence angles are used. The convergence angle of the electron beam determine the width that these diffraction disks take, a larger convergence angle results in larger diffraction spots.

Because of interference and diffraction, it is not possible to attain a perfect focus

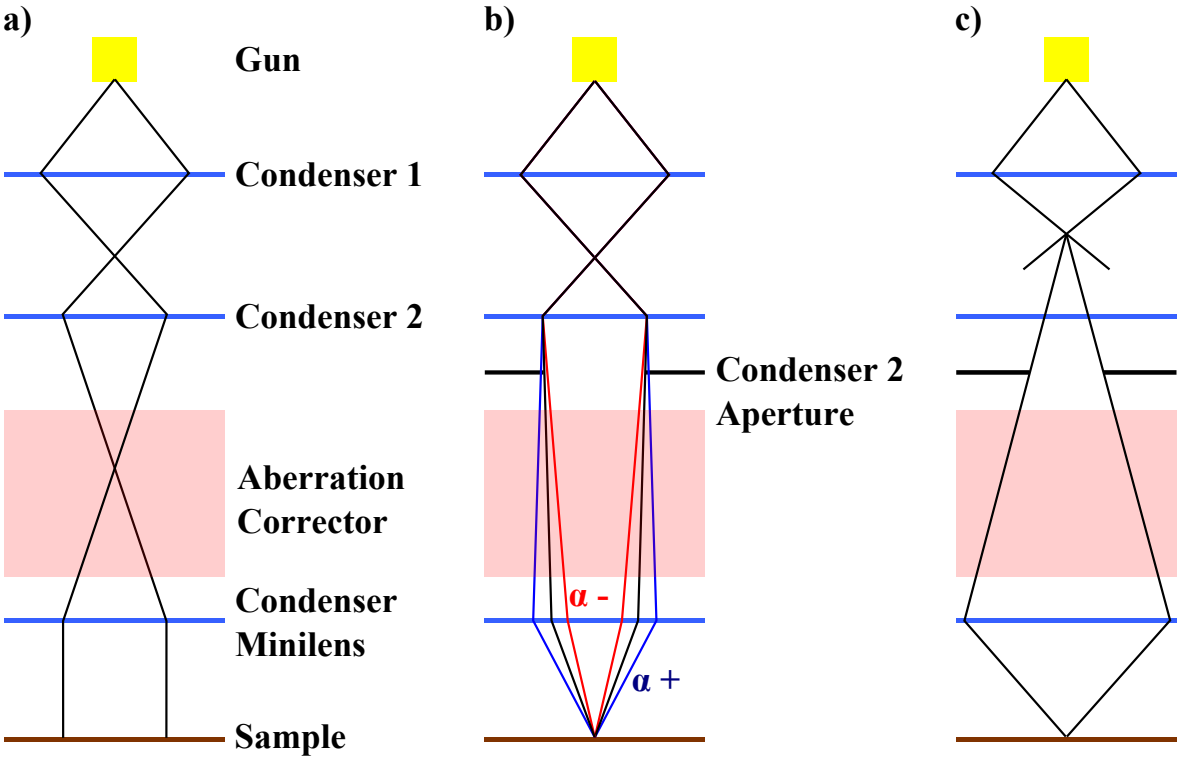

Figure 3.8: Illumination modes, a) shows a setup for parallel illumination, b) shows a setup for nanobeam diffraction and c) shows the lens setup for convergent illumination.

when an optical system exploits the wave properties of particles.[126] In 1873, Abbe established the theory for image formation in the light microscope.[127] The resolution of a perfect optical system is given by;

$$r = \frac{0.612\lambda}{nsin(\alpha)} \tag{3.9}$$

Where r is the resolution, or minimum resolvable distance between two different points. λ is wavelength of the incident light, n is the refractive index and α is the semiangle that is subtended from the focal point to the lens. $nsin(\alpha)$ is often expressed as numerical aperture (NA), so that;

$$r = \frac{0.612\lambda}{NA} \tag{3.10}$$

Abbe's theory shows that the resolution of an image is improved by either using larger NA or shorter wavelengths. If the diffraction pattern is altered in any way, this has a direct effect on the image.

The condenser aperture used in the STEM thus directly affects the resolution of the microscope. Larger apertures give a higher convergence angle, while smaller apertures

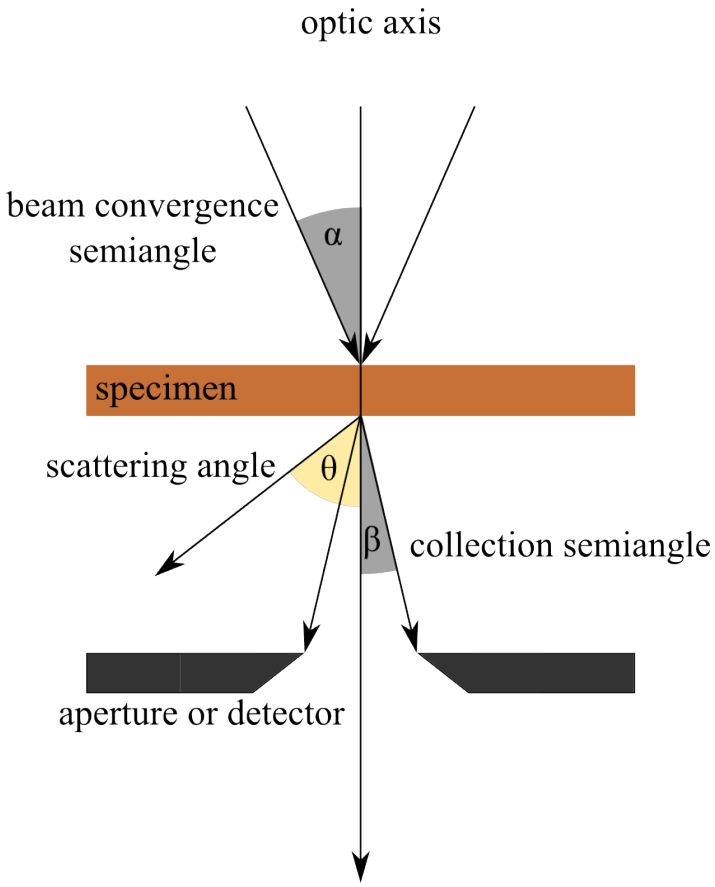

Figure 3.9: Angles that are important in STEM.

give a lower convergence angle.

There are certain angles that are important when a convergent beam is being used, these are shown in Figure 3.9. Firstly there is α, the convergence semi-angle of the beam. The angle that the beam is scattered by the specimen is called θ, while the maximum angle that can be collected in the detector is given by β.

When the microscope is set up for diffraction instead of imaging, there is a projection of the back focal plane onto a detector or viewing screen, taking the place of the image plane. A diagram of this is shown in Figure 3.10.

In the FEM experiments here, it is necessary to use electron probes with a diameter around 1-2 nm that have almost parallel illumination, this means that we have to use a focussed probe form of diffraction. The Abbe equation shown in equation 3.9 shows the relation between the size of the probe and convergence angle. As probe size decreases, the convergence angle increases. This means that there is a trade-off between the spatial resolution of the probe and angular resolution in the diffraction patterns. As the FEM technique requires angular resolution in order to distinguish details (speckles) in the diffraction patterns of the glasses inspected, this means that it will not be possible to use probes that are less than around 1 nm in this microscope.

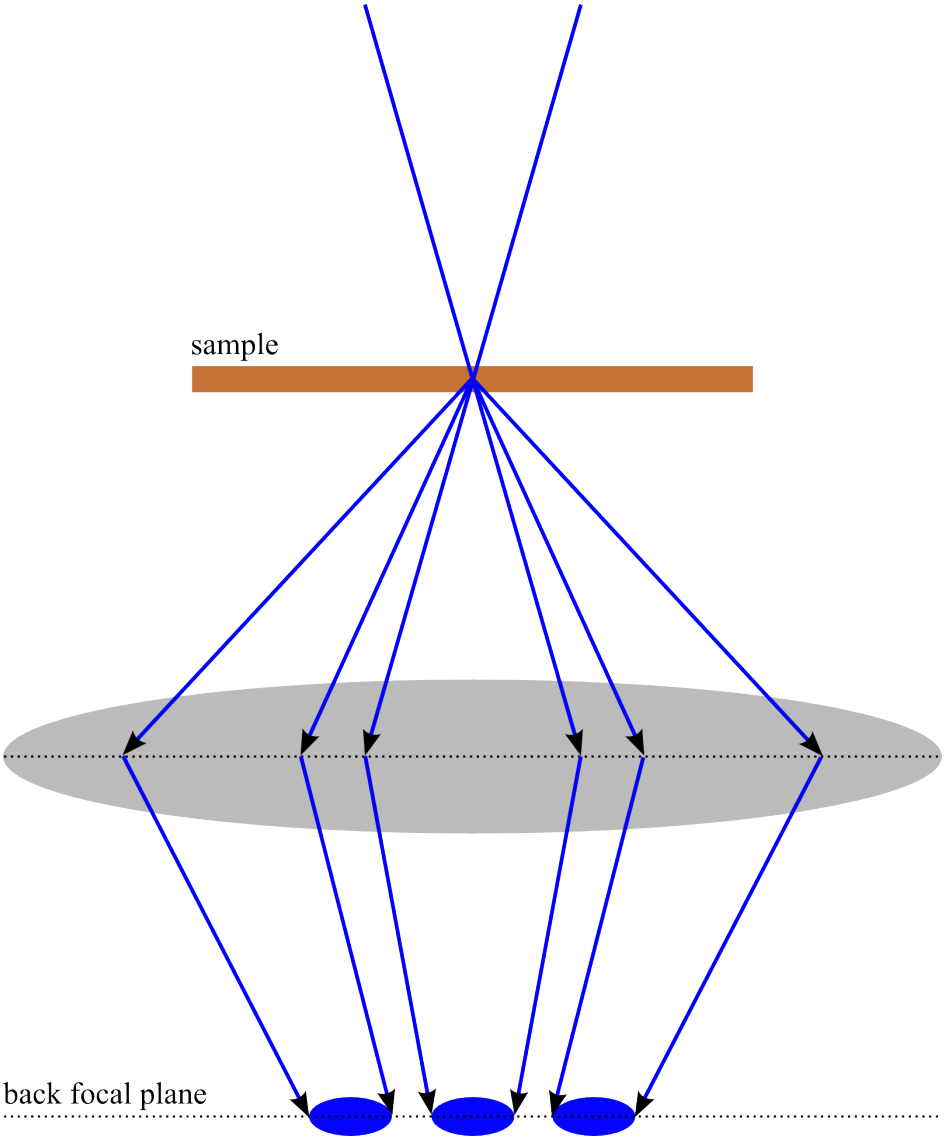

Figure 3.10: Diagram of the paths of electron rays, showing the incoming beam, sample and back focal plane.

3.5.1 Topspin Software

Control over the acquisition of the diffraction datasets presented in this thesis was achieved using the Topspin software provided by NanoMEGAS.[128] This platform is designed for precession electron diffraction with scanned acquisition.

Datasets were acquired with the precession off, and the software was used simply as a scan controller, while the microsope was in TEM mode. In diffraction mode, this setup is good for low convergence angle diffraction.

3.6 Virtual Dark Field Imaging

Dark field imaging is a method where the unscattered central electron beam is not collected by a detector and is thus excluded from the image, instead the detector is placed in such a position that it collects some of the scattered electrons. This means that the electron beam passing through empty space instead of a sample would result in a dark area in an image, while brighter areas appear when the beam passes through the sample.

Conventionally, the incident electron beam is tilted before interacting with the sample, so that instead of the incident beam, a diffracted beam passes through an aperture that is placed in the back focal plane of the objective lens.

Annular dark field imaging is a method whereby an annular detector is centred on the unscattered electron beam, but does not include it. Figure 3.4 shows two different types of detector, the ADF at lower diffraction angles and the HAADF at much higher diffraction angles.

When the full diffraction pattern is collected in a 4D dataset, it is possible to use the dataset of scanned diffraction patterns to image features in real space. This is because the diffraction pattern is indexed spatially. Rauch and Veron's VDF approach creates real space images using the intensity of each diffraction pattern from the diffraction dataset at certain regions of each diffraction pattern.[82]

Traditional VDF images are created from annular masks applied to the diffraction patterns in a dataset as seen in Figure 3.11. This is an effective way to find differences in atomic structure between different areas, especially of amorphous materials, as certain atomic bond distances are the cause of diffraction spots at each diffraction angle. In a sample that may contain different atomic structures, it is possible to find areas where there may be higher or lower amounts of each structure.

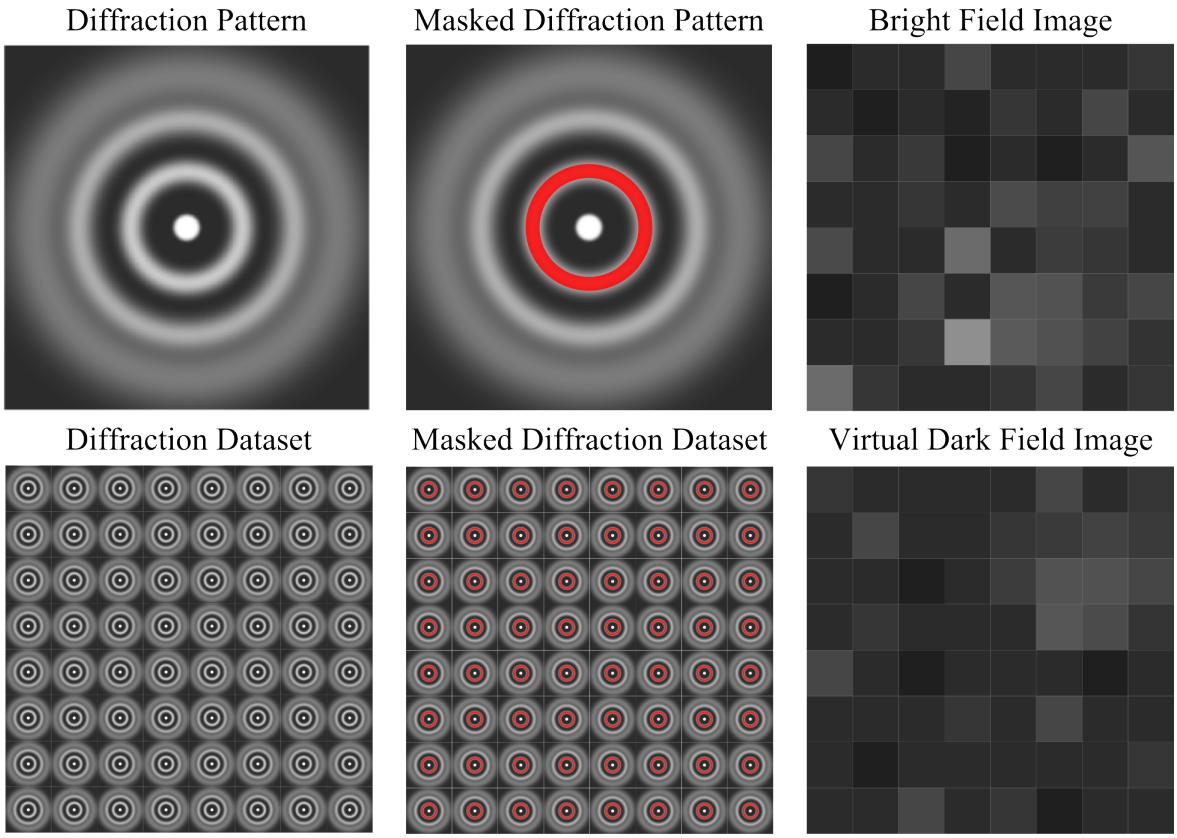

Figure 3.11: This diagram shows how a diffraction dataset has an annular mask applied to it, creating a virtual dark field image showing diffraction intensity differences at the diffraction angle of the mask.

If the sample is not amorphous, and shows diffraction spots in the same position regularly, it is possible to create masks on the diffraction dataset such that a VDF image can be created from a certain diffraction spot as shown in Figure 3.12.

Virtual bright field images can also be generated from the scanned diffraction dataset. This can be achieved by either integrating the intensity from the entire diffraction pattern, or by masking the diffraction pattern so that only the intensity of the central electron beam is recorded.

One downside to this technique is that very large datasets must be acquired, to produce images utilising very little of the data acquired.

This technique has been used to create spatial maps of phase and orientation in polycrystalline materials.[82, 129]

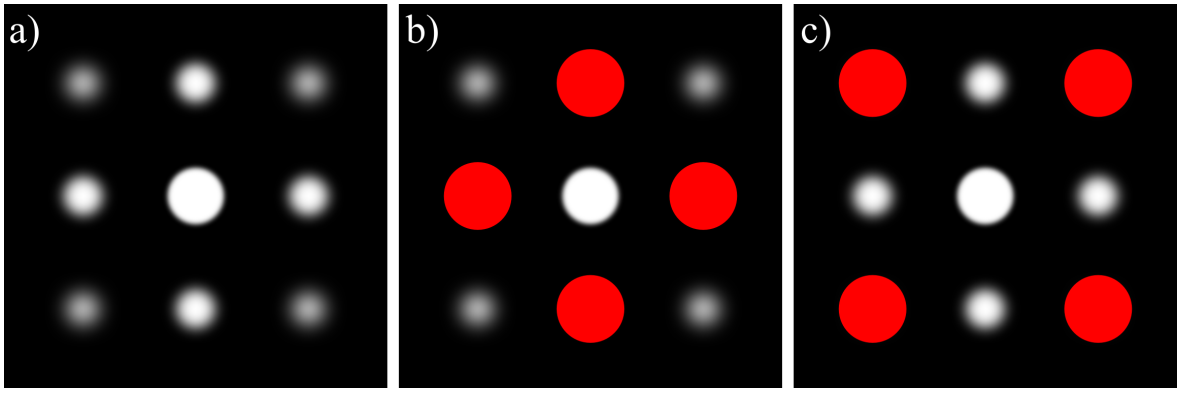

Figure 3.12: a) fcc diffraction pattern, along the [100] direction, b) mask of the four major diffraction spots (200), c) mask of the four minor diffraction spots(220).

3.7 Fluctuation Electron Microscopy

FEM is a technique that utilises diffraction in order to quantify medium range order (MRO) in a material. (MRO is around the 1-5 nm range.)

When looking at DPs obtained from a material, if there are individual ordered regions within the material, they create discrete diffraction spots. When using a small electron beam of around a namometre in diameter, only a few of these diffraction spots will be visible. When the beam is moved, the diffraction pattern changes. If a dataset formed of scanned diffraction patterns is collected, the variance between these diffraction patterns gives information on the lengthscale of the local order, this is is especially true when the probesize and scan step size are approximately the same as the length scale in the ordered regions.

The FEM technique was developed to investigate MRO by measurement of intensity fluctuations from spatially resolved diffraction patterns recorded from adjacent nanovolumes of the sample material, Treacy and Gibson used this to calculate the normalised variance.[80]

Fluctuations measured using this technique are most sensitive when the electron probe being used has a size similar to the MRO length scale that is being investigated in the material. The degree of MRO in a material is quantified by the magnitude of the variance in diffracted intensity, which is a function of the scattering vector on a length scale which is regulated by the probe size used.

While the FEM technique was initially performed with TEM dark field imaging,[80] the technique has since advanced so that it is possible to use STEM scanning diffraction.[81] Using the FEM technique with modern STEM is advantageous, as it is possible to create small electron probes that have a diameter of less than 1 nm, as well as acquire

diffraction patterns quickly enough to capture a large amount of diffraction patterns over the area of interest.

Models of atomic structure show that there are trends found in variance as the size and fraction of volume of ordered regions varies.[130, 131] The FEM technique has been used to show differences in the nanoscale ordering in amorphous germanium[81, 132, 133] and silicon[134–139] thin films, amorphous metals[140, 141] and phase change chalcogenide materials.[140, 142, 143]

While it is challenging to conduct analysis of FEM quantitively, there have been some recent advances where some information on the degree of ordering on the nanometre scale can be obtained.[138, 144] In addition to this, there have been some studies that have found ways to relate angular correlations and scattering covariance in data from FEM to information on structural properties.[145–147] Recent work at the University of Glasgow using similar techniques to Voyles and Muller,[81] found that there is MRO in amorphous Ta_2O_5.[148]

Most of this previous work at the University of Glasgow was conducted by Hart, who developed a variation on the standard FEM formula in order to counter high noise in the DPs recorded.[76, 149] His assumption was that the kinematic coherent diffraction is Gaussian distributed, and that by fitting a Gaussian filter to the diffraction pattern will average through the noise and find diffraction peaks that are real, instead of individual random noise pixels. The variance was calculated from a set of cross correlation coefficients that were obtained from a normalised cross correlation of the diffraction data and a Gaussian filter.

Figure 3.13 shows the FEM process used in this work. When an electron probe passes through the specimen, it creates a diffraction pattern. In a STEM, the probe can be rastered across the sample, generating diffraction patterns at discrete steps throughout the specimen. Different areas of the specimen such as the substrate, area of interest and capping layer will produce different diffraction patterns. The diffraction patterns from the substrate or the capping layer can be used for calibration, if they show diffraction spots from a material with known lattice parameters that can be indexed, as shown earlier in Equation 3.8. Once the beam has been rastered over the area selected, there is a dataset of diffraction patterns, that correspond to specific points on the specimen. In order to calculate the variance of the area of interest, diffraction patterns from that area are formed into a stack, then the mean and variance of each pixel through the stack is calculated.

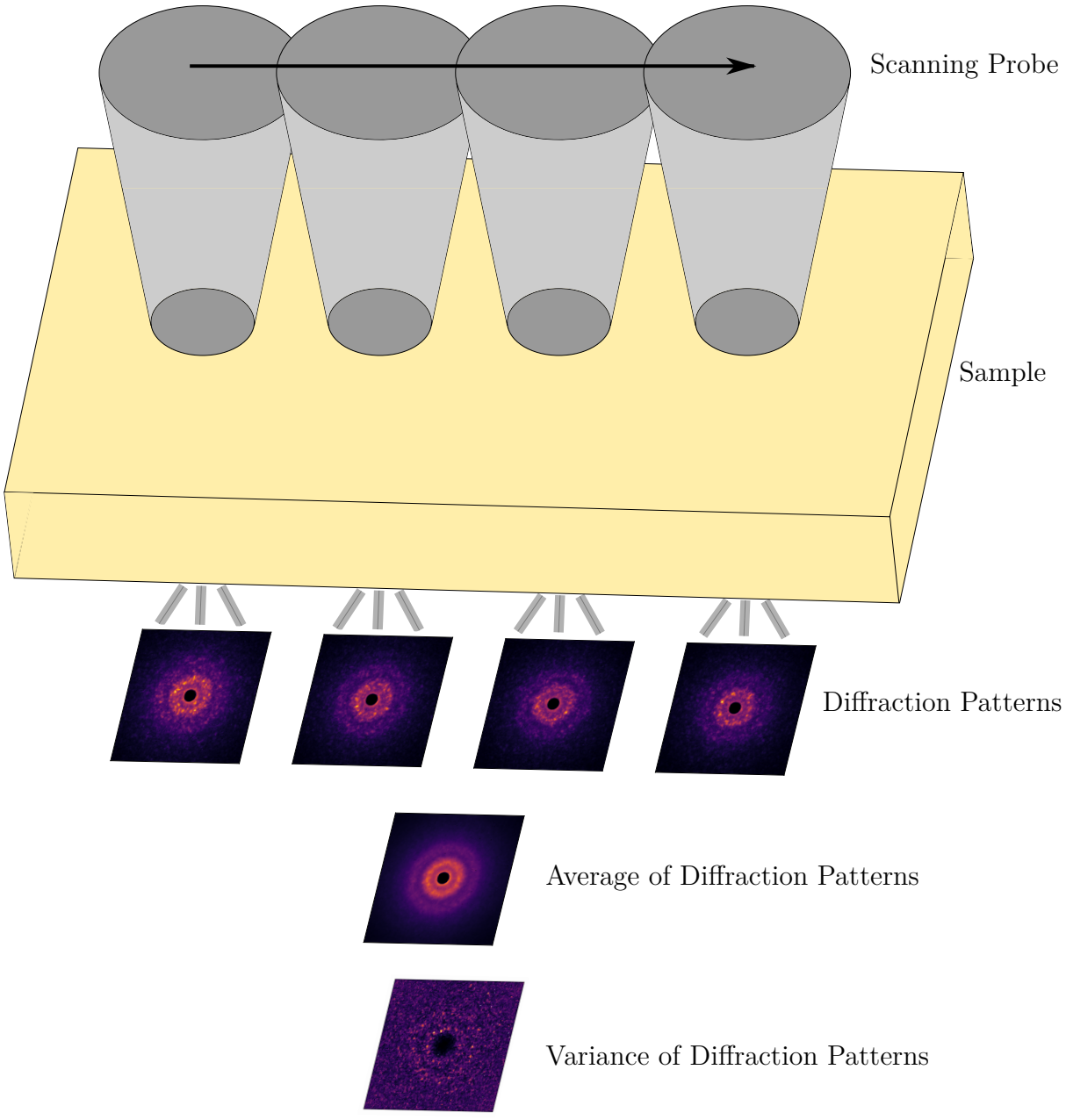

Figure 3.13: Diagram of the FEM process in the STEM. The scanning probe is rastered across the sample and DPs are collected at set intervals in the sample. After that, the mean and variance of the diffraction patterns is calculated. Redrawn from [150].

3.7.1 Kinematical Electron Scattering Theory for Fluctuation Electron Microscopy

Here the derivation of the FEM formula as described by Treacy *et al.* [150] is shown.

Kinematic electron scattering can be assumed when the scattering from a set of scatterers (atoms) is weak compared to the incident intensity from the electron source and the effect of multiple electron scattering can be disregarded. This means that the samples must be thin, as the likelihood of multiple scattering increases as the thickness of a sample increases. As scattering factors are not constant for each element and depend on Z, the definition of a thin sample changes according to the composition of elements in a sample.

We can treat the sample as an array of scattering atoms j each of which is positioned at $\boldsymbol{r}_j$. Plane wave radiation with a wavelength λ illuminates the sample, with $\chi = 2\pi/\lambda$ the amplitude of its wavevector. The illumination is inclined to the optic axis by $-\boldsymbol{q}$, which corresponds to the tilt angle of the illumination given by $sin^{-1}(|\boldsymbol{q}|/\chi)$ which can be approximated to $|\boldsymbol{q}|/\chi$ when $|\boldsymbol{q}|$ is small. Figure 3.14 shows a diagram of this setup. The incident illumination is scattered by the atom into a plane wave that is inclined by an amount $\boldsymbol{k}$ to the optic axis. This means that the scattered wave amplitude ϕ_j distant from the sample is given by

$$\phi_j(\boldsymbol{r}', \boldsymbol{r}, \boldsymbol{q}, \boldsymbol{k}) = i\lambda f_j(|\boldsymbol{k} - \boldsymbol{q}|)e^{(-i(\boldsymbol{k}-\boldsymbol{q})\cdot\boldsymbol{r}_j)}e^{(i\boldsymbol{k}\cdot\boldsymbol{r}')}, \tag{3.11}$$

where $\boldsymbol{r}'$ is a spatial coordinate positioned in the far field and $f_j(|\boldsymbol{k}-\boldsymbol{q}|)$ is the scattering factor of the atom for scattering from $\boldsymbol{k} - \boldsymbol{q}$, such that in the situation where $\boldsymbol{k} = \boldsymbol{q}$ the incident beam is not deflected at all. The vector amplitudes of q and k are given by the relation

$$q = k = \frac{2\pi}{d} \tag{3.12}$$

where d is the real space distance such that it is possible to relate q and k to real space distances.

In order to form an image, the electron scattering that is collected through a radius K_{ap} at the objective aperture, is then focussed at a far field plane that is conjugate to the sample. Each scattering atom j has a corresponding image wave function, which is denoted by u_j. The expressions for u_j are a coherent sum of all the scattered plane waves that pass through the aperture K_ap,

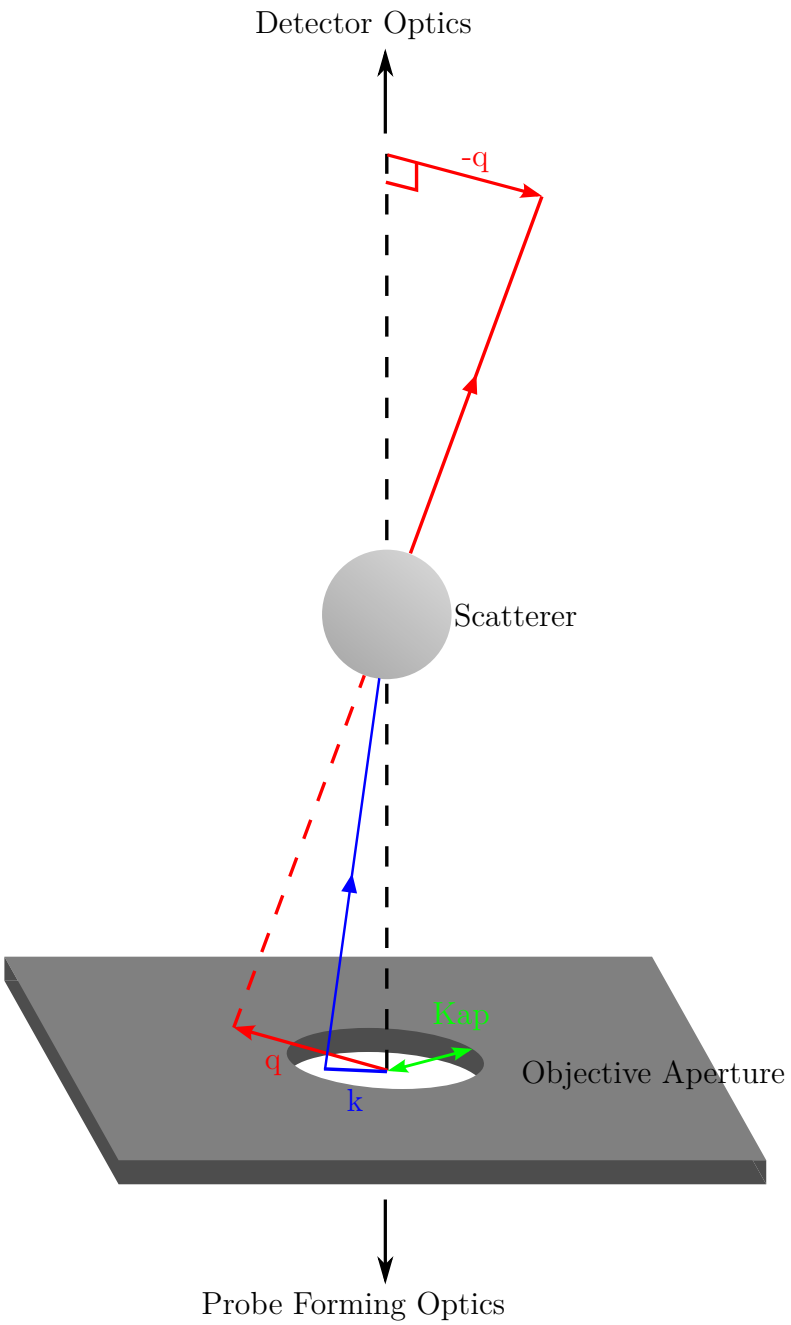

Figure 3.14: Imaging geometry of a scanned probe. Probe forming lenses (condenser lenses) and an aperture (condenser aperture) focus the radiation onto the scatterer, from which the scattering is collected by a detector/detectors. Redrawn from [150].

$$u_j(\boldsymbol{r}', \boldsymbol{r}_j, \boldsymbol{q}, K_{ap}) = \int \int_{obj} \phi_j(\boldsymbol{r}', \boldsymbol{r}_j, \boldsymbol{q}, \boldsymbol{k}) d^2\boldsymbol{k} \tag{3.13}$$

which could also be expressed as

$$u_j(\boldsymbol{r}, \boldsymbol{r}_j, \boldsymbol{q}, K_{ap}) = i\lambda e^{i\boldsymbol{q}\cdot\boldsymbol{r}_j} \int \int_{obj} f_j(|\boldsymbol{k} - \boldsymbol{q}|) e^{i\boldsymbol{k}\cdot(\boldsymbol{r}-\boldsymbol{r}_j)} d^2\boldsymbol{k} \tag{3.14}$$

When dark field imaging is being used, $|\boldsymbol{q}| > K_{ap}$ because the scattered rays do not find their way through the objective aperture.

Here, the magnification of the microscope is not taken into account, this is achieved by either mapping $\boldsymbol{r}_j$ (sample coordinate) into the far field, or equivalently $\boldsymbol{r}_j$ onto the sample plane. These approaches can be carried out, because of the mutual conjugation of the sample and image plane. This means that both $\boldsymbol{r}$ and $\boldsymbol{r}_j$ in Equation 3.14 can be thought of as being in sample coordinates, with the same scaling.

All microscopes have aberrations which affect their performance such as; defocus, spherical aberrations, astigmatism and so on. Equation 3.14 can now be modified to include these effects such that,

$$u_j(\boldsymbol{r}, \boldsymbol{r}_j, \boldsymbol{q}, K_{ap}) = i\lambda e^{i\boldsymbol{q}\cdot\boldsymbol{r}_j} \int \int_{obj} f_j(|\boldsymbol{k} - \boldsymbol{q}|) e^{i\boldsymbol{k}\cdot(\boldsymbol{r}-\boldsymbol{r}_j)} e^{i\gamma(|\boldsymbol{k}|)} d^2\boldsymbol{k} \tag{3.15}$$

where γ is the effect of the lens aberrations and is given by;

$$\gamma(|\boldsymbol{k}|) = \pi\lambda|\boldsymbol{k}|^2[\Delta f + \frac{1}{2}C_s\lambda^2|\boldsymbol{k}|^2] \tag{3.16}$$

where we have defocus Δf and the coefficient of spherical aberration C_s. Higher order aberration terms, along with the astigmatism are also existent, however FEM experiments take place using a relatively low resolution, so these other effects are not so important. While chromatic aberrations can be important, in these calculations it is assumed that there is monochromatic illumination. Defocus depends on both the strength of the lens, and the positioning of each scatterer within the sample. While this is important at higher resolution, where there is a short depth of focus in comparison to the sample thickness, it is ignored here. Using low resolution imaging, where each individual scatterer is not resolved, we can use an approximation for u_j;

$$u_j(\boldsymbol{r}, \boldsymbol{r}_j, \boldsymbol{q}, K_{ap}) = f_j(|\boldsymbol{q}|) a_j(\boldsymbol{r} - \boldsymbol{r}_j, K_{ap}) e^{i\boldsymbol{q}\cdot\boldsymbol{r}_j} \tag{3.17}$$

where the a_j terms are given by;

$$a_j(\boldsymbol{r}-\boldsymbol{r}_j, K_{ap}) = i\lambda \int\int_{obj} e^{i\boldsymbol{k}\cdot(\boldsymbol{r}-\boldsymbol{r}_j)} e^{i\gamma(|\boldsymbol{k}|)} d^2\boldsymbol{k} \tag{3.18}$$

Equation 3.17 is valid depending on the validity of our assumption that in the range of $\boldsymbol{k}$ which is subtended by the objective aperture $f_j(|\boldsymbol{k}-\boldsymbol{q}|)$ the scattering factor can be treated as a constant and taken to the outside of the integral in Equation 3.15. This approximation is known as the incoherent imaging approximation and can be applied down to resolutions of around 0.1 nm in dark field TEM imaging. This approach is equivalent to the assumption that compared to the resolution of the image, which is determined by the point spread function, each scatterer is effectively a point. The point spread function of the optical system, when it is centred on atom j at position $\boldsymbol{r}$ has an amplitude $a_j(\boldsymbol{r}-\boldsymbol{r}_j, K_{ap})$, which was given in Equation 3.18. With optical or X-ray imaging of clusters of nanoscale particles, their scattering factors can be oscillatory. Using small apertures whose width K_{ap} is far smaller than the oscillation period, the approximation used here was shown to be robust.[151]

In a microscope, there are two equivalent ways that images can be acquired. A microscope with fixed illumination has a well defined source from which the sample is irradiated, the scattering from the sample is then collected and magnified by an objective lens, following this it is projected onto an image plane using a projector lens/es. In this case, the sample and image planes are conjugate. The difference between the image and the sample is that the image has been filtered and magnified in the imaging system, most importantly the objective aperture and lens. The scanning method works by using the objective lens to form a probe that is finely focussed onto the sample, the probe is then scanned over the sample point by point. Scattering is then collected by detectors. Images can be formed by either moving the sample across a fixed probe or by rastering the probe on the sample. The collected signals are then displayed as 2D arrays of intensity.

In principle, it is possible that both fixed and scanning illumination could produce images that are identical. This is due to the Helmholtz reciprocity principle, which says that if there is a point source and point detector, if their positions are exchanged and the wave function emitted from the source is not changed, then the wave function that is detected will also not change. It is important to note that the principle does not mean that swapping detector and source will provide images that are identical in the detector plane. The equivalent wave functions only apply to the two specific points in the system, source and detector. Images that are equivalent could be obtained after the swap by the scanning of the swapped source over the original image plane, then

collecting the signal at the detector to create the image point by point.

We can interpret a_j in two different ways. When fixed illumination imaging is used, the point-spread function defining the image resolution of the microscope is a_j^2. On the other hand, in the case of the scanned probe, the probe intensity profile is given by a_j^2, determining the resolution and probed sample width of the image.

FEM investigates the variations in scattering between different sub-volumes of the sample. In this case the resolution function a_j, alongside the local thickness t of the sample, is a convenient way of delineating these sub-volumes. A simple approximation for the resolution function a_j would be a top-hat function that has uniform amplitude and phase over a width W, beyond which there is zero intensity. This would provide a cylindrical region for the sampled volume given by;

$$volume = \frac{\pi W^2 t}{4} \tag{3.19}$$

however, in a lens that is perfectly focussed, a better model for the resolution function is that of an Airy disc, which has an oscillatory decaying amplitude as distance increases from the centre. This means practically that the sampled volume is not actually a uniform section of the sample. Each individual scatterer j contributes to the final scattered intensity and is weighted by the both the local phase and amplitude of a_j, while these are both governed by K_{ap} the objective aperture and aberrations in the lenses. In general, a larger K_{ap} provides a narrower a_j. A defocussed probe affects the amplitude of a_j.

In materials that are disordered, there are fluctuations in the scattered intensity between different sub-volumes in the sample, these appear as speckles. These speckles can be quantified, where the easiest method is by calculating both the mean and variance of the intensity in an image. The equation for normalised variance is;

$$V(\boldsymbol{q}, K_{ap}) = \frac{\langle I^2(\boldsymbol{q}, K_{ap})\rangle}{\langle I(\boldsymbol{q}, K_{ap})\rangle^2} - 1 \tag{3.20}$$

where the $\langle\rangle$ symbols indicate that a mean is being taken. The second moment of intensity is given by $\langle I^2(\boldsymbol{q}, K_{ap})\rangle$, when this is normalised by $\langle I(\boldsymbol{q}, K_{ap})\rangle^2$, the dependence of $V(\boldsymbol{q}, K_{ap})$ on $f(|\boldsymbol{q}|)$ the scattering form factor is eliminated.

If we want to understand how speckles are related to correlations, it is necessary to derive the equations for both the first moment $\langle I(\boldsymbol{q}, K_{ap})\rangle$ and the second moment $\langle I^2(\boldsymbol{q}, K_{ap})\rangle$ of image intensity.

If the illumination is fixed, the wave function for kinematical dark field image is given by the sum of the scattering wave functions of each scatterer,

$$U_j(\boldsymbol{r}, \boldsymbol{q}, K_{ap}) = \sum_j u_j(\boldsymbol{r}, \boldsymbol{r}_j, \boldsymbol{q}, K_{ap}) \tag{3.21}$$

This means that the expression for dark field image intensity $I(\boldsymbol{r}, \boldsymbol{q}, K_{ap})$ is given by

$$I(\boldsymbol{r}, \boldsymbol{q}, K_{ap}) = \sum_j \sum_l u_j(\boldsymbol{r}, \boldsymbol{r}_j, \boldsymbol{q}, K_{ap}) u_l^\star(\boldsymbol{r}, \boldsymbol{r}_l, \boldsymbol{q}, K_{ap}) \tag{3.22}$$

which can be rewritten as

$$I(\boldsymbol{r}, \boldsymbol{q}, K_{ap}) = f^2(|\boldsymbol{q}|) \sum_j \sum_l a_j(\boldsymbol{r}, \boldsymbol{r}_j, K_{ap}) a_l^\star(\boldsymbol{r}, \boldsymbol{r}_l, K_{ap}) e^{-i\boldsymbol{q}\cdot\boldsymbol{r}_{jl}} \tag{3.23}$$

where we have $\boldsymbol{r}_{jl} = \boldsymbol{r}_l - \boldsymbol{r}_j$ which describes the position vector relating the scatterer i to scatterer j. It is assumed that both of these scatterers i and j have scattering factors that are similar.

As the mean image intensity $I(\boldsymbol{q}, K_{ap})$ is given by the average intensity over the sample, we have

$$\langle I(\boldsymbol{q}, K_{ap}) \rangle = \frac{f^2(|\boldsymbol{q}|)}{A} \sum_j \sum_l e^{-i\boldsymbol{q}\cdot\boldsymbol{r}_{jl}} \int\int_{sample} a_j a_l^\star d^2\boldsymbol{r} \tag{3.24}$$

where the image area A is introduced. Using Equation 3.18 it is possible to show that

$$\int\int_{sample} a_j a_l^\star d^2\boldsymbol{r} = \lambda^2 \int\int_{obj} e^{i\boldsymbol{q}\cdot\boldsymbol{r}_{jl}} d^2\boldsymbol{k} \tag{3.25}$$

which means that the mean or first moment of image intensity can now be written as

$$\langle I(\boldsymbol{q}, K_{ap}) \rangle = \frac{\lambda^2 f^2(|\boldsymbol{q}|)}{A} \sum_j \sum_l \int\int_{obj} e^{i(\boldsymbol{k}-\boldsymbol{q})\cdot\boldsymbol{r}_{jl}} d^2\boldsymbol{k} \tag{3.26}$$

The total scattering vector that the beam experiences at $\boldsymbol{k}$ in the objective aperture is given by $\boldsymbol{k} - \boldsymbol{q}$. If the total diffracted intensity that passes through the objective aperture is averaged over the image area, the average image intensity is obtained. When

large enough areas A are used, this is independent of $\gamma(|\boldsymbol{k}|)$, the microscope aberration function given in Equation 3.16.

Using Equation 3.23 we can now express the second moment of the image intensity as

$$\langle I^2(\boldsymbol{q}, K_{ap})\rangle = \frac{f^4(|\boldsymbol{q}|)}{A}\sum_j\sum_l\sum_m\sum_n e^{-i\boldsymbol{q}\cdot(\boldsymbol{r}_{jl}+\boldsymbol{r}_{mn})} \times\int\int_{sample} a_j a_l^\star a_m a_n^\star d^2\boldsymbol{r} \tag{3.27}$$

The integral over the sample can be rewritten as

$$\int\int_{sample} a_j a_l^\star a_m a_n^\star d^2\boldsymbol{r} = \lambda^2\int\int_{obj} d^2\boldsymbol{k}_1 d^2\boldsymbol{k}_2 d^2\boldsymbol{k}_3 e^{i\boldsymbol{k}\cdot(\boldsymbol{r}_{jn}+\boldsymbol{r}_{nl}+\boldsymbol{r}_{mn})} \times e^{i(-\gamma(|\boldsymbol{k}_1|)+\gamma(|\boldsymbol{k}_2|)-\gamma(|\boldsymbol{k}_3|)+\gamma(|\boldsymbol{k}_1-\boldsymbol{k}_2+\boldsymbol{k}_3|))} \tag{3.28}$$

In the majority of FEM experiments, the microscope is operating a long way from its resolution limit. By using small apertures, point spread functions that have resolutions of around 1-2 nm are created. This means that we could assume that aberration terms are zero. When the probe is close to being in focus, the limiting factor is not the aberrations. If however a study utilises a focal series, it would be necessary to include the aberration terms. When images are in focus, Equation 3.27 for the second moment of intensity can be approximated to

$$\langle I^2(\boldsymbol{q}, K_{ap})\rangle = \frac{\lambda^4 f^4(|\boldsymbol{q}|)}{A}\sum_j\sum_l\sum_m\sum_n e^{-i(\boldsymbol{q}\cdot\boldsymbol{r}_{jl}+\boldsymbol{q}\cdot\boldsymbol{r}_{mn})} \times\int\int_{obj} e^{i\boldsymbol{k}_1\cdot\boldsymbol{r}_{jn}} d^2\boldsymbol{k}_1\int\int_{obj} e^{i\boldsymbol{k}_2\cdot\boldsymbol{r}_{nl}} d^2\boldsymbol{k}_2\int\int_{obj} e^{i\boldsymbol{k}_3\cdot\boldsymbol{r}_{mn}} d^2\boldsymbol{k}_3 \tag{3.29}$$

There are two different interference terms that appear in both the first and second moments of intensity, these are F_{jl} and A_{jl}

$$F_{jl} = e^{-i\boldsymbol{q}\cdot\boldsymbol{r}_{jl}} \tag{3.30}$$

$$A_{jl} = \int\int_{obj} e^{i\boldsymbol{k}\cdot\boldsymbol{r}_{jl}} d^2\boldsymbol{k} = \frac{2J_1(K_{ap}|\boldsymbol{r}_{jl}|)}{K_{ap}|\boldsymbol{r}_{jl}|} \tag{3.31}$$

where J_1 is a first order Bessel function. F_{jl} terms are representative of the coherence strength of the interference between two scatterers j and l. Where there is plane wave illumination, as we have been using, a sinusoidal interference function is the result. A_{jl} terms are proportional to the point-spread function a_j at probe position $\boldsymbol{r} = \boldsymbol{r}_j$ because they are equivalent to $-ia_{jl}/\lambda$. Both of these functions are Hermitian so that

$$F_{jl} = F_{lj}^{\star} \quad , \quad A_{jl} = A_{lj}^{\star} \tag{3.32}$$

The illumination optics control the F_{jl} interference terms while the imaging optics control the A_{jl} terms.

Using this, we can show that the first moment of image intensity can be expressed as

$$\langle I(\boldsymbol{q}, K_{ap})\rangle = \frac{\lambda^2 f^2(|\boldsymbol{q}|)}{A} \sum_j \sum_l A_{jl} F_{jl} \tag{3.33}$$

while the second moment now becomes

$$\langle I^2(\boldsymbol{q}, K_{ap})\rangle = \frac{\lambda^4 f^4(|\boldsymbol{q}|)}{A} \sum_j \sum_l \sum_m \sum_n A_{jn} A_{nl} A_{mn} F_{jl} F_{mn} \tag{3.34}$$

This means that we can rewrite the normalised variance from Equation 3.20 as

$$V(\boldsymbol{q}, K_{ap}) = N_0 \frac{\sum_j \sum_l \sum_m \sum_n A_{jn} A_{nl} A_{mn} F_{jl} F_{mn}}{\sum_p \sum_q \sum_r \sum_s A_{pq} A_{rs} F_{pq} F_{rs}} - 1 \tag{3.35}$$

or

$$V(\boldsymbol{q}, K_{ap}) = \frac{\sum_{j,l,m,n} (N_0 A_{jn} A_{nl} - A_{jl}) A_{mn} F_{jl} F_{mn}}{\sum_{p,q,r,s} A_{pq} A_{rs} F_{pq} F_{rs}} \tag{3.36}$$

where we have $N_0 = A\pi K_{ap}^2$ which is equivalent to number of pixel elements present in the image.

Equation 3.36 shows that normalised variance is dependent on what are called 4-body correlations, which can also be called pair-pair correlations. Diffracted intensity on

the other hand is dependent on 2-body correlations, also called pair correlations. As $V(\boldsymbol{q}, K_{ap})$ is dependent on these higher order pair-pair correlations, it has a higher level of sensitivity to medium range order than that obtained from the mean diffracted intensity.

Using TEM, modification of F_{jl} properties can be achieved by changing the illumination properties, for example convergence angle.

If incoherent hollow cone illumination is used, formed by the rotation of the illumination vector $\boldsymbol{q}$ azimuthally about the optic axis, then images can be built up as an incoherent sum over all of the azimuthal angles. This means however that the F_{jl} terms would be modified to [152]

$$F_{jl} = \frac{\int_{\alpha 1}^{\alpha 2} J_0(2\pi\sigma_{jl} sin(\alpha/\lambda) cos(4\pi z_{jl} sin^2(\alpha/2)/\lambda) f(\alpha)^2 \alpha \, d\alpha}{\int_{\alpha 1}^{\alpha 2} f(\alpha)^2 \alpha \, d\alpha} \tag{3.37}$$

where J_0 is a zero-order Bessel function. In this expression, the atom position has been decomposed into σ_{jl}, which is an in-plane x-y component and z_{jl} the z-component, giving $\boldsymbol{r}_{jl} \equiv (\sigma_{jl}, z_{jl})$, where $\alpha = sin^{-1}(\lambda|\boldsymbol{q}|/2\pi)$ is the tilt angle of the cone. Because this type of illumination suppresses the lateral extent of the coherence function, interferences between atoms that are aligned in columns become more important.[153]

For each scattering atom l there is a region surrounding it where coherent scattering with atom j can occur, this region is controlled by the way that the F_{jl} and A_{jl} functions intersect. Both of these can be controlled independently. Variable coherence fluctuation microscopy refers to experiments where F_{jl} is varied, while variable resolution microscopy indicates that A_{jl} is being changed.

It is shown in Equation 3.36 that the normalised variance obtained from speckles in a dark field image depends on 4-body or pair pair correlations. The mean image intensity however is only dependent on 2-body or pair correlations. This means that normalised variance is dependent on correlations up to 4-body terms, which is to a higher order than mean image intensity. Fluctuation microscopy is sensitive to medium range order in a material, due to this dependence on the higher order of correlations.

The speckliness in a dark field image is strongly dependent on the diffraction vector $\boldsymbol{q}$. In a TEM, the method for running fluctuation electron microscopy experiments is to keep the diffraction vector $\boldsymbol{q}$ fixed and collect dark field images whose intensity varies with position $\boldsymbol{r}$. This means that data is collected as $I(\boldsymbol{q}_{fixed}, \boldsymbol{r})$. In the STEM, the sample is probed one step at a time, with the diffraction pattern from each volume collected, this was shown earlier in Figure 3.13. Thus in the case of the STEM, data

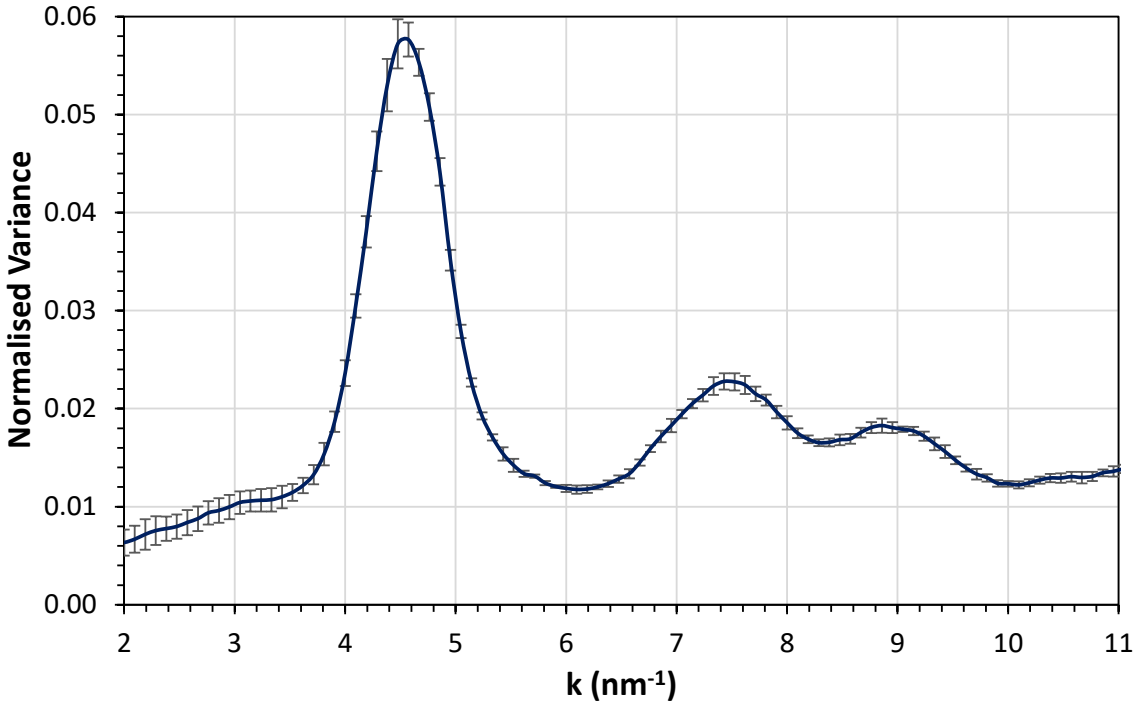

Figure 3.15: FEM variance of a diamond-like carbon film doped with W and Mo.

is collected as $I(\boldsymbol{q}, \boldsymbol{r}_{fixed})$ and it is the speckles within diffraction patterns that are important. If an experiment in the TEM took data across the same $\boldsymbol{q}$ range as the STEM, or alternatively a STEM experiment scanned over the same $\boldsymbol{r}$ range as in the TEM then each of the datasets should be identical.

In an experiment, scanning datasets containing hundreds of diffraction patterns will be collected from a sample. Datasets will be acquired using a range of different probe sizes, which can be controlled by changing the convergence angle of the illumination, which is achieved through the condenser lens system.

Each of these datasets will then run through a code which calculates their normalised variance, which is then turned into a plot of normalised variance against k as seen in Figure 3.15. There are peaks in the normalised variance at scattering angles where diffraction speckles occur, indicating that there are variations in atomic structure between different areas of the sample.

3.8 Summary

In this thesis, the samples were prepared using a gallium ion FIB, the advantages/disadvantages of using other types of FIB were discussed, such as a xenon plasma FIB, however we were limited to the equipment that was available when the samples were

being prepared.

General features of a TEM/STEM were shown, and the capabilities of the JEOL ARM200cF microscope that was used for experiments in this thesis. This microscope has some features that are well suited to FEM experiments, such as the cold-FEG electron source and the MerlinEM Medipix-III direct electron detector.[78, 115, 117, 154] One drawback to this microscope for use in FEM experiments is that the condenser lens system has two lenses, a third condenser lens would provide further flexibility in probe formation.

Electron diffraction and kinematical electron scattering was discussed. This is the basis for the theory behind the FEM technique.

FEM is sensitive to MRO in materials, due to the variance of diffraction intensity being linked to 3-body and 4-body correlations. This allows the qualitative and quantitative measurement of the MRO in a material and the length scale at which it exists.

The theory of EELS and how it can tell us about both the elements present in the sample and the relative quantities of those elements was discussed.

In the next two chapters, the techniques described here will be applied, namely FEM and EELS to describe the structure and composition of two different types of materials.

Chapter 4

Characterisation of the Atomic Structure and Composition of Materials for Superconducting Nanowire Single Photon Detectors

4.1 Introduction

In this chapter, we will show experimental results from four different superconducting nanowire single photon detector (SNSPD) materials. These were made from three different combinations of elements; $MoSi_x$, $NbSi_x$ and WSi_x. Two different methods for depositing these materials were used, co-sputtering and alloy sputtering, the details of these processes will be discussed later in this chapter.

In order to understand why we are interested in these materials, we will first take a quick look at the phenomenon of superconductivity. Following that, we will show how superconductivity can be used to form single photon detectors.

4.1.1 Superconductivity

In 1911 the phenomenon of superconductivity was first observed by Heike Kamerlingh Onnes and his research group, who observed zero electrical resistance in mercury at temperatures below 4.2 K.[155] Since that discovery, it has been found that the majority of the elements will become superconductors, if their temperature is lowered sufficiently.

When the temperature of a superconducting material becomes lower than what is called the critical temperature (T_c) of the material, it transitions into the superconducting state. This state can be characterised by two properties, the first of these is that there is no resistance to electrical current through the material. Secondly, as long as magnetic fields surrounding the material are weak, any external magnetic fields are not able to enter the superconductor, they remain at its surface. This effect was first observed by Meissner in 1933, and is now known as the Meissner effect.[156]

In 1957, three American scientists - John Bardeen, Leon Cooper and John Schrieffer formulated a theory in an attempt to explain superconductivity.[157] This theory is often referred to as BCS theory. In this theory, electrons form into pairs, known as Cooper pairs, as a result of their interactions with the vibrations (phonons) in the lattice. These Cooper pairs can move around the material without any friction. The amount of energy involved in these pairings is small, so the pairs can be broken easily by thermal energy, for this reason superconductivity usually requires extremely low temperatures to occur. This BCS theory however, does not explain how the higher temperature superconductors such as the cuprates or iron based superconductors operate.

There are two different ways to halt a superconducting state, these are; firstly, raising the temperature of the superconducting material to above the critical temperature, and secondly, increasing the applied magnetic field such that it suppresses the Meissner effect and the external magnetic field enters the material. If a superconducting material remains in its superconducting state when only a small magnetic field is present, then it is a Type I superconductor. When the magnetic field becomes larger than a certain threshold value, the field penetrates into the superconductor, which causes the superconducting state to stop. Type II superconductors are different from Type I superconductors, this is because their transition between a normal and superconducting state is not abrupt, but gradual. They allow for external magnetic fields to penetrate some of their surface, which means that they can remain in the superconducting state under much higher magnetic fields. Superconducting and non-superconducting states can coexist within Type II superconductors.

There are various different applications for superconductors, the largest of these is in

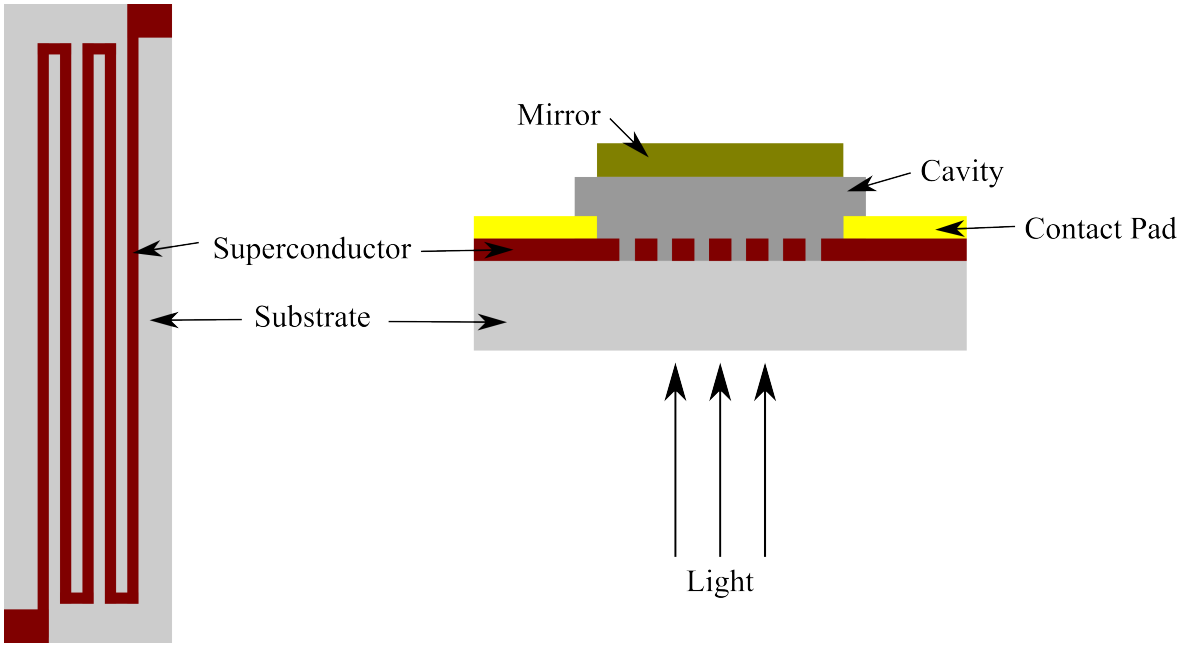

Figure 4.1: Diagram showing on the left an SNSPD deposited on a substrate and on the right an example cross section of an SNSPD device.

magnetic resonance imaging (MRI) and nuclear magnetic resonance (NMR) machines. They can also be used in particle accelerators and devices for magnetic fusion. Maglev trains also use superconducting magnets to levitate trains above the rails. A variety of different high sensitivity particle detectors also utilise superconductors. There are many potential uses for these materials, a greater understanding of how they work could result in great technological advances.

4.1.2 Superconducting Nanowire Single Photon Detectors

Almost twenty years ago, a concept for a new type of superconducting device was established, by Gol'tsman et al.[158], which was based on a nanowire made of niobium nitride. This was called a superconducting single-photon detector (SSPD) and led to the development of the superconducting nanowire single photon detector (SNSPD).

An (SNSPD) is a device that is used, as its name implies, as a single photon detector.[158] It is normally used for the detection of photons at either optical or near infrared wavelengths.[159] An SNSPD is formed of a nanowire that is both very thin and narrow, with a length much larger in comparison to its width, that has been formed into a pixel by patterning it into a larger overall shape.[159] Figure 4.1 shows a cross-section and plan view of what one of these devices may look like.

In order for the device to operate, the device is cooled so that its temperature is lower

than the superconducting critical temperature T_c. A DC current is then used to apply a bias current that is less than, but close to, the superconducting critical current of the nanowire. When a photon is incident on the nanowire, Cooper pairs are broken, such that the local critical current is reduced below that of the bias current. When this happens, that area of the nanowire will form a non-superconducting region, sometimes called a hotspot, that has an electrical resistance. There are two electrical contacts at each end of the nanowire, over which a voltage probe can be formed. As a result of this, a voltage pulse can be observed when a photon is incident on the nanowire and each individual photon incident on the nanowire can be detected.

SNSPDs have various different applications, such as: quantum key distribution, characterisation of quantum emitters, optical quantum computing, integrated circuit testing, space to ground communications, time-of-flight depth ranging and fibre temperature sensing.[158–160]

4.1.3 Materials for SNSPDs

Three materials that have been used in SNSPDs are Mo_3Si, Nb_3Si and W_3Si, which in their bulk form all share the same A15 crystal structure, as shown in Figure 4.2. In recent years, these materials have been deposited by co-sputtering or alloy sputtering techniques, which creates amorphous materials that could have a similar stoichiometry to their crystalline counterparts. This thesis studies these amorphous materials in more detail, investigating the short/medium range order and atomic composition of these materials.

The first A15 structure to be discovered was β-W in 1931.[161] These structures, which are also known as Cr_3Si or β-W, all follow the formula A_3B, A is one of the transition metals and B could be any element. Figure 4.2 shows the atomic structure they follow. They have a cubic structure with the space group $Pm\overline{3}n$, where the B site atoms follow a BCC arrangement, while the A site atoms are positioned in strings along the face centres. This means that the A atoms are in positions such as (1/2, 1/4, 0). In β-W, the atoms on both A and B sites are W, while in Mo_3Si, Nb_3Si and W_3Si the A atoms are the transition metals, while the B sites are Si.

Many A15 materials are superconductors at low temperatures. The first to be discovered was vanadium silicide V_3Si in 1953.[162] Following that initial discovery, several more A15-structured compounds were found to be superconducting.[163] In fact until the discovery of the cuprate superconductors in the 1980s, the superconductor with the highest transition temperature was Nb_3Ge at 23.2 K.[164] Lists of the superconducting critical temperature of the A15 materials can be found in a number of references [163,

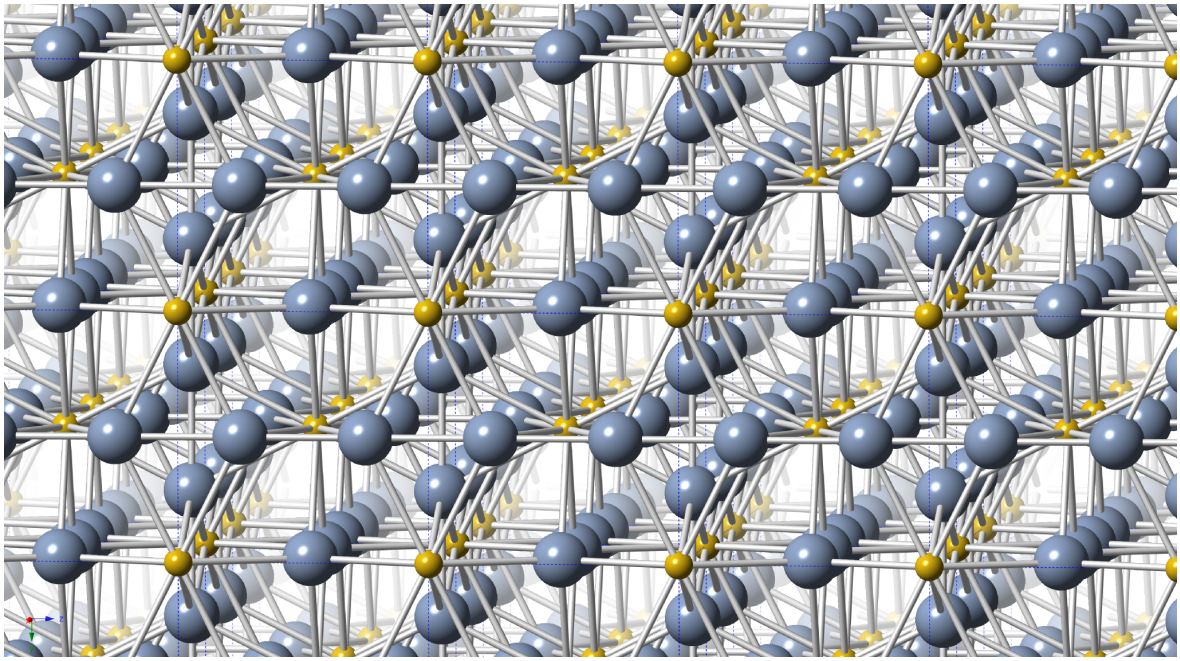

Figure 4.2: A15 crystal structure diagram created using CrystalMaker (CrystalMaker Software Ltd., Oxon, UK) for a system with Si atoms (yellow) in the centre and corner sites, while metal atoms (blue-grey) occupy the other sites.

165–167].

A15 Mo_3Si has a T_c of 1.3 K in the crystalline state,[168] however disorder in the lattice does affect this, as irradiation damage can cause the density of states at the Fermi level to increase, and T_c can rise to 7.7 K.[169–172] Nb_3Si has a higher T_c, up to 18 K, although it is very difficult to create stoichiometrically.[173] W_3Si has a much lower T_c, of less than 1.2 K.[163] Different A15 structures show variations in the extent that their electronic properties are affected by atomic structure, a material such as Nb_3Sn is heavily affected, whereas Mo_3Ge does not show a specific change in electronic properties from the arrangement of atoms.[167]

These structures are often found to have stoichiometries where the ratio A:B $\neq$ 3:1, for example when there are B atoms on A sites or alternatively voids or A atoms on B sites.[174–177] Some A15 materials can vary in their B concentration from 18-32%, such as in the case of V_3Ga.[178] In most cases the A15 phase can occur over a range of stoichiometries, sometimes with A:B $>$ 3:1. Figure 4.3 shows the Nb-Al phase diagram, where the aluminium content of the A15 phase can be as low as 18.5 %, while its maximum is at 25 %. Mo_3Si shows an A15 phase where the Si composition is between 23 and 25 %.[179] Nb_3Si has not been created in its stoichiometric form, there is always less than 25 % Si.[167]

For many years, ever since the initial work by Buckel *et al.* in 1954,[181] amorphous materials showing superconducting properties have been a subject of investigation.[182–

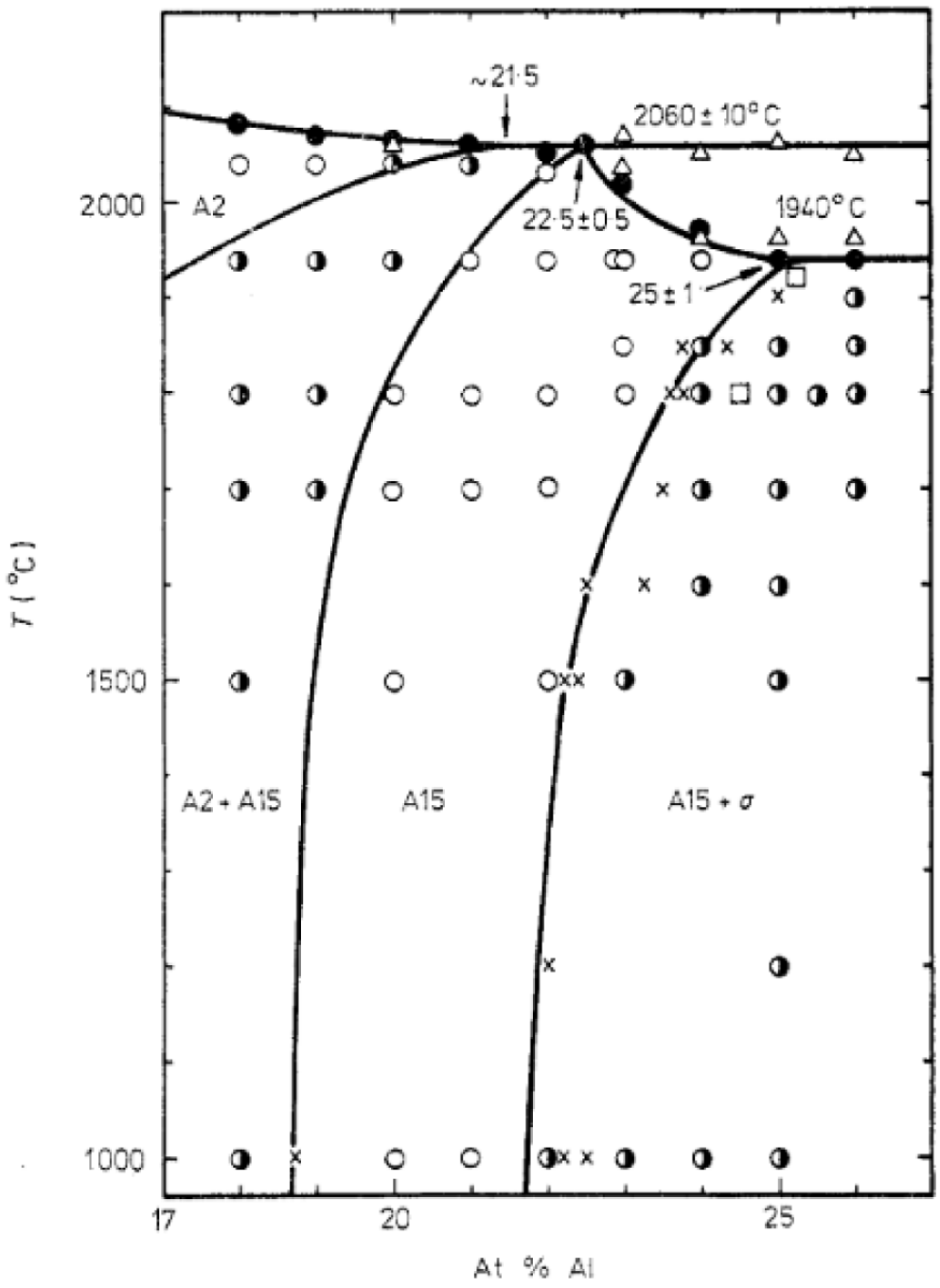

Figure 4.3: A section of the phase diagram of Nb-Al centred on Nb_3Al reproduced from Jorda et al. showing at which temperature and stoichiometries the A15 phase occurs. Open circles indicate single phase, while a half shaded circle indicates there are two phases present.[180].[a]

[a]Republished with permission of R.L. Jorda, from "A New metallurgical investigation of the niobium aluminium system", R.L. Jorda *et. al.*, **75**, 2, (1980); permission conveyed through Copyright Clearance Center, Inc.

Table 4.1: Superconducting critical temperatures for the materials investigated in this chapter.

Material	T_c
Co-sputtered MoSix no Si cap	5.3 K [188]
Co-sputtered MoSix with Si cap	5.3 K [188]
Alloy sputtered MoSix	6.0 K
Co-Sputtered NbSix	4.5 K
Co-Sputtered WSix	3.5 K

187] In recent years, transition metals and their alloys have shown promising properties, resulting in increased interest.[186, 187] The superconducting properties of these materials have been shown to be directly affected by their atomic structure and composition. One of the advantages that these materials have is that they can be cycled between room and cryogenic temperatures repeatedly whilst remaining stable in their structure. The optimisation of these materials for each possible application, alongside examination of how atomic/structural properties of these materials affect their superconducting properties is an ongoing obstacle.

A set of 5 samples created from thin films of amorphous superconductors with nominal compositions close to an A_3B on Si substrates, including three $MoSi_x$ samples, one $NbSi_x$ and one WSi_x, were examined in the work reported in this chapter. The T_c of each sample is shown in Table 4.1. The aim was to investigate what could be determined about both the atomic structure and composition of these samples using FEM and EELS as well as discover whether they show any similarity to the crystalline A15 compounds in structure or chemistry.

One of the particular benefits of the co-sputtered $MoSi_x$ films studied here was that they were found to have high optical absorption at infrared wavelengths, where the Si capped sample was slightly higher, especially at wavelengths of less than 600 nm.[188] This could mean that the optical efficiency of SNSPD devices could increase using co-sputtered $MoSi_x$ thin films. Banerjee et al. found that in the mid infrared range at wavelengths of around 1500-2200 nm, they would be a material that is optically efficient and would be useful in SNSPD detectors that operate in that region.

Please note, all samples analysed in this chapter were sputtered or co-sputtered onto Si targets in the School of Engineering by Archan Banerjee working with Prof. Robert Hadfield. Any measurement of superconducting properties was also made by these persons. FIB preparation, STEM data acquisition and subsequent analysis was performed in the School of Physics and Astronomy by myself, working with academic and technical staff that are responsible for the facilities.

4.2 Experimental Setup

4.2.1 Deposition Procedures and Sample Preparation

The films that are investigated in this chapter were deposited using sputtering techniques. The most simple process was that used in the $MoSi_x$ alloy sputtered film, where an alloy of 75 % Mo and 25 % Si was sputtered onto an oxidised Si wafer, that had an SiO_2 oxide layer 150 nm thick.

Co-sputtering is a process where two different targets are sputtered onto the substrate simultaneously. In order to adjust the composition of the film being sputtered, the power supplied to each of the targets can be varied.

All of the films investigated in this chapter apart from the one mentioned above were deposited using the co-sputtering process. The co-sputtering process for the co-sputtered $MoSi_x$ films was set up with a target discharge current of 0.3 A for the Mo target and with a RF target power of 125 W for Si.[188]. The $MoSi_x$ layers both have thicknesses of 5 nm and were deposited onto oxidised Si wafers. One of these films was subsequently coated with a Si capping layer (Sample A), while the other was not (Sample B). For the $NbSi_x$ sample, the Nb was sputtered with a target power of 350 W, while the Si was sputtered with a power of 100 W. The thin film layer has a thickness of 30 nm and was deposited onto a Si substrate that had an oxide layer of approximately 150 nm. The WSi_x film was deposited onto an oxidised Si wafer, that had an oxide layer of approximately 150 nm. The thickness of the film is roughly 3 nm, and a capping layer of Si 2 nm thick deposited on top of it. The estimated composition of the sample from the deposition process was 85:15 W to Si.

All of the films were prepared as TEM cross-section samples using the FIB method outlined in Chapter 3. Each of the samples was coated with protective capping layers; co-sputtered $MoSi_x$ with gold, alloy $MoSi_x$ with gold, $NbSi_x$ has a platinum layer and the WSi_x a gold layer.

4.2.2 FEM Microscope Setup

There are various different variables within the microscope that can be changed to form an electron probe with the required properties. Condenser aperture, excitation of both condenser lenses and the condenser minilens, spot size and exposure time. These are the settings that determine the properties of the probe, such as convergence angle, size and current.

Prior to recording the diffraction datasets, images of the probe were recorded using the Gatan Orius SC1000A. An example is shown in Figure 4.4a. This probe is very astigmatic and is somewhat different from what a point spread function should look like. Rotational averages of the probe intensity were then calculated. As the probes were astigmatic and not perfectly round, there is an error of around 10 %.

In order to calculate the convergence angle of the probe, diffraction patterns from a crystalline silicon sample were captured, as seen in Figure 4.4b, the distance between two Bragg reflections is measured, which is used to calibrate the image into mrad, the radius of the diffraction disks is the convergence semi-angle of the beam.

Probe current for each dataset was calculated by finding the total detector counts per DP, converting that to electron dose per DP and then calculating beam current.

Below, the various parameters that were used for each of the materials are listed.

4.2.2.1 Co-Sputtered $MoSi_x$ FEM Microscope Settings

Datasets were taken from this sample at only one probe size, the microscope settings and probe parameters of this are shown in Table 4.2. Camera length was kept constant at 120 cm for all of the measurements.

Table 4.2: Microscope settings used in FEM experiments on the $MoSi_x$ film deposited by co-sputtering Mo and Si.

Probe Size (nm) ± 10%	Convergence Angle (mrad)	Probe Current (pA)	CA (um)	Exposure Time (ms)
2	0.87	38	10	100

4.2.2.2 Alloy $MoSi_x$ FEM Microscope Settings

Datasets taken from this sample at three probe sizes, the microscope settings and probe parameters of these are shown in Table 4.3. Camera length was kept constant at 120 cm for all of the measurements.

4.2.2.3 Co-Sputtered $NbSi_x$ FEM Microscope Settings

Datasets taken from this sample at three probe sizes, the microscope settings and probe parameters of these are shown in Table 4.4. Camera length was kept constant at 120 cm for all of the measurements.

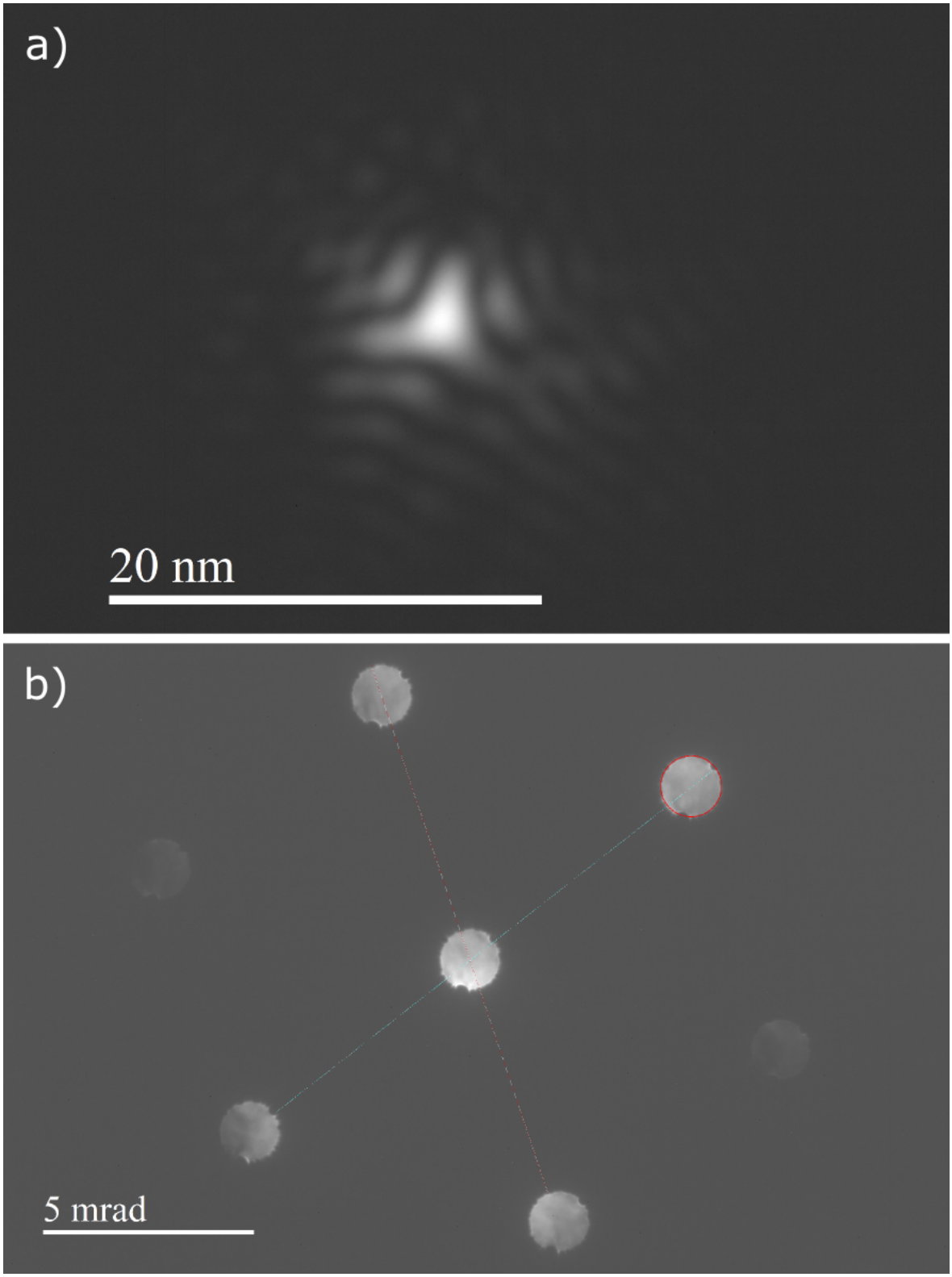

Figure 4.4: Images of a) focussed probe while using a condenser aperture of 10 μm, used for calculating probe size, b) crystalline silicon diffraction pattern, obtained under the same microscope parameters for calculating convergence angle.

Table 4.3: Microscope settings used in FEM experiments on the $MoSi_x$ film deposited from $MoSi_{.25}$ alloy.

Probe Size (nm) ± 10 %	Convergence Angle (mrad)	Probe Current (pA)	CA (um)	Exposure Time (ms)
2.2	0.87	10.25	10	50
2	0.87	10.25	10	50
1	2.16	20.79	20	100

Table 4.4: Microscope settings used in FEM experiments on the $NbSi_x$ film deposited by co-sputtering Nb and Si.

Probe Size (nm) ± 10%	Convergence Angle (mrad)	Probe Current (pA)	CA (um)	Exposure Time (ms)
3	0.87	6.5	10	30
2.6	0.87	6.5	10	30
2	0.87	4.45	10	variable (see 4.3.1)
1.2	2.16	32.3	20	30
1	2.16	21.5	20	variable (see 4.3.1)

4.2.2.4 Co-Sputtered WSi_x FEM Microscope Settings

Datasets taken from this sample at three probe sizes, the microscope settings and probe parameters of these are shown in Table 4.5. Camera length was kept constant at 120 cm for all of the measurements.

Table 4.5: Microscope settings used in FEM experiments on the WSi_x film deposited by co-sputtering W and Si.

Probe Size (nm) ± 10%	Convergence Angle (mrad)	Probe Current (pA)	CA (um)	Exposure Time (ms)
2.5	0.87	18.5	10	30
2.3	0.87	18.5	10	30
1	2.16	25.4	20	30

4.2.3 FEM Data Processing

Once the datasets had been acquired, MATLAB code shown in Appendix A.3.2 was used to calculate the normalised variance. Then python code (Appendix A.3.3) was used to create VDF images, including using the fpd package.[189]

4.2.4 EELS Microscope Setup

All of the EELS-SI was carried out using the JEOL ARM200cF and Gatan GIF Quantum ER spectrometer/energy filter. An accelerating voltage of 200 kV was used, with a convergence angle of 29 mrad and spectrometer acceptance angle of 36 mrad.

4.3 Experimental Results

4.3.1 Effect of Exposure Time on Variance

Exposure time can have a significant effect on the data obtained from FEM experiments. Early FEM experiments obtained using hollow cone dark-field imaging adjusted the exposure time with scattering angle and/or objective aperture.[152, 190] The advent of FEM using the STEM meant that the exposure time had to be optimised so that it is long enough to reduce noise, while short enough so that it does not damage the sample or cause probe drift to become an issue.[81]

Before we inspect each of the films in more detail, the effect of exposure time on the normalised variance of the $NbSi_x$ film was inspected at two different illumination conditions as shown in Table 4.4. Firstly with a probe diameter of 2 nm (10 μm aperture) then with a probe diameter of 1 nm (20 μm aperture). Four different exposure times were used at the 2 nm probe diameter, these were 10 ms, 40 ms, 100 ms and 400 ms. Five exposure times were used in the case of the 1 nm probe diameter; 10 ms, 20 ms, 30 ms, 40 ms and 100 ms. The normalised variance curves resulting from these are shown in Figure 4.5.

Figure 4.5a shows variance curves from the 2 nm probe. There is a significant difference between the variance curve with a 10 ms exposure and the other three, while the main variance peak remains fairly consistent over all four curves, the variance curve is significantly higher at all other values of k. The differences are not as significant between the variance curves obtained at exposure times of 40, 100 and 400 ms. There is a clear reduction in variance at higher values of k with longer exposure time due to the increase in SNR with exposure time. The difference in SNR ratio means that there is a very large difference in the variance curve between exposure times of 10 and 40 ms, while the difference between 40 ms exposure and the 100/400 ms exposure times is much smaller. If the increase in data quality continues at a similar rate to that shown, it appears that above 400 ms exposure time there will only be small changes in data quality with relatively large changes in exposure time. The main variance peak

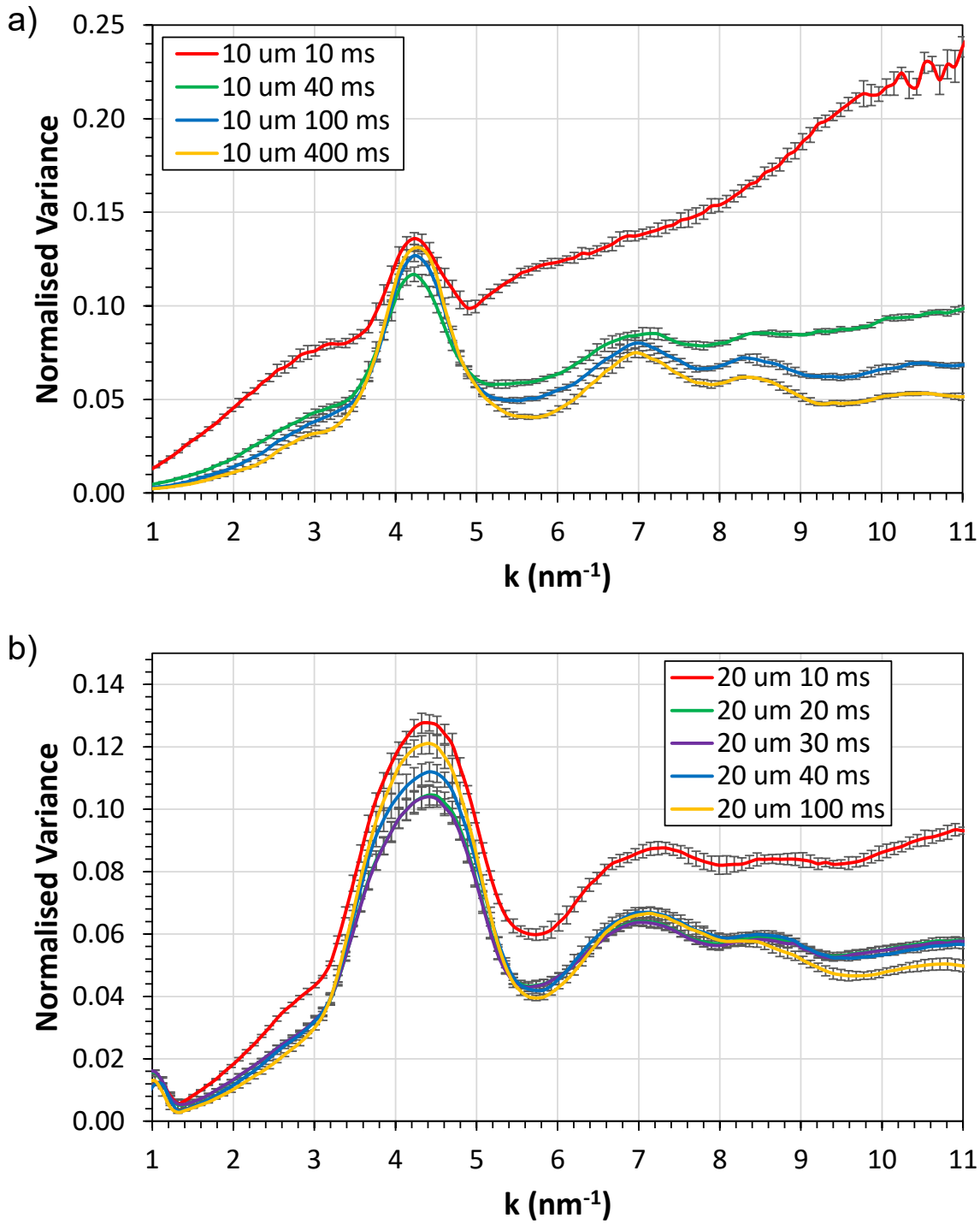

Figure 4.5: Normalised variance of the co-sputtered $NbSi_x$ at various exposure times at two different illumination conditions. a) shows results from an 2 nm probe diameter and b) from a 1 nm probe diameter.

is largest for the 10 ms data, although if that curve is ignored the magnitude of the first variance peak increases with exposure time.

Figure 4.5b, variance curves obtained using a 1 nm probe at 5 different exposure times are shown. There is initially a large change in the variance curve between the 10 ms and 20 ms exposure time, however as the exposure time is further increased, there is very little change. Similarly to the 2 nm probe, the main variance peak is largest at the shortest exposure time, while the general trend is that it increases with longer exposure time. There is very little difference between the 20 ms, 30 ms and 40 ms exposure times at higher k values, while there is a slight decrease when the exposure time is raised to 100 ms. While the probe size is smaller in this case, it has a higher probe current, and subsequently much higher probe current per unit area. It follows that SNR in the 1 nm probe is higher than the 2 nm probe for the same exposure time. Higher probe current allows for shorter exposure times, although this may come at some cost with respect to the spatial coherence of the illumination.[191]

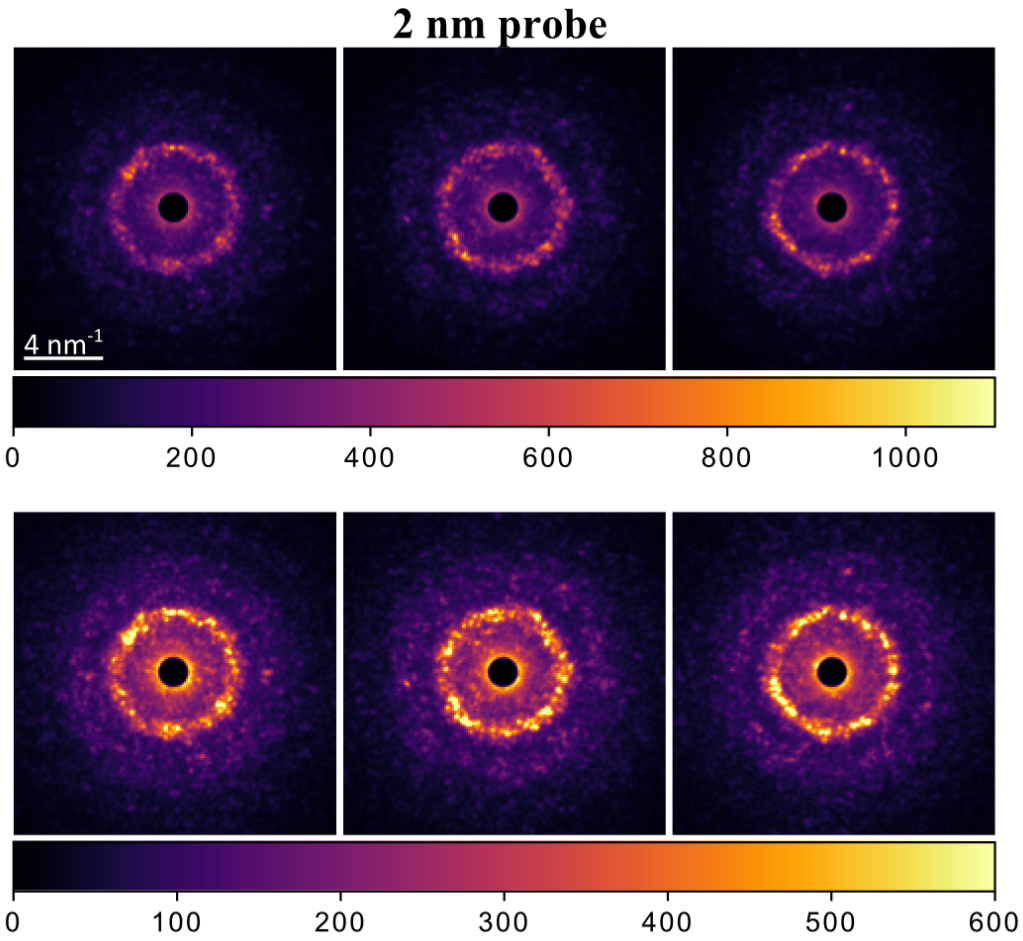

Figure 4.6: Example diffraction patterns from the 2 nm probe size used on this co-sputtered $MoSi_x$ sample. The pairs of diffraction patterns shows images of the same diffraction patterns with different maximum pixel intensity in order to show the inner (upper) and the outer (lower) diffraction peak more clearly.

4.3.2 FEM and VDF imaging

4.3.2.1 Co-Sputtered $MoSi_x$

This sample consists of a layer of $MoSi_x$ approximately 8 nm thick, which was deposited using the co-sputtering method. A 2 nm probe size was used to inspect this sample. Examples of the diffraction patterns found from this sample are shown in Figure 4.6. These DPs show that there is one main diffraction speckle ring, with another area containing what appears to be multiple rings close together at higher scattering angles.

Figure 4.7 shows the normalised variance curve obtained from this sample, There is a large peak at k of 4.5 nm^{-1} as well as some smaller peaks between 6.5-9 nm^{-1}, most notably at k values of 6.85 nm^{-1} and 7.6 nm^{-1}. There is also a small peak at 10.4 nm^{-1} which may be due to noise and a small bump just below 3 nm^{-1}. The main variance peak occurs at a scattering angle very close to that of the largest scattering peak in A15 Mo_3Si. There are also multiple smaller scattering peaks from A15 Mo_3Si

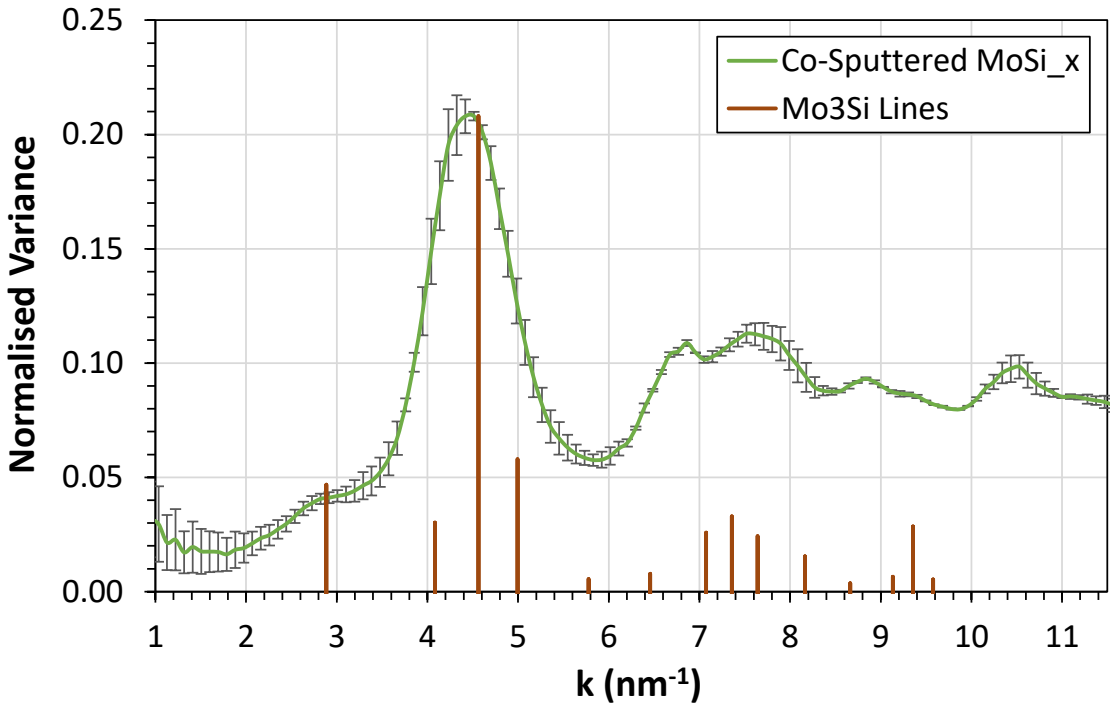

Figure 4.7: Normalised variance of the co-sputtered $MoSi_x$ film. Peak positions and relative heights of x-ray diffractogram peaks in A15 Mo_3Si are overlaid on the graph.[192]

in the 6.5-9 nm^{-1} range, as well as close to the bump just below 3 nm^{-1}.[192] These results suggest that the SRO must be rather A15-like.

Images of the sample area are shown in Figure 4.8, where there is a BF image, followed by four annular VDF images with annular apertures that are positioned at peaks in the variance data. We can see from the BF image that there is not a very large area from which diffraction patterns can be used to calculate the variance. There are a few reasons for this, one is the thickness gradient between the left and right of the scan area, while there are also interface areas where the substrate (below the sample) and capping layer (above the sample) come into contact with the sample. This means that it is difficult to obtain high quality data from this dataset.

All of the annular VDF images in Figure 4.8 show that there are small areas towards the bottom of the $MoSi_x$ layer that scatter more than the rest of the film. None of the AVDF images look particularly different from each other. It is difficult to see from these images whether there are any interesting features within the film due to the low resolution of the images in comparison to the film thickness.

Annular variance images were calculated from the same annular regions that the AVDF images shown previously were obtained from, these are shown in Figure 4.9. These show that there are single pixels/DPs that have a much higher variance than the rest of the film, these are all located towards the extremities of the film at the interface with the substrate. While these brighter spots may indicate that there are ordered areas of 2

nm or smaller at the edges of the film, it is difficult to ascertain any useful information about the structure within the centre of the film from these images.

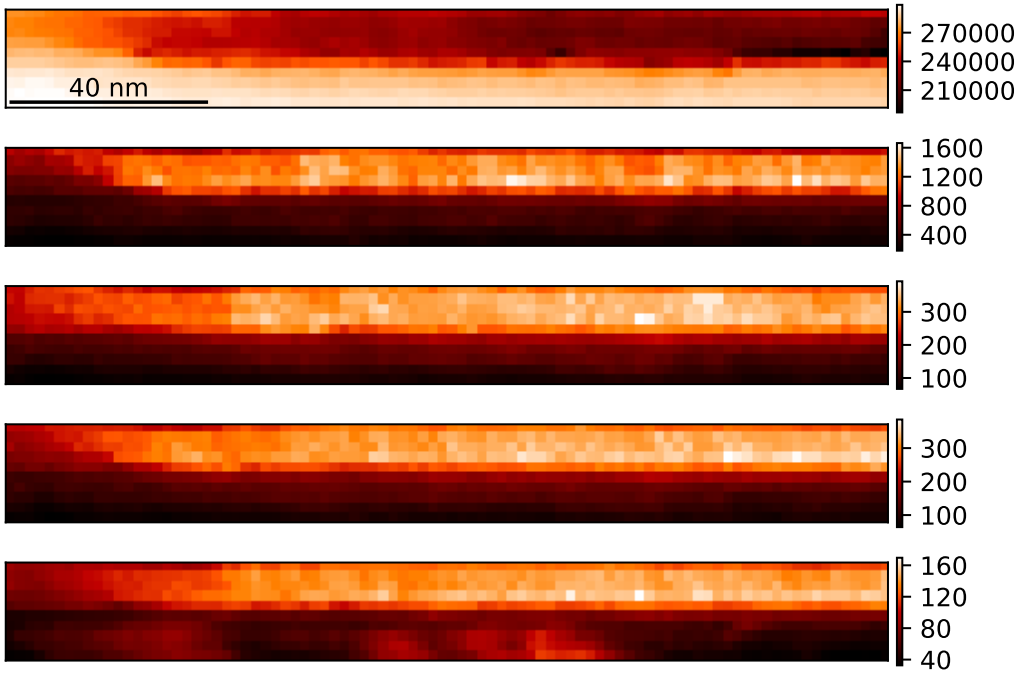

Figure 4.8: BF and VDF images from the co-sputtered $MoSi_x$ film (each image is on a different color scale). The first image shows the bright field image, the next four images are annular VDF images taken in the range; k = 4.3 - 4.5 nm^{-1}, k = 6.75 - 6.95 nm^{-1}, k = 7.5 - 7.7 nm^{-1} and k = 10.4 - 10.6 nm^{-1} respectively.

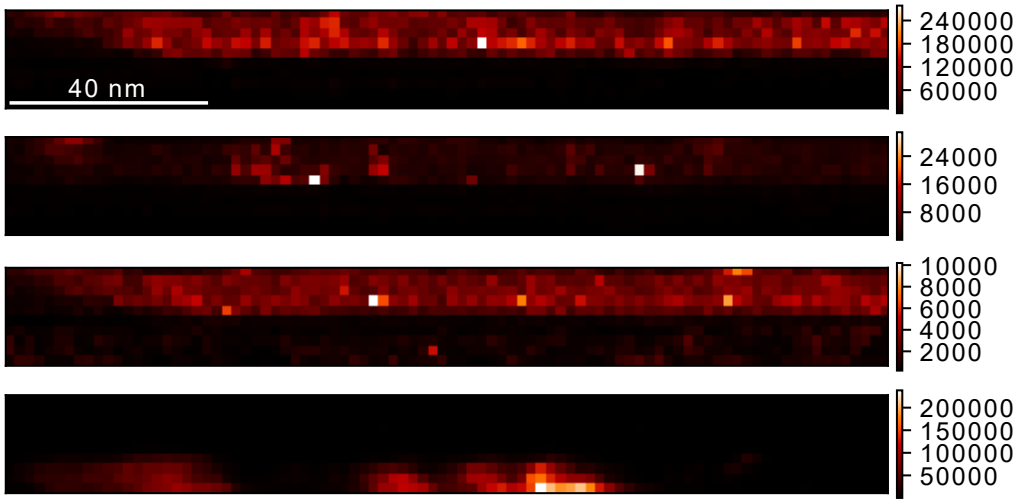

Figure 4.9: Annular variance images from the co-sputtered $MoSi_x$ film (each image is on a different color scale). The images are calculated from the annular ranges; k = 4.3 - 4.5 nm^{-1}, k = 6.75 - 6.95 nm^{-1}, k = 7.5 - 7.7 nm^{-1} and k = 10.4 - 10.6 nm^{-1} respectively.

Other VDF images were created using circular apertures with a diameter of 1 nm^{-1}, a set of four images were generated at each of three three different scattering angles used.

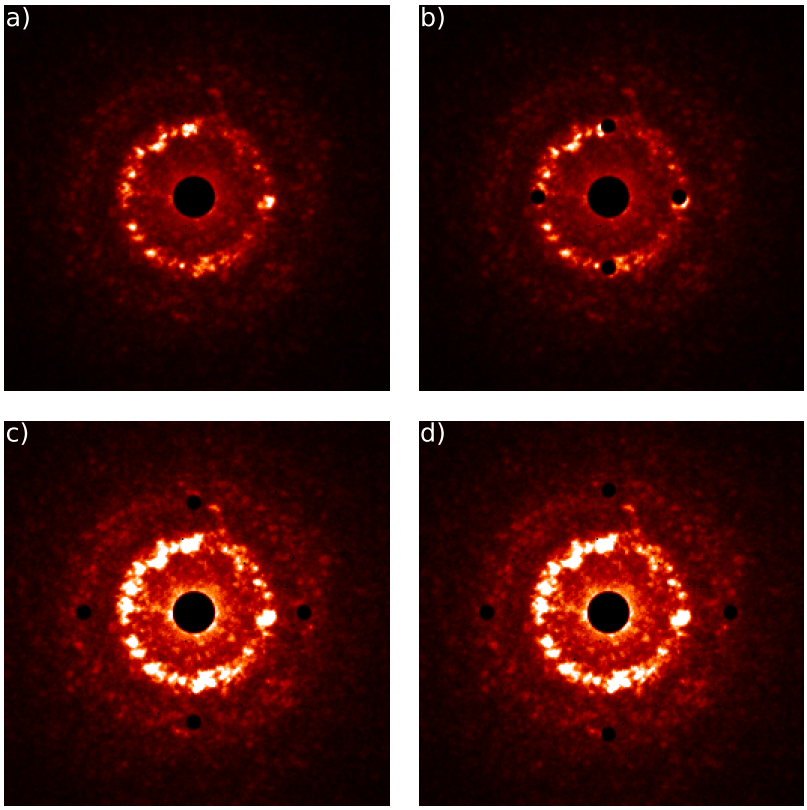

Figure 4.10: a) DP from the co-sputtered $MoSi_x$ film. Then using four circular apertures of diameter 1 nm^{-1} positioned on the diffraction pattern for variance peaks at b)4.5 nm^{-1}, c) 6.85 nm^{-1} and d) 7.6 nm^{-1}.

Figure 4.10 shows the location of these apertures on the DP. VDF images generated from these apertures are shown in Figure 4.11.

At the first variance peak (Figure 4.11a) there are areas of the film that scatter more intensely than others. Some of these are single pixels, while there are also some that are larger, up to 3-4 pixels in size. The most notable bright area occurs in the first image, where there is a bright area in the centre. This area is formed of a very bright pixel, which is within a cluster of 3-4 brighter pixels. In general there are also areas of the sample that scatter more than other areas, but not at dramatically different intensity levels to the rest of the film.

Figure 4.11b shows the VDF images from the circular apertures that were centred at $k = 6.85$ nm^{-1}. The top two images do not show any bright areas in comparison to the bottom two images. In the bottom two images there is a bright spot that appears to be in the same position, in the third image the cluster appears larger, containg four pixels whereas in the fourth image there are only two. As the two apertures used were opposite each other, this indicates an area of the sample that contains a region that could be more crystalline in structure. While in the bottom image the cluster appears in the transitional area betwen film and substrate, in the third image the cluster extends into the centre of the film.

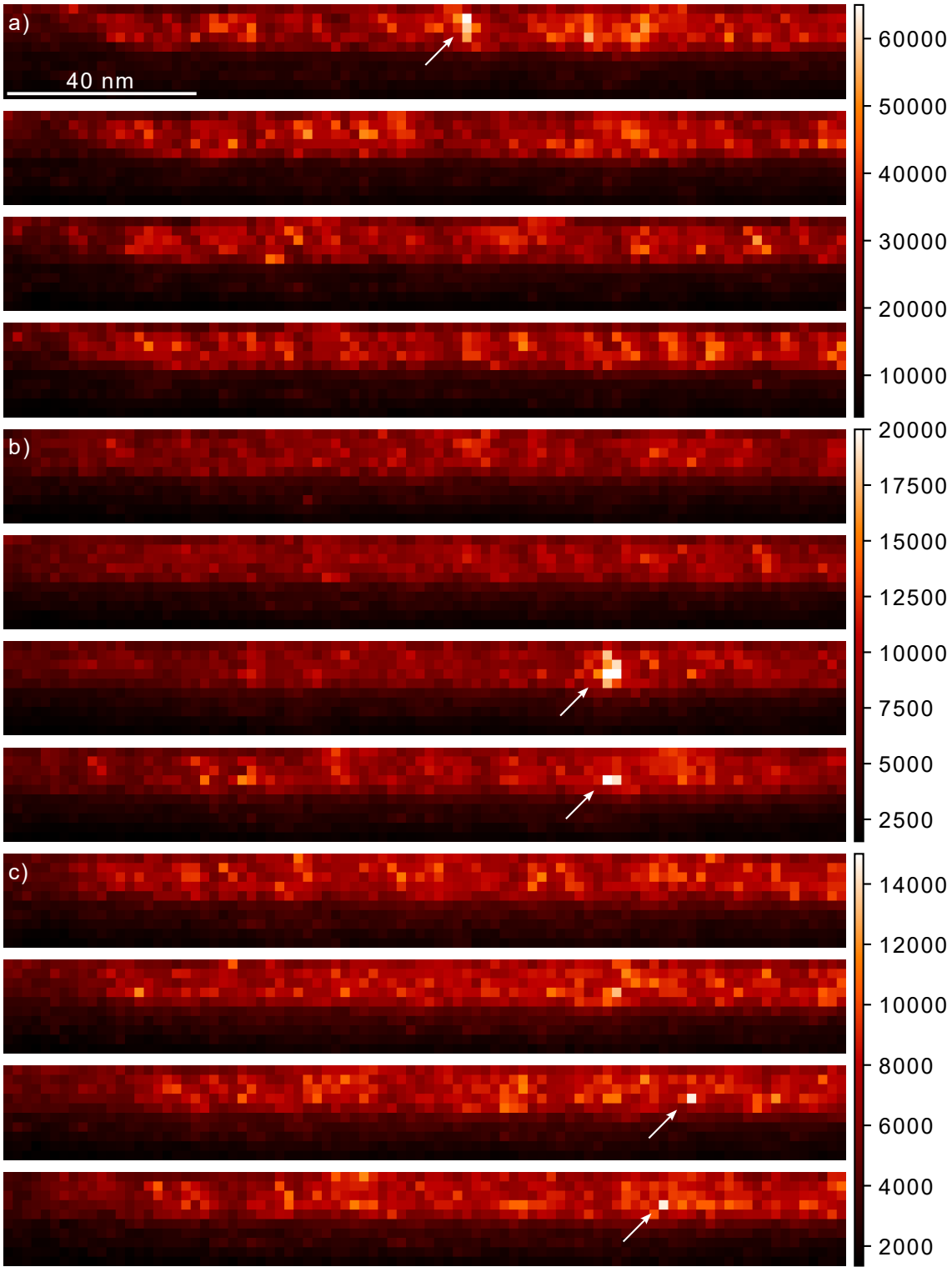

Figure 4.11: VDF images of the co-sputtered $MoSi_x$ film, taken using four different circular apertures of diameter 1 nm^{-1} positioned on the diffraction pattern for variance peaks at a)4.5 nm^{-1}, b) 6.85 nm^{-1} and c) 7.6 nm^{-1}. Each set of four images are on different color scales.

Single pixels of increased brightness are also seen in the VDF images with circular apertures centred at $k = 7.6$ nm^{-1} (Figure 4.11c), the two brightest single pixel spots appear in the third and fourth image towards the bottom of the film, while there are some less bright spots that appear throughout the film, although in most cases these are in the lower or higher transitional regions of the film.

In general, this sample appears to show more MRO in the interface region between the oxidised Si (SiO_2) substrate and the film than in the film itself. However there are some clusters of 3-4 pixels indicating that there are ordered regions of up to 6-8 nm in size. It is possible that the interface structure is being changed by extra silicon getting into that region. Clear results from the film are difficult to find, due to its small thickness in comparison to the probe size.

4.3.2.2 Alloy Sputtered $MoSi_x$

Three different probe sizes were used to inspect this sample. These were 2.2 nm, 2 nm and 1 nm. (See Table 4.3.) We can see example diffraction patterns from each of these probe sizes in Figure 4.12. These diffraction patterns show that the diffraction spots/speckles in each diffraction pattern can vary somewhat. It is difficult to see much difference between the diffraction patterns produced by the 2.2 nm and 2.0 nm probe, however the diffraction patterns from the 1.0 nm probe are markedly different in appearance. This is largely due to the fact that the 20 μm condenser aperture was used to generate this probe, so it has a higher convergence angle than the other two probes and thus worse angular resolution. Diffraction spots/speckles from the 1.0 nm probe also appear to be more defined than those seen using a 2.2 nm or 2.0 nm probe.

The variance curves obtained at these three probe sizes are shown in Figure 4.13. There are three peaks that appear in each of the curves, these are at scattering angles of 4.55 nm^{-1}, 7.4 nm^{-1} and 9 nm^{-1}. Superimposed onto the variance curves are lines representing the scattering angles from Mo_3Si, where the magnitude of these lines has been normalised to the height of the largest variance peak.

The first of these peaks, at 4.55 nm^{-1} is the largest of the three, while the other two peaks are of similar magnitude to each other, but much smaller than the 4.55 nm^{-1} peak.

It is also possible that there is a small bump in the variance at around 3 nm^{-1}, similar to that seen earlier in the co-sputtered $MoSi_x$, although this is very small.

Again, the peaks in the normalised variance suggest that the film has SRO similar to that of A15 Mo_3Si.

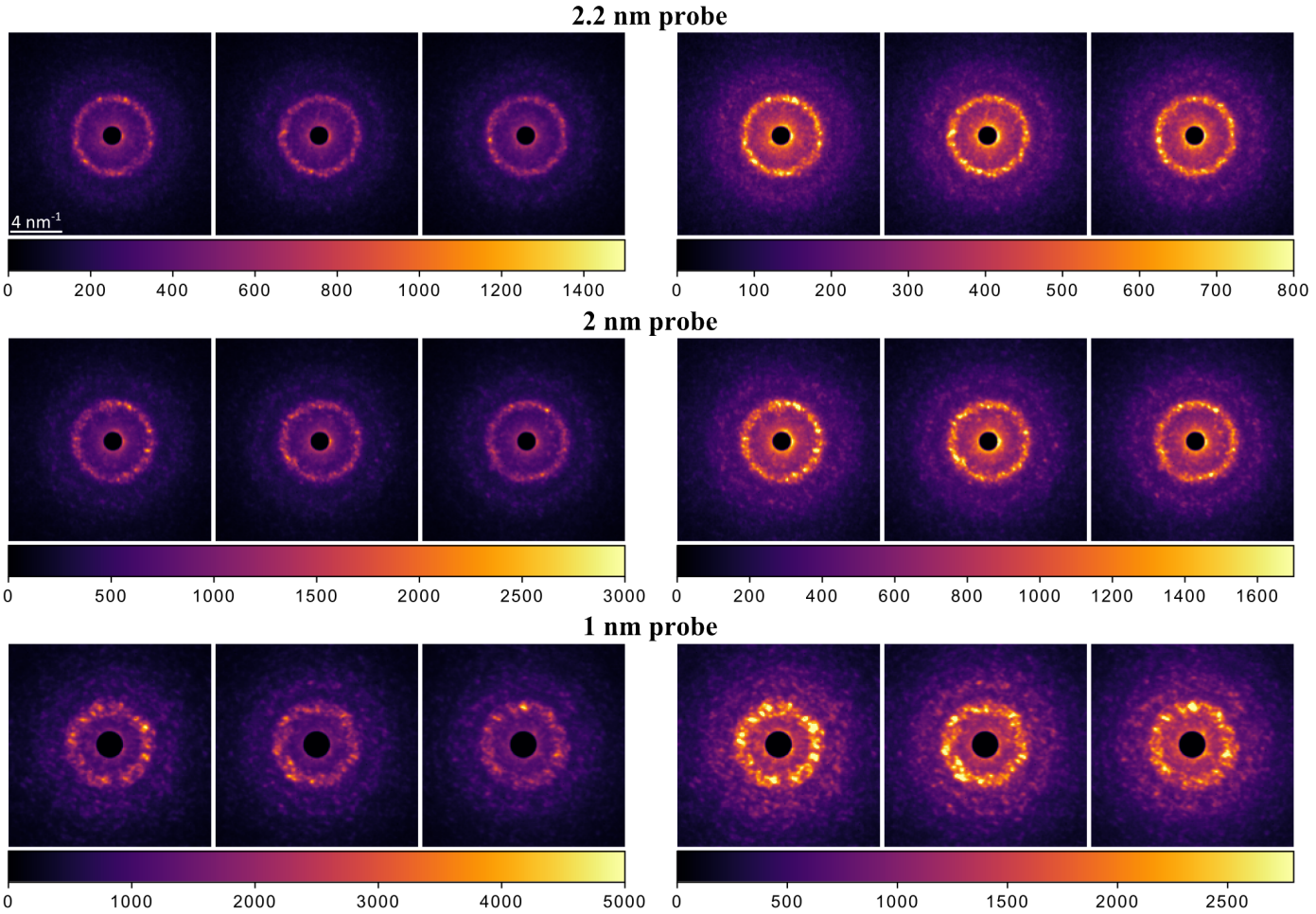

Figure 4.12: Example diffraction patterns from each of the probe sizes used on this alloy $MoSi_x$ sample. Each pair of diffraction patterns shows images of the same diffraction patterns with different maximum pixel intensity in order to show the inner (upper) and the outer (lower) diffraction peak more clearly.

Both the 2.2 nm and 1 nm probe curves are average curves of two datasets obtained using the same probe parameters. Error bars shown for the 2.2 nm and 1 nm probe are as a result of calculating the standard deviation of these same two datasets. One dataset was used to obtain the variance of the 2 nm dataset. Variance was calculated from three horizontal lines through the scanbox and the error bars represent the standard deviation in the variance from these three areas of the film.

We can see that there is a general trend that as the probe size gets smaller, the magnitude of the variance increases. This can be seen in the change in peak height between the 2.2 nm and 2 nm probe, but is especially apparent when considering the difference between the 2 nm and 1 nm probe sizes.

4.3.2.3 VDF Images

BF and annular VDF images obtained from this sample at probe sizes of 2.2 nm, 2 nm and 1 nm are shown in Figure 4.14. The annular VDF images are obtained from annular apertures 0.2 nm^{-1} wide that are centred on each of the three main variance peaks.

Images shown in the first column of Figure 4.14 show resuls from the 2.2 nm probe size. It appears from the BF image that there are transition regions between the centre of the film and the a-SiO_2 substrate and capping layer. These appear to be in the order of 5 nm in thickness, leaving a region in the centre of the film that is around 4 nm thick. All three of the annular VDF images show that there are some regions of the sample that have higher scattered intensity than others, however this is not a huge difference. All of the annular VDF images seem to be similar in appearance, all of them show their brightest areas within the centre of the film. When comparing all three of the annular VDF images, it does not appear that there are clusters of pixels that consistently show noticeably higher or lower intensity consistently in all three images.

The second column in Figure 4.14 shows the BF and annular VDF images obtained from the 2 nm probe. Similarly to images shown from the 2.2 nm probe, significant transition regions are visible with only a 4 nm region in the centre of the film that does not appear to form part of the transitional area. The first annular VDF image at 4.45-4.65 nm^{-1} shows more variability in intensity within the film than those at 7.35-7.55 nm^{-1} and 8.95-9.15 nm^{-1}. Bright clusters and single pixels are visible in all of the images. They each show clusters of brighter pixels, in some cases up to around 3/4 pixels in size representing ordered regions up to 6-8 nm in size, as well as a larger amount of bright individual pixels.

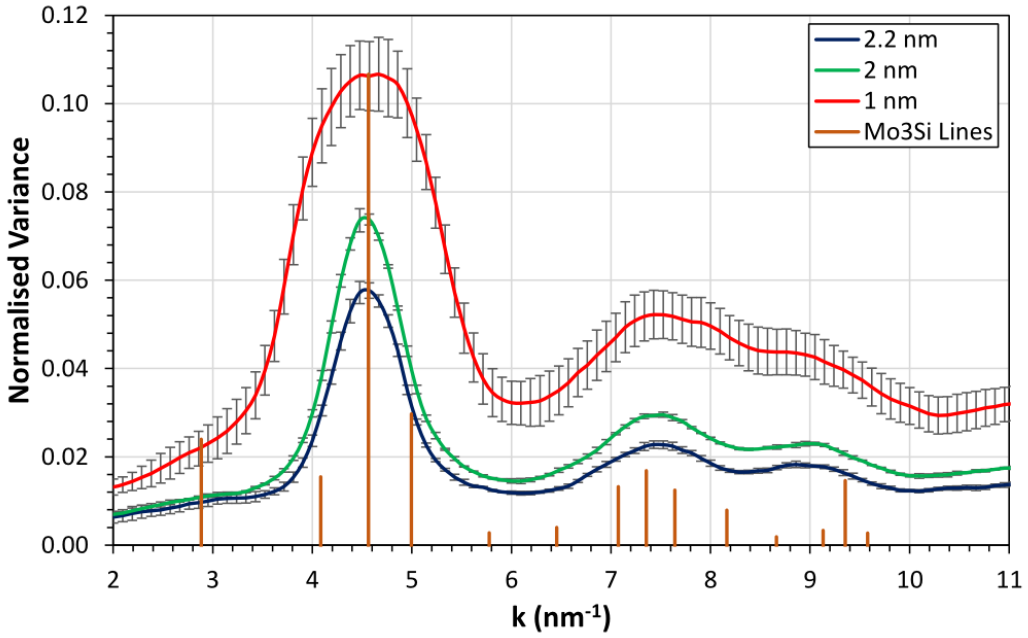

Figure 4.13: FEM variance curves from the alloy $MoSi_x$ sample at three different probe sizes.

BF and annular VDF images obtained using the 1 nm probe are shown in the third column of Figure 4.14. As the step size used in this dataset was 1 nm rather than the 2 nm used in the previous images, it should be easier to view any structural features. A visual estimate on the thickness of the transitional areas from the BF image show that they are around 5 nm thick, while the centre of the film is also approximately 5 nm across. The annular VDF images show that there are both small clusters and single pixels with increased intensity within the film, these are most obvious in the image taken from 4.45-4.65 nm^{-1}, where a high proportion of the bright pixels appear towards the top interface region of the film, while they also occur in other regions of the film.

In addition to the annular VDF images, radial variance images were also produced. These are obtained by calculating the variance in intensity of pixels within the annular aperture. This was calculated in the same range of k as the VDF images. Figure 4.15 shows these images for the 2.2 nm, 2 nm and 1 nm probe.

Results obtained from the 2.2 nm probe show a single bright pixel in the 4.45-4.65 nm^{-1} range, 3 in the 7.35-7.55 nm^{-1} range and >3 (three very bright and others that are not quite as bright but still stand out) in the 8.95-9.15 nm^{-1} range. None of these bright pixels are present concurrently in more than one of the images, indicating that the bright pixels could show areas of higher order, but this order is only seen in the DP at the diffraction ring being inspected. These results would indicate that there are ordered regions within the sample $\leq$ 2 nm in size.

The middle column of Figure 4.15 shows the results from the 2 nm probe. There are two brighter single pixels from the 4.45-4.65 nm^{-1} range, which are fairly close together, although clearly not part of the same cluster. These bright pixels are not replicated in the image at 7.35-7.55 nm^{-1} where four bright pixels are seen, including a cluster of two pixels. Finally the 8.95-9.15 nm^{-1} image shows one bright pixel, as well as a few others that stand out from the rest of the film.

Images obtained from the 1 nm probe (third column of Figure 4.15) show more detail than the previous images. There is one pixel that is much brighter than the rest of the film towards the bottom of the image obtained from the 4.45-4.65 nm^{-1} range. Within the image at 7.35-7.55 nm^{-1}, there were 5-6 bright pixels as well as a some small clusters that appeared brighter. Last of the images was the one obtained at 8.95-9.15 nm^{-1}, where there were two bright single pixels, as well as some other single pixel areas that stood out from the rest of the film.

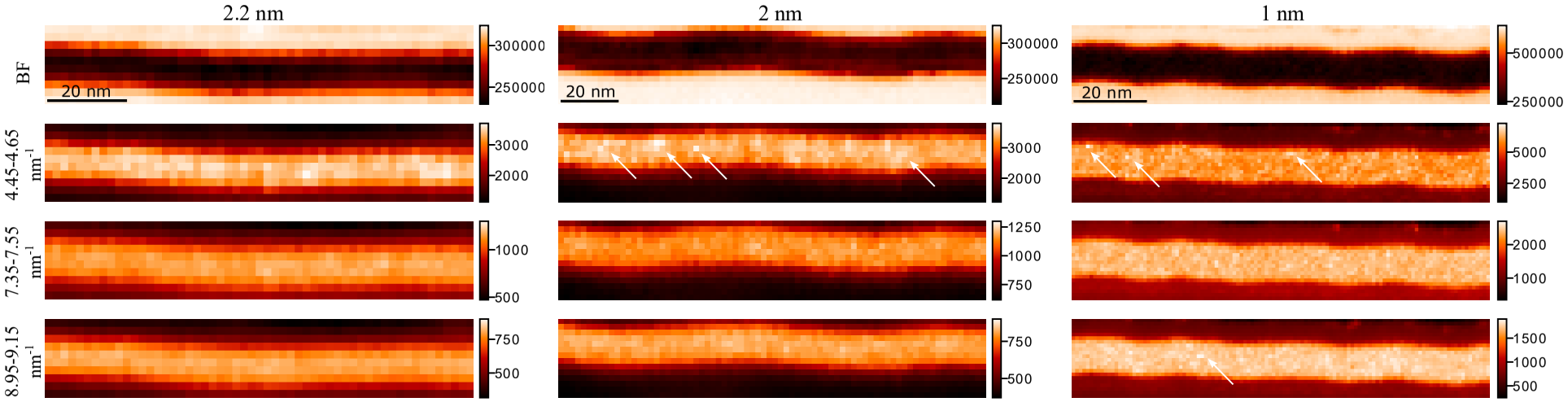

Figure 4.14: BF and annular VDF images from the alloy $MoSi_x$ film (each image is on a different color scale). Each column shows images from the three different probe sizes used, while the rows show the results of the different apertures.

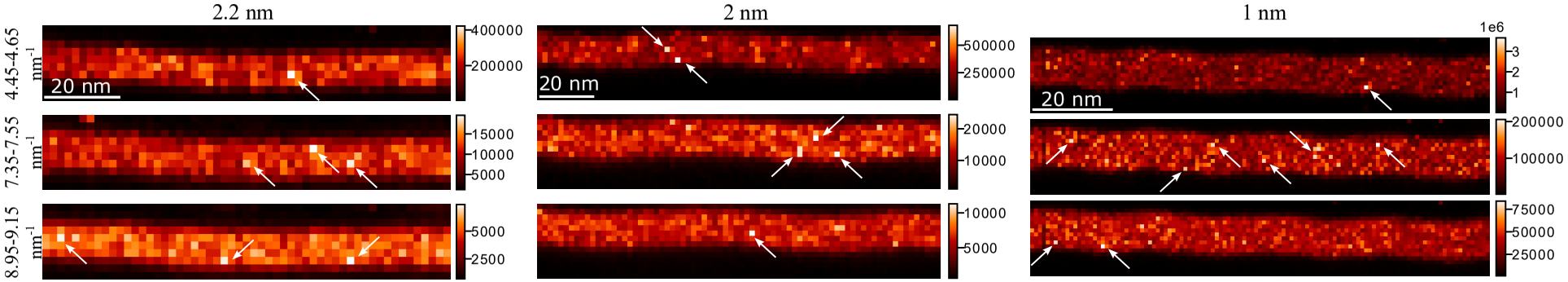

Figure 4.15: Radial variance images from the alloy $MoSi_x$ film (each image is on a different color scale). Each column shows images from the three different probe sizes used, while the rows show the results of the different apertures.

As earlier in 4.3.2.1, circular apertures 1 nm^{-1} in diameter are centred on the three main variance peak positions to examine the spatial extent of particular diffraction features. VDF images formed from these apertures are shown in Figure 4.16 for the 2.2 nm probe, Figure 4.17 shows data from the 2 nm probe and Figure 4.18 in the case of the 1 nm probe. In these images, the apertures are positioned at 0, 90, 180 and 270 degrees from the centre of the diffraction pattern, such that the first/last two images are formed from apertures opposite each other.

As mentioned earlier, images formed from the diffraction dataset using the 2.2 nm probe are shown in Figure 4.16. In the first set of images (Figure 4.16a), taken at k of 4.55 nm^{-1}, there are some single pixel bright spots, most notably in the second image. The bright areas are generally single pixels, or small clusters of up to 3 pixels in size, meaning that some ordered regions extend up to 6 nm. They are spread throughout the sample, unlike the co-sputtered $MoSi_x$ film where they were mostly found at the edges. It appears that there are longer range features, where there are brighter and darker regions in the images, although these brighter regions are at lower intensity than the very bright pixel areas mentioned earlier.

Now we move on to the VDF images obtained from circular apertures positioned at the second variance peak (Figure 4.16b). There are some areas where there is a single pixel brighter than its surroundings, or small clusters of up to two pixels.

The last set of VDF images from the 2.2 nm probe were obtained from the third variance peak (Figure 4.16c). There is a single bright pixel on the right of the first image, then a few bright pixels and small clusters in the second image. Interestingly the third image appears to show a higher intensity throughout the film in general than in all three of the other images, including one particularly bright pixel. Lastly, the fourth image shows a bright cluster in the middle of the image.

Images obtained from the 2 nm probe are shown in Figure 4.17. In the first set of images (Figure 4.17) formed from apertures placed over the DP at the first variance peak, there is one very bright pixel in the second image, while the other images mostly show small clusters at lower intensity, as well as a few single pixels as well. There are brighter and darker regions within the film in each of the images.

Figure 4.17b shows the images from the second variance peak. These show some similar results to those seen in Figure 4.16b, especially the second image with its solitary bright pixel. Overall the images show two very bright single pixels, and there is generally brighter and darker patches throughout the film.

The last set of images from the 2 nm probe, obtained from apertures placed at the

third variance peak are seen in Figure 4.17c. Bright single pixels are present in the third and fourth images, while there is a cluster of two pixels in the second image, the first image shows some pixels/clusters at higher intensity than the film, but not as much as the other images. A cluster of two pixels is present in the second image, while the third and fourth show mostly single pixels, although one area on the left of the third image is probably a cluster of two pixels.

Images from the 1 nm probe are shown in Figure 4.18. Images from apertures placed on the DPs at the first variance peak are shown in Figure 4.18a. Right on the edge of the second image there is a single bright pixel, that is much brighter than anywhere else in the other three images. All of the images show regions that are darker/lighter, with some of the lighter regions containing single pixel bright spots or small clusters of bright pixels, these are most obvious in the first and fourth images. As these images are at a higher spatial resolution, the size of ordered regions becomes clearer and appear up to 3-4 nm in size.

The next set of images from the 1 nm probe are shown in Figure 4.18b, where they are formed from circular apertures positioned at the second variance peak. These images show single pixel bright spots, some of which are connected to slightly less bright pixels which are still brighter than the film in general.

Last of the VDF images from this sample are those from circular apertures positioned at the third variance peak (Figure 4.18c). Most of the bright areas are formed of single pixel bright spots, along with a few composed of two or three pixels of up to 3 nm in size. The generally brighter and darker regions within the film are also apparent.

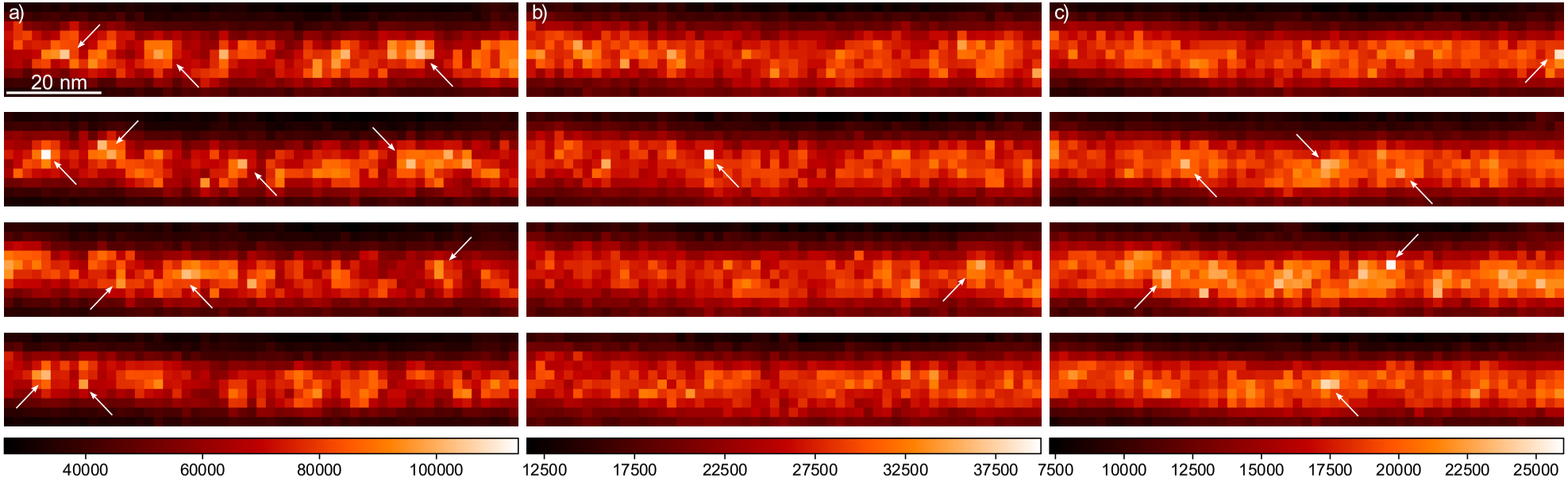

Figure 4.16: VDF images of the alloy $MoSi_x$ film, generated from dataset with 2.2 nm probe size. Images formed using circular apertures placed on the DP at the position of the variance peaks at k values of a) 4.55 nm^{-1}, b) 7.4 nm^{-1} and c) 9.0 nm^{-1}. Each set of four images is on a different color scale.

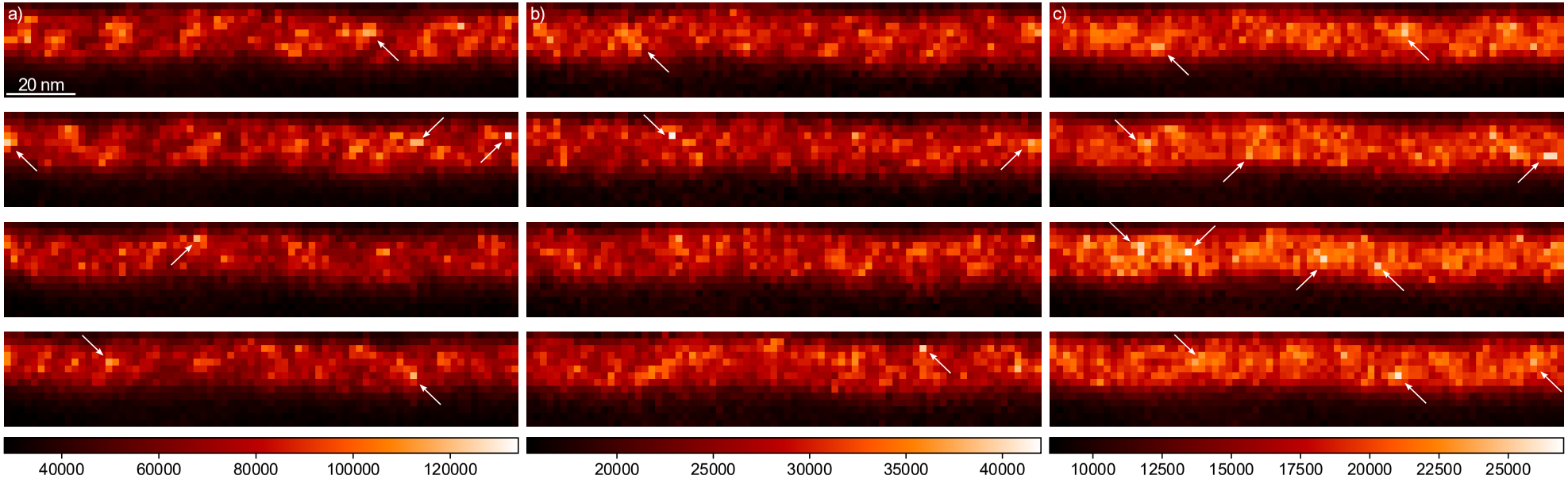

Figure 4.17: VDF images of the alloy $MoSi_x$ film, generated from dataset with 2 nm probe size. Images formed using circular apertures placed on the DP at the position of the variance peaks at k values of a) 4.55 nm^{-1}, b) 7.4 nm^{-1} and c) 9.0 nm^{-1}. Each set of four images is on a different color scale.

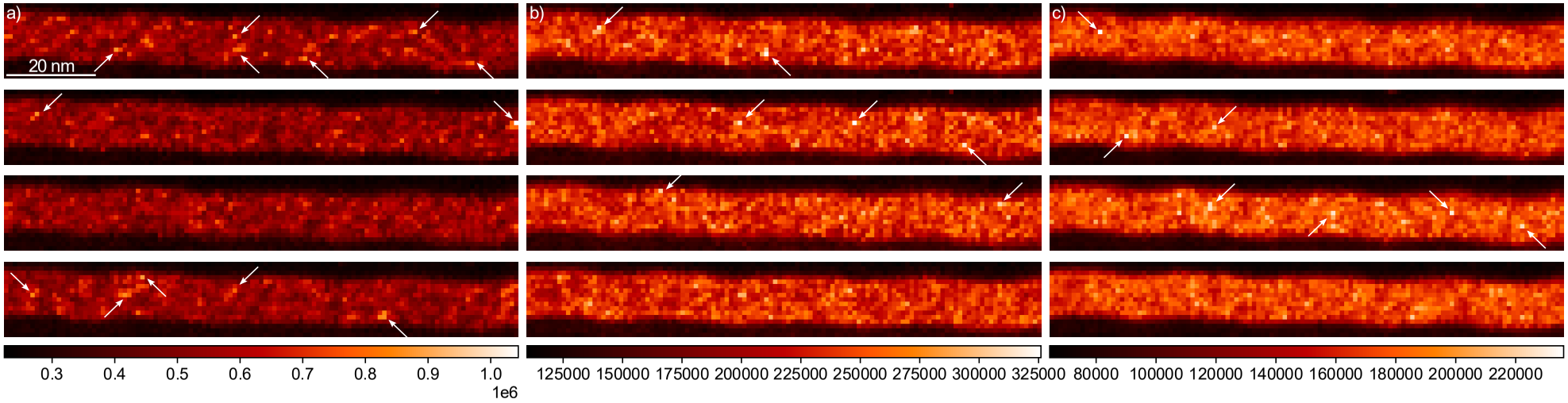

Figure 4.18: VDF images of the alloy $MoSi_x$ film, generated from dataset with 1 nm probe size. Images formed using circular apertures placed on the DP at the position of the variance peaks at k values of a) 4.55 nm^{-1}, b) 7.4 nm^{-1} and c) 9.0 nm^{-1}. Each set of four images is on a different color scale.

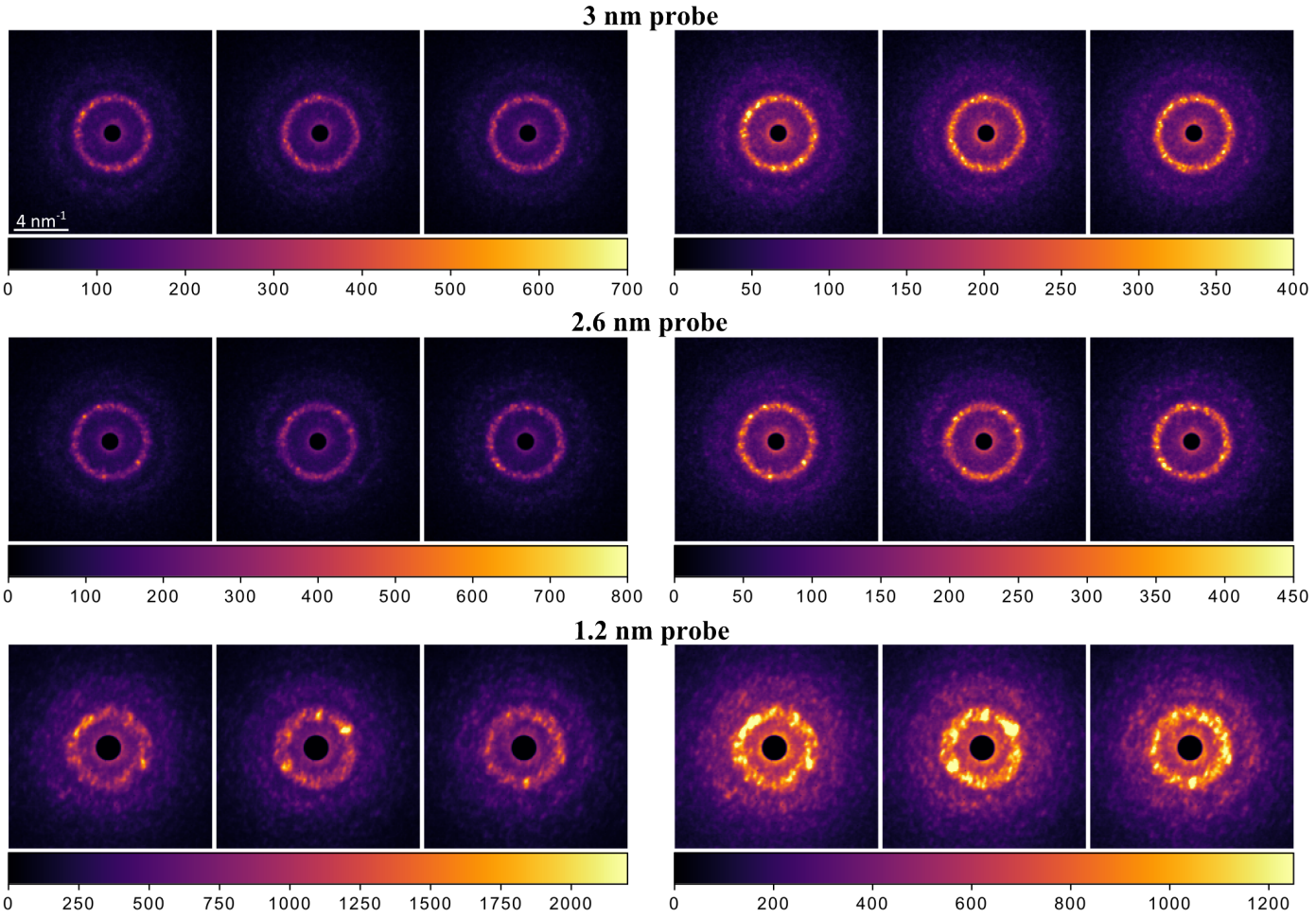

Figure 4.19: Example diffraction patterns from each of the probe sizes used on this $NbSi_x$ sample. Each pair of diffraction patterns shows images of the same diffraction patterns with different maximum pixel intensity in order to show the inner (upper) and the outer (lower) diffraction peak more clearly.

4.3.2.4 Co-Sputtered $NbSi_x$

As with the previous two samples, three different probes were used generating diffraction datasets from which variance curves were calculated and VDF images were created from this sample. These probes had FWHM of 3 nm, 2.6 nm and 1.2 nm, full details are given in Table 4.4. Example diffraction patterns obtained using each of these probe sizes are shown in Figure 4.19. Similarly to the $MoSi_x$ film, some diffraction patterns appear to have stronger diffraction spots/speckle than others. There is not really much of a visible difference between the 2.6 nm and 3 nm probe diffraction patterns, while the 1.2 nm probe shows considerable differences, due to the effects discussed earlier.

The variance curves from this sample are shown in Figure 4.20. Similarly to the $MoSi_x$ samples discussed previously, there are three main peaks visible in the variance curve. These are not in the same position as in $MoSi_x$, and are positioned at scattering angles of 4.25 nm^{-1}, 7.0 nm^{-1} and 8.45 nm^{-1}. This change in peak positions could be due to the difference in lattice parameter when comparing A15 Mo_3Si to A15 Nb_3Si, where their lattice parameters are 4.90 Å[192] and 5.16 Å[193] respectively. As in the $MoSi_x$ films discussed before, the main peak is the first of the three, while the second and third peaks are much smaller, and similar in magnitude to each other. We do however see that in the case of the 1.2 nm probe size, the third peak is smaller than the second peak compared to the variance from the two larger probes. These results suggest SRO that is A15-like.

Each of the variance curves is calculated from an average of three datasets obtained at the same probe size, and the error bars correspond to the standard deviation of the variance obtained from these three datasets.

Again we see that the magnitude of the main variance peak becomes larger as the probe size is decreased, indicating that the MRO in this sample is smaller than the 2.5 - 3 nm length scale.

4.3.2.5 VDF Images

BF and annular VDF images for each of the probe sizes used, at scattering angles of 2.7 $Å^{-1}$ and 4.4 $Å^{-1}$ are shown in Figure 4.21. BF images from all three probe sizes show transitional regions at the top and bottom of the film of between 6-10 nm. The BF image from the 1.2 nm probe shows some structure within the film while the other two BF images do not. Annular VDF images taken in the k range of 4.2-4.4 nm^{-1} show some bright pixels and clusters at all three probe sizes, in the image from the 2.6 nm probe size there is a bright cluster of up to 6 nm in size to the right of the image. In

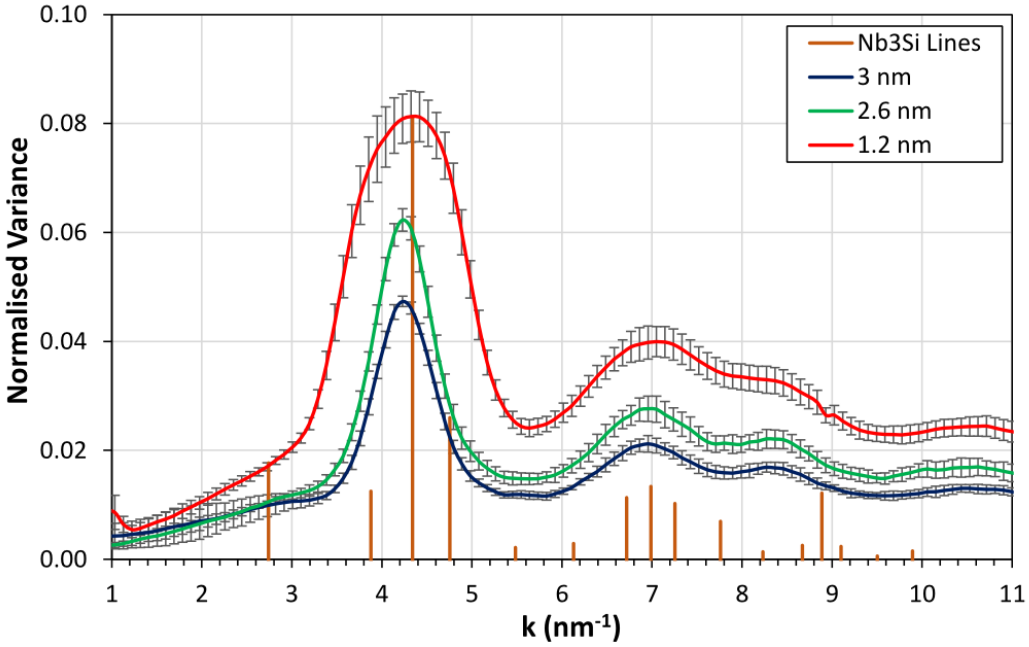

Figure 4.20: FEM variance curves from the co-sputtered $NbSi_x$ sample at three different probe sizes.

the annular VDF images at 6.9-7.1 nm^{-1} and 8.35-8.55 nm^{-1} and probe sizes of 3 nm and 2.6 nm there is very low intensity in the VDF images and it is difficult to see any structure within the film. By contrast, in the images from the 1.2 nm probe, there are bright single pixels and clusters of up to 4 nm throughout the film. A higher spatial resolution in the image due to the 1 nm step size allows for better estimation of the transitional regions towards the top and bottom of the film. These appear to be 7 nm in thickness, which concurs with the earlier estimation of between 6-10 nm when a 2 nm step size was in use. An estimate on the size of ordered regions from the annular VDF images would be between 1-4 nm.

Radial variance images obtained from all three probe sizes are shown in Figure 4.22. The image from the 3 nm probe size obtained from 4.2-4.4 nm^{-1} which is the first variance peak, shows two bright single pixels situated closely together. In the other images from the k ranges 6.9-7.1 nm^{-1} and 8.35-8.55 nm^{-1}, there is one very bright single pixel in each, as well as other pixels and clusters that are slightly brighter than the rest of the film.

Next, the radial variance images from the 2.6 nm probe will be inspected. Firstly there is a single bright pixel towards the top of the image obtained from the first variance peak at 4.2-4.4 nm^{-1}. There are rather more bright spots visible within the film in the image at 6.9-7.1 nm^{-1}, then the image at 8.35-8.55 nm^{-1}. Bright pixels in the three images from the 2.6 nm probe were spread around different areas of the film and are not noticeably concentrated either in the centre or in the transitional regions.

The final radial variance images from the $NbSi_x$ sample were obtained using the 1.2 nm probe size. The first of these images shows a few brighter spots within the film, in addition to a cluster of bright pixels 2 nm in size. The second and third images show mostly individual bright pixels, with a few clusters up to 2 nm visible as well.

Now we move on to the VDF images formed from circular apertures placed on the DPs. The first set of these images is formed from apertures placed at the three variance peaks in the dataset obtained with the 3 nm probe, these are shown in Figure 4.23a. The first of these images shows several bright pixels, situated within regions of the film that are generally brighter. Bright areas within the second image are most prominent in the transitional areas. In the third image there are a few bright spots that are closer to the centre of the film, most noticeably to the left of the image. Finally the fourth image shows a bright cluster towards the right of up to 8 nm. It does not look like the brightest areas within any of the images are replicated in the other images.

At the second variance peak, VDF images formed from the 3 nm probe (Figure 4.23b) appear similar to those observed from the first variance peak. The first image shows a large brighter area on the left, which contains clusters of bright pixels, while there are a couple of bright pixels elsewhere, the image does not however have any areas that have as high intensity as those seen in the other three images. The second and fourth images show bright pixels towards the centre of the film, however the third image shows brighter pixels in the transition areas.

Now we look at the third set of circular apertures, placed at the third variance peak. Figure 4.23c shows these images. There are a few bright pixels in the first and second images, although these are at lower intensity than the brightest pixels in the third and fourth image. In the third image there are a few bright pixels, often adjacent to other pixels that are brighter than the film in general indicating that there could be ordered regions up to 6 nm.

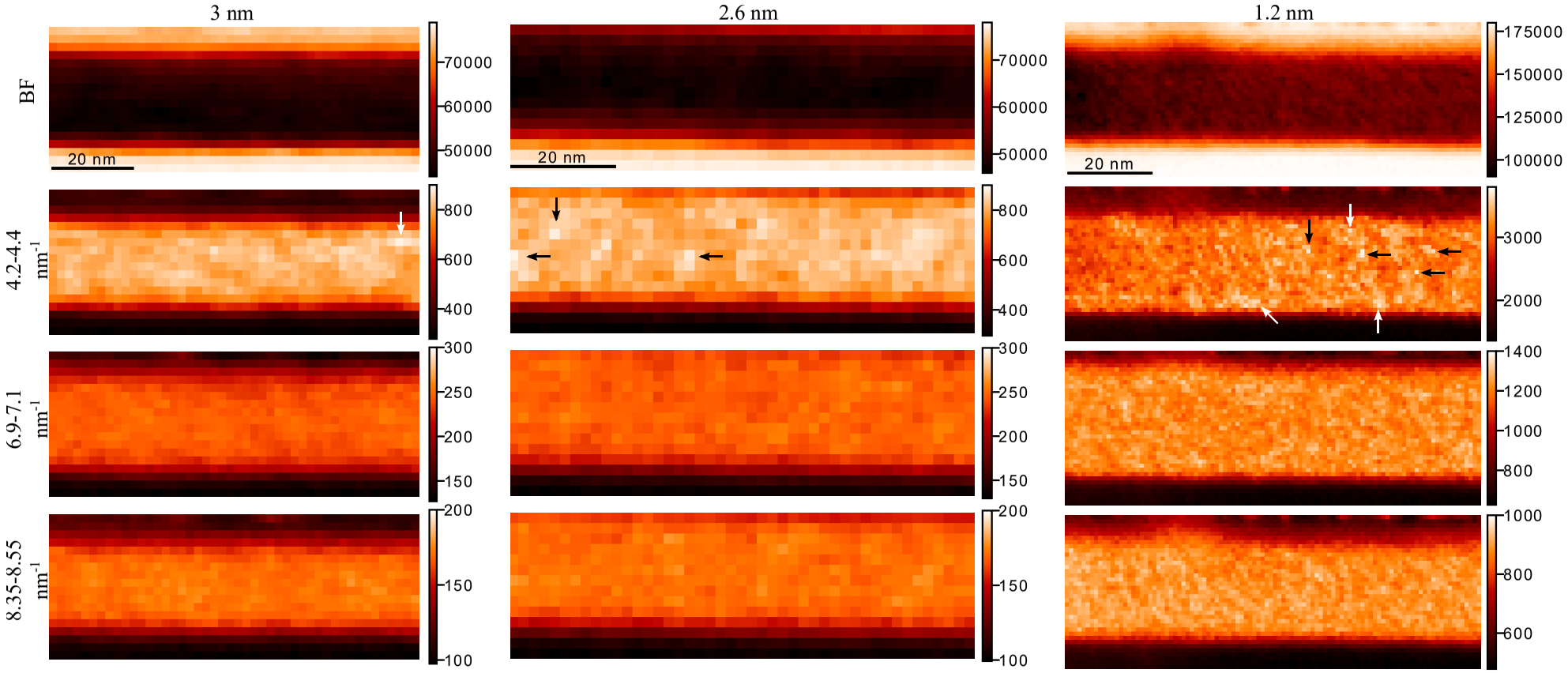

Figure 4.21: BF and annular dark field images from the co-sputtered $NbSi_x$ film (each image is on a different color scale). Columns show images obtained at the different probe sizes. Rows show the images obtained from the different virtual annular apertures used.

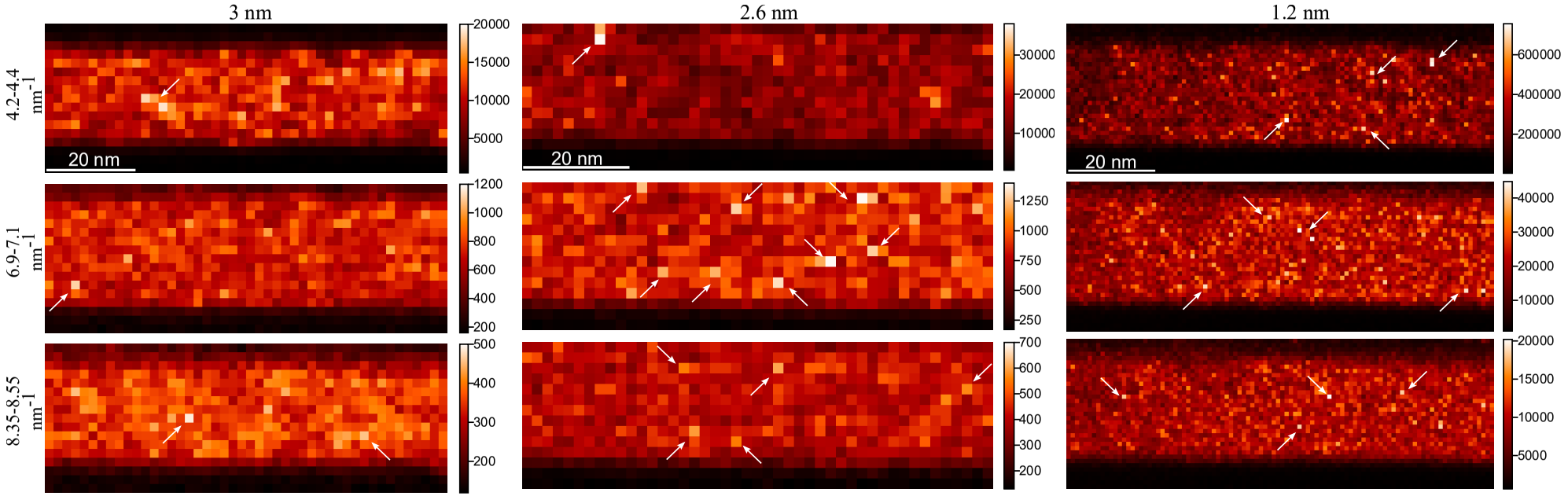

Figure 4.22: Radial variance images from the co-sputtered $NbSi_x$ film (each image is on a different color scale). Each column shows results from a different probe size. Rows show images obtained over different annular regions.

Images formed from the circular apertures from a dataset obtained using a 2.6 nm probe can be seen in Figure 4.24. Pictures obtained from application of the apertures to the first variance peak (Figure 4.24a) shows a similar story to the 3 nm probe. A single bright pixel is seen in the first image, while there are also some brighter areas within the film, mostly towards the left of the image. A similar pattern is observed in the second and third images, where there are some bright pixels, mostly adjacent to pixels brighter than the film in general. There are a couple of areas to the right hand side of the fourth image where there are larger clusters of bright areas up to 6 nm in size, as well as some brighter pixels in the central portion of the film.

Figure 4.24b shows VDF images from the second variance peak of the dataset obtained with a 2.6 nm probe diameter. For the most part the brightest areas in the images are single bright pixels, however there are some clusters of 4-6 nm.

Last of the images from the 2.6 nm probe size are those obtained from apertures applied to the third variance peak, as shown in Figure 4.24c. There are not so many bright spots within these images, especially in the first and second images. There are a few bright pixels in the third image. In the fourth image there is a pixel that is brighter than any found in the other three images, it is positioned within a region of the film that is brighter than the rest of the film in general.

Images formed from the 1.2 nm probe are shown in Figure 4.25. Images from the apertures placed at 4.25 nm^{-1} can be seen in Figure 4.25a. It appears that there is a diagonal slant in the images, likely due to sample drift. The brightest pixels in all of the images appear mostly as single pixels, however in some cases there are clusters of two or three pixels representing ordered areas up to 3 nm. All of the brightest pixels appear within a brighter area of the film or in the interface with the capping layer at the top of the film.

Images formed with the 1.2 nm probe with apertures at the second variance peak are shown in Figure 4.25b. In the first and second images there are more bright pixels to the right of the image than the left, although these do not seem to match up with each other between images. Brighter areas in the third and fourth image do not appear to have any bias towards either side of the image. There are also more bright pixels present in the third and fourth images compared to the first two. Again we observe that the brightest pixels appear within brighter areas and clusters of up to 3 nm are visible.

The last of the VDF images is taken from the 1.2 nm probe dataset with apertures placed at the third variance peak and are shown in Figure 4.25c. These images have the brightest areas right at the very top of the film in the transition area, so it is difficult

to see as much detail in these images compared to those seen previously. Again it is observed that the brightest pixels generally occur within brighter areas.

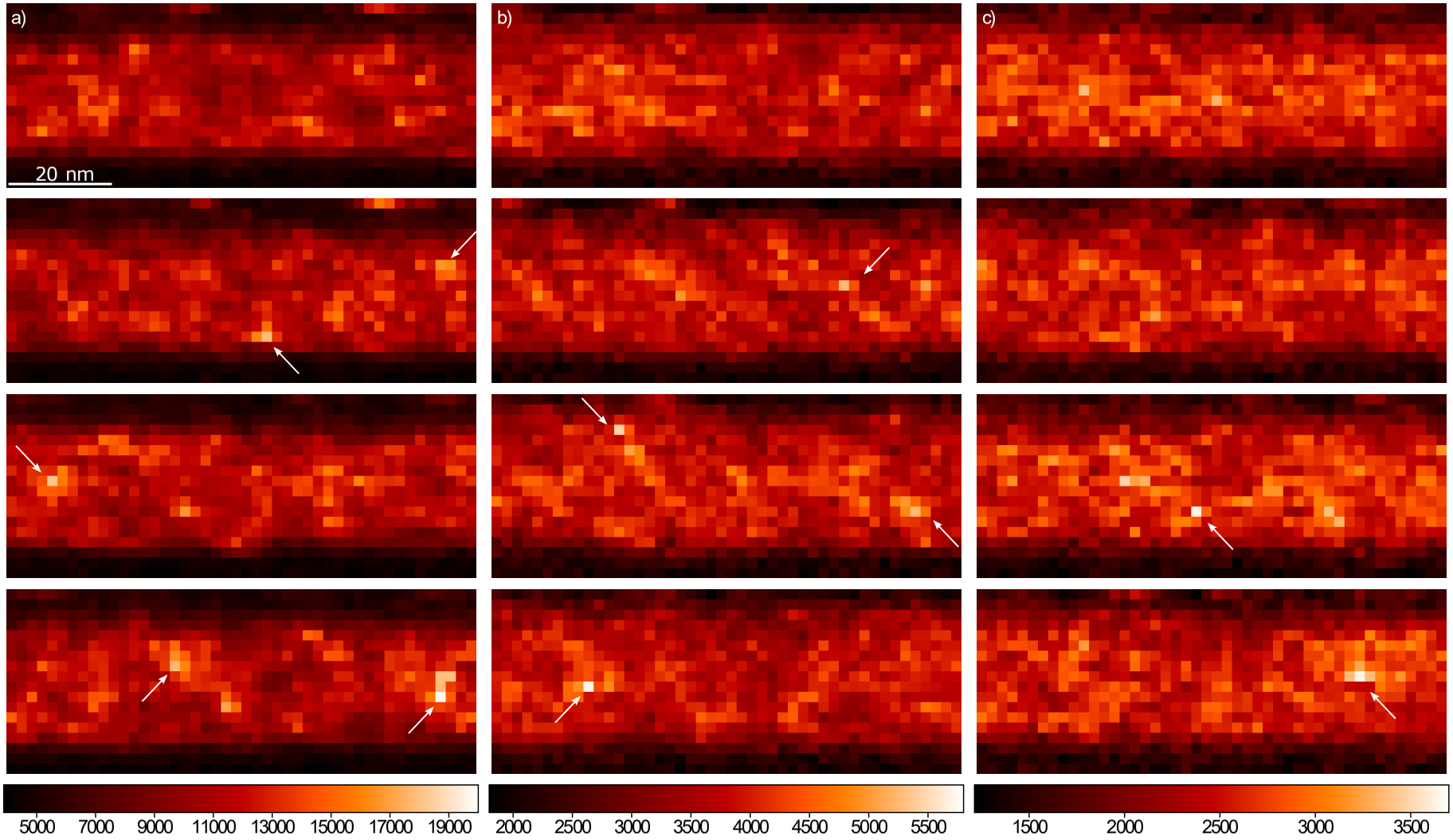

Figure 4.23: VDF images of the co-sputtered $NbSi_x$ film, generated from a dataset with 3 nm probe size. Images formed using circular apertures placed on the DP at the position of the variance peaks at k values of a) 4.25 nm^{-1}, b) 7.0 nm^{-1} and c) 8.45 nm^{-1}. Each set of four images is on a different color scale.

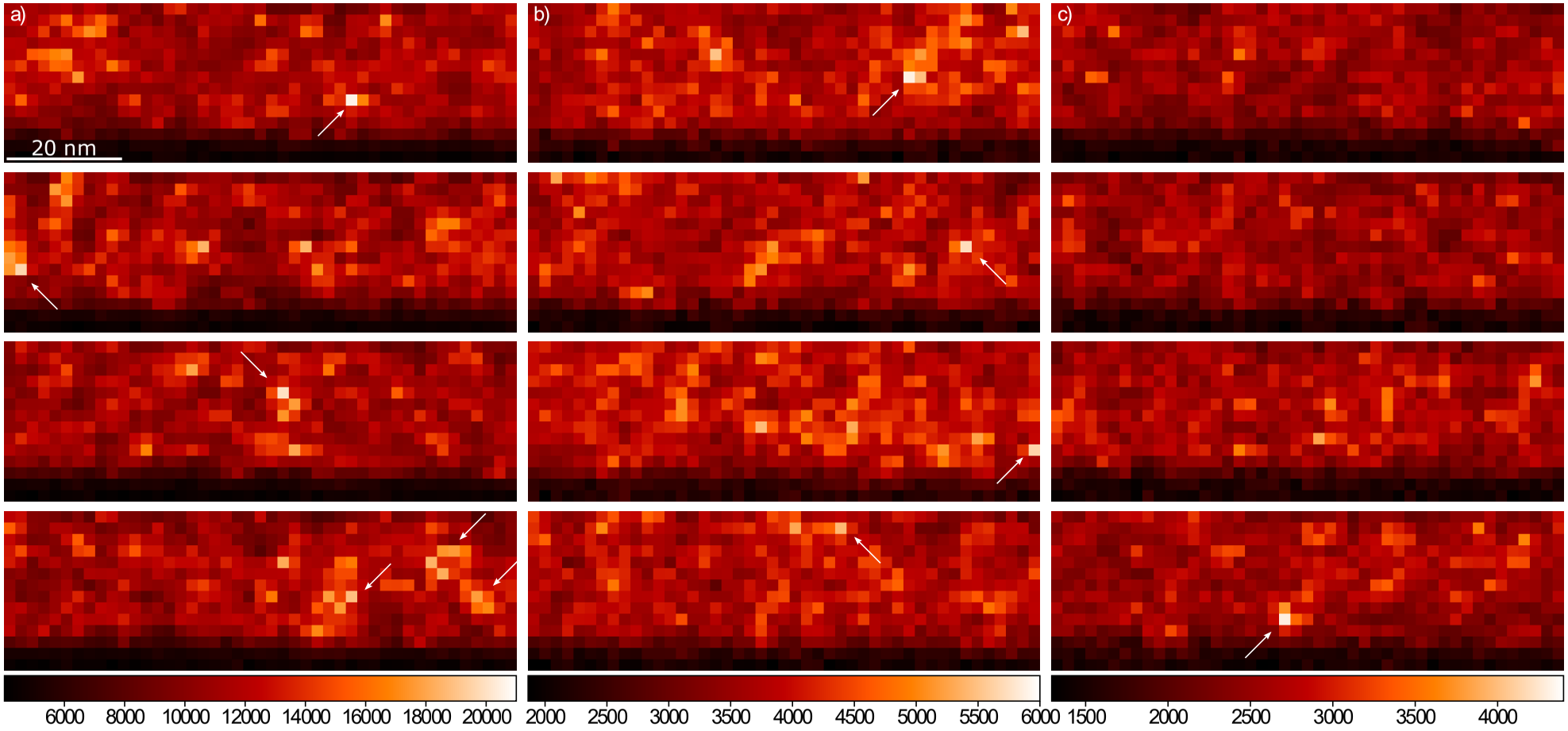

Figure 4.24: VDF images of the co-sputtered $NbSi_x$ film, generated from a dataset with 2.6 nm probe size. Images formed using circular apertures placed on the DP at the position of the variance peaks at k values of a) 4.25 nm^{-1}, b) 7.0 nm^{-1} and c) 8.45 nm^{-1}. Each set of four images is on a different color scale.

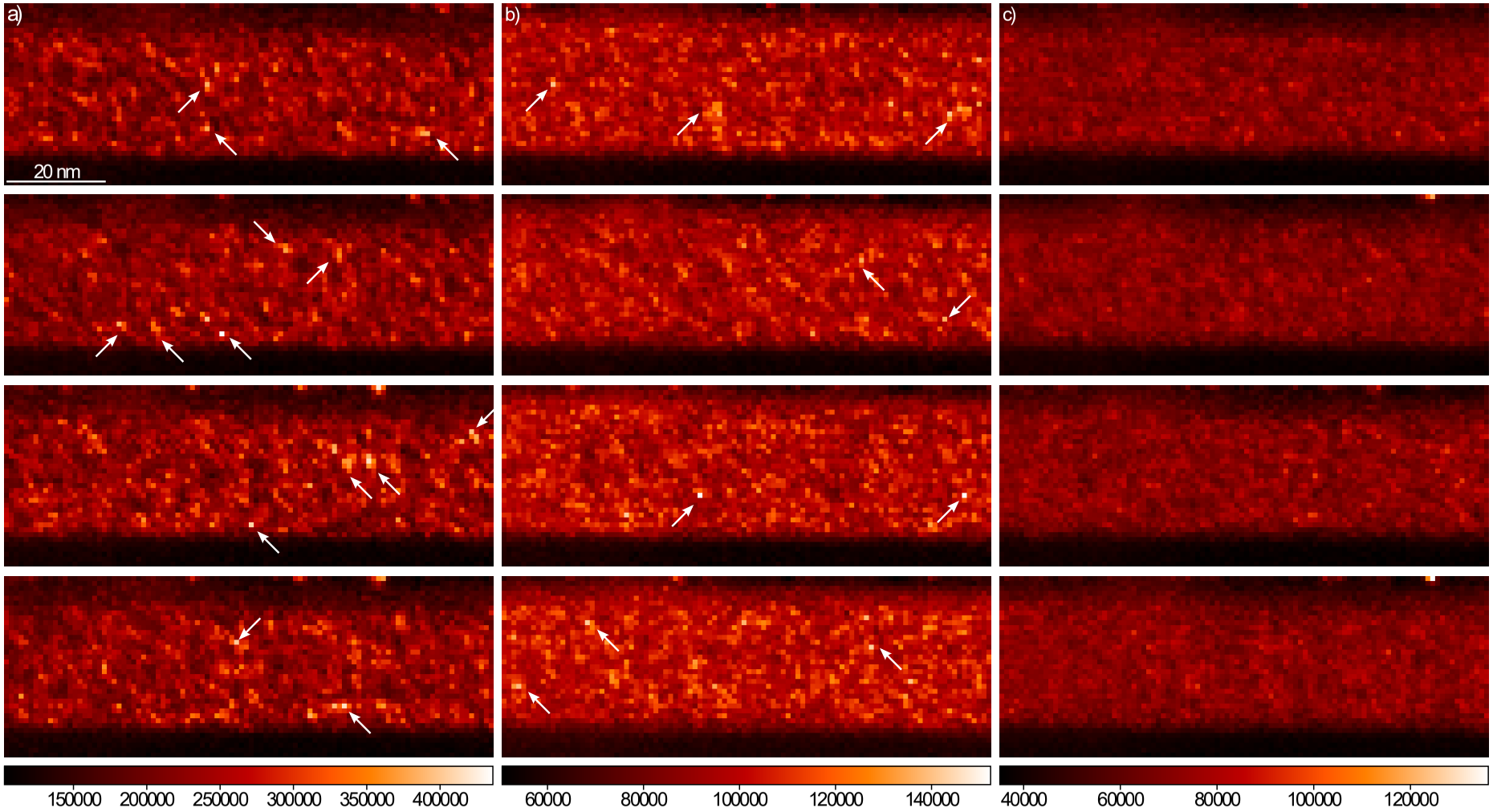

Figure 4.25: VDF images of the co-sputtered $NbSi_x$ film, generated from a dataset with 1.2 nm probe size. Images formed using circular apertures placed on the DP at the position of the variance peaks at k values of a) 4.25 nm^{-1}, b) 7.0 nm^{-1} and c) 8.45 nm^{-1}. Each set of four images is on a different color scale.

4.3.2.6 Co-Sputtered WSi_x

There were difficulties in the analysis of this sample, as the WSi_x layer is so thin. Three probe sizes were used, details of these can be seen in Table 4.5. Example diffraction patterns from the layer can be seen in Figure 4.26. There are noticeable differences in the diffraction patterns even with the same probe size, where some diffraction patterns have much more diffracted intensity at the first diffraction peak than others.

Figure 4.27 shows variance curves from three different probe sizes. Variance peaks are positioned at k = 4.5 nm^{-1}, k = 7.25 nm^{-1} and k = 8.75 nm^{-1}. There are features that remain the same as the other films, such as the similar arrangement of peaks, with a large initial peak followed by two smaller peaks. This would indicate that the structure of the film is largely similar to that of the $MoSi_x$ and $NbSi_x$ films looked at previously. The main variance peak occurs at the same scattering angle as one of the diffraction peaks found in A15 W, indicating that the film shares some structural features with A15 W, similarly to the other films investigated earlier.

4.3.2.7 VDF Images

BF and annular VDF images from each of the probe sizes can be seen in Figure 4.28. These images show how thin the film was and the difficulty of ascertaining which if any diffraction patterns belong to the WSi_x film itself. Especially with the larger probe sizes, where it is likely that a diffraction pattern containing diffraction from the film also contains some diffraction from either the substrate or capping layer. It is only in the images from the 1.2 nm probe size that the different regions of the substrate, film and capping layer can be seen clearly, especially with regards to the annular VDF images.

BF and annular VDF images obtained using a probe size of 2.5 nm are shown in the first column of Figure 4.28. The BF image shows a very thin red line where the WSi_x film is and it appears that there is no area in the centre of the film that is unaffected by transitional areas. There is not much interesting information available from the annular VDF images, in fact it barely stands out from the rest of the image, especially in the image taken over the 8.55-8.75 nm^{-1} range. For this film, 1 nm would be the upper limit on MRO, although this is very uncertain as the layer is so thin.

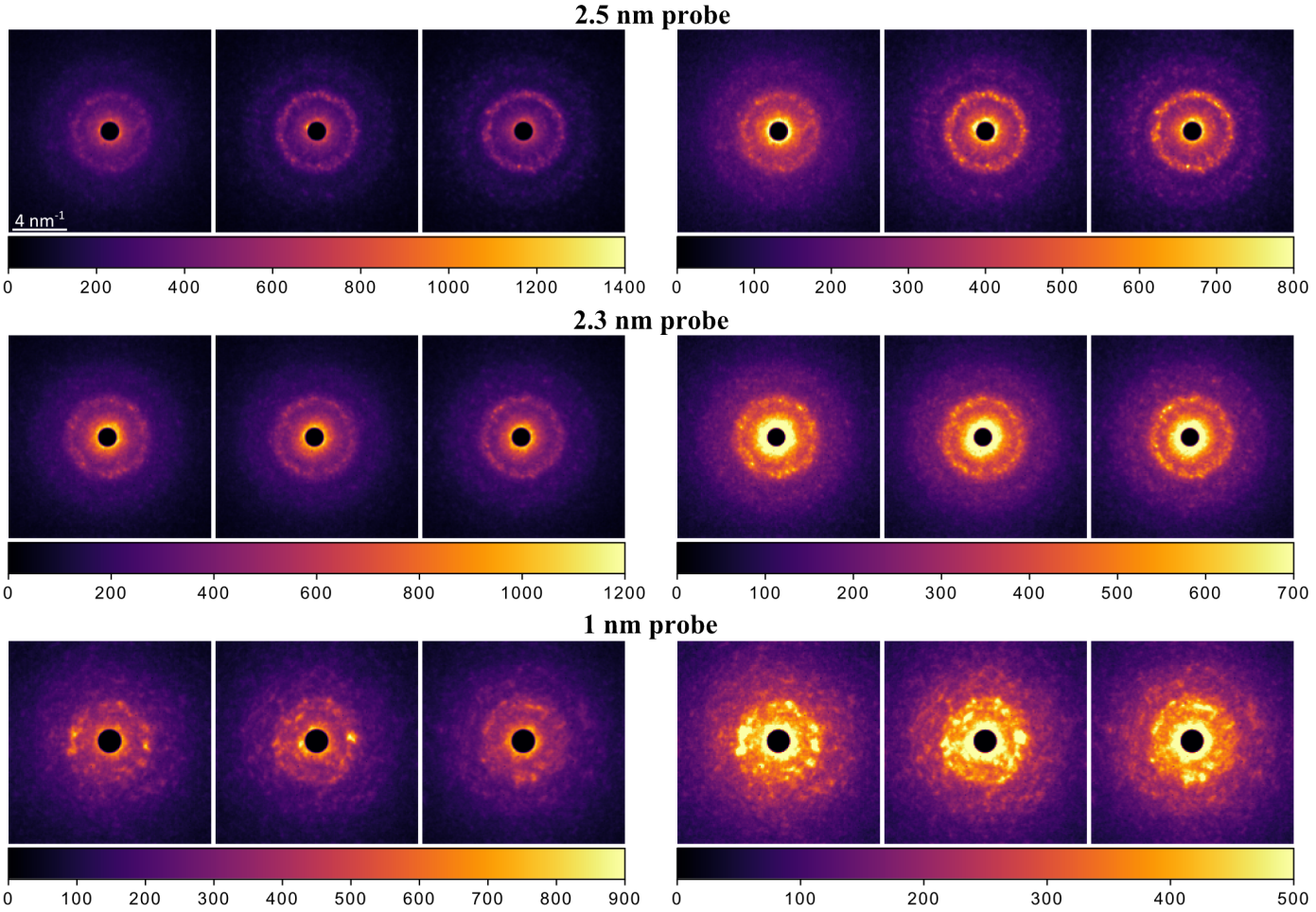

Figure 4.26: Example diffraction patterns from each of the probe sizes used on this WSi_x sample. Each pair of diffraction patterns shows images of the same diffraction patterns with different maximum pixel intensity in order to show the inner (upper) and the outer (lower) diffraction peak more clearly.

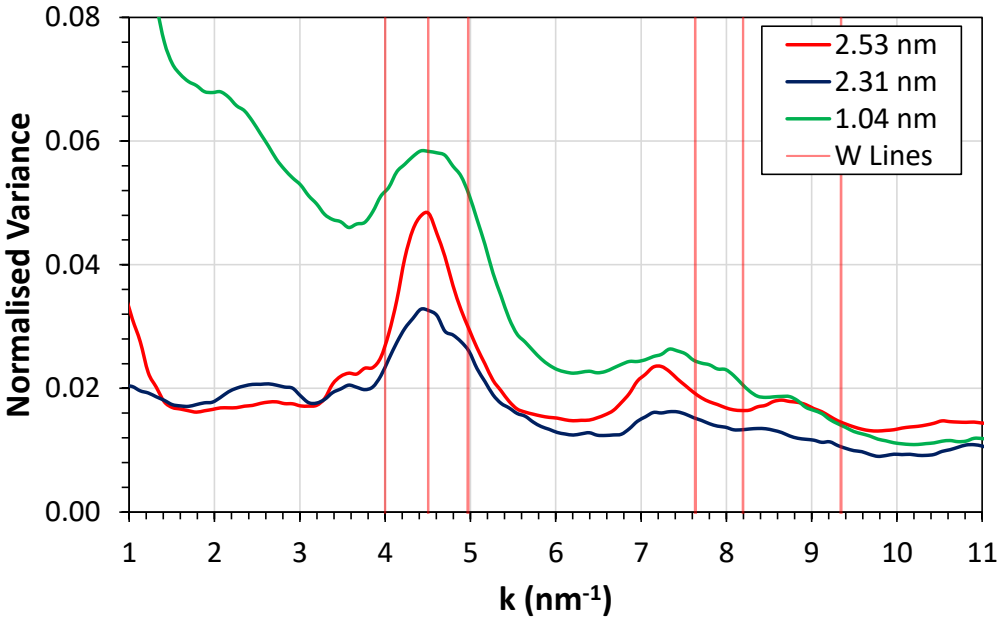

Figure 4.27: FEM variance curves from the co-sputtered WSi_x sample at three different probe sizes.

Images obtained from the 2.3 nm probe size are shown in the second column of Figure 4.28, there are thicker areas of the film to the left and right of the images. Similarly to the previous set of images from the 2.5 nm probe, the film does not stand out very much from the substrate and capping layer in the annular VDF images.

A probe size of 1 nm shows images with a higher spatial resolution, these are shown in the third column of Figure 4.28. It is interesting that in the third image, taken from a scattering range around the second variance peak (7.15-7.35 nm^{-1}), there are bright areas at both of the interfaces between the film and substrate/capping layer.

Radial variance images taken from this sample did not show very much, Figure 4.29 shows images obtained using the 2.3 and 1 nm probe size, images from the 2.5 nm probe size are not shown as it was not possible to generate any that showed anything useful. There are bright spots towards both interfaces in all three images from the 2.3 nm probe. The first image from the 1.2 nm probe shows bright spots in the interface with the capping layer, while the second image shows bright spots at both interfaces, the third image shows bright spots at the interface between substrate and film. None of the images show bright spots within the film itself.

VDF images formed from circular apertures are shown in Figures 4.30,4.31 and 4.32 for the 2.5 nm, 2.3 nm and 1.2 nm probe size respectively. At a probe size of 2.5 nm, there is almost no detail of the film visible in any of the images. Images from the 2.3 nm probe size mostly show bright areas in the interface areas or capping/substrate layers. At the 1 nm probe size the film is visible in each of the images, however all fo the brighter areas are not within the film itself but in the interface areas.

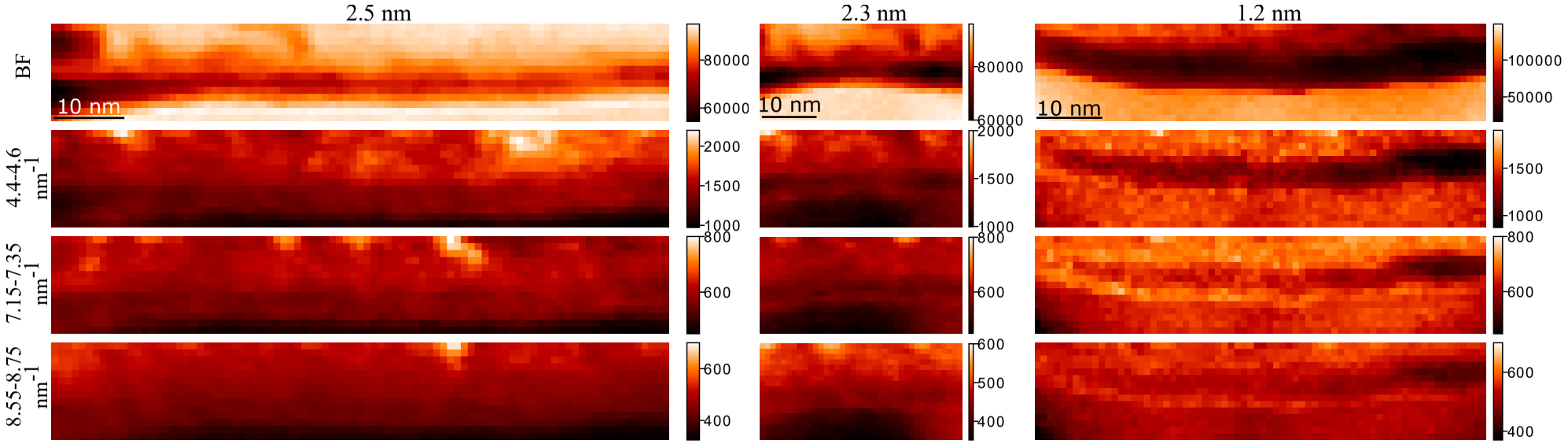

Figure 4.28: BF and annular dark field images from the co-sputtered WSi_x film (each image is on a different color scale). Each column shows images obtained at the three different probe sizes used, while the rows show images obtained using a set of annular masks.

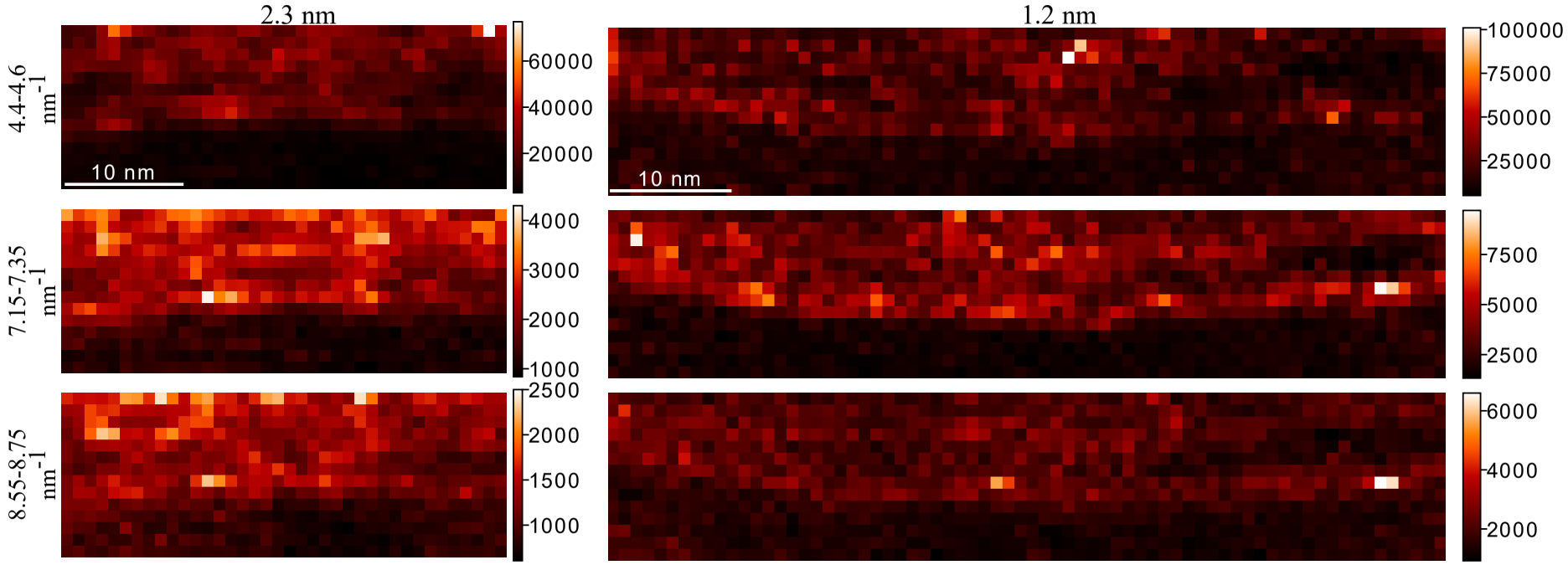

Figure 4.29: Radial variance images from the co-sputtered WSi_x film (each image is on a different color scale). Columns show images from the different probe sizes used. Rows show images obtained from different annular regions.

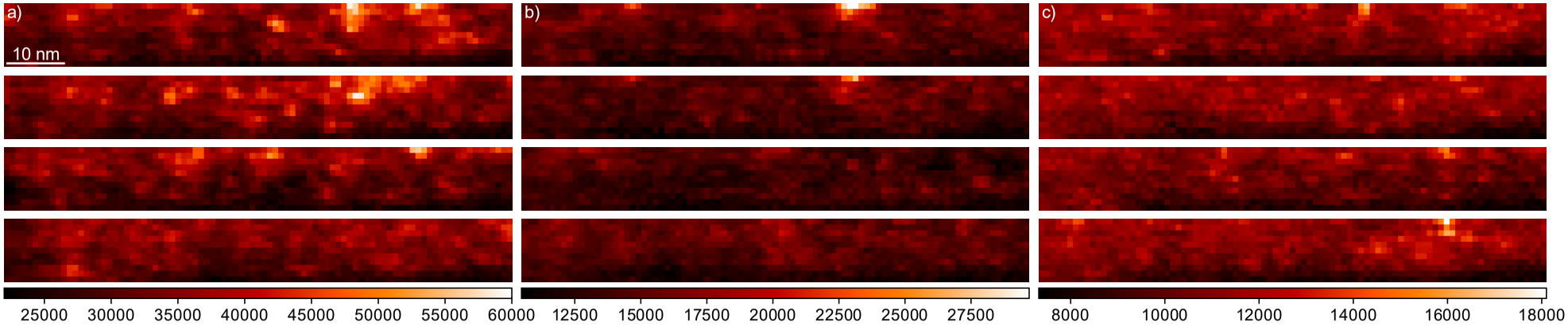

Figure 4.30: VDF images of the co-sputtered WSi_x film, generated from a dataset with 2.5 nm probe size. Images formed using circular apertures placed on the DP at the position of the variance peaks at k values of a) 4.5 nm^{-1}, b) 7.25 nm^{-1} and c) 8.75 nm^{-1}. Each set of four images is on a different color scale.

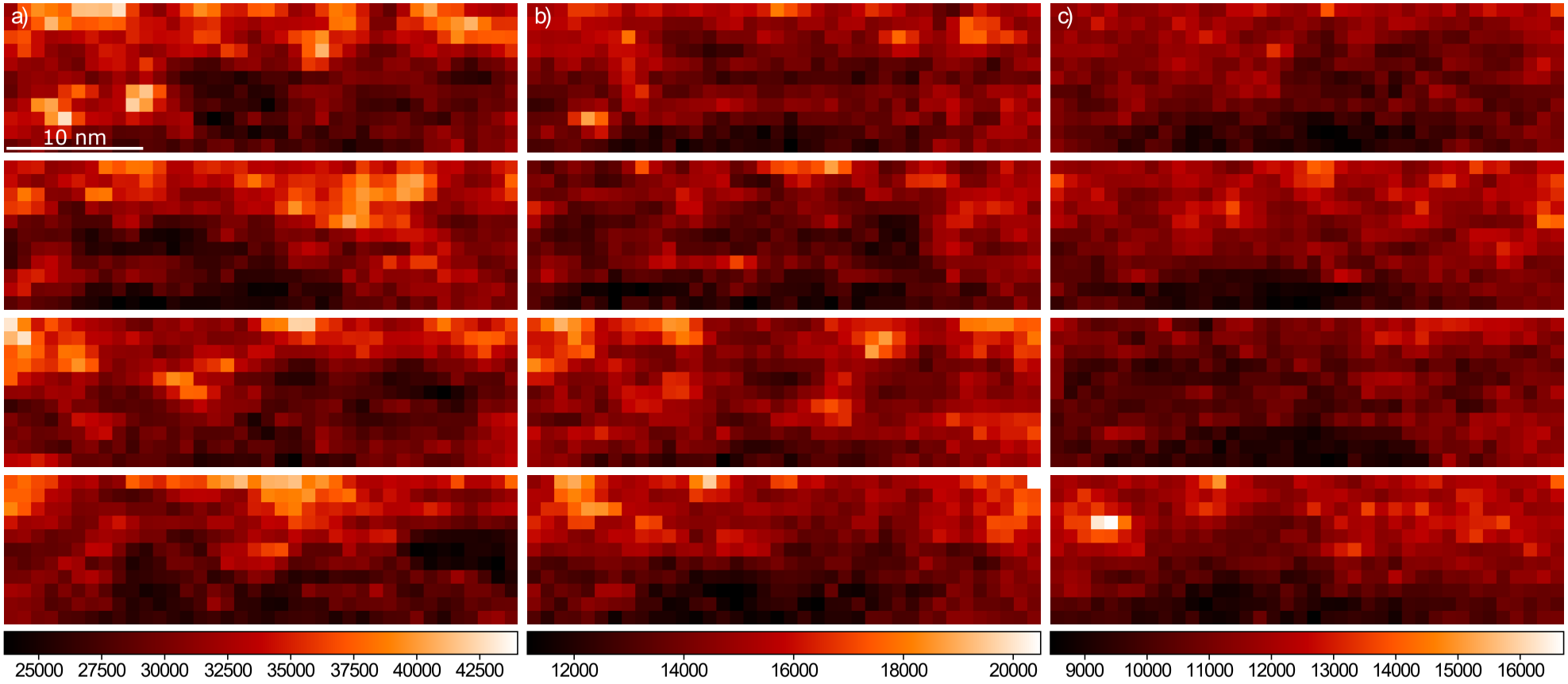

Figure 4.31: VDF images of the co-sputtered WSi_x film, generated from a dataset with 2.3 nm probe size. Images formed using circular apertures placed on the DP at the position of the variance peaks at k values of a) 4.5 nm^{-1}, b) 7.25 nm^{-1} and c) 8.75 nm^{-1}. Each set of four images is on a different color scale.

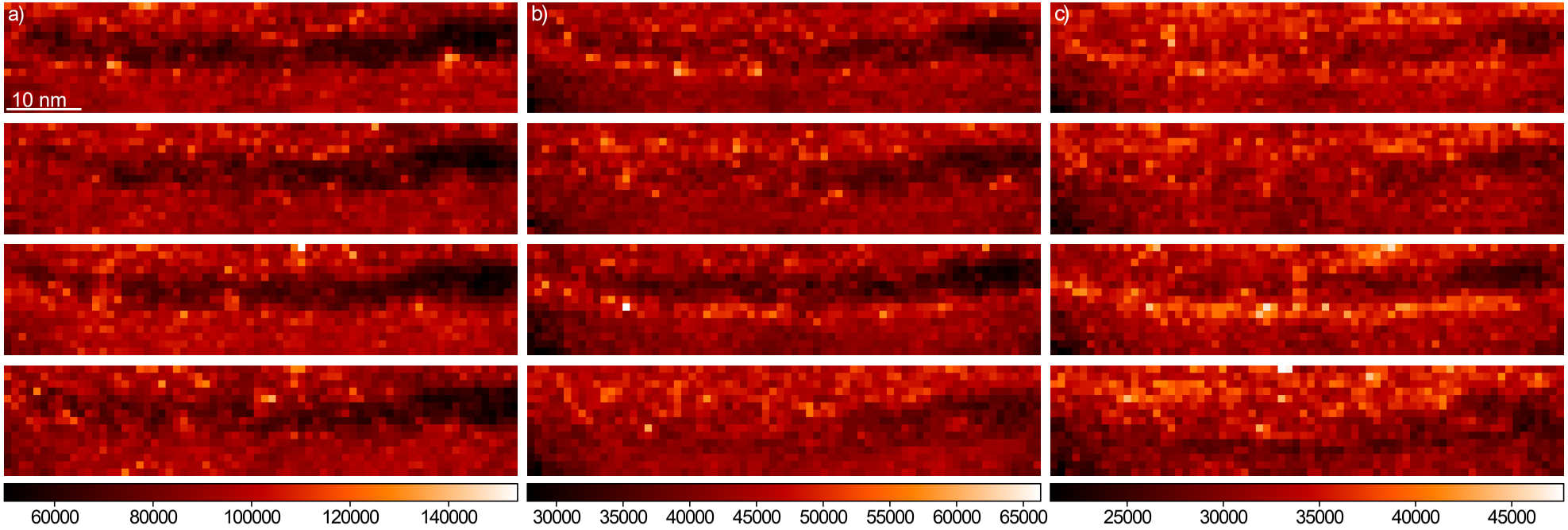

Figure 4.32: VDF images of the co-sputtered WSi_x film, generated from a dataset with 1.2 nm probe size. Images formed using circular apertures placed on the DP at the position of the variance peaks at k values of a) 4.5 nm^{-1}, b) 7.25 nm^{-1} and c) 8.75 nm^{-1}. Each set of four images is on a different color scale.

4.3.3 EELS

4.3.3.1 Co-Sputtered $MoSi_x$

As discussed earlier there are two co-sputtered $MoSi_x$ samples, both of which are analysed here. There were three EELS-SI datasets taken from each of the samples. These were formed of a low-loss and high-loss spectrum image, low-loss images were taken over energy ranges of -30:230 eV in Sample A and -30:130 eV in Sample B, with high-loss images in the range 1200:3250 eV (Sample A) and 1100-3150 eV (Sample B).

EELS-SI spectrum intensity maps as well as energy loss spectra from both samples are shown in Figures 4.33,4.34. Peaks used in the quantification of the sample are highlighted on the energy loss spectra.

Quantification of both samples was carried out using the *Digital Micrograph Elemental Quantification* plugin. The EELS edges of Mo at energy losses of 2520 eV (L_3) and 2625 eV (L_2) were used, as well as the Si K edge at 1839 eV, these edges are shown in Figures 4.33(e,f),4.34(e,f).

There is a bump in the spectrum on the higher energy side of the Si K edge at approximately 1865 eV, this bump is more defined in Sample A than Sample B, as is shown in Figures 4.33e, 4.34e.

There is some recent work by MacLaren et al., which has found that there are shoulders to the high-energy side of both the Mo L_3 and L_2 edges in a thin film of amorphous Mo, whereas these shoulders do not appear in a thin film of MoO_2.[107] Figure 4.35 shows a background subtracted, Fourier ratio deconvolved Mo $L_{2,3}$ edges from BCC obtained in that work, along with those found in all of the $MoSi_x$ films investigated here. Some kind of shoulder appears to be present on the high energy side of the Mo $L_{2,3}$ edges of the amorphous $MoSi_x$ films investigated here. These shoulders do not match with the appearance of the shoulders observed in nanocrystalline Mo by MacLaren et al..[107] Figure 4.35 shows that $L_{2,3}$ edges in body centred cubic Mo are both taller and narrower than those found in the $MoSi_x$ films that are investigated here. In addition to the shape of the peaks, there are three other areas of interest that are highlighted in Figure 4.35 by red, blue and yellow boxes. Firstly, the red area highlights that there is a shoulder on the high energy side of the BCC Mo is not present, or is much smaller in the co-sputtered $MoSi_x$ films that are being studied here. There is a small bump highlighted by the blue box that is present in both of the co-sputtered samples, but not in the BCC Mo or in a film sputtered from an alloy target. Finally, in the yellow area there are small bumps visible in the co-sputtered films, which do not appear to be present in the other samples, although it is difficult to distinguish in the alloy sputtered

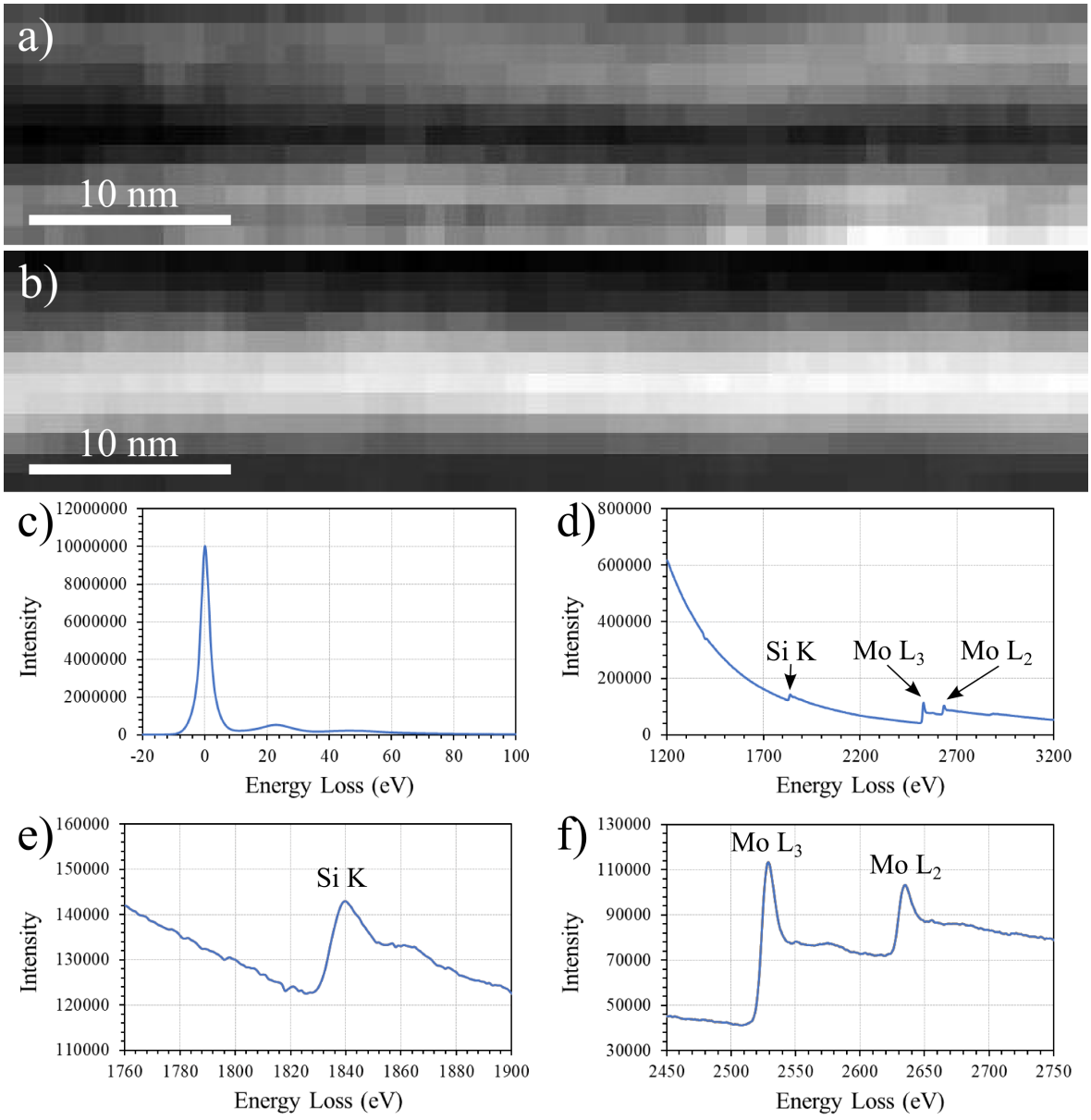

Figure 4.33: EELS-SI analysis of the co-sputtered $MoSi_x$ sample with Si cap (Sample A), showing; a) map of EELS background-subtracted signal from the Si-K edge over a 150 eV range starting from 1820 eV; b) map of background-subtracted signal from the Mo $L_2, 3$ edges over a 150 eV range starting from 2499 eV; c) low loss spectrum; d) full energy range view of the high loss spectrum from the $MoSi_x$ film; e) detail of the Si K edge; and f) detail of the Mo $L_2, 3$ edges.

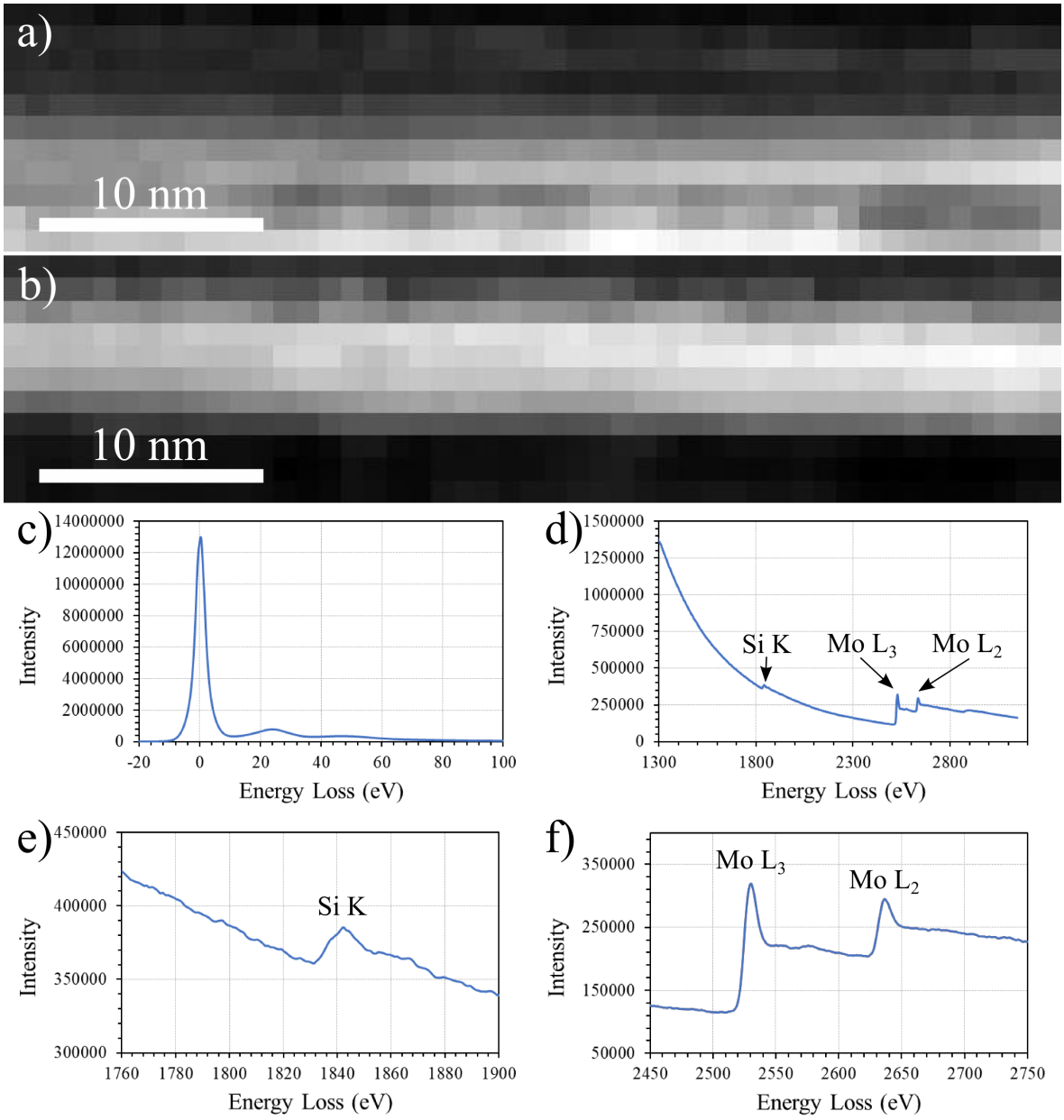

Figure 4.34: EELS-SI analysis of the uncapped co-sputtered $MoSi_x$ sample (Sample B), showing; a) Map of EELS background-subtracted signal from the Si-K edge over a 150 eV range starting from 1821.4 eV;b) Map of background subtracted signal from the Mo $L_2, 3$ edges over a 150 eV range starting from 2498.4 eV;c) low loss spectrum, d) full energy range view of the high loss spectrum from the $MoSi_x$ film; e) detail of the Si K edge; and f) detail of the Mo $L_2, 3$ edges.

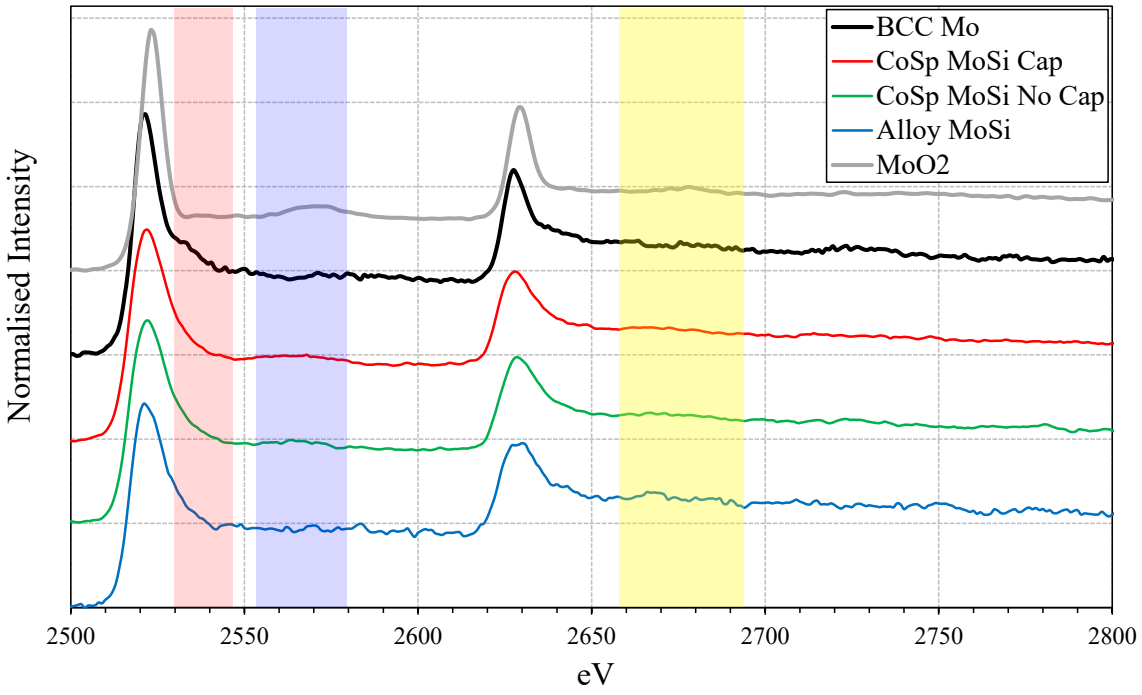

Figure 4.35: Background subtracted, Fourier deconvolved Mo $L_2, 3$ EELS edges from BCC Mo,[107] MoO_2,[84] co-sputtered $MoSi_x$ with capping layer, co-sputtered $MoSi_x$ without capping layer and $MoSi_x$ sputtered from an alloy target. Red, blue and yellow regions indicate areas of particular interest.

Table 4.6: Interatomic distances from Mo atoms to neighbouring atoms in the A15 Mo_3Si structure.

Bond	Interatomic Distances (Å)	Number of Occurences
Mo - Mo	2.449	2
Mo - Si	2.738	4
Mo - Mo	2.999	8
Mo - Si	4.414	4
Mo - Mo	4.581	16

film, due to noisier data.

The bonding of the Mo atoms within the film affect the shape of the Mo $L_{2,3}$ edges. Table 4.6 gives the interatomic distances and number of occurrences within A15 Mo_3Si. A Mo atoms two closest neighbours in that structure are two more Mo atoms, with an interatomic distance of 2.45 Å. Following those two Mo atoms there are four Si atoms at a distance of 2.74 Å, then eight Mo atoms at 3.00 Å. The interatomic distance in BCC Mo is 2.73 Å, greater than that found in Mo-Mo nearest neighbours in the A15 Mo_3Si structure, while it is close to that of the shortest Mo-Si interatomic distance. Nearest neighbour bonds largely dominate the EELS edge shape, which could go some way towards explaining the reason that the Mo $L_{2,3}$ edges in the $MoSi_x$ films are fairly similar to those in BCC Mo and much more similar than MoO_2, but are still distinct.

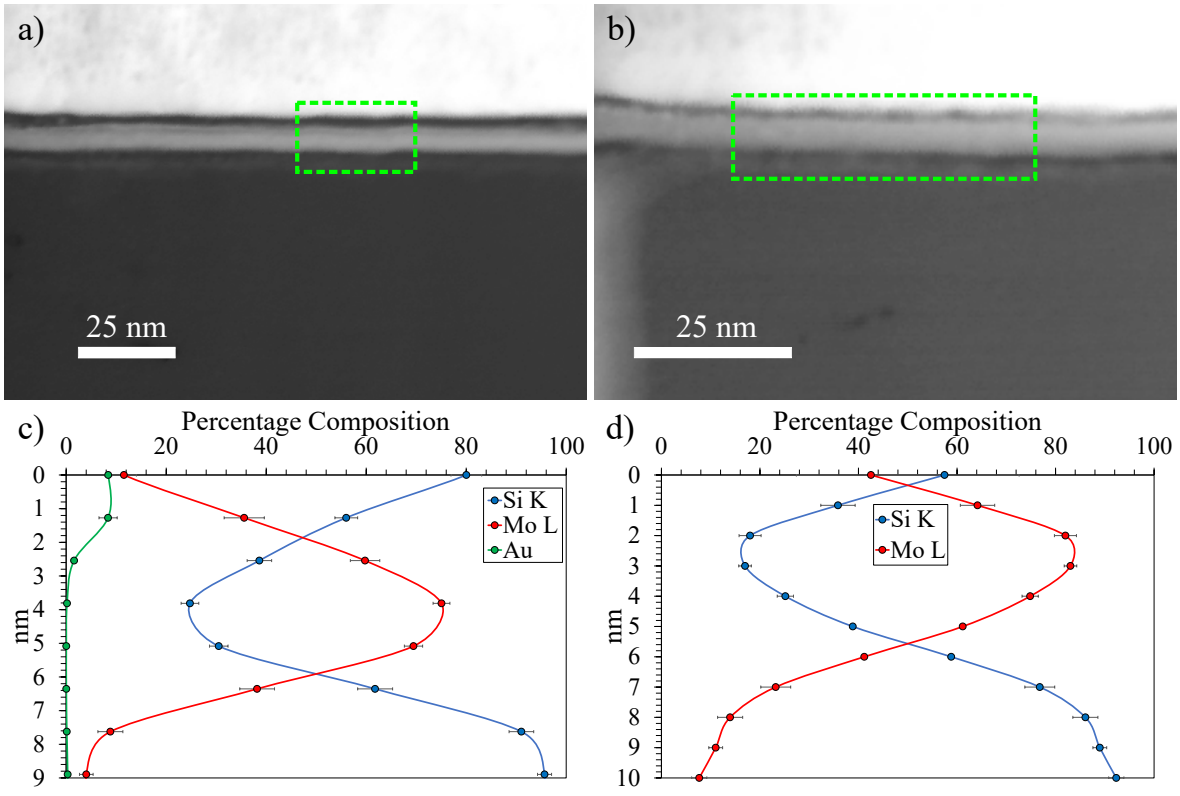

Figure 4.36: HAADF survey images of the areas scanned by EELS-SI of a) sample A (Si capped) and b) sample B (uncapped), with the green boxes indicating the scan areas. EELS-SI composition plots of the scanned areas, showing the concentration of Si and Mo in c) sample A and d) sample B.

This would suggest that there is less charge transfer than in an oxide, although the structure is significantly altered from the metallic one.

The $MoSi_x$ samples here are formed of a narrow layer, this means that in Sample A only one data point shows the composition in the central part of the film, while there are two data points in Sample B. Figure 4.36c,d shows the compositions of Samples A and B. The composition of Sample A is close to 76:24 Mo:Si in the centre of the film, and the Mo concentration decreases towards the edges of the film. Sample B has a composition of close to 83:17 in the centre. This is a fairly significant difference, and could be due to the amorphous Si capping layer present on Sample B. Another possible reason for this is the lack of data points in the centre of Sample A, which could mean that the measured composition is not representative of the actual composition in the centre of the film.

There are certain factors that affect the composition percentages presented here, some of these are; beam size, sample thickness and beam spreading. It was found that both of the samples had a thickness of approximately 25 nm. The sample with a Si capping layer has EELS signal from an Au protective layer over the top 5 nm of the spectrum image, although there is no Au signal in the centre of the film. On the other hand,

the uncapped sample shows Au signal in the top 3 nm of the EELS spectrum image, which includes the pixels directly above the central part of the film. Beam diameter should be less than 1 nm, which would indicate that there is beam spreading as the electron beam passes through the films. Analysis from the EELS data indicate that the beam spreading occurs over about 2 nm in both films. This could affect the atomic composition that was calculated using EELS.

4.3.3.2 Alloy Sputtered $MoSi_x$

There were three EELS-SI datasets obtained from this sample. Low-loss spectra were taken over an energy range of -20:252 eV, while the high-loss spectra were taken at 1300:3349 eV. It is expected that there is some similarity between the EELS spectra obtained from this sample and those from the co-sputtered $MoSi_x$ films previously discussed. There could be some differences, as the film thickness and film preparation process are not the same. EELS-SI elemental maps of this sample are shown in Figure 4.37, as well as the energy loss spectra themselves. Positions of the peaks used in quantifying this sample are highlighted.

There appears to be a small shoulder to the high-energy side of both the Mo L_2 and L_3 edges, shown in Figure 4.37f. There is also a small peak at approximately 2550 eV, following the L_3 edge, this shows some similarity to the co-sputtered $MoSi_x$, however it is more pronounced in this sample.

Figure 4.38 shows Si and Mo composition maps, alongside the percentage composition for this sample. This shows that the ratio of Si:Mo remains fairly consistent througout the film, though there are some areas that have a higher Mo content, where there are brighter pixels on the Mo map. There is a transitional area between the film and the substrate, which appears to have a length of around 2-4 nm.

EELS-SI analysis using the elemental quantification plugin estimates that in the centre of the film, the composition is close to 80 % Mo and 20 % Si (Figure 4.38). These percentages remain fairly constant through the sample. Interestingly, the ratio here is approximately halfway between those found in the two co-sputtered samples, although slightly closer to the possibly more reliable value calculated from Sample B.

As shown earlier in Figure 4.35, the background-subtracted deconvolved Mo $L_{2,3}$ edges in this sample, are slightly different to those found in the co-sputtered $MoSi_x$ films. In the red area, they appear largely similar, while in the blue area there does not seem to be a bump in the alloy sample, the yellow area has a much noisier spectrum in the alloy $MoSi_x$, so it is difficult to ascertain whether there is any effect there..

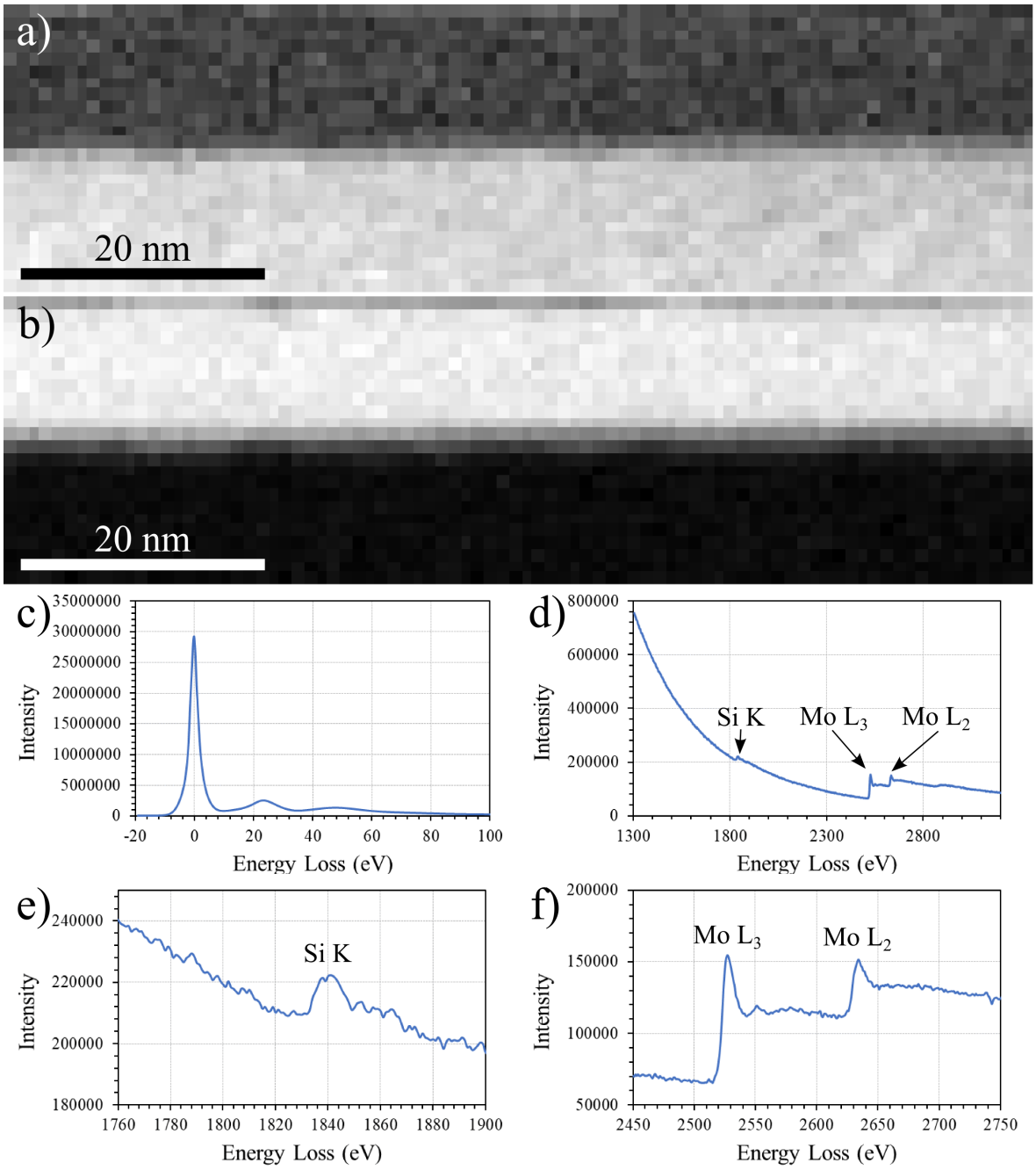

Figure 4.37: EELS-SI analysis of the sputtered-alloy $MoSi_x$ sample, showing; a) map of EELS background subtracted signal from the Si-K edge over a 151 eV range starting from 1820 eV; b) map of background subtracted signal from the Mo $L_2, 3$ edges over a 151 eV range starting from 2048 eV; c) low loss spectrum; d) full energy range view of the high loss spectrum from the $MoSi_x$ film, e) detail of the Si K edge and f) detail of the Mo $L_2, 3$ edges.

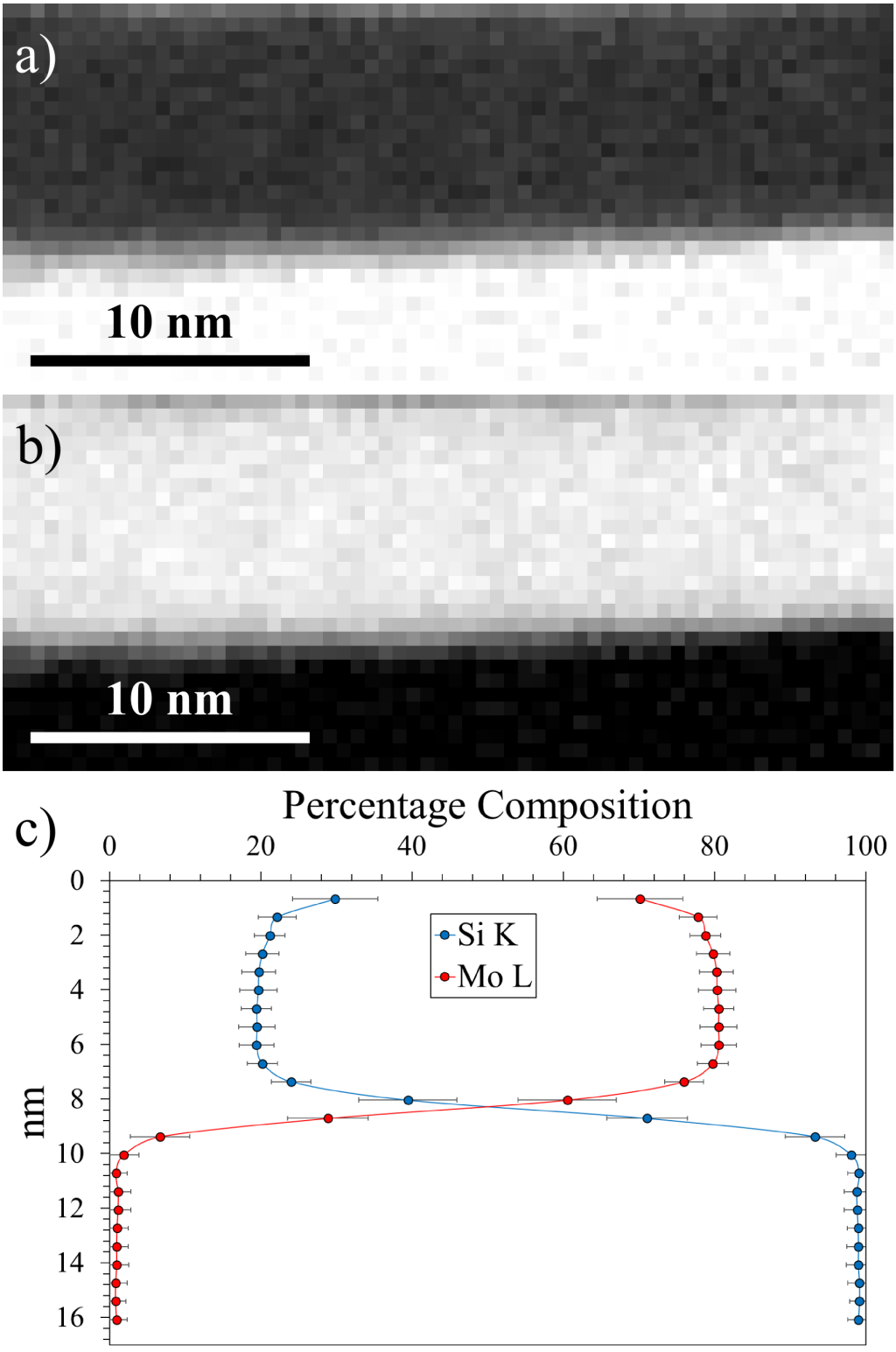

Figure 4.38: Images showing a representation of a) Si percentage composition and b) Mo percentage composition. These are a result of EELS-SI analysis of the Si K absorption edge and the Mo L absorption edge.c) shows composition of alloy deposited $MoSi_x$, from EELS-SI analysis of the Si K edge and the Mo L edge.

4.3.3.3 Co-Sputtered $NbSi_x$

For this sample, three EELS-SI datasets were recorded, with their low-loss spectra taken over an energy range of -20:299 eV and high-loss over 1303-3348 eV, so that it was possible to record the Nb L edges could be captured.

EELS-SI spectrum intensity maps from this sample, along with EELS spectra are shown in Figure 4.39. Edges used in the quantification are highlighted.

As before, EELS-SI analysis was carried out with the Digital Micrograph ® Elemental Quantification plugin, the edges used were the Si K edge and the Nb $L_{2,3}$ edges. Figure 4.39e shows that there are not any significant bumps following it at 1865 eV, in contrast to the $MoSi_x$ films. Nb edges are shown in Figure 4.39f, there is an interesting similarity in the profile of the energy loss spectrum profile of the $NbSi_x$ film to the $MoSi_x$ films. There are also two small subsidiary peaks, which are positioned at approximately 2400 eV and 2420 eV.

The Si and Nb composition within the film is shown in Figure 4.40. Within the film, the Si and Nb percentage composition remains fairly consistent, with around 85 % Nb to 15 % Si. There were no initial estimates given to us on the composition of this film, but it has a Nb concentration much higher than in a stoichiometric A15 structure. Sample B of the $MoSi_x$ sample showed a similarly high A:B ratio, where A:B is greater than 3:1, Sample A from the $MoSi_x$ film had an A:B ratio closer to the stoichiometric 3:1, however as the film was rather thin (5 nm), the amorphous Si capping layer could have affected the percentage composition calculated from that sample. This possibility is further backed up by the fact that the transition between film and substrate shown in Figure 4.40 takes place over at least 5 nm.

4.3.3.4 Co-Sputtered WSi_x

EELS-SI datasets from this sample were taken with a low-loss energy range of -20:294 eV and high-loss of 1304:3349 eV.

Figure 4.41 shows the EELS spectra obtained from this sample. This shows that peaks from W and Si overlap and it wasn't possible in this case to estimate the composition/stoichiometry of this sample. The W $M_{4,5}$ edge appears to be very similar to that found in the EELS atlas in Gatan Digital Micrograph, it is quite difficult to see the Si K edge between the W M_5 and M_4 edges. In spite of that, when a background subtraction and normalisation to post-edge intensity is carried out, a small change in the shape of the edge is visible, which could be attributed to the Si K edge. This feature

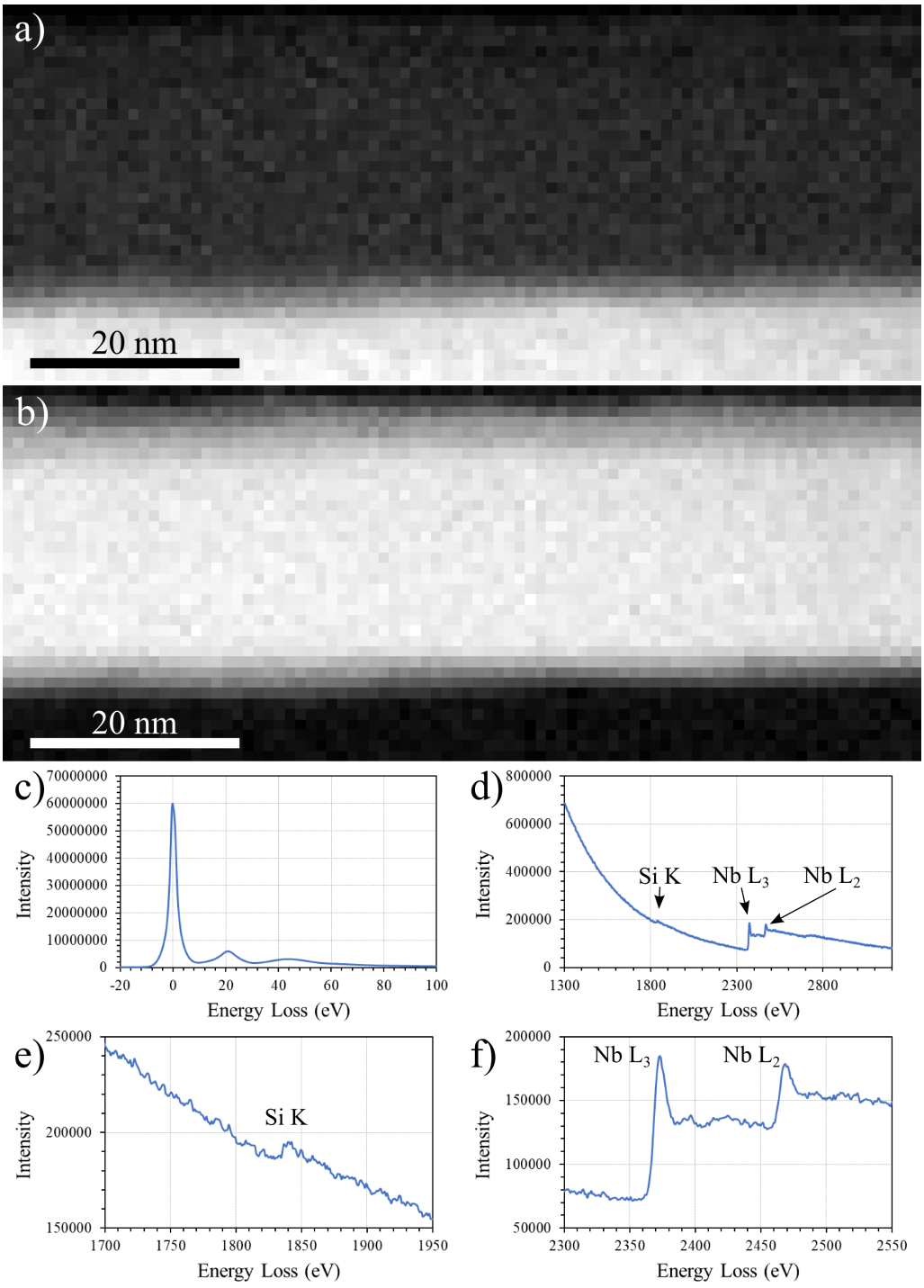

Figure 4.39: EELS-SI analysis of the co-sputtered $NbSi_x$ sample (with end cap), showing; a) map of background-subtracted EELS signal from the Si-K edge over a 149 eV range starting from 1824 eV; b) map of background subtracted signal from the Nb $L_2, 3$ edges over a 149 eV range starting from 2357 eV; c) low loss spectrum; d) full energy range view of the high loss spectrum from the NbSix film; e) detail of the Si K edge; and f) detail of the Nb $L_2, 3$ edges.

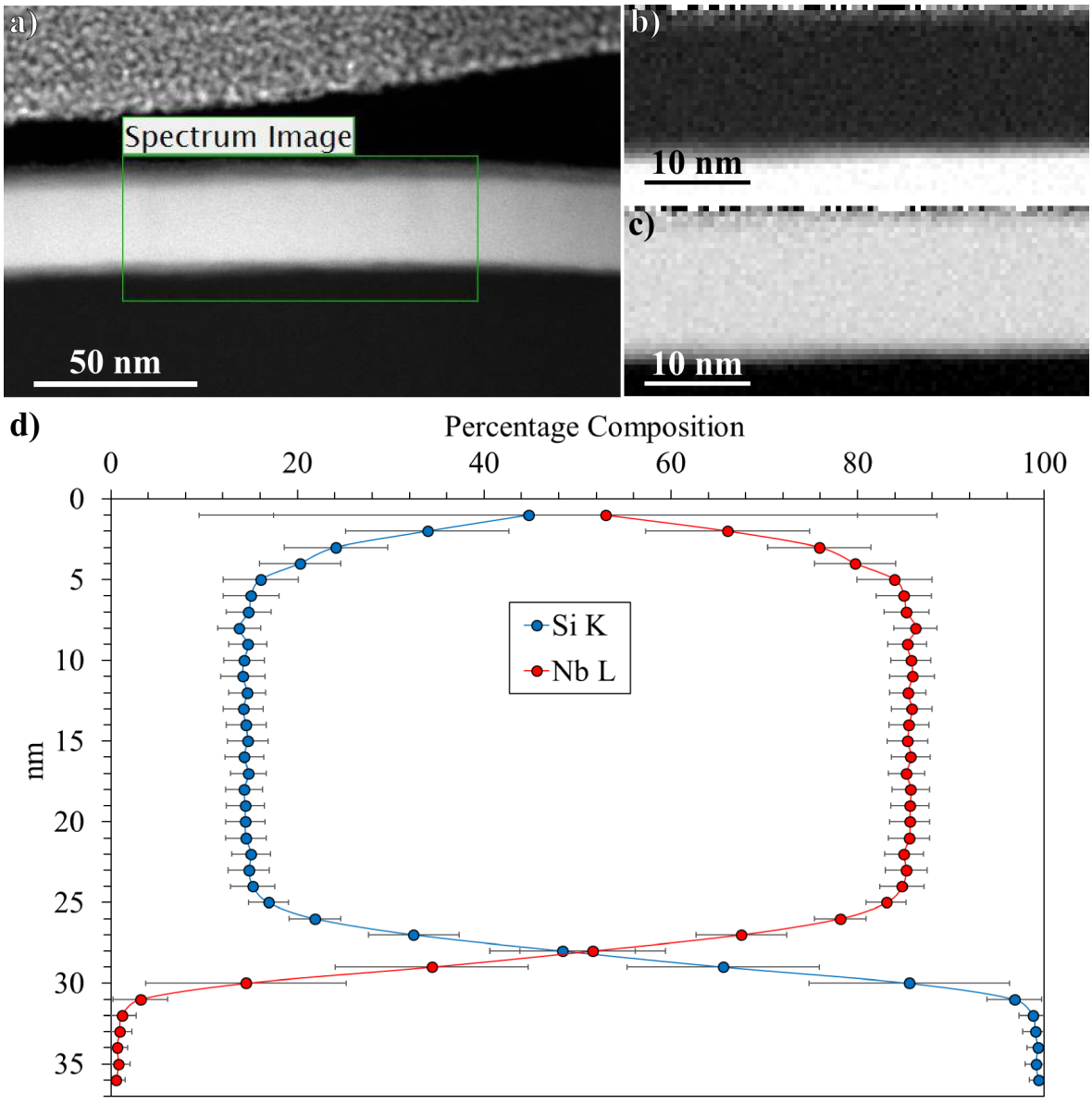

Figure 4.40: HAADF survey image of spectrum image area for the cosputtered $NbSi_x$ sample, b) and c) show images giving a representation of b) the Si percentage composition and c) Nb percentage composition. These are a result of EELS-SI analysis of the Si K absorption edge and the Nb L absorption edge. d) Composition of co-sputtered $NbSi_x$, from EELS-SI analysis of the Si K edge and the Nb L edge.

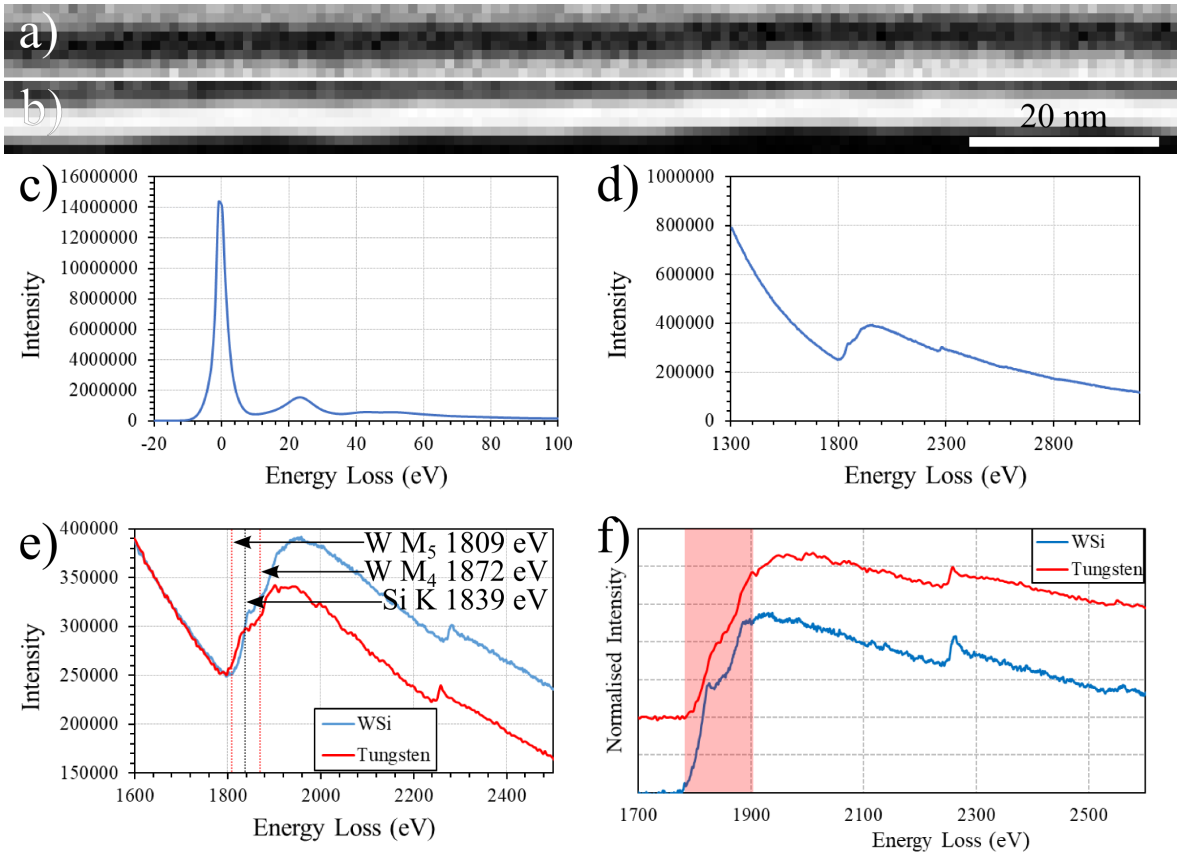

Figure 4.41: EELS-SI analysis of the co-sputtered WSi_x sample, showing; a) image of low loss spectrum intensity, b) image of high loss spectrum intensity, c) low loss spectrum, d) full energy range view of the high loss spectrum from the WSi_x film; e) detail of the Si K edge and the overlapping W $M_{4,5}$ edge as well as the EELS atlas W $M_{4,5}$ edge f) background subtracted spectrum from e).

is highlighted in Figure 4.41f.

Figure 4.42 shows intensity maps of this sample at various energy losses that are associated with either Si or W. Figure 4.42d,e show images of the sample formed by looking at the energy losses associated with these edges. There is only a small increase in the signal in the Si area of the sample if you view the energy losses that are associated with the Si K edge.

The two major edges in W occur at 1809 eV (M_5) and 1872 eV (M_4). Because of this, there are issues in calculating the percentage composition of this sample, due to their proximity to the Si K edge (1839 eV). W $M_{4,5}$ is a strong edge, because it arises from the promotion of electrons from filled *3d* states into free *p* or *f* states above the Fermi level. This means that there are ten starting states and many final states. The Si K edge is weak and arises from the promotion of electrons from filled *1s* states into *p* states, there are only two starting states and fewer final states. Due to this the intensity of the W edges should be around five times higher in a system with an equal ratio of W to Si. As this film has a W:Si ratio of around 3:1, the intensity of the Si

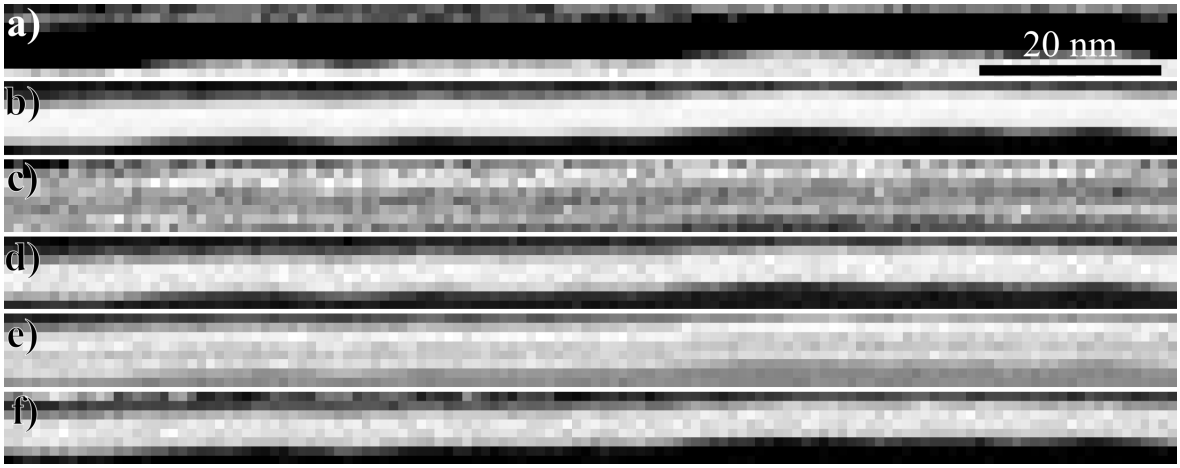

Figure 4.42: Maps of the WSi_x sample, showing the signal from the a) Si K edge and b) W $M_{4,5}$ edge as calculated by the Digital Micrograph elemental quantification plugin. Maps show the images generated from the EELS-SI dataset for background-subtracted energy loss windows of c) 98-102 eV (Si L edge), d) 1800-1824 eV (W M_5 edge), e) 1833-1869 eV (Si K edge, with W-M_5 contribution) and f) 2270-2295 eV (W M_3 edge). All maps have the same scale.

K edge will be around 1/15 of that of the W $M_{4,5}$ edge. This means that the Si K edge is very difficult to see in the presence of W. Figure 4.42a,b show the Si and W signals calculated by the Digital Micrograph elemental quantification plugin. It may be possible to quantify the composition of this film using the multiple linear least squares (MLLS) method of Craven et al., however it would be difficult and there would be large errors as a result of the high W content.[194] There are other Si edges which could possibly be used, such as the $L_{2,3}$ edge at around 99 eV. This could be used to show the Si as seen in Figure 4.42c, however it is difficult to carry out a quantification at that edge due to background subtraction issues at rather low energies because of the EXELFS from lower lying edges, such as the W-O edges. There is also a W $N_{4,5}$ edge at approximately 250 eV which could possibly be used for quantification, as the Ta $N_{4,5}$ edge has been used in quantification previously by Harry et al..[30] In the future, it may be possible to quantify this sample using the methods mentioned, however in the present case it was not feasible within the time available for this work.

4.4 Discussion

This chapter has inspected the structural properties of five different SNSPD samples, using FEM, VDF and EELS-SI techniques.

The first experimental section in this chapter covered the effect that probe properties and exposure time have on the FEM variance. As expected, in accordance with

previous literature, the results showed that increasing the exposure time caused a decrease in the variance at higher scattering angles, due to lower shot noise.[81, 138, 191, 195–197] This effect is not only dependent on the exposure time, but also the beam current. For example, in this experiment the beam current is higher when using a 20 μm aperture compared to a 10 μm aperture, this means that if data from the same exposure times but different apertures are compared, the advantage gained from using a longer exposure time will be greater for the smaller aperture.

Results (Figure 4.5) showed that when using the 10 μm condenser aperture, an exposure time of 10 ms is too small due to high noise. A decrease in noise at higher scattering angles correlated with an increase in the first variance peak height, in the three curves that were obtained at 40, 100 and 400 s. Similar effects were seen when the 20 μm condenser aperture was used, although due to the higher beam current the effect on the variance curve due to a longer exposure time was much smaller for the same exposure time. There was a significant decrease in the variance at higher scattering angles between 10 ms and 20 ms exposure times, however at exposure times larger than 20 ms, there were not huge differences in the variance curve at higher scattering angles. The main peak height also increased in size with longer exposure times.

Unfortunately these results were obtained after the rest of the data had been obtained, and it wasn't possible to retake measurements at longer exposure times than the 30 ms and 50 ms used. Further experiments to find the optimum exposure time such as those carried out by Radic et al. would be a further step that could be taken to improve the quality of results.[197]

Recent developments show that changing the probe diameter by altering the convergence angle produces greater normalised variance than if the probe diameter is changed by defocussing the beam.[197] In the results that are presented in this thesis, probe size variation was achieved by either changing the condenser aperture and thus the convergence angle, or by defocussing the probe. This is one area of the experiment that could be improved, by using a microscope that has the capability for easily altering the convergence angle, for example using three condenser lenses.

All of the films studied here show variance plots that are in accordance with short range order that is A15-like (Figures 4.13,4.20,4.27),[192, 193, 198] each of them show broad variance peaks centred at scattering angles where one would expect to see sharp diffraction peaks for a crystalline material, while none of them show any long range order. The Nb silicide film shows variance peaks that are at noticeably lower scattering angles than those found in the Mo and W silicides. It is already well known that A15 Nb_3Si has a larger lattice parameter (5.16 Å) and thereby larger interatomic spacing and smaller diffracted angles than those observed in A15 Mo_3Si (4.90 Å).[192, 193]

This result is also consistent with general trends in the periodic table where group IVa transition elements tend in both their metallic forms and their compounds to have larger lattice parameters than group Va transition elements.

In each of the films investigated at different probe sizes here, there are features in the variance curves that follow a similar pattern. The main peak height, as well as the variance at higher scattering angles increases as the probe size decreases (with the exception of the WSi_x film). These results could indicate that the MRO in these samples is closer to 1 nm than 2 nm.

The VDF technique was originally used to view features such as dislocations in low carbon steel, the grain structure in an alumina thin foil or the separation of crystalline and amorphous areas in nanocrystalline NiTi.[82] It was also used to show that increased ordering occurs due to thermal annealing in amorphous Ta_2O_5 glasses.[149] Here various types of VDF images and annular variance images were shown, in order to find out more information about the size and distribution of MRO within these films.

VDF images from the co-sputtered $MoSi_x$ film showed that there are more ordered areas at the film interfaces with the substrate and capping layer than within the film. The size of the brighter spots within the film appear to suggest that the size of more ordered regions are between 1-8 nm in size, with most around 1-2 nm. Similarly the alloy $MoSi_x$ seems to show ordered areas of around the same size, although again the film layer is not very thick, making it difficult to discern. As the $NbSi_x$ layer is thicker, it was easier to find ordered regions within the centre of the film itself, similarly to the $MoSi_x$ films, the size range of the ordered areas appears to be 1-8 nm. There was very little that could be seen in the WSi_x sample, as it is extremely thin.

All of these results suggest that the majority of ordered regions in each film are 1 nm or less, and that there may be a few regions that exceed this and approach nanocrystalline dimensions of around 8 nm. It is more difficult to come up with solid conclusions from the WSi_x film as it is so thin. VDF images could possibly be limited by the time stability of any structural order, which will be investigated in Chapter 5, so these conclusions could be limited by that factor.

Both the FEM and VDF results seem to provide some evidence for MRO, most of which is on a length scale of approximately 1 nm, while there may also be some larger ordered areas extending up to 8 nm. These results are similar to those of Hart et. al. who found ordered areas up to 6 nm in size in VDF images of Ti:Ta_2O5 films.[149]

In the Mo and Nb silicide films where it was possible to estimate their atomic compo-

sition, each was found to be rich in A atoms compared to the nominal 3:1 ratio in A15 structures. Co-sputtered $MoSi_x$ was found to have a composition of 76:24 ± 2 (Sample A) and 83:17 ± 2 (Sample B), alloy sputtered $MoSi_x$ 80:20 ± 2 and Co-sputtered $NbSi_x$ 85:15 ± 3. (The W:Si ratio in the W silicide film could not be quantified in this work due to the overlap of the W-$M_{4,5}$ and Si-K edges.) These results appear to fit with previous conclusions that A15 structures often have a maximum B atom content at or slightly above A_3B, but there can be an extension down to much lower content.[174–178] Further analysis using appropriate standards would enable more accurate determination of the compositions of these films. As these are metastable amorphous films, it is possible that the A15-like short range order may have been stabilised at compositions with lower B content than would be seen on an equilibrium phase diagram. The mechanism of this non-stoichiometry is the interesting question. Are there A atoms on the B sites, alternatively are there voids on the B sites? The current work does not resolve this question, but this has been considered by other workers.[174–177]

A15 structures are known to produce superconducting properties in many materials along the A-atom chains, including in these silicides. The fact that these all form A15-like short range order, and that the composition is estimated to be similar to those found in A15 structures, suggests an explanation for why the superconducting properties are excellent in all the films studied here. The lack of grain boundaries may reduce the scattering of Cooper pairs and improve the properties over those in conventional polycrystalline A15 superconductors. Further work would be needed to explore in more detail the connections between composition, deposition conditions, SRO, MRO and superconducting properties in these materials.

Chapter 5

Investigations of the Fluctuation of Glass Structures as a Function of Time

5.1 Introduction

Some glasses are more stable than others, based on factors such as their environmental conditions or chemical composition. Some glasses show an observable change in shape with time due to their own weight, for example the Kelvin tar glacier found at the University of Glasgow. For a gradual change in shape such as this to occur, there must be atom movements taking place within the glass.

2-level systems are talked about when discussing the properties of glasses and losses in these systems, such as internal friction or losses in both acoustic and electromagnetic waves.[199–201] These are of critical relevance to the performance of mirror coatings in LIGO, even a small loss of energy from a photon would cause it to lose coherence with other photons in the laser cavity.[202] Most of what is discussed is in terms of fundamental simplistic models and the fitting of macroscopic data to these models, there are no microscopic studies of what goes on at the atomic scale.[203–206]

It is possible to conduct a microscopic study of the time variation of structure in some glasses, using techniques used in earlier chapters, with fast pixelated detectors with low noise.

One approach to doing this could be to expose a small area of a glass to an electron beam, collecting a set of diffraction patterns with short exposure times, then conducting a quantitative analysis of changes in the diffraction patterns obtained as a function of time.

Different types of glass are more or less stable under an electron beam. Various factors determine how the structure changes, for example beam energy or beam current density. The dominant effect could be different in different types of material. Answering these questions could help in deciding which experimental parameters are appropriate for FEM experiments

In the case of materials that are less stable under an electron beam, it may be the case that their structure changes significantly enough that an experiment that investigates the spatial changes in diffraction patterns (such as FEM) would be affected. Even materials that are more stable under an electron beam could be affected. Rezikyan *et. al.* found that decoherence, especially displacement decoherence, strongly contributes to the suppression of speckles.[191] Displacement decoherence refers to the effect where the local structure of a material changes significantly as it interacts with the electron beam during exposure.

Quantitative studies on the differences between DPs may show different results depending on the type of material being inspected. Mechanisms by which beam damage take place can be different between conducting and insulating samples.

Various effects could alter the diffraction pattern, such as radiation damage or charging. Knock-on damage from elastic collisions between electrons and atoms is largely dependent on the beam energy, while damage due to radiolysis is more dependent on the beam current density.[207]

Different materials require differing levels of energy input to change their structure, either on a macroscopic or microscopic scale. In this chapter we will look at four different areas. Two glasses containing metals are inspected here; the centre of the $NbSi_x$ film that was used in the FEM analysis in Chapter 4, and a Ti:Ta_2O_5/SiO_2 multilayer film that will be described in the next section. Both of the silica glasses investigated here are part of the two TEM cross-sectional samples that the metal containing glasses form part of, these are firstly, the oxidised SiO_2 layer that forms the substrate of the $NbSi_x$ film, secondly, the SiO_2 layer in the Ti:Ta_2O_5/SiO_2 multilayer film.

This chapter investigates the timescale over which the structure of these materials changes, this is achieved by analysis of DPs collected when an electron probe is focussed

onto the same area of a sample continuously. The sum of squares difference (SOSD) of diffraction patterns is used, in combination with correlation microscopy to calculate these timescales.

5.2 LIGO Ta_2O_5/SiO_2 Multilayer Film

The first detection of a gravitational wave occurred in September 2015.[208] Since that first detection there have been multiple further observations.[209–217]

Gravitational waves were first predicted by Albert Einstein in his General Theory of Relativity in 1916, this theory predicted that due to asymmetric acceleration of mass, gravitational waves that travel at the speed of light in space-time are generated.[218] These waves are a superposition of two polarisations, which are h_+ and h_x, these are offset by an angle of 45°.[219]

A strain is induced transverse to the direction of propogation in the space-time medium by the gravitational wave, this is called h. This differentially changes the distance between two points, where the orthogonal components expand and contract simultaneously.

The important equation which makes it possible to detect gravitational waves is

$$h = \frac{2 \triangle L}{L} \tag{5.1}$$

where L is the distance between two particles and the change in distance between the two points due to a passing gravitational wave is $\triangle L$.

In order to detect gravitational waves, Michelson type based interferometers that are extremely sensitive to changes in displacement are used. When a gravitational wave passes the detector, one arm of the detector will expand, while the other contracts, this leads to the optical interference in the interferometer changing, as there has been a change in the relative path length, this gives a detectable signal to a photodiode. There are multiple detection sites, currently the main ones are the two LIGO detectors located at Hanford and Livingston in the USA and the VIRGO detector in Italy.[220, 221] This use of multiple detection sites enables the triangulation of the gravitational wave source.

At the end of each arm of the interferometer in the LIGO detectors are test masses formed of ultra-pure fused silica with a mirror coating on the surface. These consist

of a high reflectivity dielectric mirror stack, formed of alternating layers of 25 % TiO2 doped Ta_2O_5 (Ti:Ta_2O_5) as a high refractive index layer and SiO_2 as a low refractive index layer.[220] Any pair of high refractive index / low refractive index materials will give high reflectivity at a specific wavelength, so long as the thickness of each layer is $\lambda/4$. There are three factors that need to be optimised. 1 - minimising the optical absorption. 2 - minimising the light scattering. 3 - minimising the loss due to thermal noise. Whilst there may be many materials that might do 1 and 2, this combination of materials is particularly good at 3.[222–224]

This material was fabricated using ion beam sputtering (IBS) by members of the LIGO collaboration. IBS is a technique where ions such as argon are accelerated towards a target material, when the ions strike the target with sufficient energy, the momentum of the ions is transferred, causing atoms to be ejected from the surface of the target and onto the substrate. If a metal-oxide thin film is desired, oxygen may be injected into the sputtering chamber, such that a metal-oxide film is produced by sputtering from a pure metal target. Fused silica disc substrates were used.

TEM sample preparation was also carried out by members of the LIGO collaboration.

5.3 Electron Correlation Microscopy

He *et al.* reported on electron correlation microscopy for studying the local atom dynamics in a supercooled liquid.[225]

Time over which speckle intensity persists corresponds to the timeframe that the particular structure causing the speckle persists over. Persistence time can be statistically measured using the time autocorrelation function.

$$g_2(t) = \frac{\langle I(t')I(t'+t)\rangle}{\langle I(t'\rangle^2} \tag{5.2}$$

where you have t' which is the time of a frame in the series of diffraction patterns, t is the delay time following t' and $\langle\rangle$ indicate averaging over all t'.

The Kohlrausch-Williams-Watt (KWW) equation which describes the structural relaxation process in glass is

$$f(t) = f(0) \times \exp\left(-\frac{t}{\tau}\right)^{\beta} \tag{5.3}$$

where the time dependent quantity $f(t)$ is the intermediate scattering function, there is a delay time t, relaxation time τ and a fitting parameter β which is known as the stretching exponent. The relationship between $g_2(t)$ and τ is given by

$$g_2(t) = 1 + A \times \exp\left[-2\left(\frac{t}{\tau}\right)^{\beta}\right] \tag{5.4}$$

where A is instrument-dependent and represents a scaling parameter that is related to the diffraction intensity variation.

A mask was applied to each of the diffraction datasets to block out the central beam, as well as remove areas of the pattern at higher scattering angles.

$g_2(t)$ was calculated for each pixel in the masked diffraction pattern using the equation

$$g_2(p) = \frac{(N-p)\sum_{i=0}^{N-p-1} I(i)I(i+p)}{[\sum_{i=0}^{N-p-1} I(i)][\sum_{i=0}^{N-p-1} I(i+p)]} \tag{5.5}$$

where the total number of frames is given by N and p is the frame/time index.

In order to improve the signal to noise ratio, $g_2(t)$ was also averaged over an annular range positioned at the main diffraction ring of each material.

Standard non-linear least squares fitting was used to fit equation 5.4 to $g_2(t)$ of each pixel in the diffraction pattern, as well as to the average from the annular region. Before this fitting took place, $g_2(t)$ was resampled, so that it is evenly distributed in $\log(t)$ to avoid the fits being more weighted towards the datapoints at higher t at the expense of accurate fitting at lower t.

5.4 Experimental Parameters

In contrast to the previous chapter, where the probe was scanned across the sample, here it remains in one position while DPs are captured. In each case, the following procedure was taken, a thin area of the sample is found such that the diffraction patterns obtained are very speckly, then the beam was focussed, then blanked. Using the Merlin software a time sequence was set up, where the number of images and exposure time was selected and the detector settings mentioned in 3.3.4.2 were used. A small shift in the beam position is then made, ensuring that no damage from previous exposure while the beam was being focussed affects the dataset. Next the beam is

unblanked and the acquisition of images begins. If the sample is time-stable under the electron beam, no changes should be seen in the diffraction pattern. All of the results were obtained using the JEOL ARM200F, at 200 kV in TEM mode, similarly to the previous chapters for classic FEM. Condenser apertures of 10 μm and 20 μm were used to give probe sizes that were $\approx$ 2 nm or $\approx$ 1 nm respectively. A table showing all of the experimental parameters used in this experiment is shown in Table 5.1.

For this experiment, data was taken in three separate batches. First of these was the acquisition of 1000 DPs using a 2 nm probe, each of these patterns had an exposure time of 1 ms, providing a dataset over 1000 ms (1 s). Two datasets were acquired from the $NbSi_x$ film described earlier in Chapter 4, one from the film itself, the other from the SiO_2 substrate of that film. Secondly, images of 500 DPs were captured with a 1 nm probe, each with an exposure time of 21.6 ms, giving datasets over a period of 10.79 s. Two sets of data were obtained using this setup from similar regions of the $NbSi_x$ sample as above. Finally, datasets of 500 DPs with 21.6 ms exposure times were again obtained, however in this case the probe size was 2 nm. Two datasets were taken from the Ti:Ta_2O_5/SiO_2 multilayer film described earlier, one from each of the layers.

Table 5.1: Illumination conditions for each of the datasets acquired in this chapter.

Dataset	**$NbSi_x$ & SiO_2 Substrate**	**$NbSi_x$ & SiO_2 Substrate**	**Ti:Ta_2O_5/SiO_2 Multilayer Film**
Exposure Time (ms)	1	21.6	21.6
Probe Size (nm)	2	1	2
Probe Current (pA)	32.1	19.5	4.0
Semi-convergence Angle (mrad)	0.87	2.16	0.87
Raw detector counts	800,000	10,400,000	2,160,000
Electron Dose (e^-)	200,000	2,600,000	540,000
Electron Density (e^-/nm^2)	16,000	835,000	43,000

Different processes were applied to the data to extract useful information about how the diffraction patterns changed with time.

FEM techniques were applied to the datasets in this chapter. Different timescales can be analysed, by changing how the DPs are inputted into the variance calculation. For example, in a dataset containing N diffraction patterns at an exposure time of t, A adjacent diffraction patterns could be summed together to form a new dataset that has N/A patterns and an exposure time of At for each pattern. This technique was used

in the later analysis.

Similarly to the VDF imaging shown in previous chapters, virtual apertures were applied to each DP in the dataset, then the intensity within those apertures was summed in each DP. This enables the summed intensity within that aperture to be plotted against time.

A visual method of inspecting the differences in diffraction patterns is to calculate the difference in intensity between two DPs and show the location within the DP that the differences in intensity appear.

Full code listings for this analysis are shown in Appendix B.5.

Please note, the samples analysed in this chapter were prepared as described earlier in Chapter 4, and section 5.2. STEM data acquisition and subsequent analysis was performed in the School of Physics and Astronomy by myself working with my supervisor Dr. I. MacLaren.

5.4.1 Possible sources of error

Microscopes that utilise CFEG electron sources are subject to instabilities in emission characteristics. Any contaminants on the tip can change its shape and work function. Stray electric fields can also affect the emission of electrons. Changes to the beam current are directly represented in the counts recorded on the detector for each DP.

By integrating the detector counts of each DP in a dataset it is possible to calculate the current per frame. Over a time period of 10 s, variations in current per frame were found to be as large as 5%. To adjust for this effect, each dataset was normalised so that the total counts per DP was the same.

Sample drift over a large enough distance will cause some spatial differences to the DP. If the spatial drift of the sample over the full dataset exceeds around half of the probe size, then the values of τ measured will be dominated by the drift effect changing which region of the sample is under the beam.[225] The sample will naturally drift at a rate of up to 0.1 nm per minute in the microscope used here when the microscope is in stable condition. Over a ten second acquisition with a 2 nm beam, contributions from this should be negligible. Additionally, there are magnetic field deflections that occur at this site when subway trains pass nearby, these occur every couple of minutes and would likely cause larger spatial drift in the form of jumps in position, in comparison to the general spatial drift. These larger jumps in position would be visible as sudden changes to the diffraction pattern, so each dataset must be inspected to ascertain whether such

an event has occurred. Typically, experiments conducted using this method have beam drift of up to 0.2 nm per minute.[225–227]

The time each dataset is recorded over should be much longer than τ, ideally at least 40τ to obtain results that are reliable.[226] Frame time is another important parameter for obtaining accurate calculations of τ. An ideal frame time should be less than 0.1τ to ensure sufficient sampling.[226]

5.5 Time Variation Using 1 ms Exposure Time

5.5.1 $NbSi_x$ 1 ms Exposure

As described earlier, 1000 DPs were obtained from this sample, with an exposure time of 1 ms, resulting in a cumulative time of 1 s.

Firstly we will inspect DPs from various regions throughout the dataset. Figure 5.1 shows twelve DPs that are equally spread throughout the dataset. Most of the electron scattering goes into a diffuse inner ring, within which there are discrete speckles clearly visible. Some of these speckles persist over all the DPs in the dataset, a timescale of 1 second. Arrows overlaid on the 0.0 ms DP show some of these speckles. We observe that while there are minor changes to the DP as a function of sample exposure time, overall these speckles and other features tend to remain visible from beginning to end of this dataset. From this we can conclude that no large scale changes in structure take place in the film over the time period and beam conditions used.

When we compare twelve consecutive DPs, as shown in Figure 5.2, it is seen that there are only very minor changes to the DPs over this short timescale shown.

Figure 5.3 shows the spatial variance alongside various temporal variance curves obtained by virtually altering the dataset to change the exposure time. The first graph shows that the temporal normalised variance is significantly smaller than that found in the spatial variance of the same film. As might be expected, when the virtual exposure time is increased, the variance curves decrease in their variance magnitude, which can be clearly seen in the lower graph. All of the temporal variance curves appear very similar, with nearly all of the peaks present in each curve. These results suggest that there is very little temporal fluctuation in the DP within this dataset.

Next we inspected the intensity of four of the more prominent diffraction speckles as a function of time. Figure 5.4 shows the areas of the DP that were used, overlaid on an image of the summed intensity of all 1000 DPs. The total intensity (detector counts) from boxes with a diameter of 8 pixels was calculated for each DP. Figure 5.5 shows the intensity of these spots as a function of time. The first spot (Spot1) shows a fairly steady increase in intensity with time, with some small fluctuations along the way. Spot2 and Spot3 show more noticeable changes than those observed in Spot1, with Spot3 showing larger changes in spot intensity in general. Spot4 remains fairly consistent, though there are small fluctuations, most notably before 200 ms and after 700 ms. Nevertheless, all these changes are subtle and fairly minor.

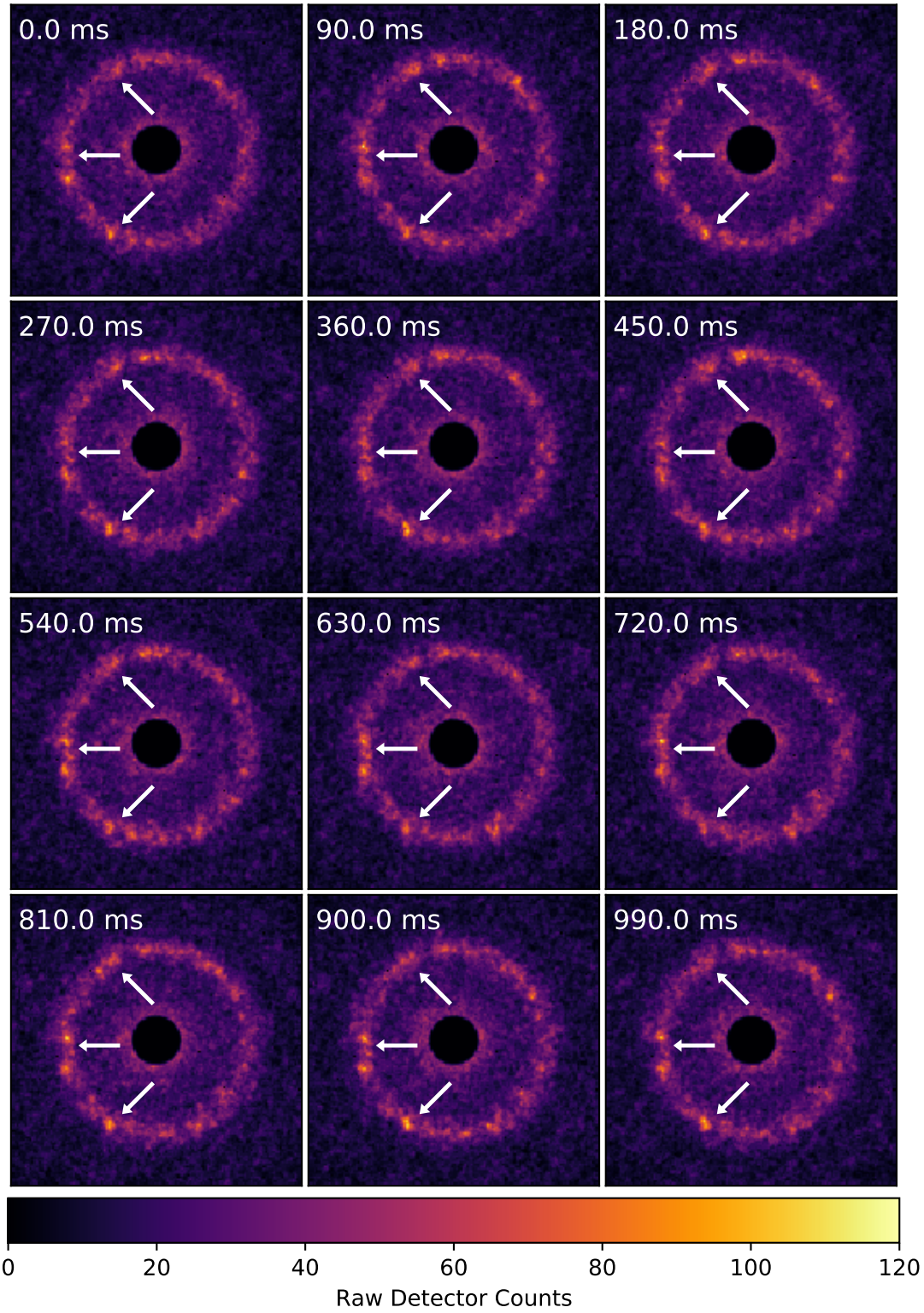

Figure 5.1: DPs obtained from the $NbSi_x$ film using an exposure time of 1 ms. This figure shows patterns taken from the dataset at regular 90 ms intervals. Arrows show some areas of the DP where diffraction spots are present in all DPs shown.

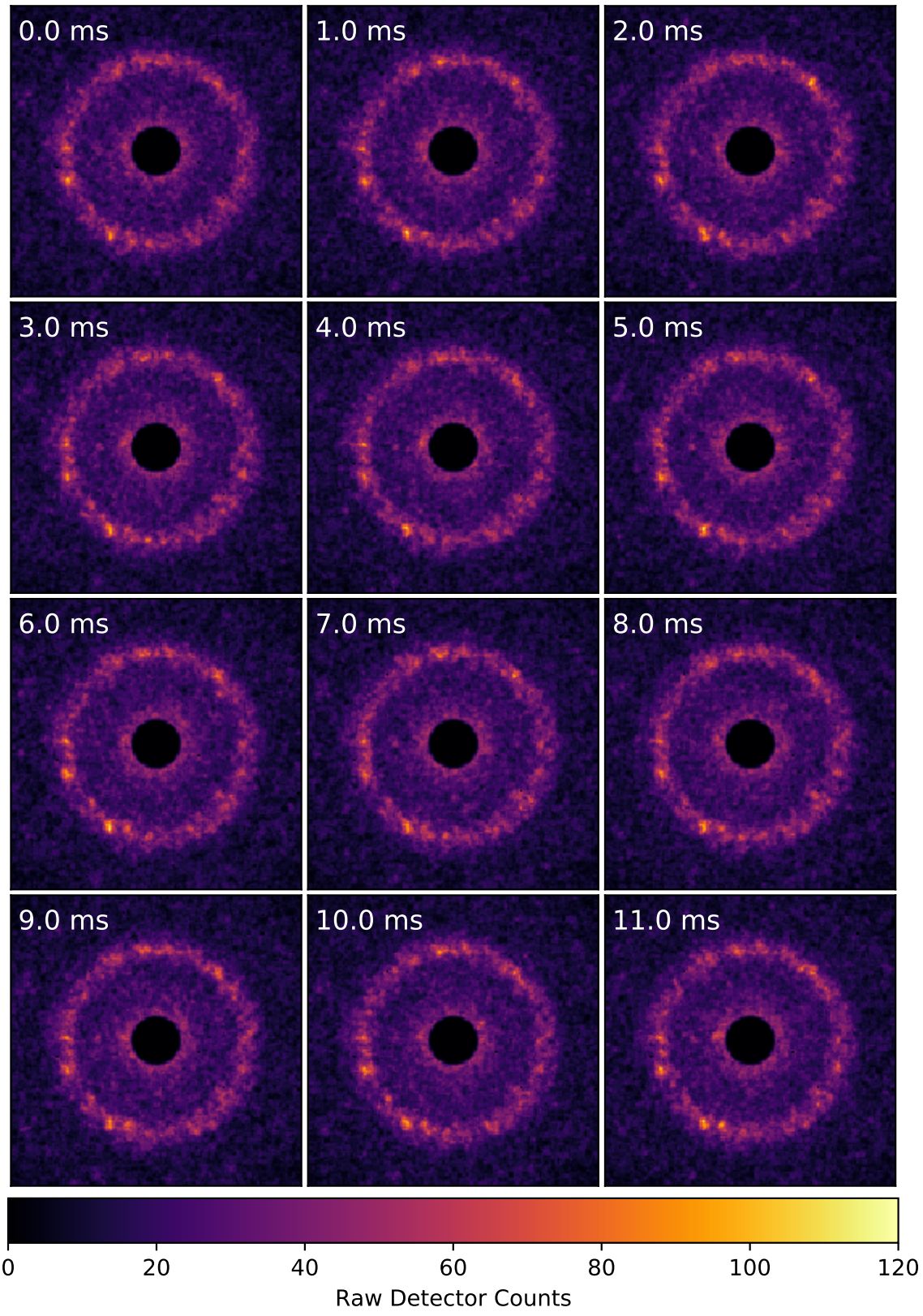

Figure 5.2: DPs obtained from the $NbSi_x$ film using an exposure time of 1 ms. This figure shows twelve consecutive patterns taken from the dataset.

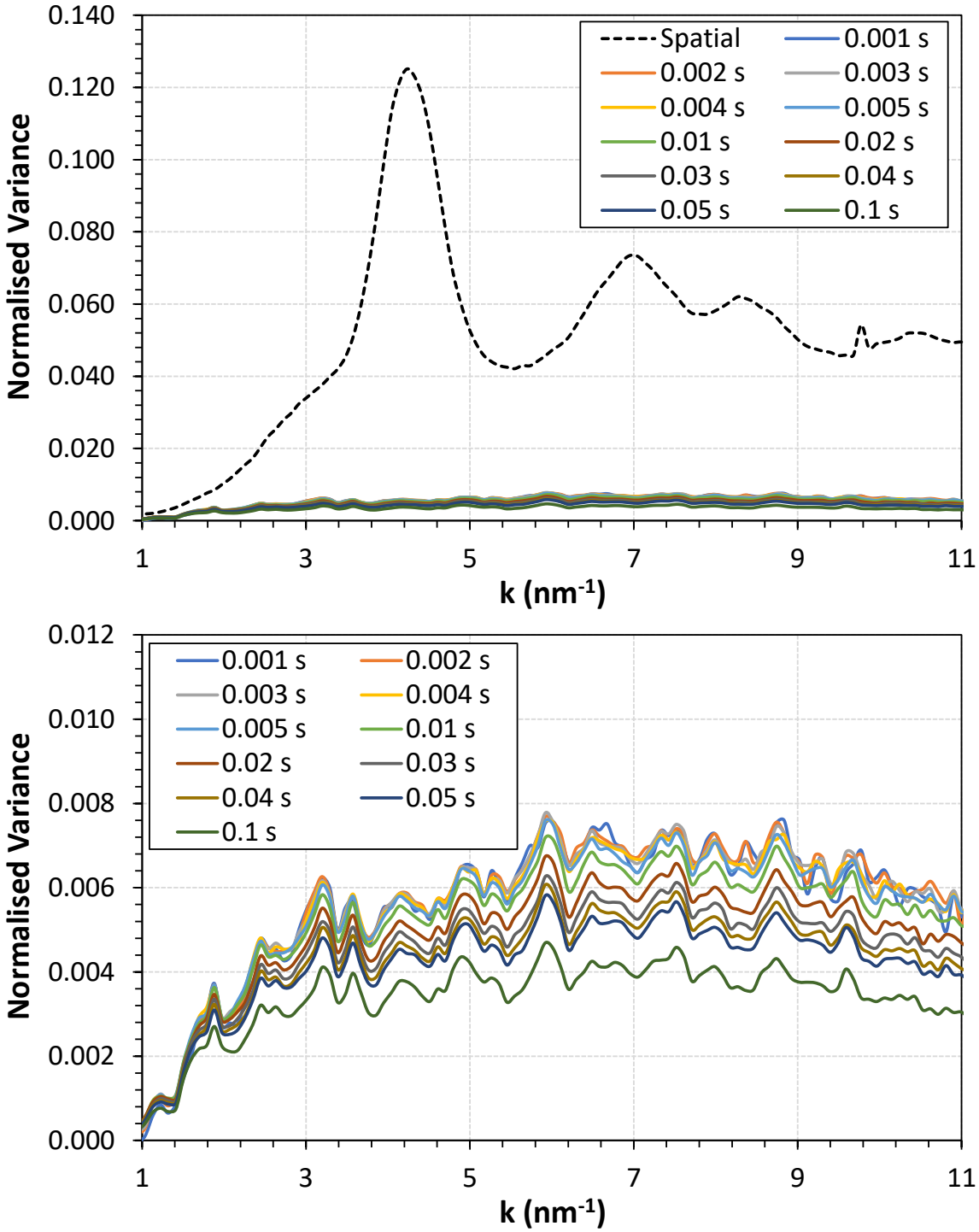

Figure 5.3: Normalised variance obtained from the $NbSi_x$ diffraction patterns at 1 ms exposure time. Variance curves from the summed diffraction patterns over eleven different timeframes are shown. The top graph includes the spatial variance, to show how large the temporal variance is in comparison.

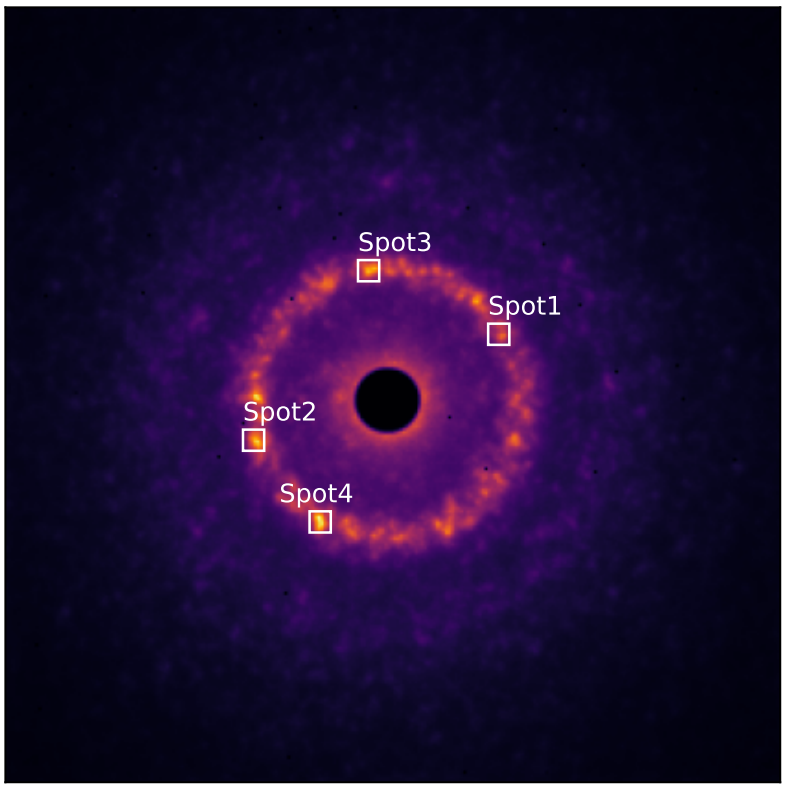

Figure 5.4: Sum of all 1000 DPs in the dataset obtained from the $NbSi_x$ film, showing selected diffraction spots.

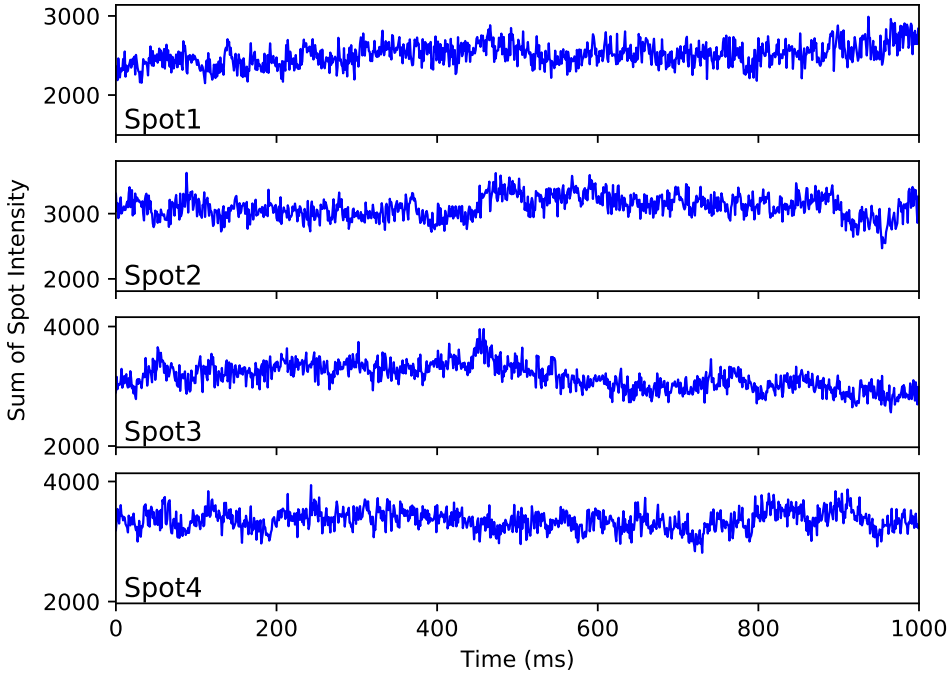

Figure 5.5: Line plots of the summed intensity within each of the four spots as a function of time. Shown over the full time range of the experiment

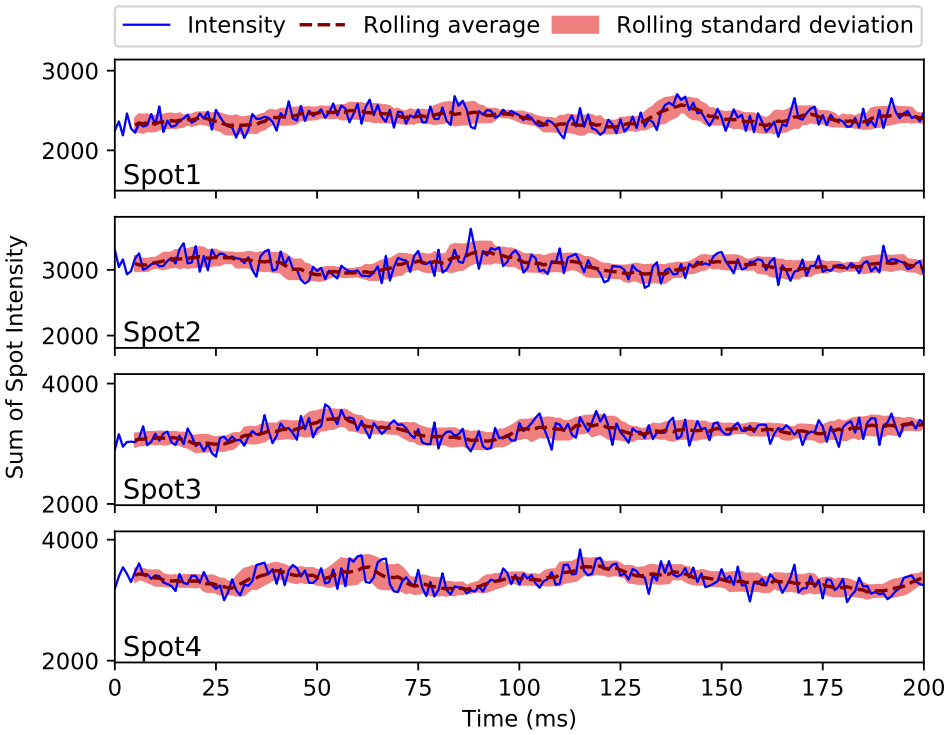

Figure 5.6: Plots of the summed intensity for the first 200 ms of the dataset within each of the four spots. A rolling average and standard deviation from a window 11 patterns wide are overlaid.

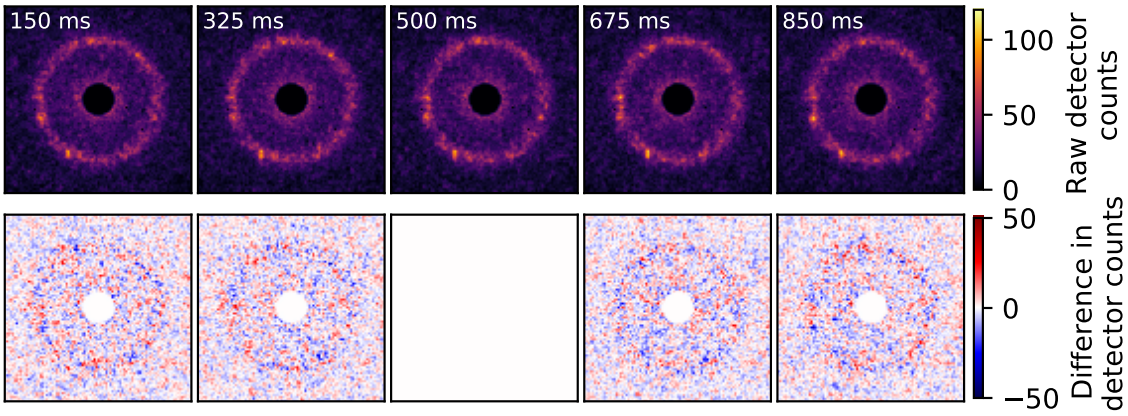

Figure 5.7: This figure shows five DPs obtained with an exposure time of 1 ms from the $NbSi_x$ layer. These are spread at 175 ms intervals through the dataset. The top row shows the DPs, while the bottom row shows the absolute difference in intensity (detector counts) between the central DP in the top row and the DP directly above it.

Figure 5.6 shows the same data, but only for the first 200 ms of the experiment. A line indicating the rolling average over a window of 11 DPs has been added to the plot, where the window is centred on the pattern in question. The rolling standard deviation over the same window has also been highlighted, in order to show where the intensity within the spot has changed more noticeably, compared to the patterns around it. It is apparent from this plot that for most of the patterns in the first 200 ms, the change in spot intensity fits within 1 σ of the average over the 11 DP window. There are some places where the spot intensity falls outside of this 1 σ range, but most of the spot intensity falls within.

To get a sense of the differences in intensity taking place through the dataset, plots showing the difference in intensity between DPs were calculated and are shown in Figures 5.7,5.8. Differences in DPs that are spread at 175 ms intervals (Figure 5.7) show that some features increase/decrease in intensity as a function of time, in similar fashion to that shown earlier in Figure 5.5, while there are more differences between the DPs that are further from the central DP, these are mostly not obvious at first glance. Differences between adjacent DPs (Figure 5.8) show much smaller changes in intensity compared with those found when there is a larger time interval between DPs.

Figure 5.8 shows that there are already significant differences to patterns that are only 1 ms apart ($\Delta t = 1$), these occur all over the field of view, not only in the diffuse ring. This suggests that these differences are dominated by shot noise differences at this timescale. With increasing time differences between patterns (Figure 5.7) real changes in intensity in this inner ring will become more significant.

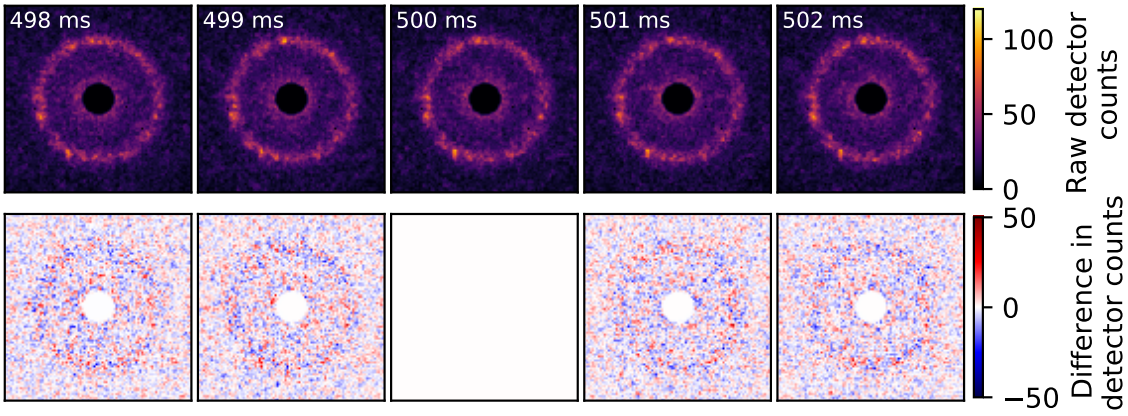

Figure 5.8: This figure shows five consecutive DPs obtained with an exposure time of 1 ms from the $NbSi_x$ layer. The top row shows the DPs, while the bottom row shows the absolute difference in intensity (detector counts) between the central DP in the top row and the DP directly above it.

5.5.2 SiO_2 Substrate 1 ms Exposure

The first of the SiO_2 glasses to be inspected is the substrate of the $NbSi_x$ film, in this case an exposure time of 1 ms was used, with a probe size of 2 nm and probe current 32.1 pA. 1000 DPs were collected, forming a dataset with a total time of 1 s.

Some example DPs from the dataset are shown in Figure 5.9, there are arrows pointing to some of the more prominent diffraction speckles visible on these patterns. There are no obvious diffraction rings on these patterns, instead it appears that there is a circular region surrounding the central spot, the intensity within this region decreases as you move further away from the central spot. Consecutive DPs are shown in Figure 5.10, these display some diffraction speckles in all of the patterns, but for the most part, speckles are not very long lived and disappear after a few ms. Arrows in the figure point to a diffraction speckle that is present in all of the patterns shown, although this does vary in intensity significantly. It would appear from these patterns that the ordered regions responsible for these diffraction speckles last less than 50 ms and that over a timescale of $\approx$ 10 ms some speckles almost disappear while new ones begin to appear.

Figure 5.11 shows the temporal variance obtained from this dataset. Each of the variance curves show the same shape, with an initial peak at around 2.5 nm^{-1} followed by a plateau that extends until around 8.5 nm^{-1}, after that the variance starts to drop. The magnitude of the variance decreases as the virtual exposure time is increased, ending up with a main variance peak that is 6 times smaller with an exposure time of 0.1 s compared to 0.001 s.

An image of the summed intensity of all DPs, shown in Figure 5.12 displays that it is difficult to distinguish any diffraction speckles which propagate through the full 1000 ms timescale of this dataset. The intensity of four diffraction speckles (8 pixel diameter boxes) was calculated as a function of time and is shown in Figure 5.13. A rolling average of the intensity was then calculated using a window of 11 DPs, and is shown in Figure 5.14. Table 5.2 shows the FWHM of intensity peaks found from the rolling average of intensity, all four of the values are fairly similar, three of them between 16-18 ms, while the fourth is slightly higher, at 23.5 $\pm$ 6.9 ms.

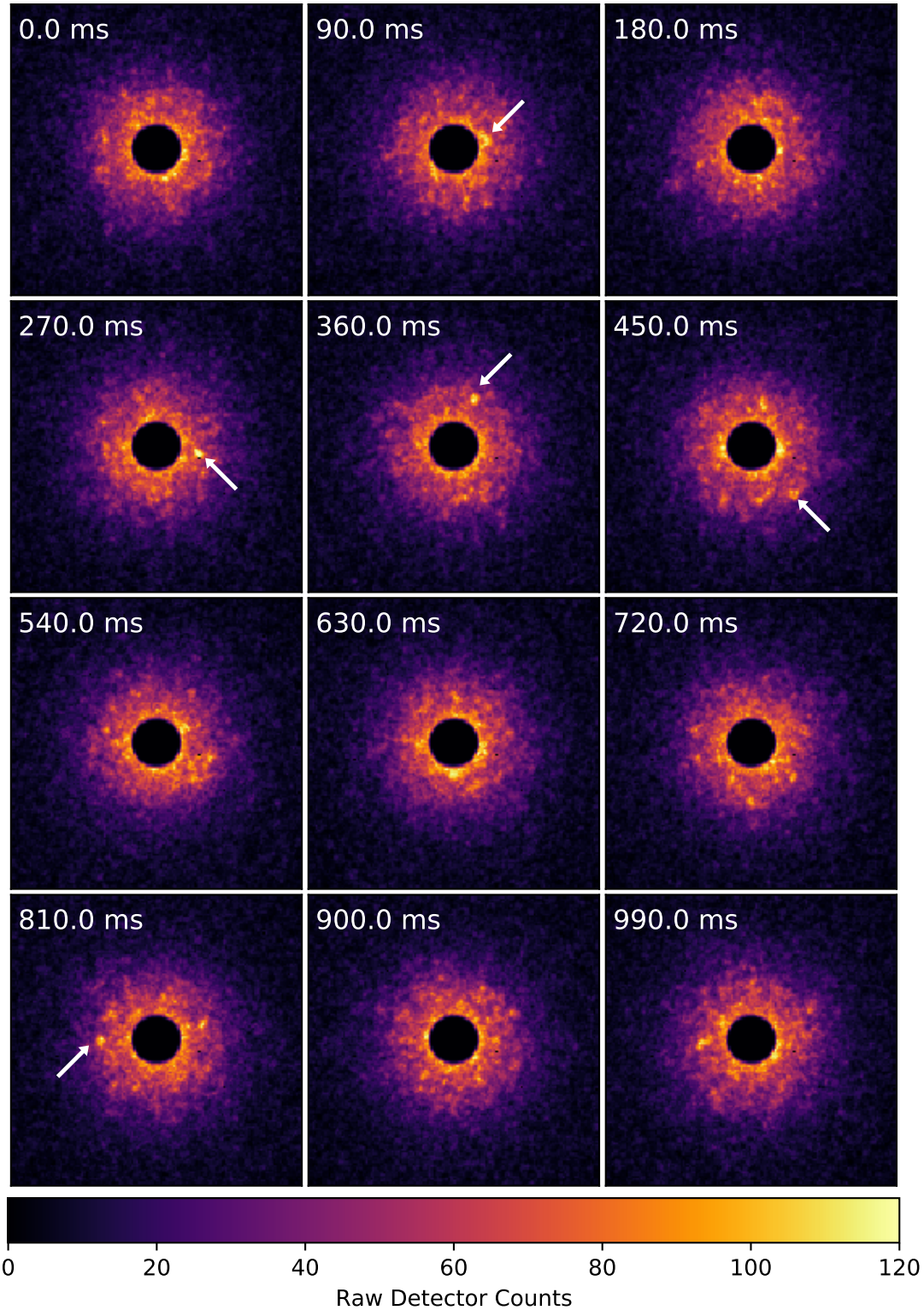

Figure 5.9: DPs obtained from the SiO_2 substrate of the $NbSi_x$ film using an exposure time of 1 ms. This figure shows patterns taken from the dataset at regular 90 ms intervals. Arrows show some features of interest present in the patterns shown.

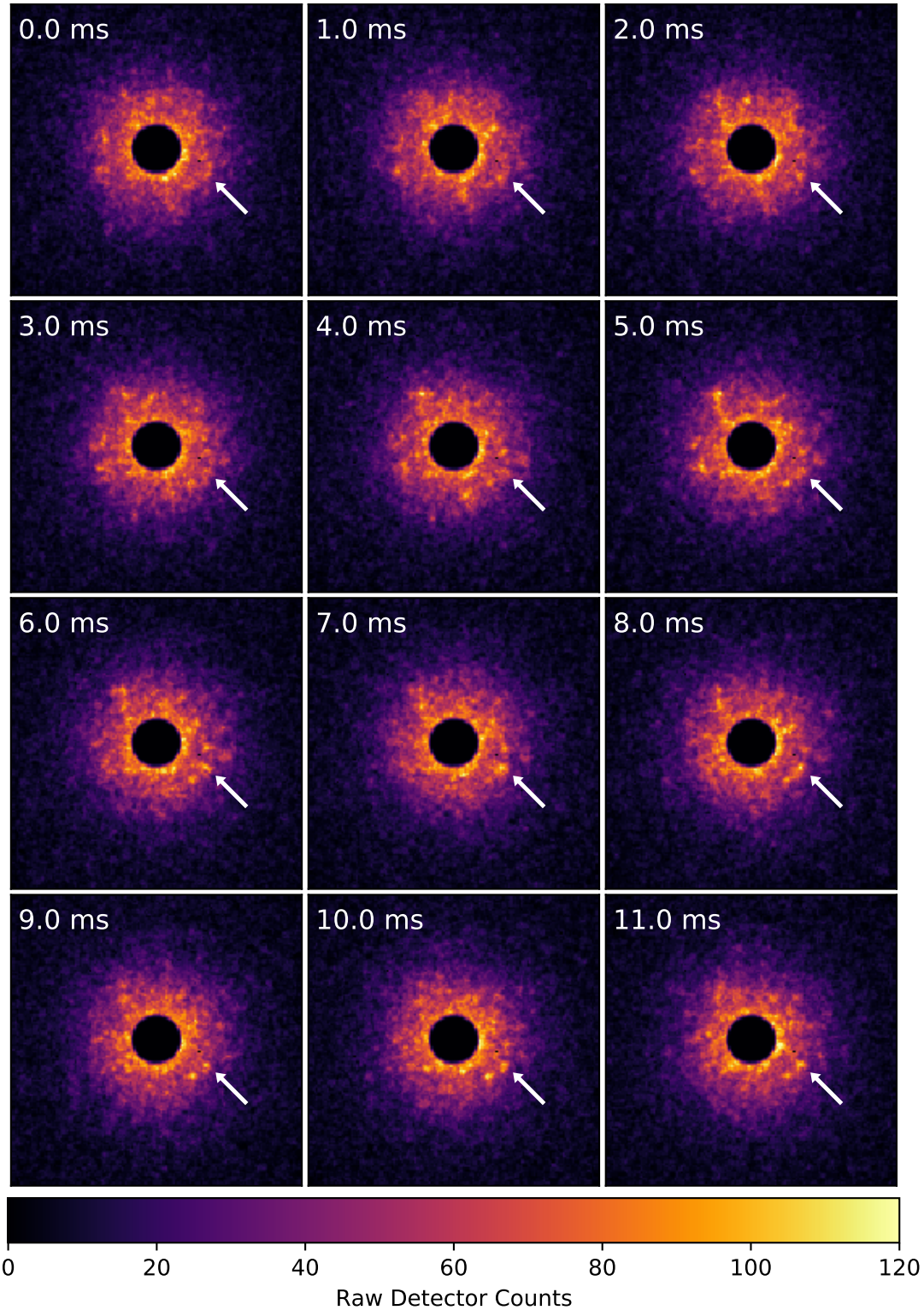

Figure 5.10: DPs obtained from the SiO_2 substrate of the $NbSi_x$ film using an exposure time of 1 ms. This figure shows twelve consecutive patterns taken from the dataset. Arrows show some features of interest present in the patterns shown.

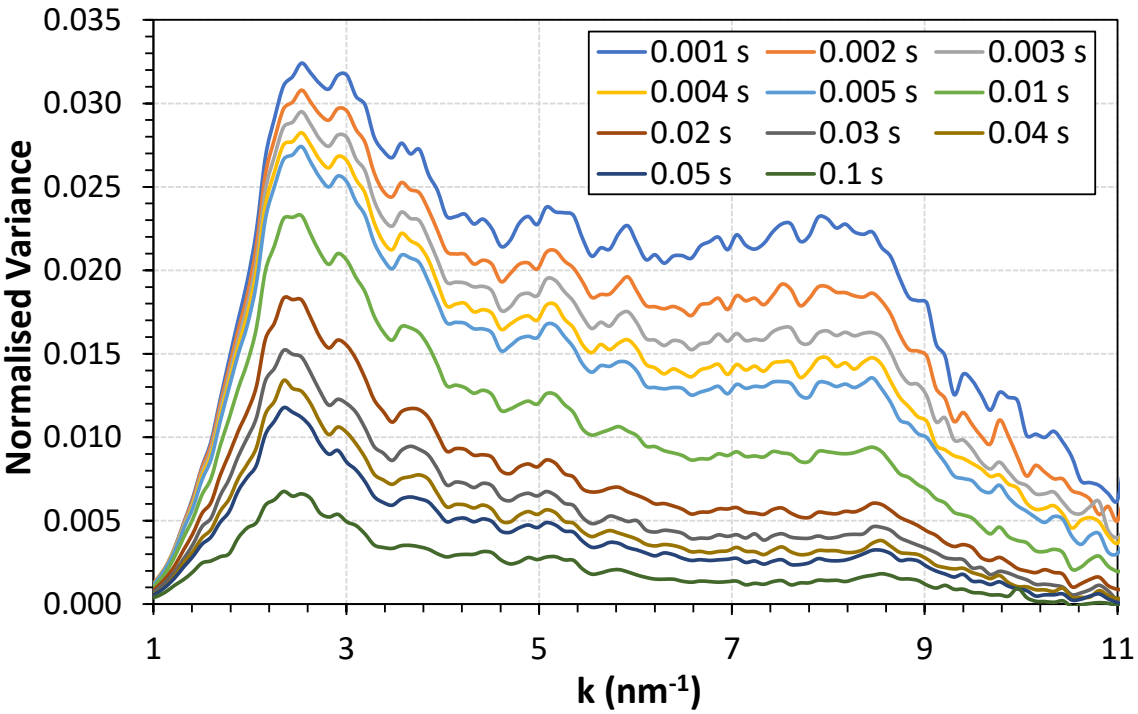

Figure 5.11: Normalised variance obtained from diffraction patterns at the SiO_2 substrate using 1 ms exposure time. Variance curves from the summed diffraction patterns over eleven different timeframes are shown.

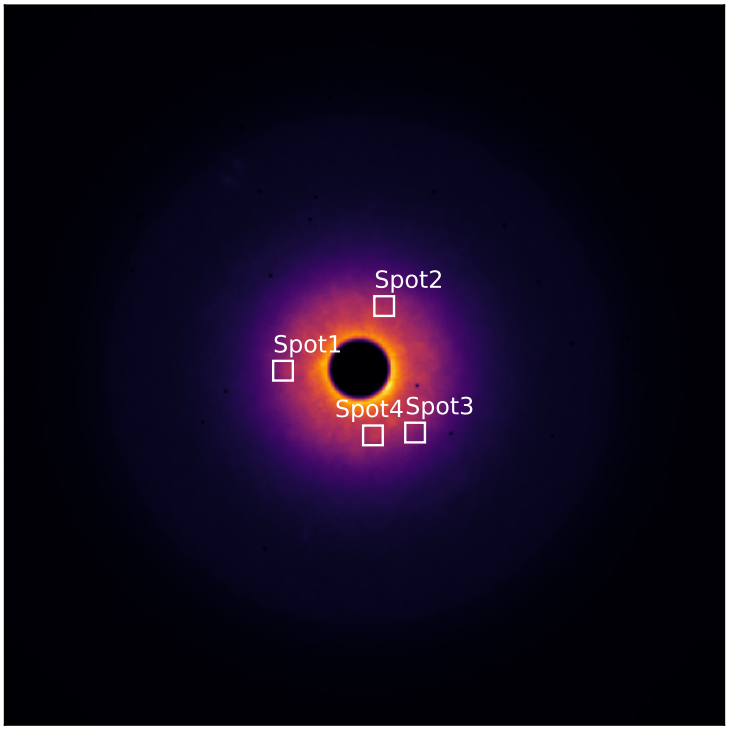

Figure 5.12: Sum of all 1000 DPs from the SiO_2 substrate of the $NbSi_x$ film, showing selected diffraction spots.

Table 5.2: Analysis of the FWHM of intensity peaks from four spots in the DPs obtained from the SiO_2 substrate of the $NbSi_x$ film using a 1 ms exposure time.

Spot	**Number of peaks**	**FWHM (Mean) ms**	**FWHM (σ) ms**
1	5	17.8	3.3
2	4	23.5	6.9
3	4	16.3	4.8
4	7	17.5	5.2

The differences between DPs at 175 ms intervals is shown in Figure 5.15, nearly all of the differences in intensity occur within the circular region surrounding the central spot, although there are some positioned further away. It is apparent from this that there are speckles in the 500 ms DP that are not seen in the four other DPs, these can be seen in the red areas in the 125 ms, 325 ms, 675 ms and 850 ms difference plots, while the blue areas indicate diffraction speckles that are not present in the 500 ms DP. Figures 5.16,5.18 show the differences in the DPs that are adjacent to each other, there is much less difference in these images. While Figure 5.16 does not show any strong diffraction speckles, there are some present in Figure 5.18. One speckle to the left of the beam decreases in intensity as time increases, while simultaneously there is a speckle above and slightly to the right of the beam that is increasing in intensity.

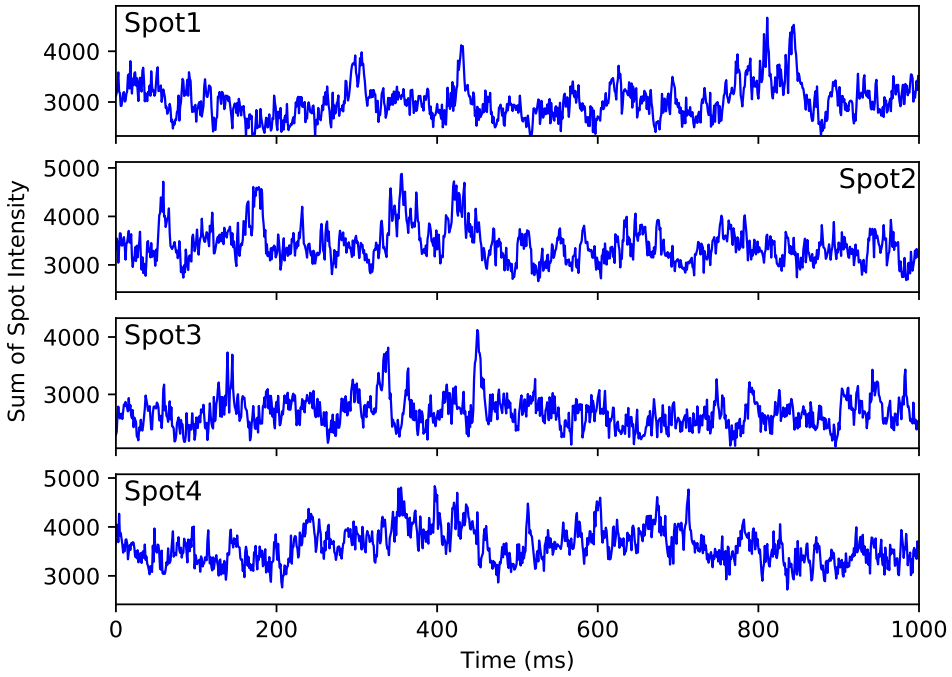

Figure 5.13: Line plots of the summed intensity within each of the four spots as a function of time.

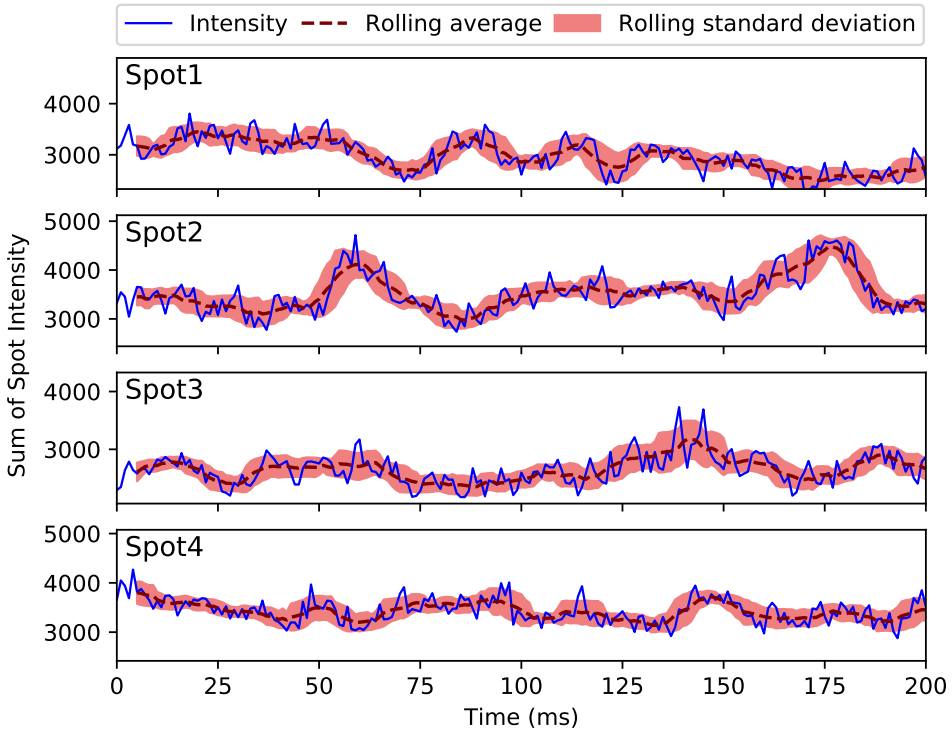

Figure 5.14: Plots of the summed intensity for the first 200 ms of the dataset within each of the four spots. A rolling average and standard deviation from a window 11 patterns wide are overlaid.

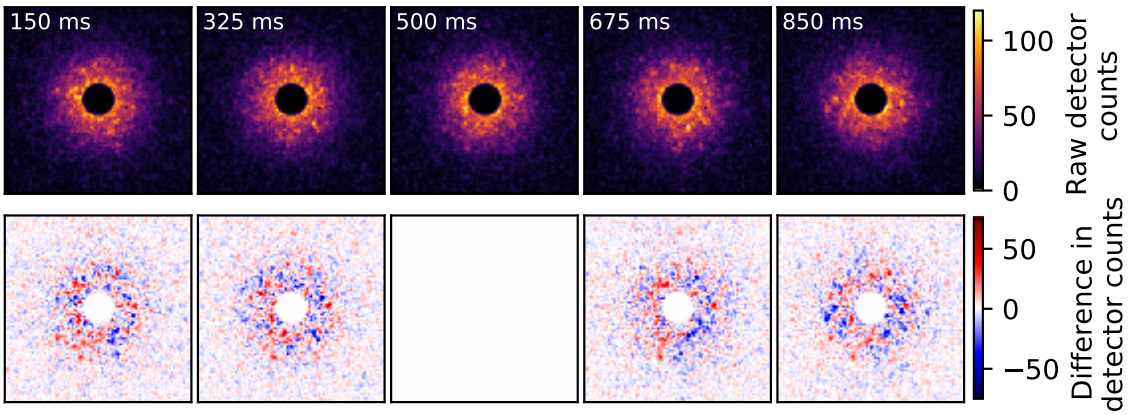

Figure 5.15: This figure shows five DPs obtained with an exposure time of 1 ms from the SiO_2 substrate of the $NbSi_x$ layer. These are spread at 175 ms intervals through the dataset. The top row shows the DPs, while the bottom row shows the absolute difference in intensity (detector counts) between the central DP in the top row and the DP directly above it.

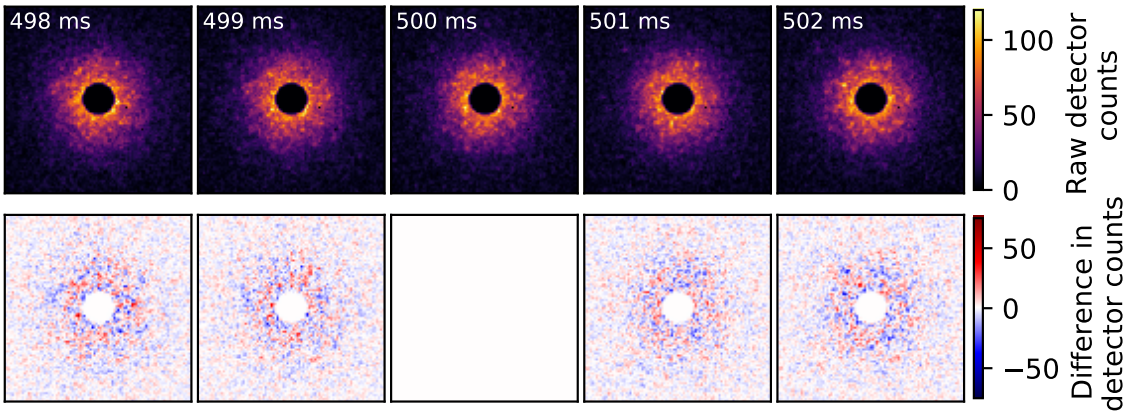

Figure 5.16: This figure shows five consecutive DPs obtained with an exposure time of 1 ms from the SiO_2 substrate of the $NbSi_x$ layer. The top row shows the DPs, while the bottom row shows the absolute difference in intensity (detector counts) between the central DP in the top row and the DP directly above it.

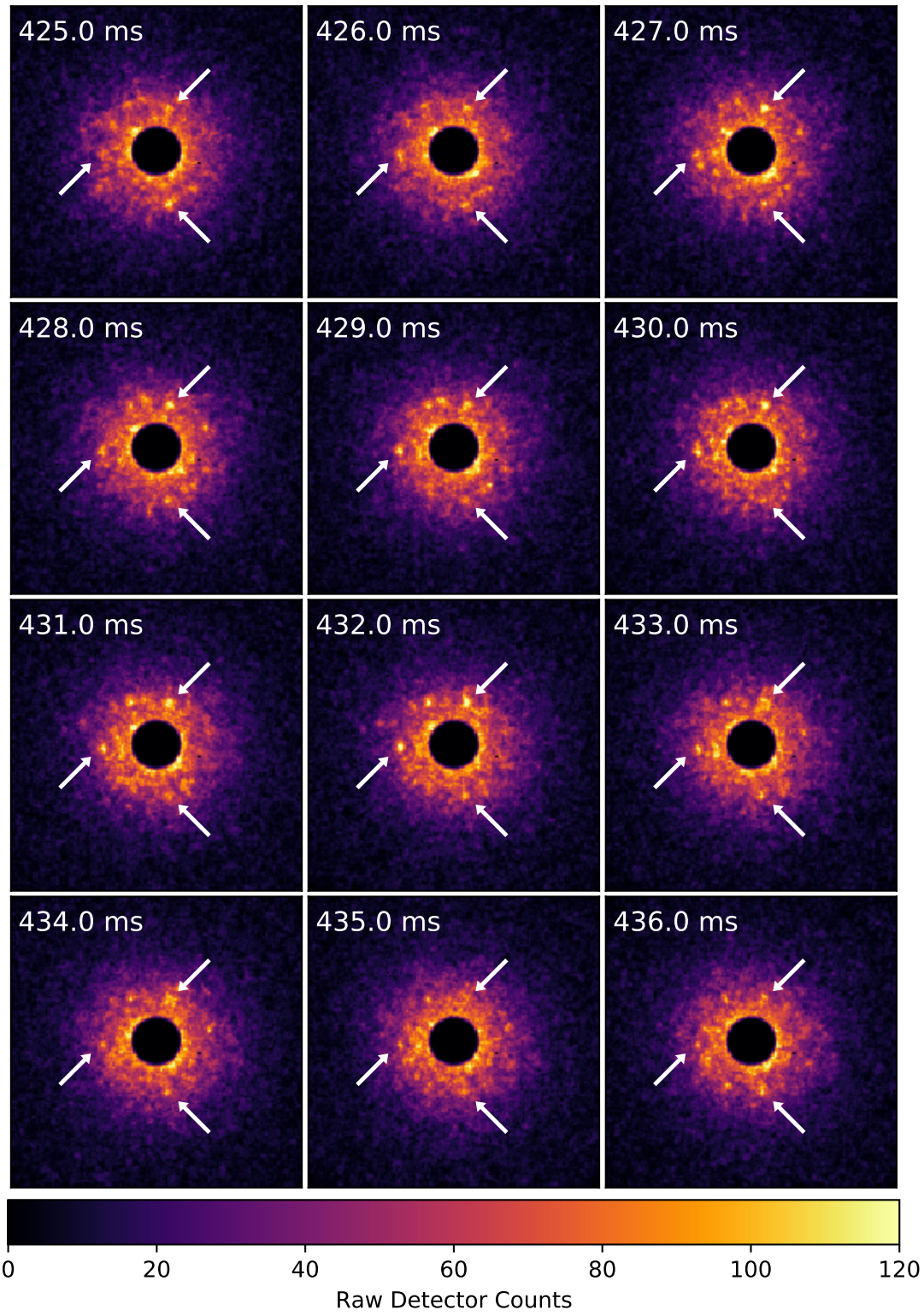

Figure 5.17: DPs obtained from the SiO_2 substrate of the $NbSi_x$ film using an exposure time of 1 ms. This figure shows twelve consecutive patterns taken from the dataset. Arrows show some features that are present to some extent in the all of the patterns shown.

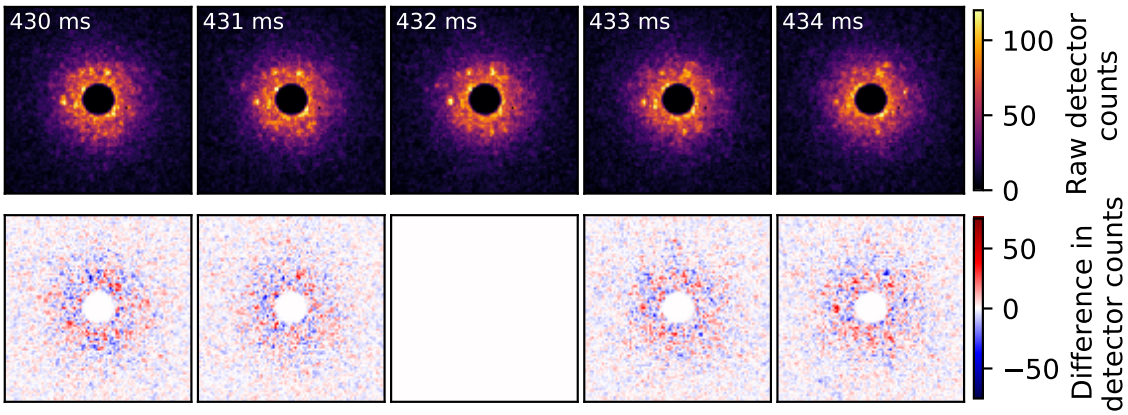

Figure 5.18: This figure shows five consecutive DPs obtained with an exposure time of 1 ms from the SiO_2 substrate of the $NbSi_x$ layer. The top row shows the DPs, while the bottom row shows the absolute difference in intensity (detector counts) between the central DP in the top row and the DP directly above it.

5.6 Time Variation Using 21.6 ms Exposure Time

5.6.1 $NbSi_x$ 21.6 ms Exposure

While still using the same sample as previously with the 1 ms exposure, all the other experimental parameters are different for this set of data. An exposure time of 21.6 ms was used, and 500 DPs were collected, so that the overall dataset time was 10.79 s.

Probe size was decreased to 1 nm, with a corresponding increase in semi-convergence angle. In addition to this, there was an increased probe current. The increase in semi-convergence angle means that the DPs look considerably different to those shown in the previous subsection, as the diffraction speckles are noticeably larger. Figure 5.19 shows twelve DPs spread through the dataset, an arrow on each of the DPs indicates one of the speckles that appears consistently throughout all twelve images. It is noticeable that there are some bright speckles that are not consistent through the dataset. It appears that this sample changes more under the experimental conditions used here, however it should be noted that the total exposure time of the beam on the sample is more than 10 times higher than in the previous subsection.

Consecutive DPs as shown in Figure 5.20, do not appear to show that there is any significant change in the structure of the material over these 21.6 ms intervals. There are only slight changes to the DP between 0 ms and 237.4 ms.

Figure 5.21 shows the normalised variance curves obtained from this dataset, alongside the spatial variance calculated previously. The variance here is significantly higher than what was seen in the dataset with 1 ms exposure time. At the main spatial variance peak there is only a very small peak in the variance, the temporal variance also does not show peaks at the other peak positions in the spatial variance. As expected, the temporal variance decreases as the virtual exposure time increases.

Next we looked at the intensity of selected spots in the DP as shown in Figure 5.22, where the boxes are 8 pixels in diameter. It is shown that there are significant changes to the intensity of these spots in Figure 5.23. These are much more obvious than those shown earlier for the 1 ms exposure time in Figure 5.5. This is another indicator that much more structural change is evident here than shown in the previous subsection. A rolling average of spot intensity was calculated over a window of 5 DPs, a section of this rolling average is shown in Figure 5.24. Again nearly all of the intensity fits within 1 σ of the intensity rolling mean. Analysis of the FWHM of the peaks in intensity of each spot was carried out, with results shown in Table 5.3.

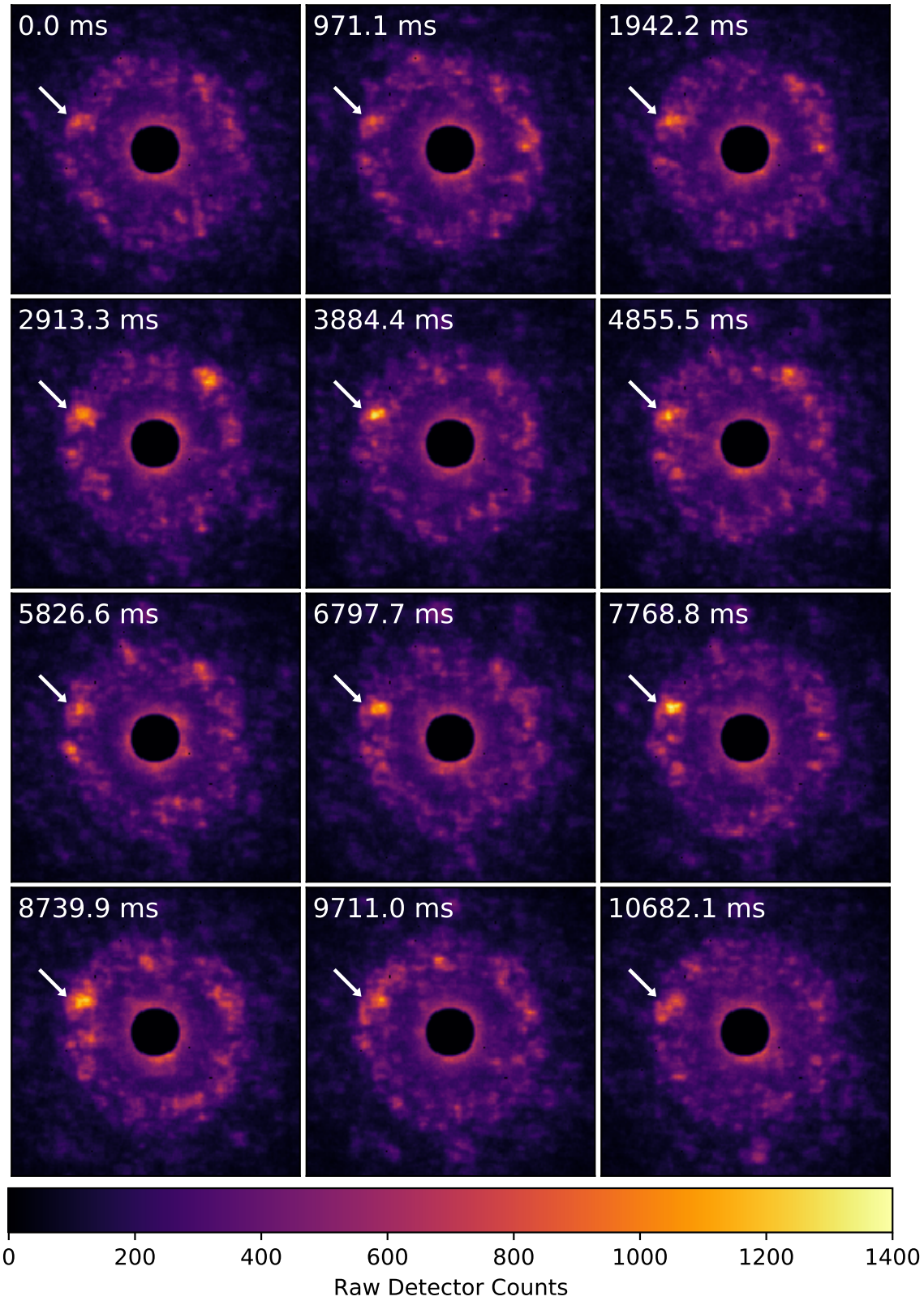

Figure 5.19: DPs obtained from the $NbSi_x$ film using an exposure time of 21.6 ms. This figure shows patterns taken from the dataset at regular 971.1 ms intervals. Arrows are pointing to features that are present in each of the DPs shown.

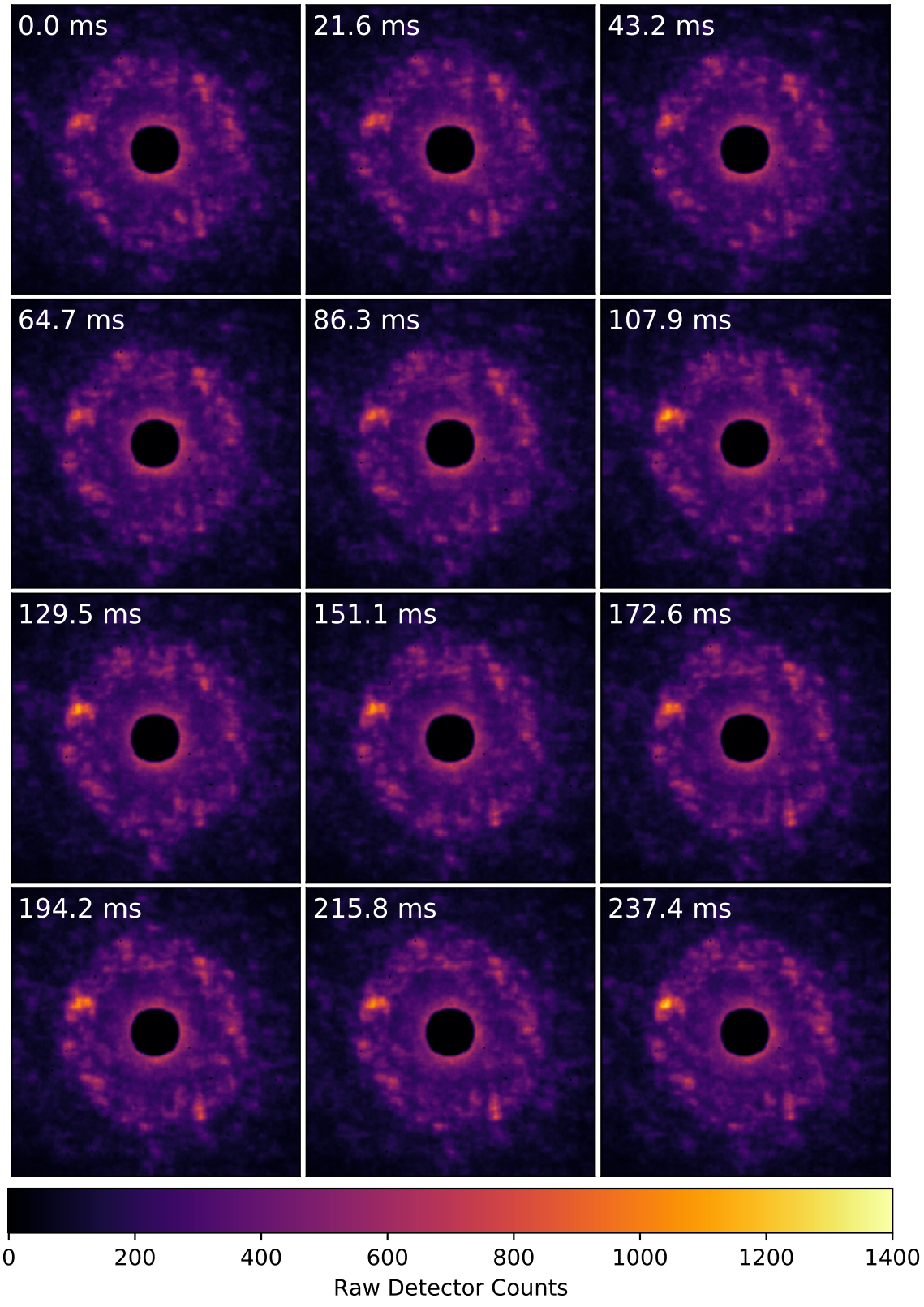

Figure 5.20: DPs obtained from the $NbSi_x$ film using an exposure time of 21.6 ms. This figure shows twelve consecutive patterns taken from the dataset.

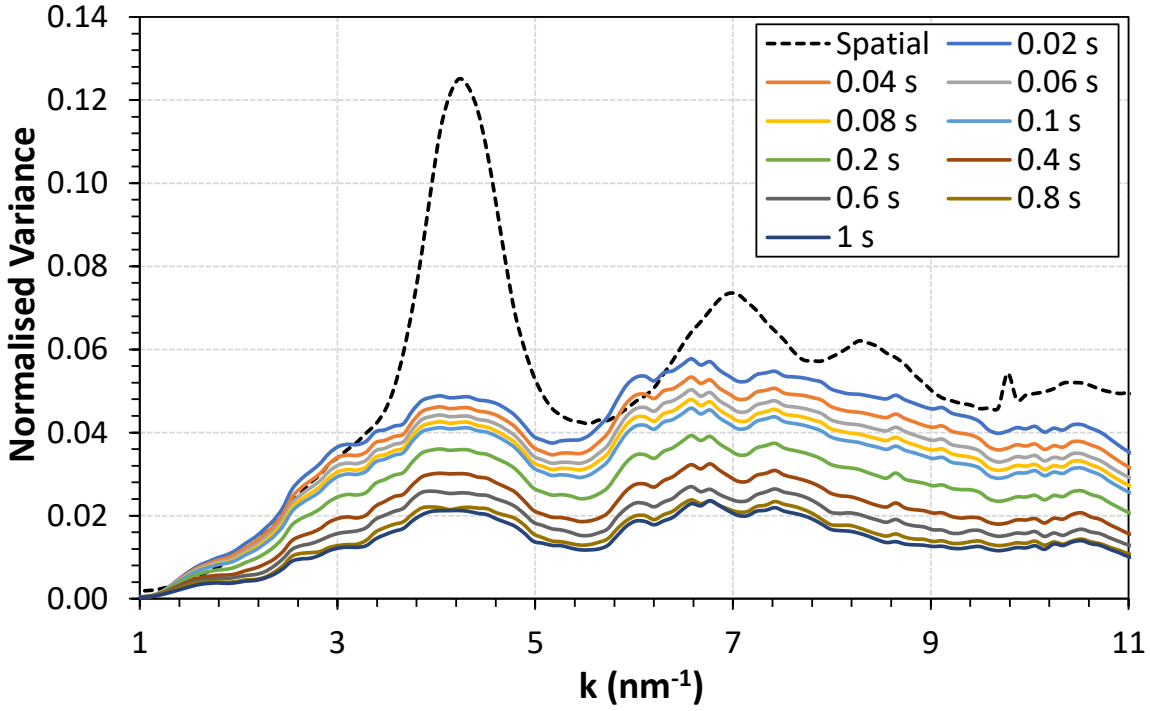

Figure 5.21: Normalised variance obtained from the $NbSi_x$ diffraction patterns at 21.6 ms exposure time. Variance curves from the summed diffraction patterns over ten different timeframes are shown.

Table 5.3: Analysis of the FWHM of intensity peaks from four spots in the DPs obtained from the centre $NbSi_x$ film using a 21.6 ms exposure time.

Spot	**Number of peaks**	**FWHM (Mean) ms**	**FWHM (σ) ms**
1	0	NA	NA
2	3	163.7	50.4
3	1	109.9	NA
4	2	158.6	19.7

Inspection of the difference in intensity between DPs shows some interesting results. Differences over a longer timescale are shown in Figure 5.25, this shows that there are a lot of changes occurring in the speckle pattern, these mostly occur within the main diffuse ring, while there are also areas in the rings further from the central beam. Changes between consecutive DPs are much smaller and are shown in Figure 5.26. One thing that is immediately apparent is that the DP starts to show noticeable differences over a timescale as small as 43.6 ms. Difference plots over increments of 2158 ms, as were shown in Figure 5.25, generally show that differences remain fairly similar as the time difference from the reference pattern increases. There are however areas where the differences invert over the larger time interval. This does not appear to be the

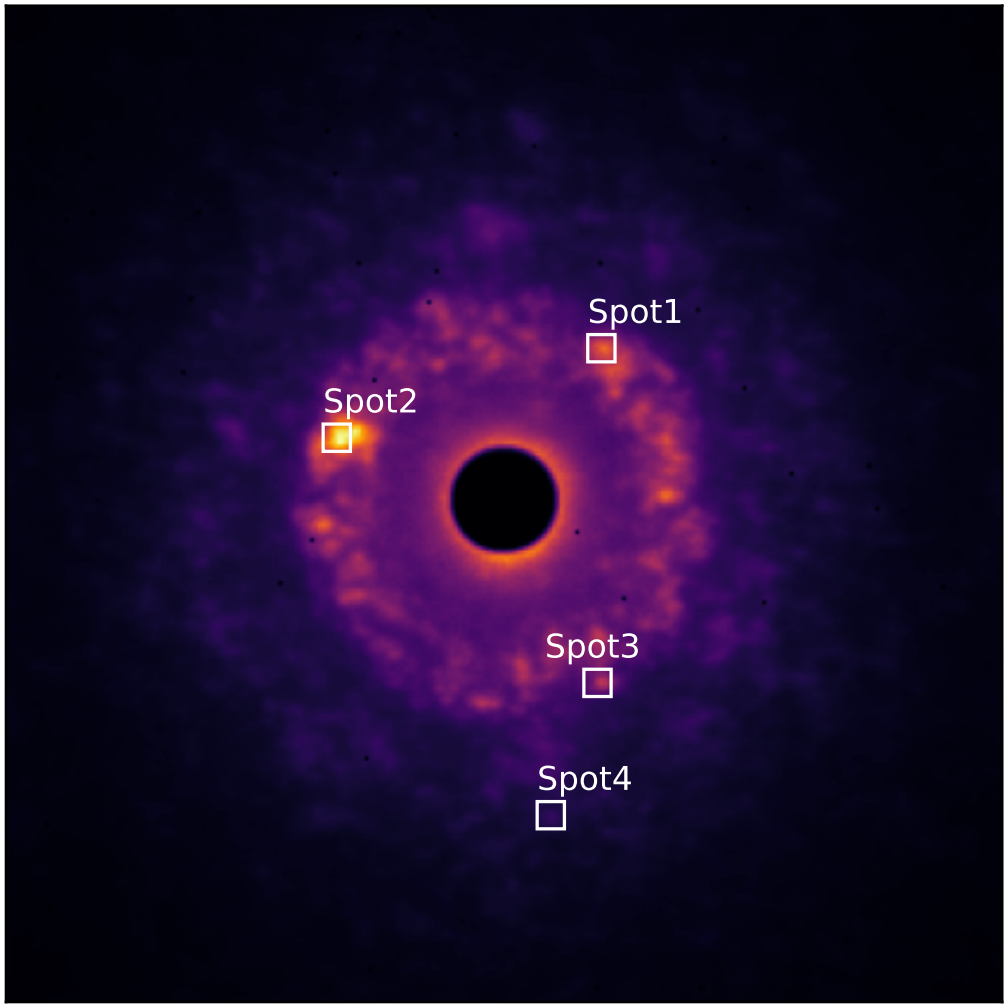

Figure 5.22: Sum of all 500 DPs from the $NbSi_x$ film, showing selected diffraction spots.

case over the shorter time intervals seen in Figure 5.25, where differences are nearly all increases to previous differences as you move further from the reference pattern.

Results from the previous dataset (Figure 5.8, 1 ms exposure time) showed what appeared to be large shot noise contributions to the differences between patterns. Using a larger exposure time, in this case 21.6 ms appears to significantly decrease this effect. Differences between adjacent diffraction patterns are now mostly within the diffuse ring and result from differences in intensity from speckles, and as such are therefore arising from real structural changes, which are no longer obscured by detector shot noise.

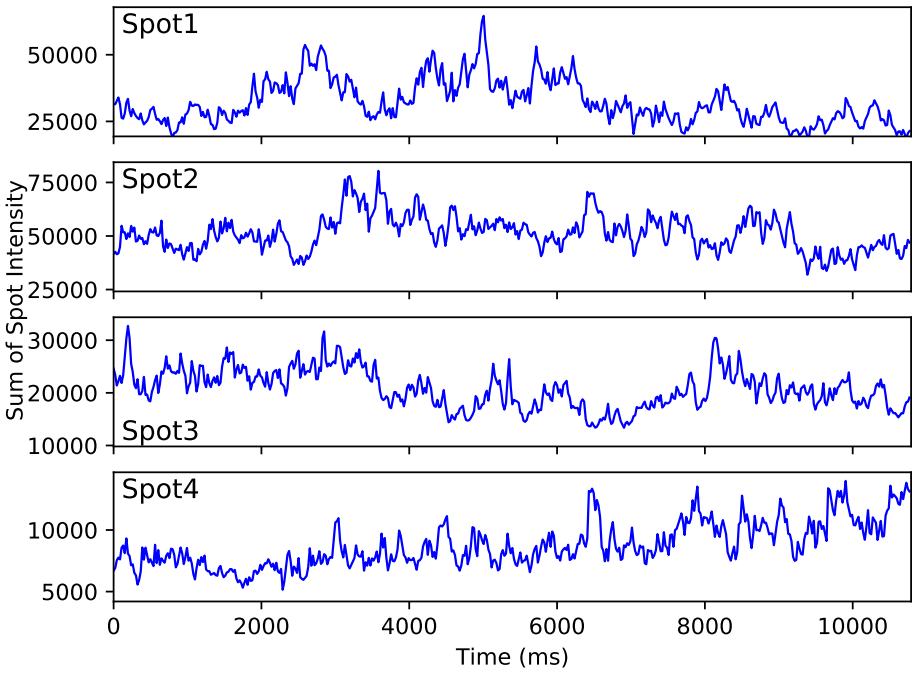

Figure 5.23: Line plots of the summed intensity within each of the four spots as a function of time.

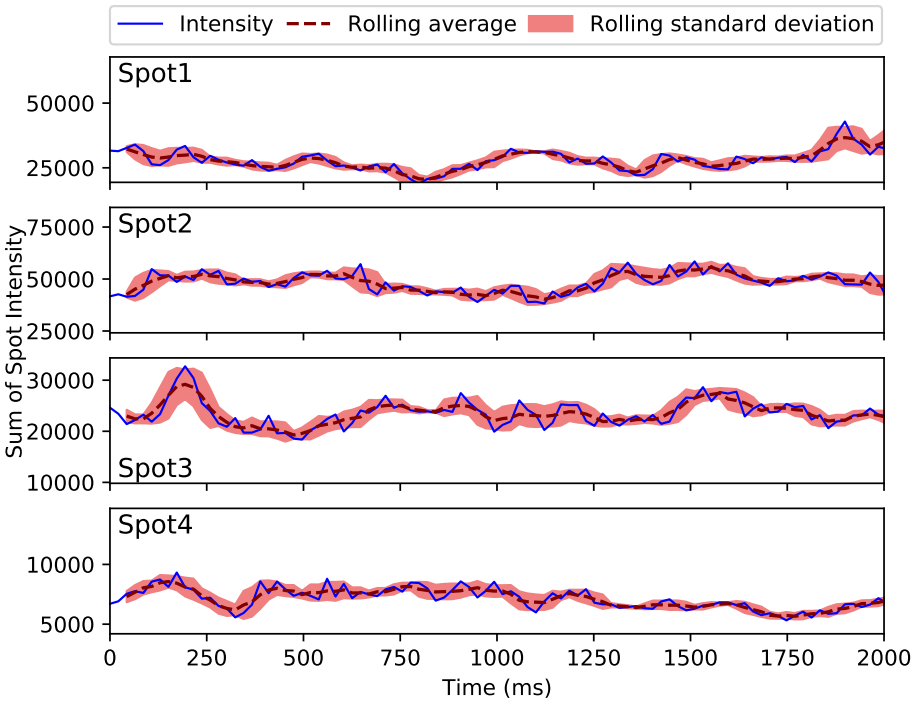

Figure 5.24: Plots of the summed intensity for the first 2000 ms of the dataset within each of the four spots. A rolling average and standard deviation from a window 5 patterns wide are overlaid.

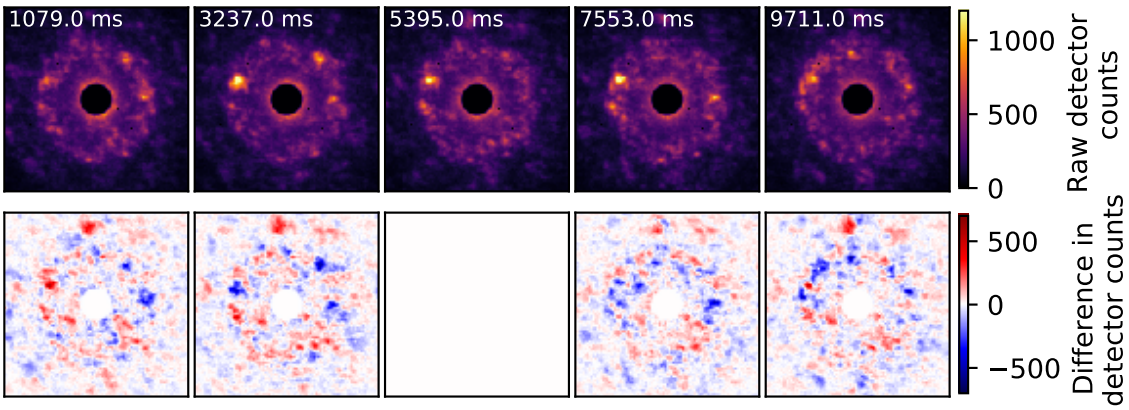

Figure 5.25: This figure shows five DPs obtained with an exposure time of 21.6 ms from the $NbSi_x$ layer. These are spread at 2158 ms intervals through the dataset. The top row shows the DPs, while the bottom row shows the absolute difference in intensity (detector counts) between the central DP in the top row and the DP directly above it.

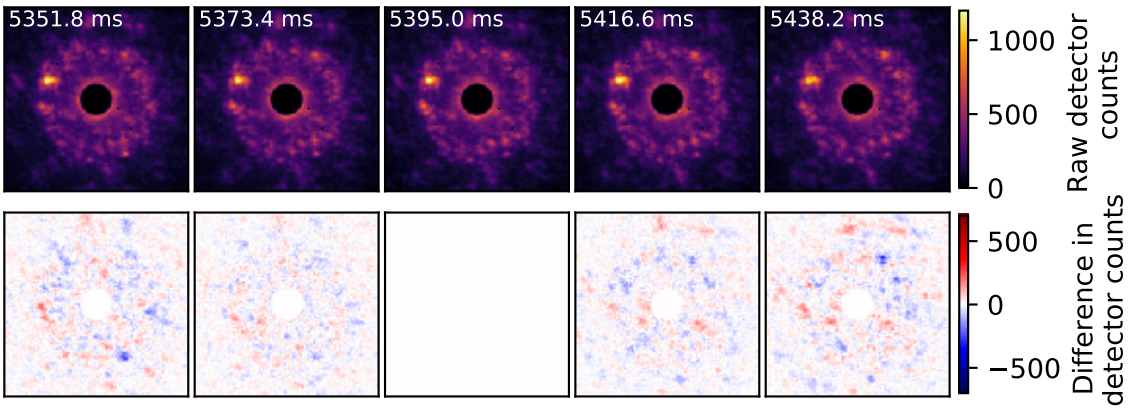

Figure 5.26: This figure shows five consecutive DPs obtained with an exposure time of 21.6 ms from the $NbSi_x$ layer. The top row shows the DPs, while the bottom row shows the absolute difference in intensity (detector counts) between the central DP in the top row and the DP directly above it.

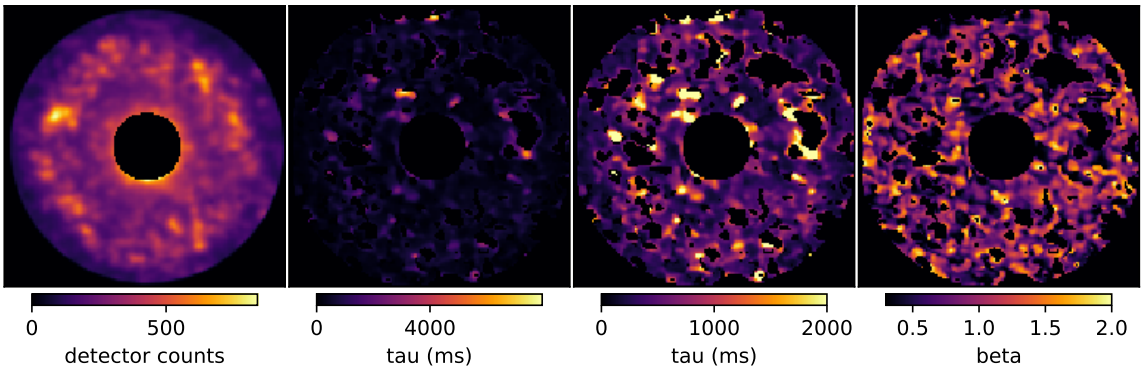

Figure 5.27: Images of the masked version of the first $NbSi_x$ diffraction pattern in the dataset, along with the τ and β values calculated from each pixel. Two different images of τ are shown, with both the full range as well as the detail at the lower end (0-2000 ms) of the τ range.

Results of the non-linear least squares fitting of Equation 5.4 to each pixel of the $NbSi_x$ diffraction dataset is shown in Figure 5.27. Most of the pixels show a τ value less than 2000 ms, while there are some small regions that have a much higher τ, including some that are up to around 8000 ms. In some areas the quality of the fit was too low and so they were ignored, these areas are most easily visible in the map of β.

Figure 5.28a,b,c shows the results of curve fitting to individual pixels from speckles within the $NbSi_x$ diffraction pattern, alongside a histogram (Figure 5.28d) showing the τ distribution obtained from the masked dataset. The histogram shows a wide spread of τ values, with the most common between 200-400 ms, though there is a long tail to the distribution and the mean value is 581 ms.

A fit to the average of $g_2(t)$ obtained from an annular range around the main diffraction peak is shown in Figure 5.28e, alongside histograms of the values of τ and β calculated from each pixel in that region (Figure 5.28f. The averaged $g_2(t)$ results in a τ value of 826 ms and stretching parameter β of 0.73, while the mean τ and β values from the fits to the individual pixels are 717 ms and 0.9 respectively. There is a noticeable difference in the τ distribution found in the annular ring (Figure 5.28f) to that from the whole masked diffraction pattern (Figure 5.28d), where it is shifted to higher τ if only the values calculated from the region around the first diffraction peak are shown. Overall the annular region has a τ of around 800 ms with β around 0.7, which is reproduced in individual speckles. There are also long lived speckles that are very different with τ over 2 s and up to 8 s and with a lower β, around the 0.5-0.6 range.

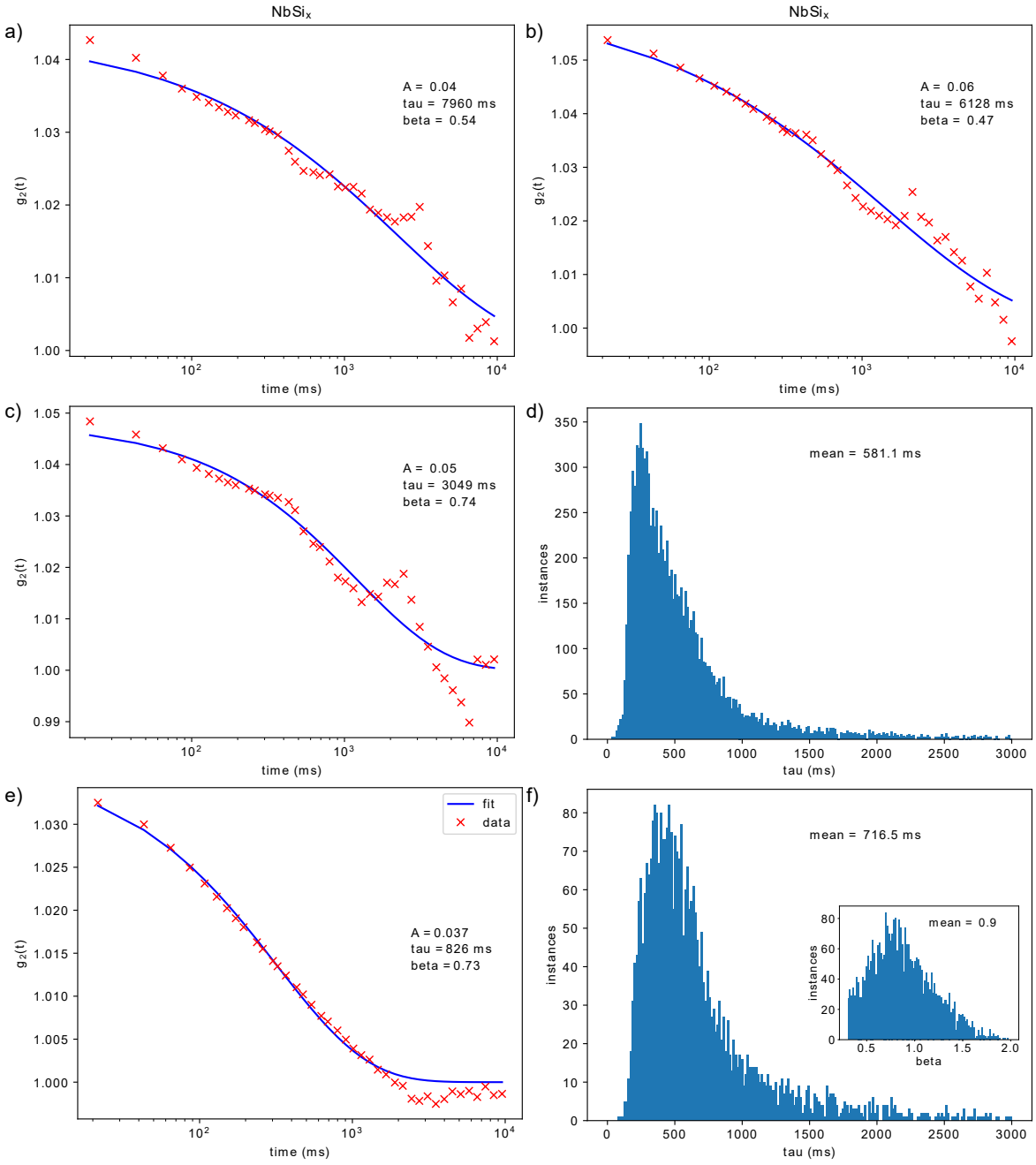

Figure 5.28: a), b) and c) show examples of non-linear least squares KWW fitting to $g_2(t)$ from pixels in the $NbSi_x$ diffraction patterns. d) shows a histogram of the wide distribution of τ values calculated from all of the pixels in the masked pattern. Results from the annular masked region are shown in e) KWW fit to average of each pixels $g_2(t)$ and f) histograms of τ and β calculated from each pixel.

5.6.2 Ti:Ta_2O_5 21.6 ms Exposure

Now a different sample is examined, the Ti:Ta_2O_5 layer from the A-LIGO multilayer high reflectivity mirror coating as discussed earlier in section 5.2. As the thickness of the layers are $\lambda/4$ to maximise reflectivity, the layer thickness is approximately 266 nm, although in practice the layer is slightly thinner.[220] This dataset used a probe size of 2 nm, positioned in the centre of a Ti:Ta_x2O_5 layer, and a smaller probe current of 4.3 pA. 500 DPs were collected, each with an exposure time of 21.6 ms.

DPs through the dataset are shown in Figure 5.29, these show that there is a diffuse inner ring containing some brighter diffraction speckles, and two outer rings that are very close together. While there are features that remain present in some capacity throughout the dataset, these change in their intensity significantly. An arrow indicates the position of a speckle that is present throughout most of the dataset. These changes in intensity are also fairly obvious when looking at twelve consecutive DPs as shown in Figure 5.30.

Variance curves from this dataset are shown in Figure 5.31, there are peaks in the temporal variance in roughly the same positions that they are found in the spatial variance.

Boxes 8 pixels in diameter surrounding diffraction spots are shown in Figure 5.32. As before these indicate areas from which the intensity as a function of time is plotted in Figure 5.33. Spot1 decreases in intensity throughout the dataset, with a few peaks of around 500 ms scattered throughout. Spot1, Spot2 and Spot3 all show increases and decreases in intensity over a longer timescale. Spot2 starts high, then decreases until around 3000 ms before increasing until around 5000 ms, following that it drops until 6000 ms, after which it increases steadily. Spot3 starts at lower intensity then between 2000 ms and 4500 ms remains at a higher intensity before dropping until 5000 ms, where it remains at a fairly consistent intensity before it starts slowly increasing at 9000 ms. Rolling averages of the intensity created using a 5 DP window are shown in Figure 5.34. In this case, no suitable peaks were found in the plot, so it was not possible to calculate the mean FWHM of intensity in each spot.

Differences between DPs at 2158 ms intervals are shown in Figure 5.35, where the largest differences are mainly found in the first diffraction ring, while there are also some found in the outer two diffraction rings also. There is an interesting feature persistent in all four difference images, this can be seen in where there is a red spot below and slightly to the right of the central beam, outside the main diffracted ring. This is the result of a diffraction speckle present in the central pattern that is not present in the other four. It is also visible that the speckle from Spot3 increases in

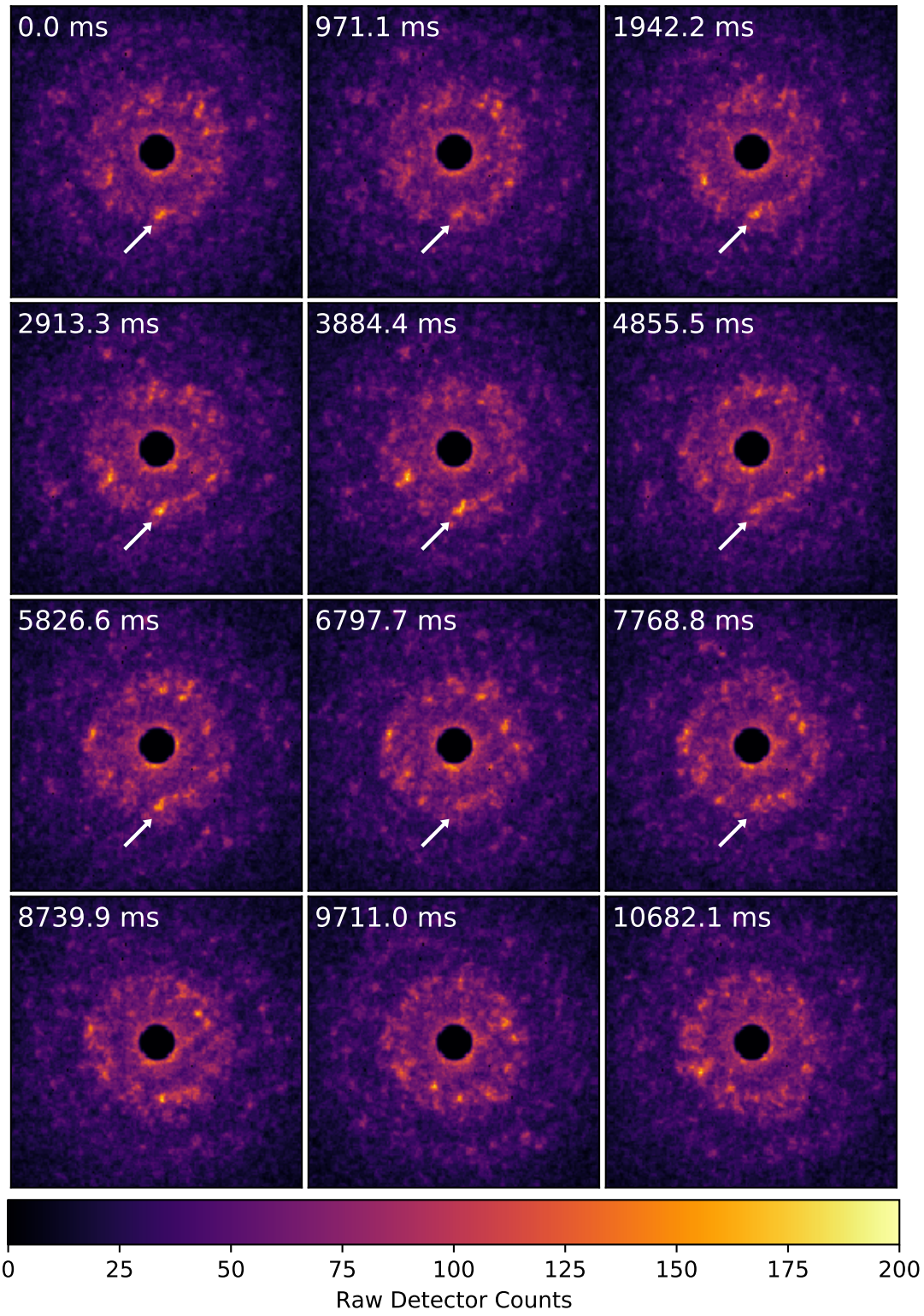

Figure 5.29: DPs obtained from the Ti:Ta_2O_5 film layer using an exposure time of 21.6 ms. This figure shows patterns taken from the dataset at regular 971.1 ms intervals. Arrows are pointing to features that are present to some extent in all of the patterns shown.

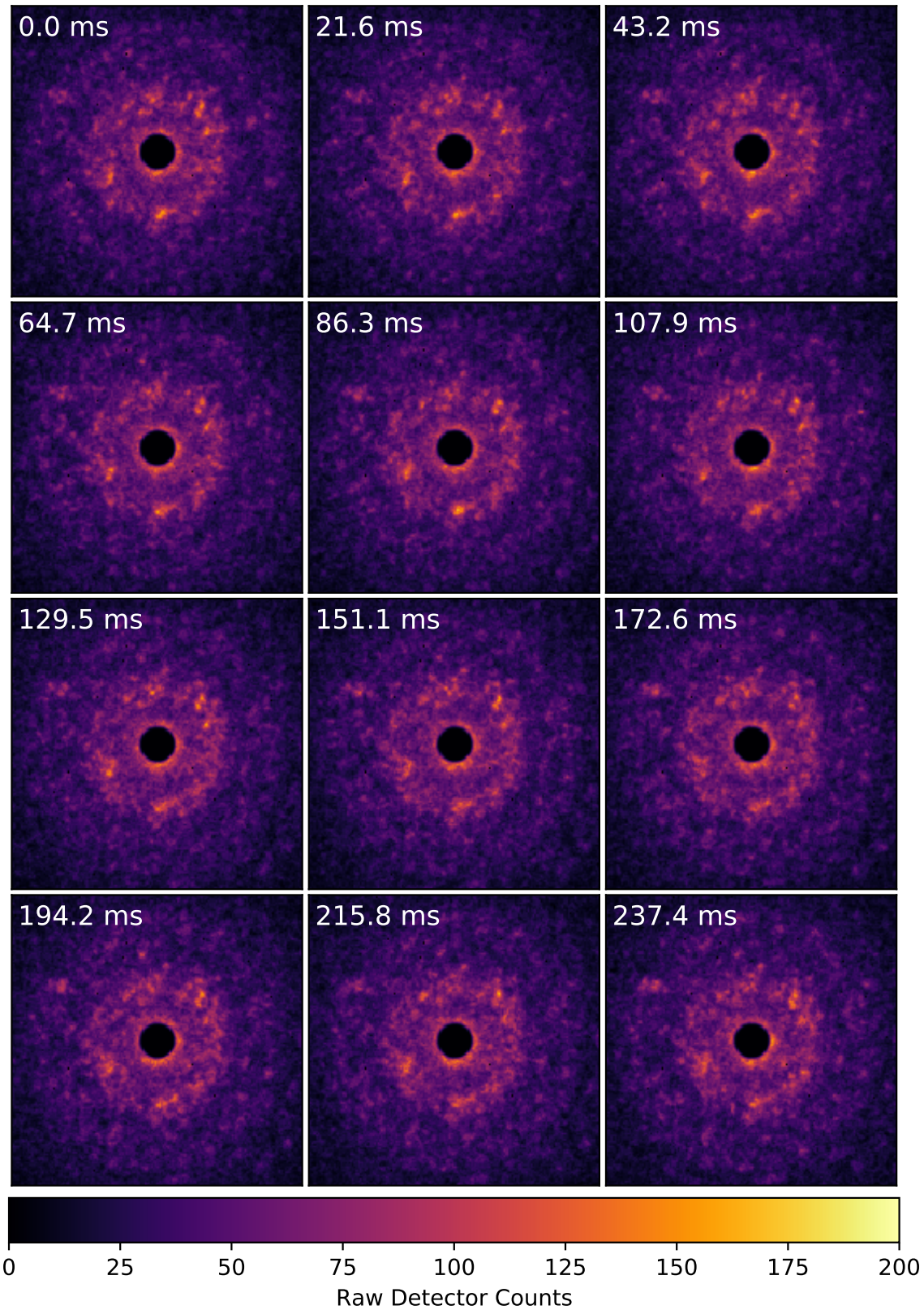

Figure 5.30: DPs obtained from the Ti:Ta_2O_5 film layer using an exposure time of 21.6 ms. This figure shows twelve consecutive patterns taken from the dataset.

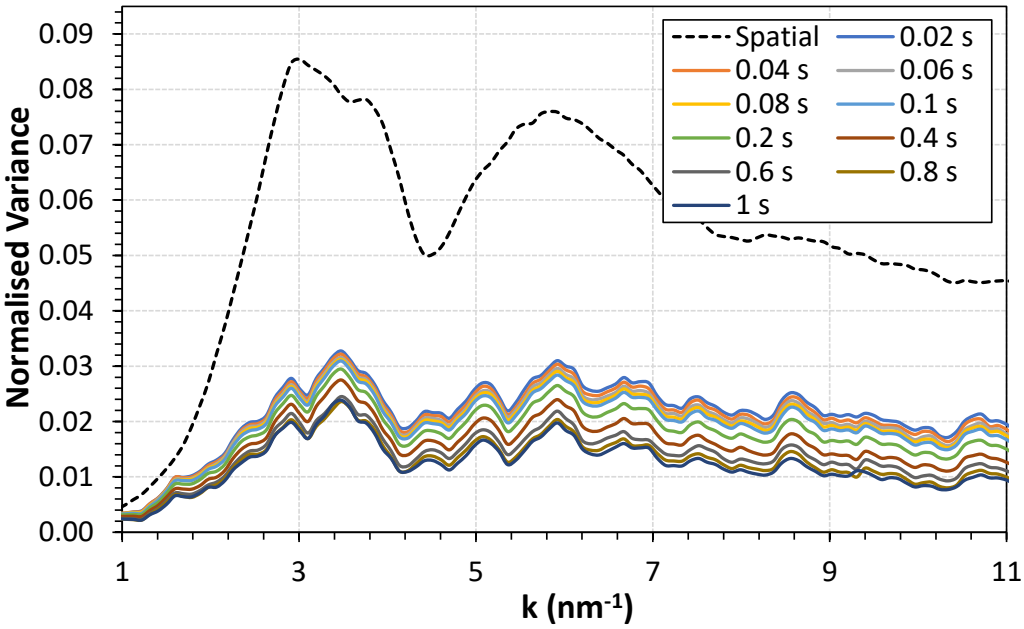

Figure 5.31: Normalised variance obtained from the Ti:Ta_2O_5 diffraction patterns at 21.6 ms exposure time. Variance curves from the summed diffraction patterns over ten different timeframes are shown.

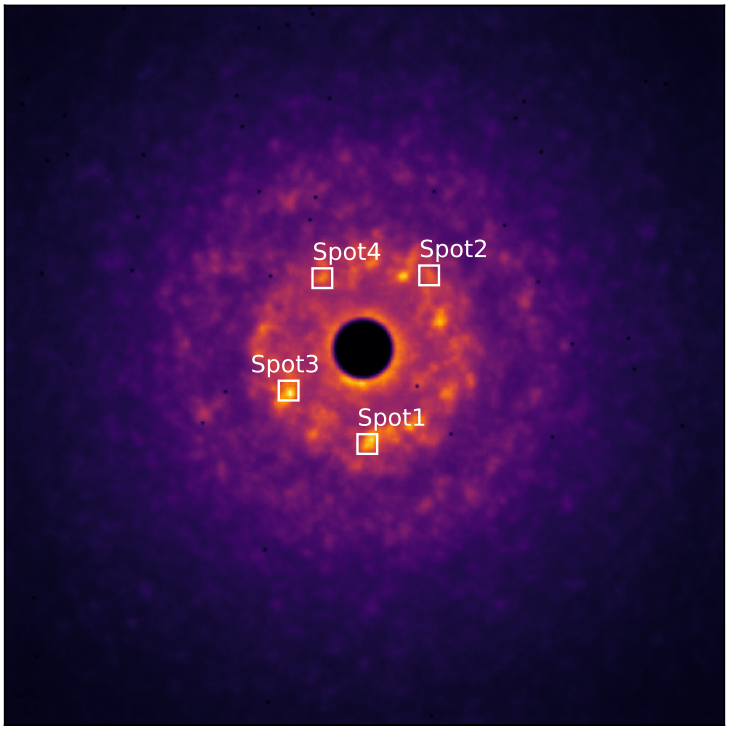

Figure 5.32: Sum of all 500 DPs from the Ti:Ta_2O_5 film, showing selected diffraction spots.

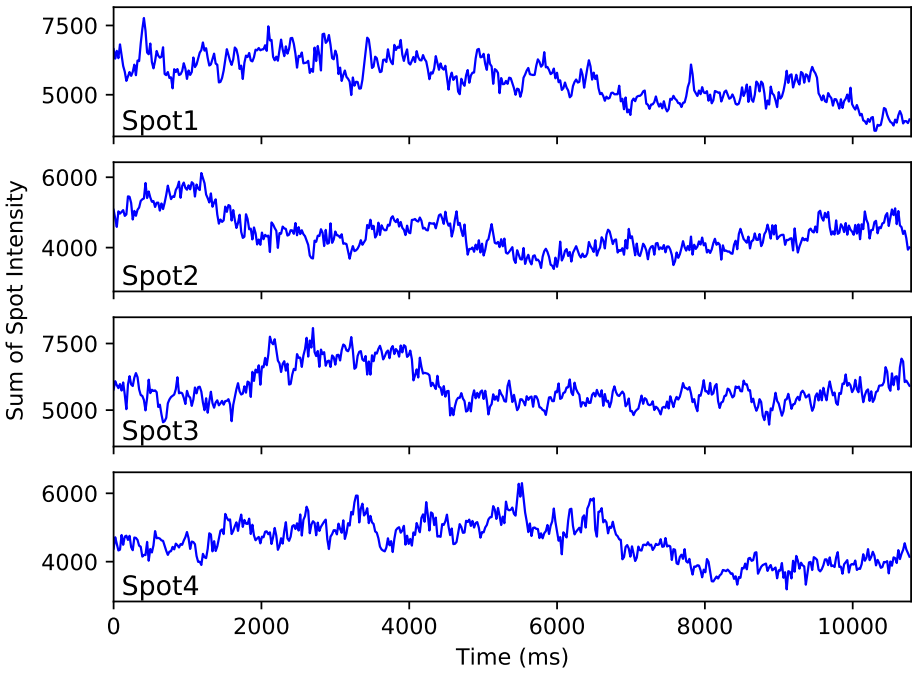

Figure 5.33: Line plots of the summed intensity within each of the four spots as a function of time.

intensity from 5395.0 ms to 3237.0 ms, but then when the DP a further 2158 ms further back (1079.0 ms) is shown, it has decreased in intensity. The way that this intensity change happens could indicate that the ordered region corresponding to that diffraction speckle becomes more ordered, then decreases in order. Figure 5.36 shows the differences between adjacent DPs. As expected there are only small changes in intensity between adjacent DPs, these are mostly found within the principal diffuse diffraction rings.

Figure 5.37 shows the first diffraction pattern in the masked Ta_2O_5 dataset, as well as the τ and β values calculated from the $g_2(t)$ of each pixel in the DP. A majority of the pixels show τ of less than 1000 ms, while there are some areas which are above 10,000 ms.

It was difficult to obtain a good fit to this dataset, Figure 5.38a, b, c shows a set of three KWW fits to $g_2(t)$ from individual pixels, only b has a particularly good fit. Figure 5.38d shows a histogram of the values of τ calculated from each pixel, where there is a peak around 800-1000 ms, overall the mean value of τ was 1728 ms.

When the annular mask is applied around the main diffraction peak and the average $g_2(t)$ is calculated, the KWW fit is not that good, as seen in Figure 5.38e, where τ of 2366 ms and β of 1.19 was calculated. Histograms of the distribution of τ and β from the pixels contained in the annular region show a mean τ of 2045 ms and β of 1.04. In general τ is longer than in the $NbSi_x$ film, at around 2400 ms, β is slightly higher at

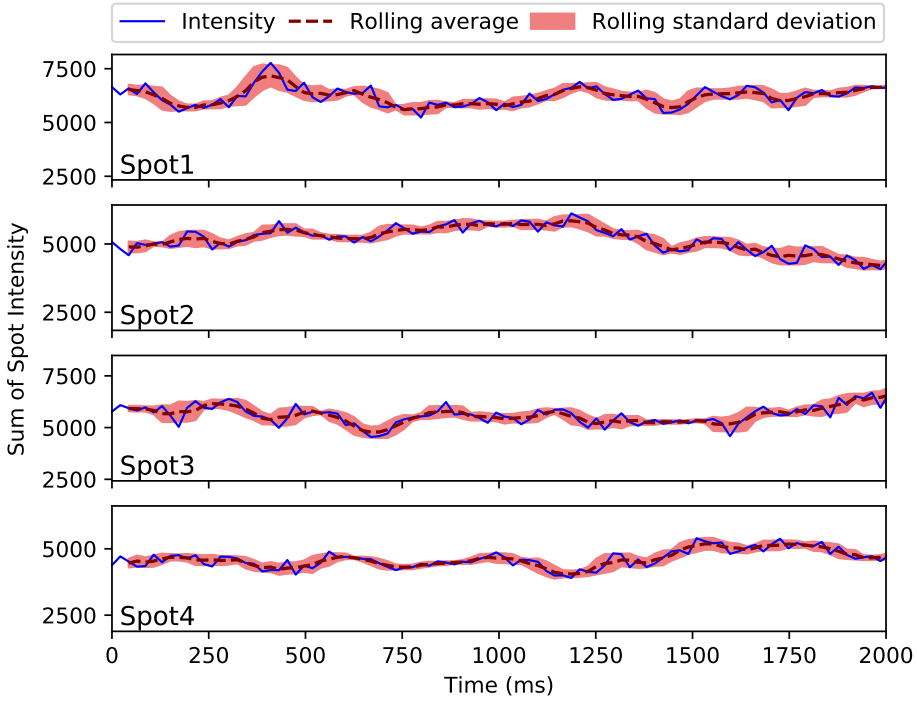

Figure 5.34: Plots of the summed intensity for the first 2000 ms of the dataset within each of the four spots. A rolling average and standard deviation from a window 5 patterns wide are overlaid.

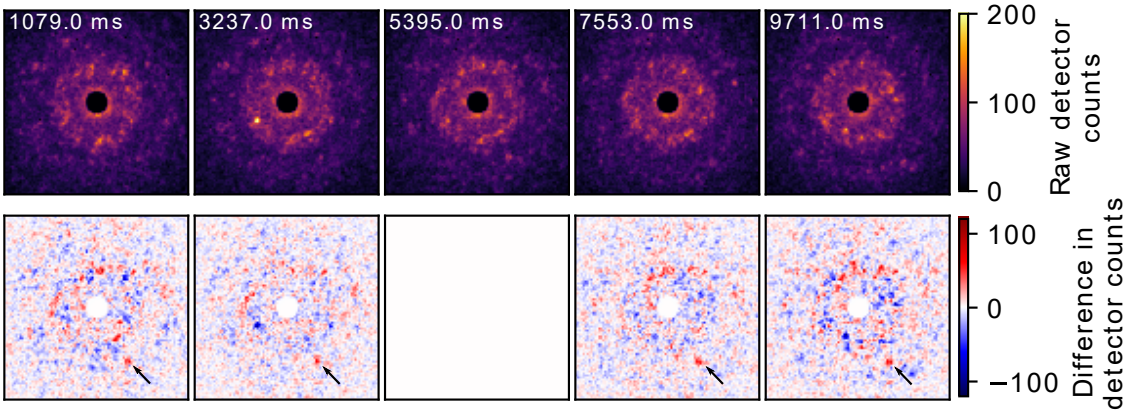

Figure 5.35: This figure shows five DPs obtained with an exposure time of 21.6 ms from the Ti:Ta_2O_5 film layer. These are spread at 2158 ms intervals through the dataset. The top row shows the DPs, while the bottom row shows the absolute difference in intensity (detector counts) between the central DP in the top row and the DP directly above it.

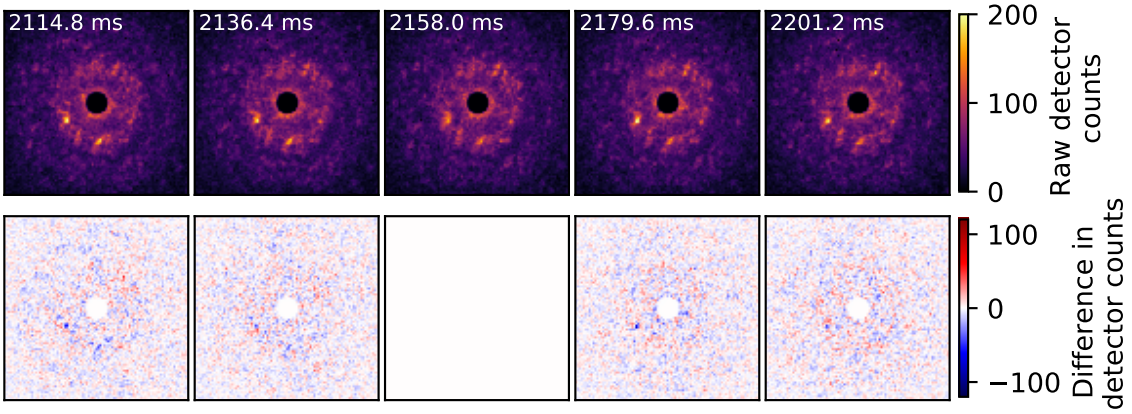

Figure 5.36: This figure shows five consecutive DPs obtained with an exposure time of 21.6 ms from the Ti:Ta_2O_5 film layer. The top row shows the DPs, while the bottom row shows the absolute difference in intensity (detector counts) between the central DP in the top row and the DP directly above it.

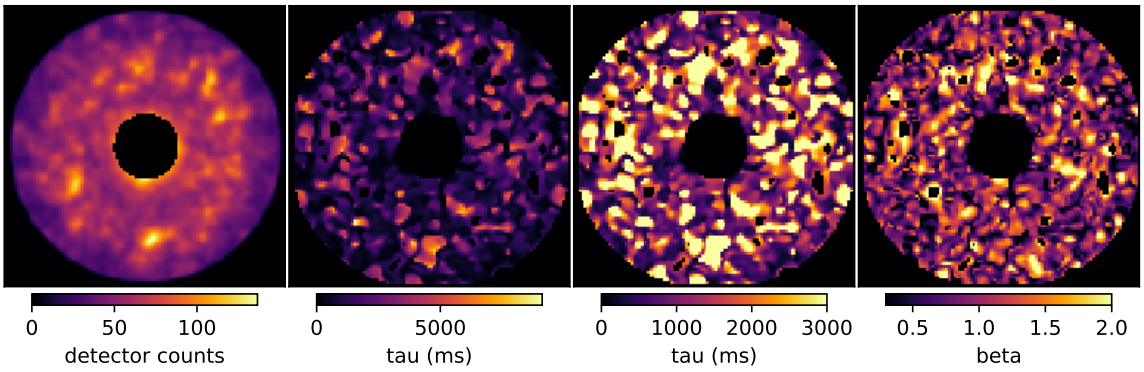

Figure 5.37: Images showing the masked version of the first Ta_2O_5 diffraction pattern in the dataset, along with the τ and β values calculated from each pixel. Two ranges of τ are shown, the full range as well as a smaller range so that more detail is visible in the 0-3000 ms range.

1.04 and more uncertain.

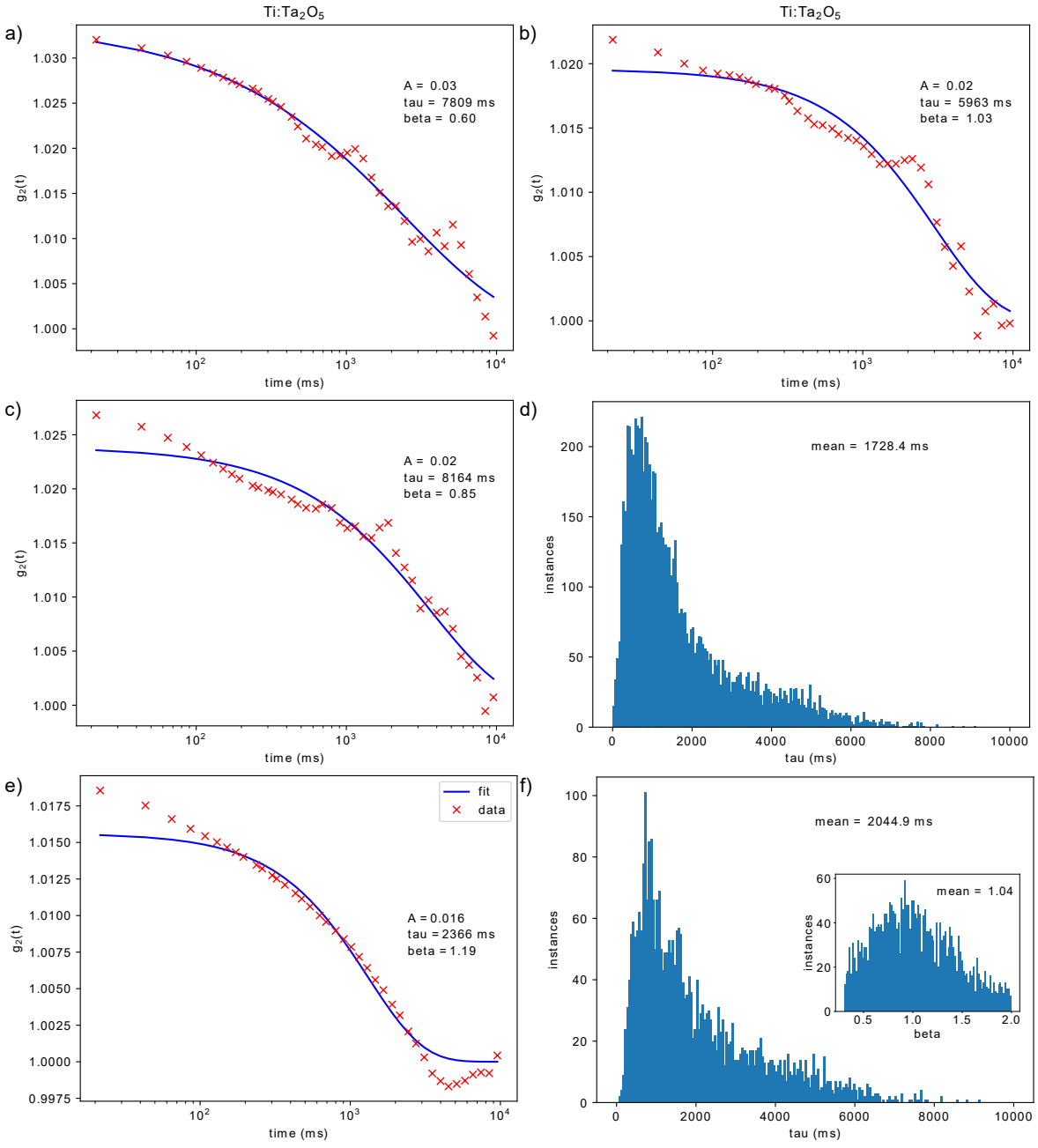

Figure 5.38: a), b) and c) show examples of non-linear least squares KWW fitting to $g_2(t)$ from pixels in the Ta_2O_5 diffraction patterns. d) shows a histogram of the wide distribution of τ values calculated from all of the pixels in the masked pattern. Results from the annular masked region are shown in e) KWW fit to average of each pixels $g_2(t)$ and f) histograms of τ and β calculated from each pixel.

5.6.3 SiO_2 Substrate 21.6 ms Exposure

In this section a similar area of the sample is examined as in the previous section, however the experimental parameters are different. Most notably the exposure time has increased to 21.6 ms, the probe current is now 19.5 pA and probe size has been decreased to 1 nm. 500 DPs were collected, meaning that the total time of this dataset is 10.79 s.

Some examples of the resulting DPs spread throughout the dataset are shown in Figure 5.39. Similarly to the DPs from the 1 ms exposure, the patterns do not show many prominent diffraction speckles and the diffracted intensity is mostly spread in a diffuse cirular region around the central beam. Consecutive DPs from the dataset are shown in Figure 5.40, some speckles can be seen, although it is difficult to see any that persist over multiple patterns.

For this dataset, the variance looks slightly different to that found using a 1 ms exposure time. Figure 5.41 shows ten temporal variance curves, with a similar shape to that found using an exposure time of 1 ms. The height of the main variance peak at 0.02 s exposure time is very close to that found with the same exposure time virtually obtained in the 1 ms dataset. At the higher virtual exposure times, the variance drops significantly and becomes extremely low, while the position of the main variance peak moves towards the right of the graph. This indicates that over a timescale of 1 s, the structural variations always average to effectively the same pattern, putting an upper limit on the timescale over which any trace of the structure is seen, and emphasising that SiO_2 has a particularly short time over which any structure persists.

The sum of all DPs in the dataset is shown in Figure 5.42, similarly to the results in the previous section, there are not any prominent diffraction speckles and the image looks like what could be expected from a DP from an amorphous sample with a much larger electron beam used. Intensity of four diffraction speckles as a function of time is shown in Figure 5.54, where each of the spots show some sharp peaks, this is to be expected as the exposure time is more than 20 times larger in this dataset. A rolling average over 5 patterns was calculated and is shown in Figure 5.45, the FWHM of intensity peaks in these plots are shown in Table 5.4, which appears to show FWHM of just over 100 ms.

Differences between DPs are shown in Figure 5.46 for patterns at 2158 ms intervals and Figure 5.47. Most of the differences are contained within the circular region around the central spot. As expected, over a longer timescale there are large differences between DPs, these differences are completely different when a DP $\pm$ 2158 ms away is compared to another that is a further 2158 ms away from the 5395.0 ms pattern. There are some

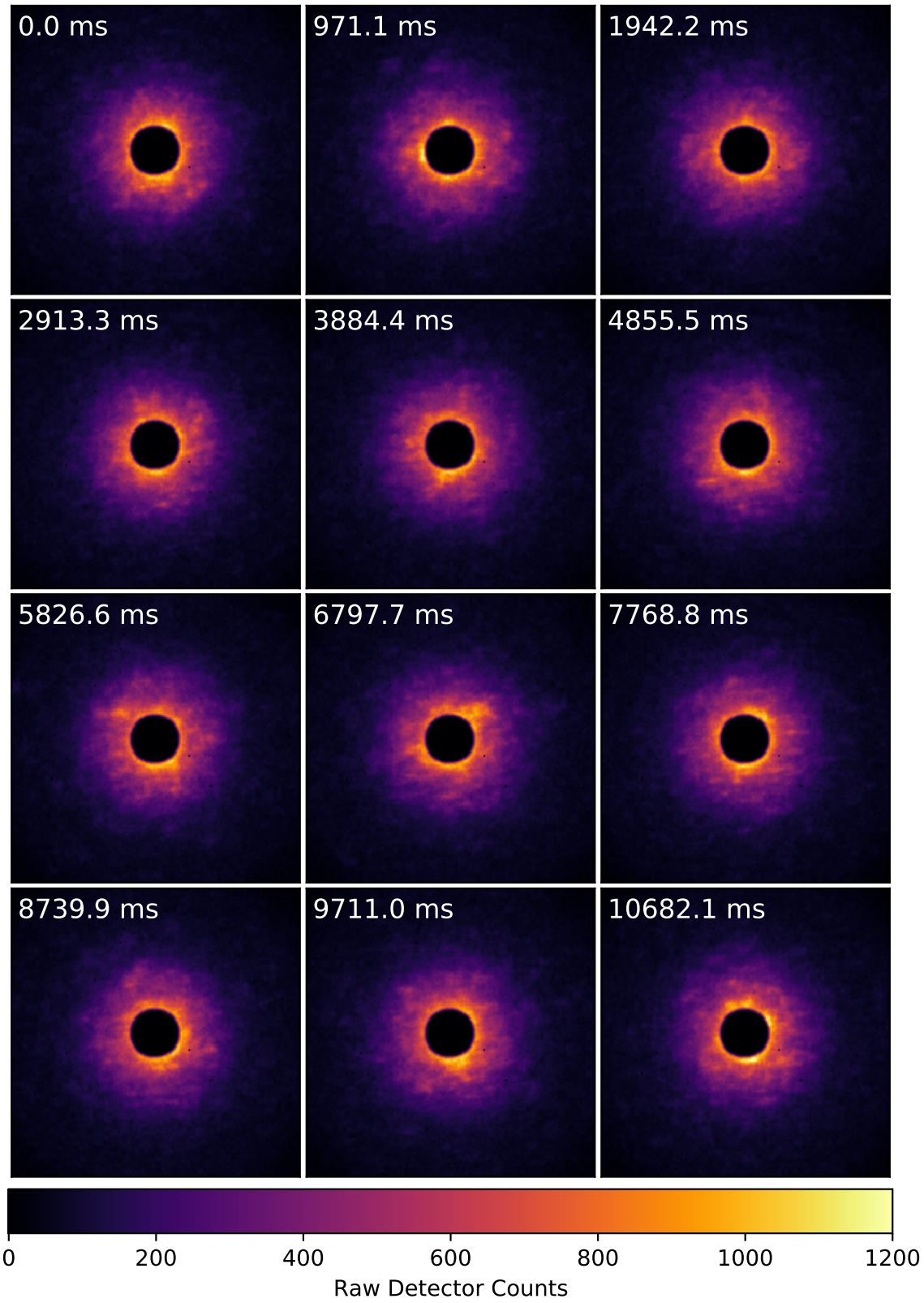

Figure 5.39: DPs obtained from the SiO_2 substrate of the $NbSi_x$ film using an exposure time of 21.6 ms. This figure shows patterns taken from the dataset at regular 971.1 ms intervals. Arrows are pointing to features of interest.

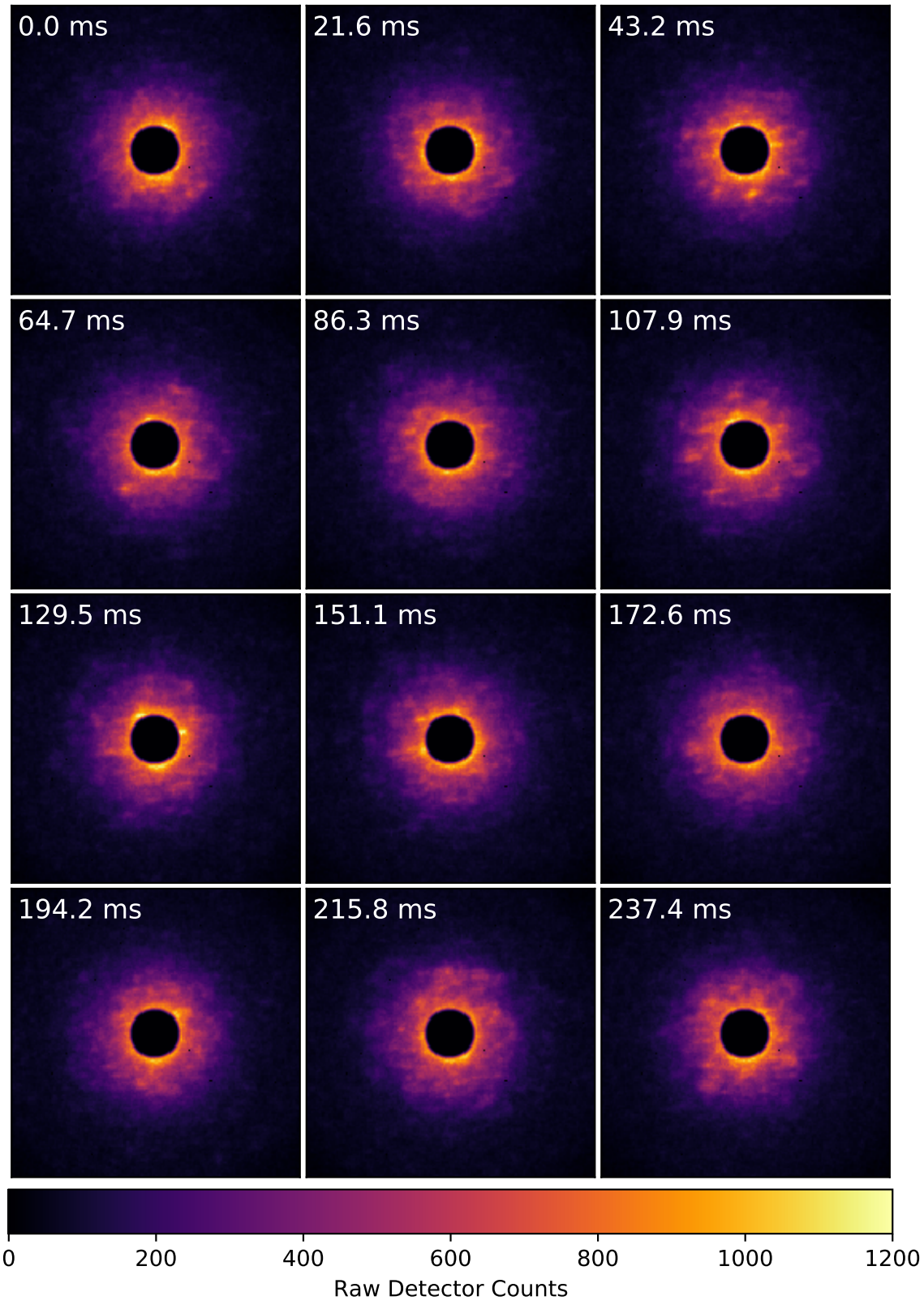

Figure 5.40: DPs obtained from the SiO_2 substrate of the $NbSi_x$ film using an exposure time of 21.6 ms. This figure shows twelve consecutive patterns taken from the dataset. Arrows are pointing to features of interest.

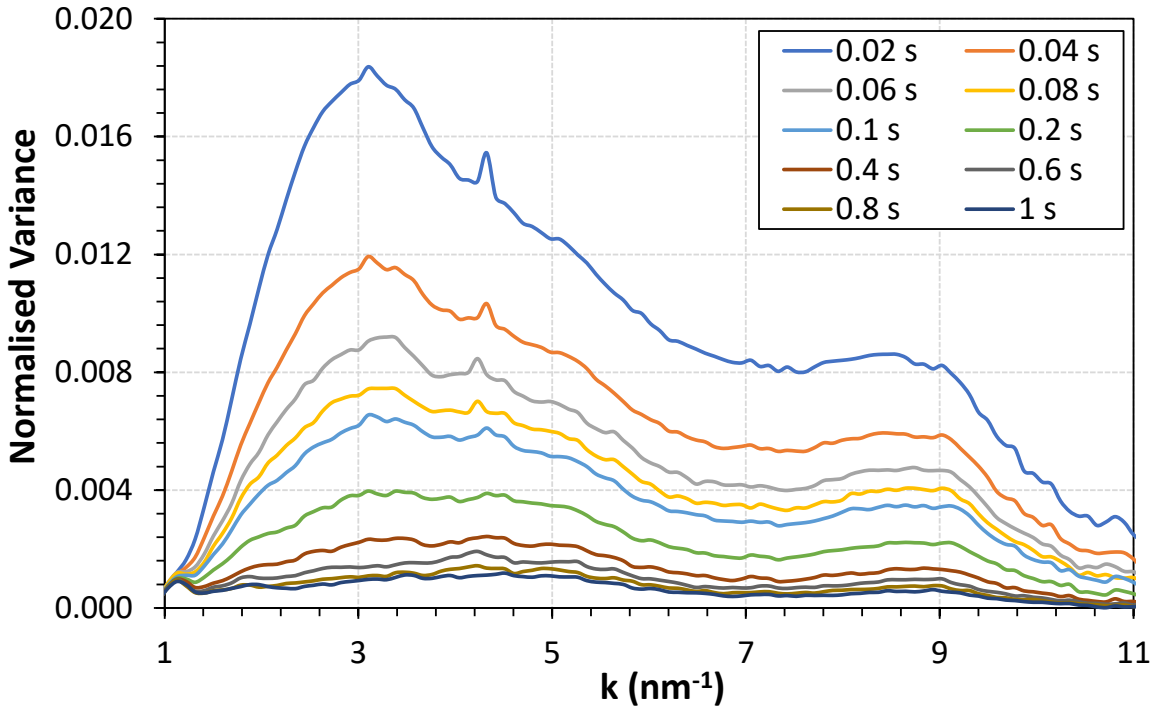

Figure 5.41: Normalised variance obtained from diffraction patterns at the SiO_2 substrate using 21.6 ms exposure time. Variance curves from the summed diffraction patterns over ten different timeframes are shown.

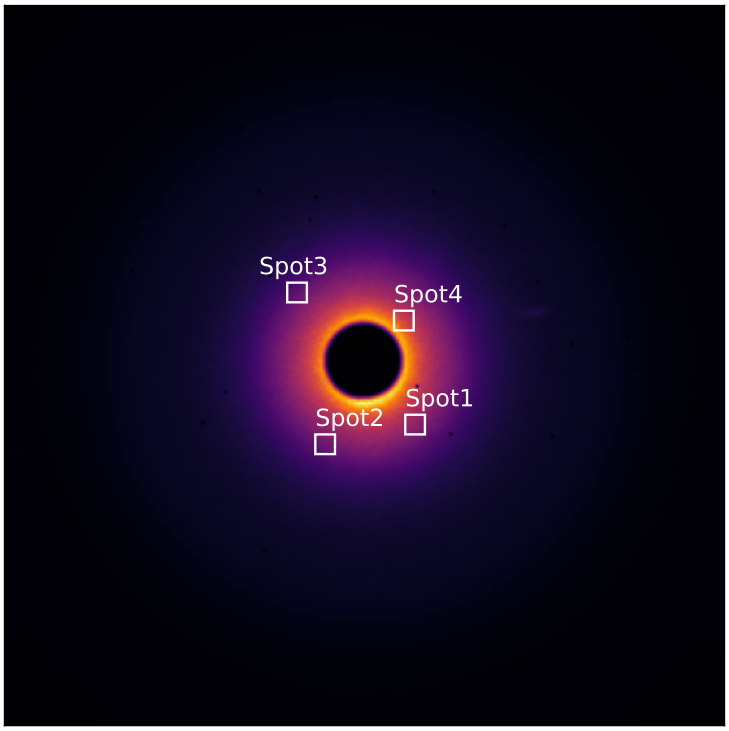

Figure 5.42: Sum of all 500 DPs from the SiO_2 substrate of the $NbSi_x$ film, showing selected diffraction spots.

Table 5.4: Analysis of the FWHM of intensity peaks from four spots in the DPs obtained from the SiO_2 substrate of the $NbSi_x$ film using a 21.6 ms exposure time.

Spot	**Number of peaks**	**FWHM (Mean) ms**	**FWHM (σ) ms**
1	1	134.8	NA
2	3	109.6	9.2
3	3	104.3	10.2
4	7	107.4	7.8

differences that appear in all four images, this is due to the diffraction speckles in the reference pattern not being present in the other four patterns. Figure 5.47 shows a speckle starting to appear after the 10272.1 ms DP, while interestingly it also shows a speckle present in all five DPs apart from the 10250.5 ms pattern, this is visible immediately to the left of the central beam.

A further twelve consecutive DPs are shown in Figure 5.43 from a region of the dataset where there is a peak in the SOSD plots. These show some speckles that are more prominent than those shown earlier in Figure 5.40, indicating that this sample changes in its structure during the timescale of this experiment.

SiO_2 is known to be unstable under an electron beam, so it is expected that τ values obtained will be small. Figure 5.49 shows the first diffraction pattern in the diffraction dataset, as well as the τ and β values calculated from each pixel. Most of the highest τ values are not from the main diffraction ring, indicating that speckles in that ring are very short lived, for the most part with τ less than 250 ms.

A set of fits to individual pixels from the masked pattern are shown in Figure 5.49a,b,c, each of which have low values of τ up to around 250 ms. A histogram of all the values of τ calculated from the masked diffraction pattern can be seen in Figure 5.49d, where the mean value is 98 ms, compared to the $NbSi_x$ and Ta_2O_5 films investigated earlier, the distribution is much narrower. When KWW fits to an average $g_2(t)$ from the annular region around the main diffraction peak are calculated, *tau* is found to be 80 ms, with β of 0.75, as seen in Figure 5.49e. Here the mean value of τ in the annular region (85 ms) is smaller than from the whole masked region (98 ms), while the τ distribution (Figure 5.49f) is similar. β within the annular region shows a lot of variation, with no clear peak.

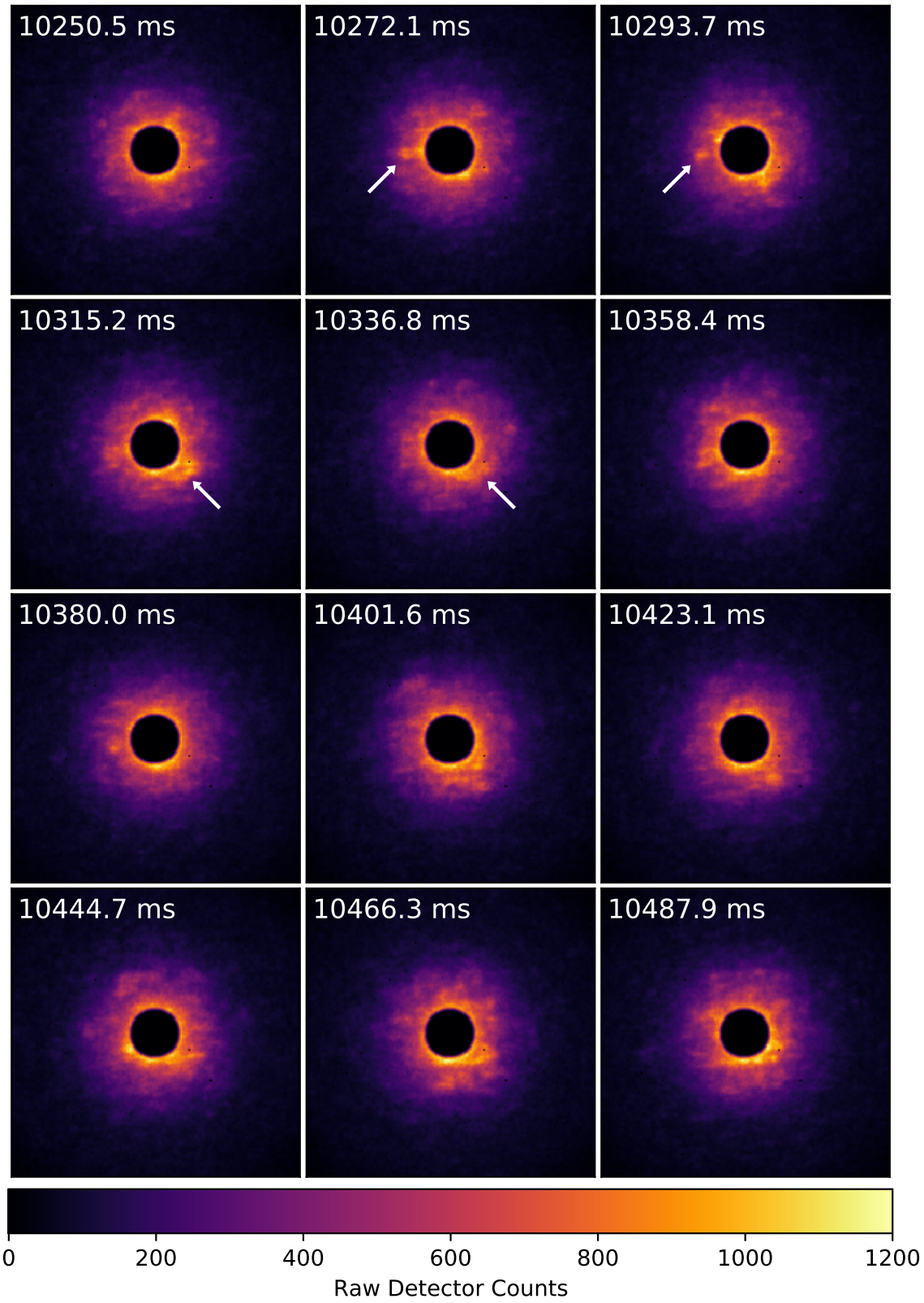

Figure 5.43: DPs obtained from the SiO_2 substrate of the $NbSi_x$ film using an exposure time of 21.6 ms. This figure shows twelve consecutive patterns taken from the dataset. Arrows are pointing to features of interest.

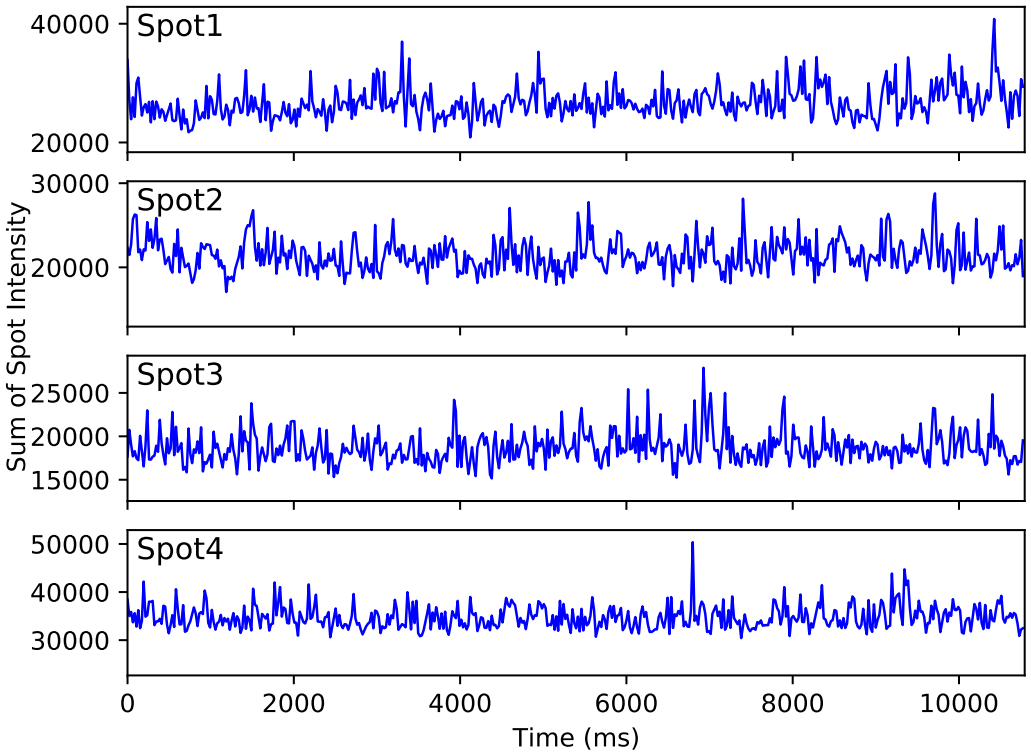

Figure 5.44: Line plots of the summed intensity within each of the four spots as a function of time.

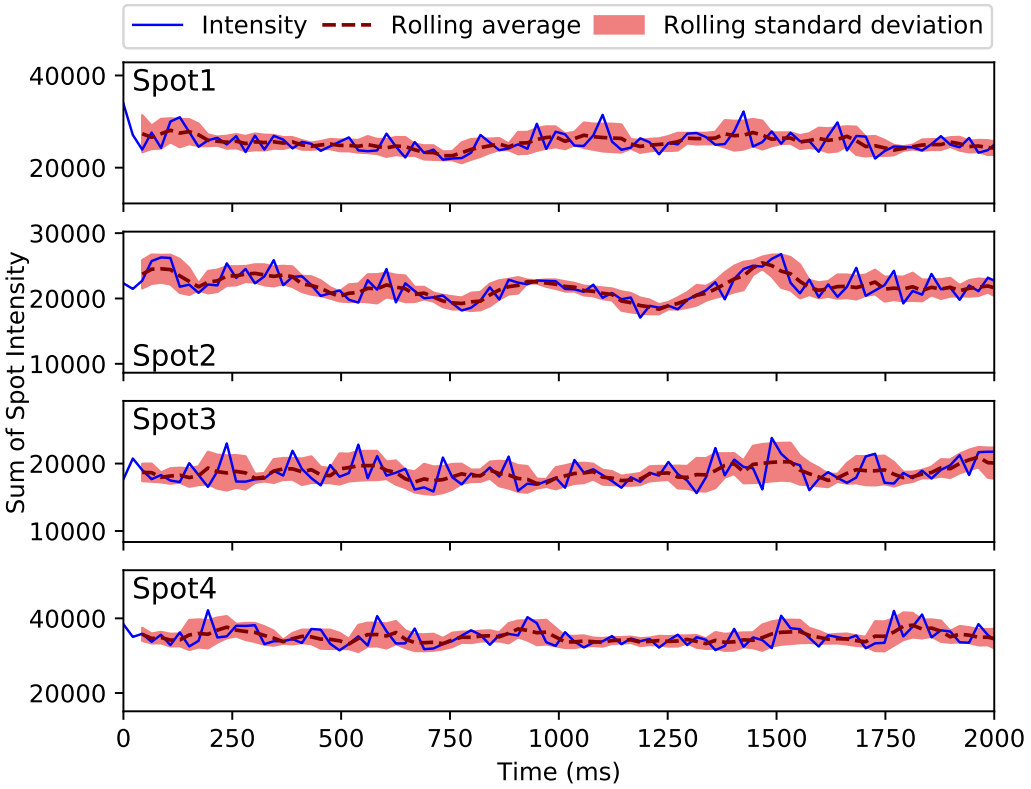

Figure 5.45: Plots of the summed intensity for the first 2000 ms of the dataset within each of the four spots. A rolling average and standard deviation from a window 5 patterns wide are overlaid.

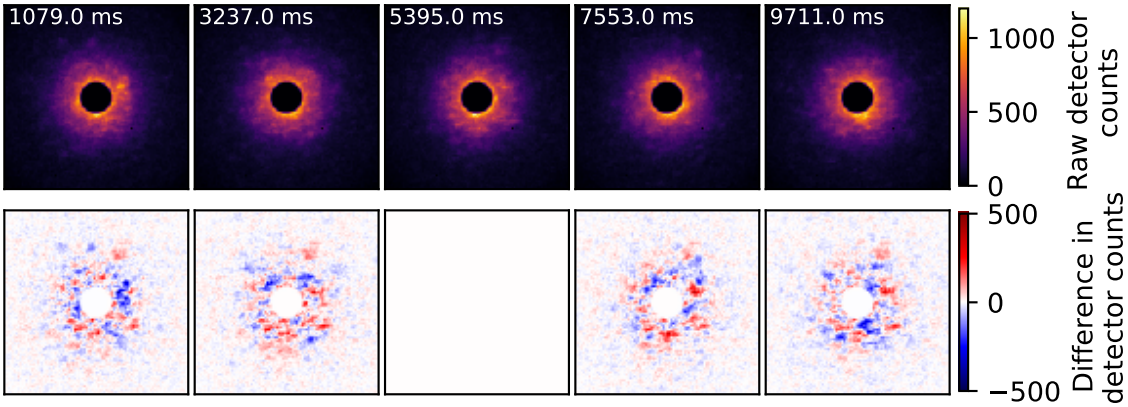

Figure 5.46: This figure shows five DPs obtained with an exposure time of 21.6 ms from the SiO_2 substrate of the $NbSi_x$ layer. These are spread at 2158 ms intervals through the dataset. The top row shows the DPs, while the bottom row shows the absolute difference in intensity (detector counts) between the central DP in the top row and the DP directly above it.

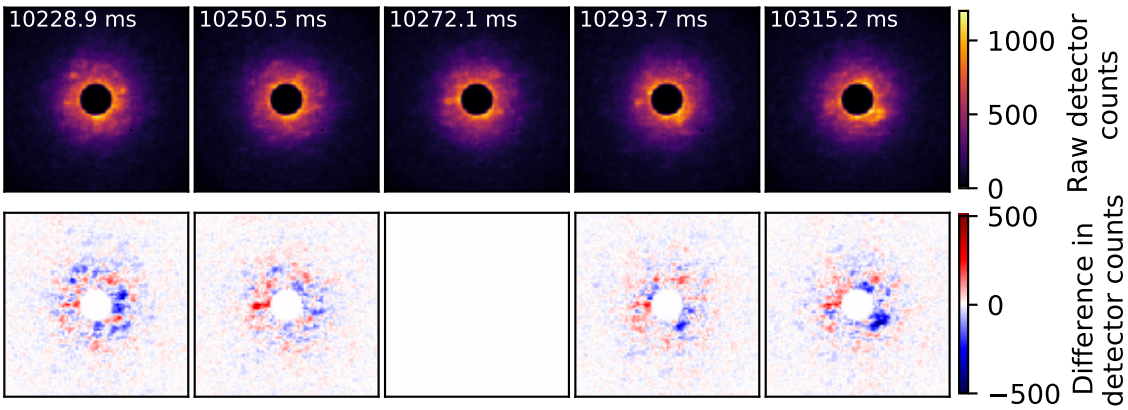

Figure 5.47: This figure shows five consecutive DPs obtained with an exposure time of 21.6 ms from the SiO_2 substrate of the $NbSi_x$ layer. The top row shows the DPs, while the bottom row shows the absolute difference in intensity (detector counts) between the central DP in the top row and the DP directly above it.

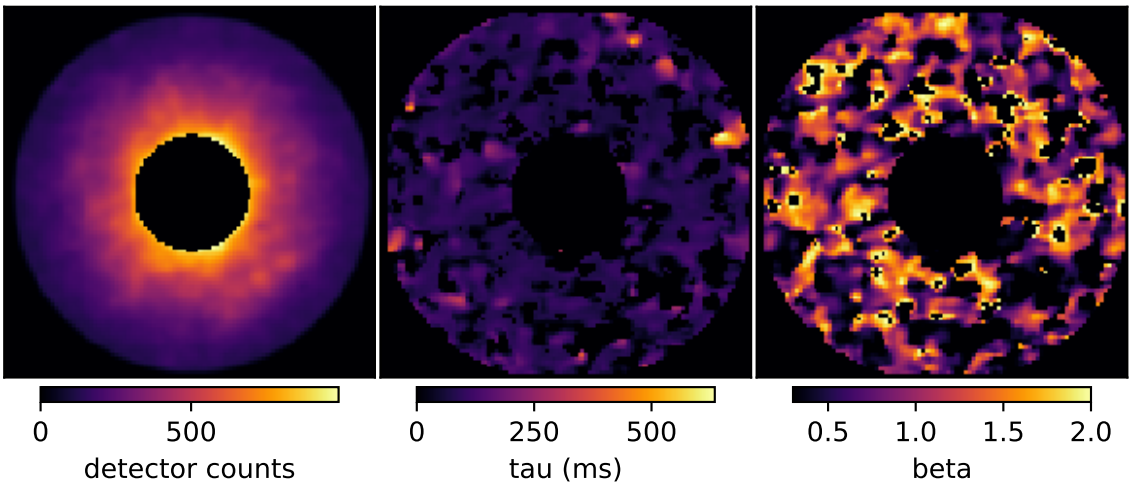

Figure 5.48: Images from the SiO_2 substrate of the $NbSi_x$ film showing the masked version of the first SiO_2 diffraction pattern in the dataset, along with the τ and β values calculated from each pixel.

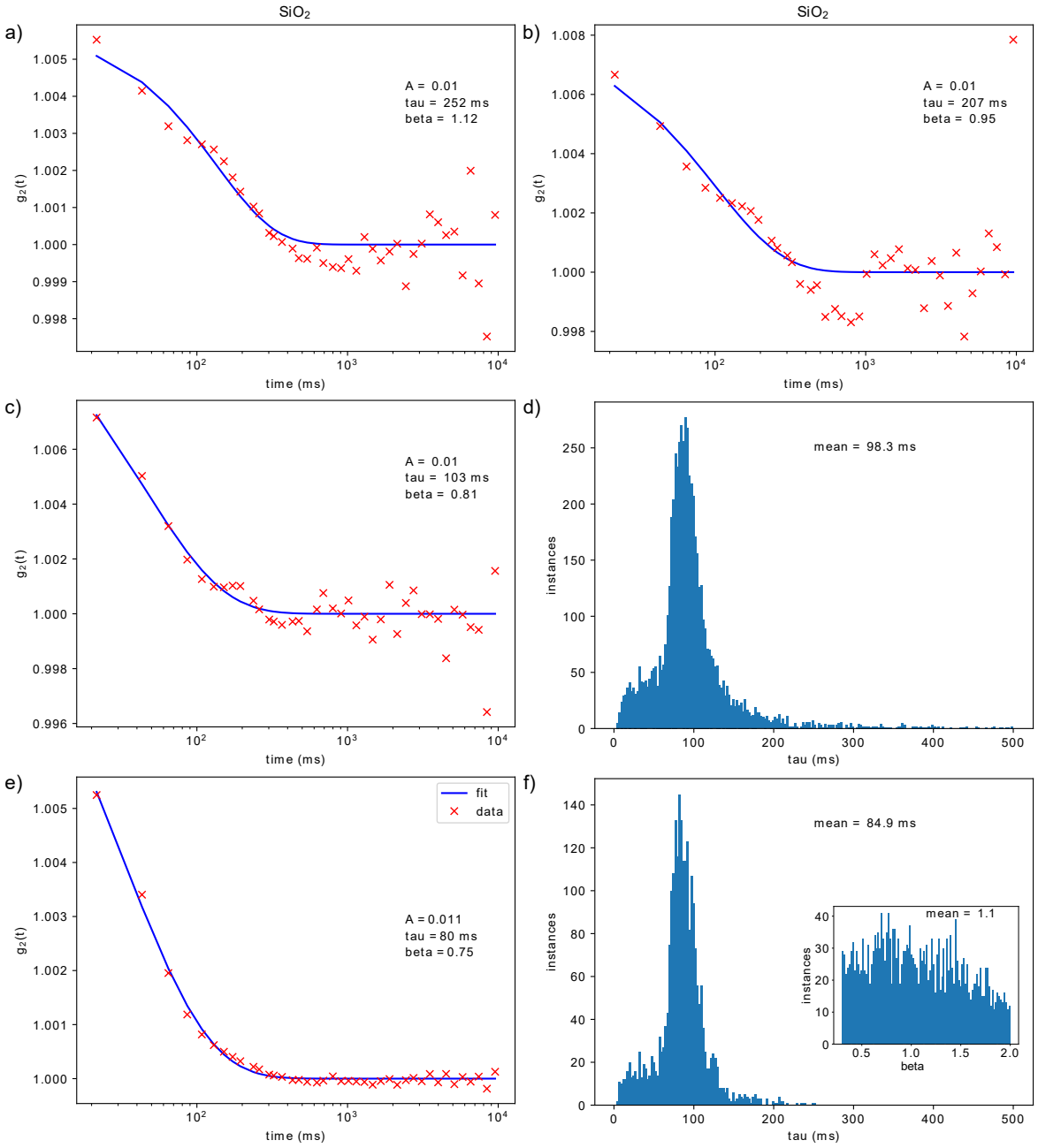

Figure 5.49: a), b) and c) show examples of non-linear least squares KWW fitting to $g_2(t)$ from pixels in the SiO_2 diffraction patterns from the substrate of the $NbSi_x$ film. d) shows a histogram of the distribution of τ values calculated from all of the pixels in the masked pattern. Results from the annular masked region are shown with e) a KWW fit to the average $g_2(t)$ of all the pixels and f) histograms of τ and β calculated from each pixel.

5.6.4 SiO_2 Multilayer Film 21.6 ms Exposure

The final film to be analysed in this chapter is the SiO_2 layer from the A-LIGO film as mentioned earlier in section 5.2. This was again carried out with 21.6 ms exposure time, but with probe size of 2 nm and a probe current of 4 pA. Again, 500 DPs were collected.

Twelve DPs equally spread through the dataset are shown in Figure 5.50. These are somewhat different to those seen in the SiO_2 in the previous two sections. While there is a diffuse circle around the central beam, there are many more prominent diffraction speckles visible, indicating that this sample could be more ordered than the SiO_2 previously inspected. Unlike the $NbSi_x$ and Ti:Ta_2O_5 glasses, none of these speckles appear throughout the dataset, they are much shorter in duration. Consecutive DPs are shown in Figure 5.51, where arrows indicate one of the more prominent diffraction speckles present in these DPs. Over this time period, there is some change in the patterns, although not as quickly as in the other SiO_2 sample.

Figure 5.52 shows the spatial and temporal variance obtained from this sample. Interestingly, the shape of the spatial variance curve matches with the shape of the temporal variance curve, and is very similar in magnitude to the temporal variance curves obtained over similar exposure times (there may be a difference in sample thickness between the area used to calculate the spatial variance and the area used here to calculate the temporal variance). The variance curves shown here are very similar in shape to those obtained from the SiO_2 substrate (Figure 5.3) at the 1 ms exposure time, however the magnitude of the variance here is much higher for the same exposure time.

Similarly to the previous data on the SiO_2 substrate, the sum of all the DPs, seen in Figure 5.53 shows that there are no speckles that last for a significant enough proportion of the dataset to be seen. Four 8 pixel diameter boxes were chosen for an analysis of how the intensity within those boxes changes as a function of time. The results of this calculation is shown in Figure 5.54. There are large variations in intensity, with each of the spots showing multiple peaks, showing that there were multiple speckles that appeared and disappeared throughout the exposure to the electron beam. Figure 5.55 shows the rolling average in intensity calculated using a rolling window of 5 patterns. Results from peak-fitting of these plots give FWHM as shown in Table 5.5, where the FWHM are mostly close to 150 ms, apart from Spot 2 which shows a significantly smaller value close to 120 ms.

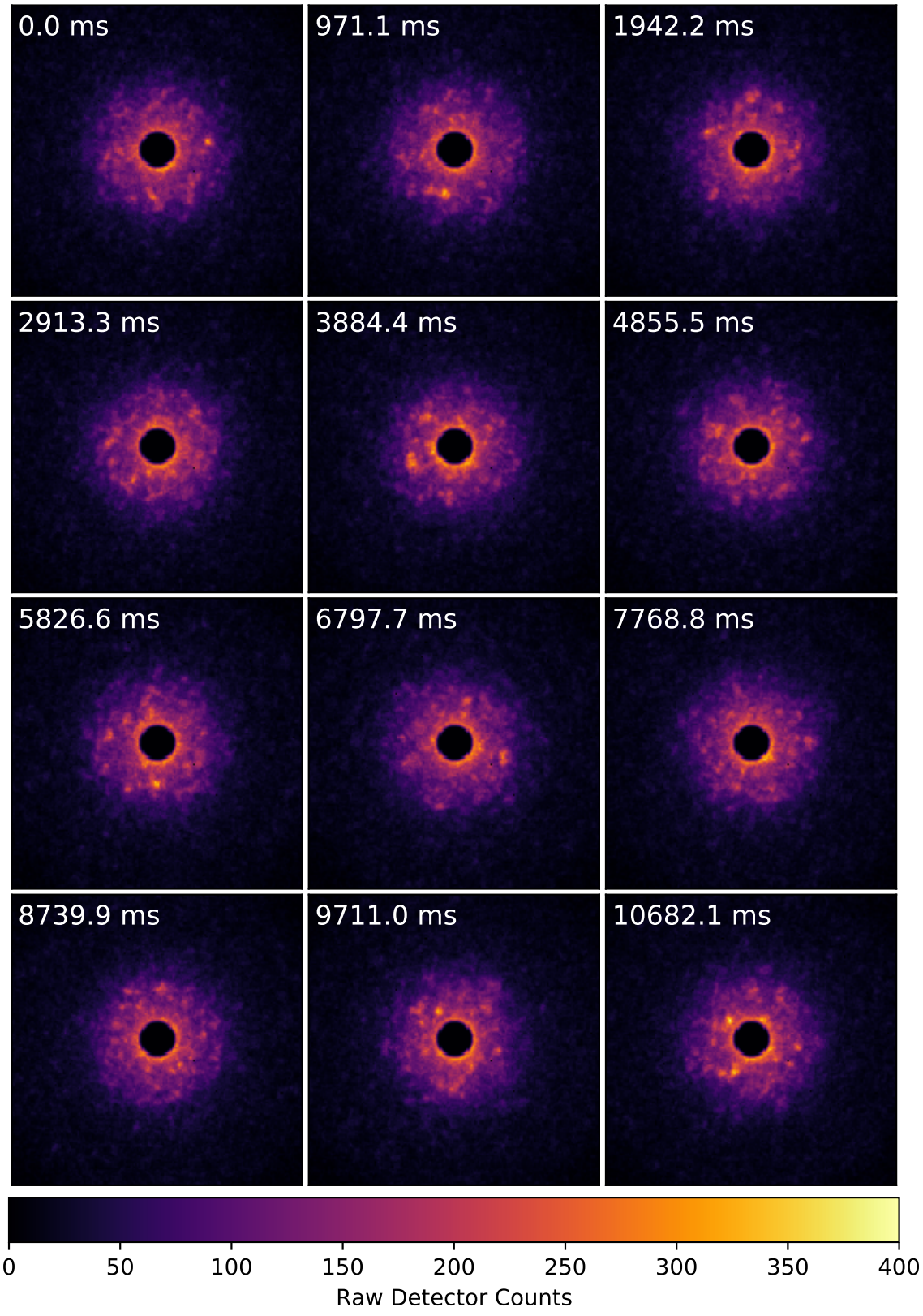

Figure 5.50: DPs obtained from the SiO_2 multilayer film layer using an exposure time of 21.6 ms. This figure shows patterns taken from the dataset at regular 971.1 ms intervals. Arrows are pointing to features of interest.

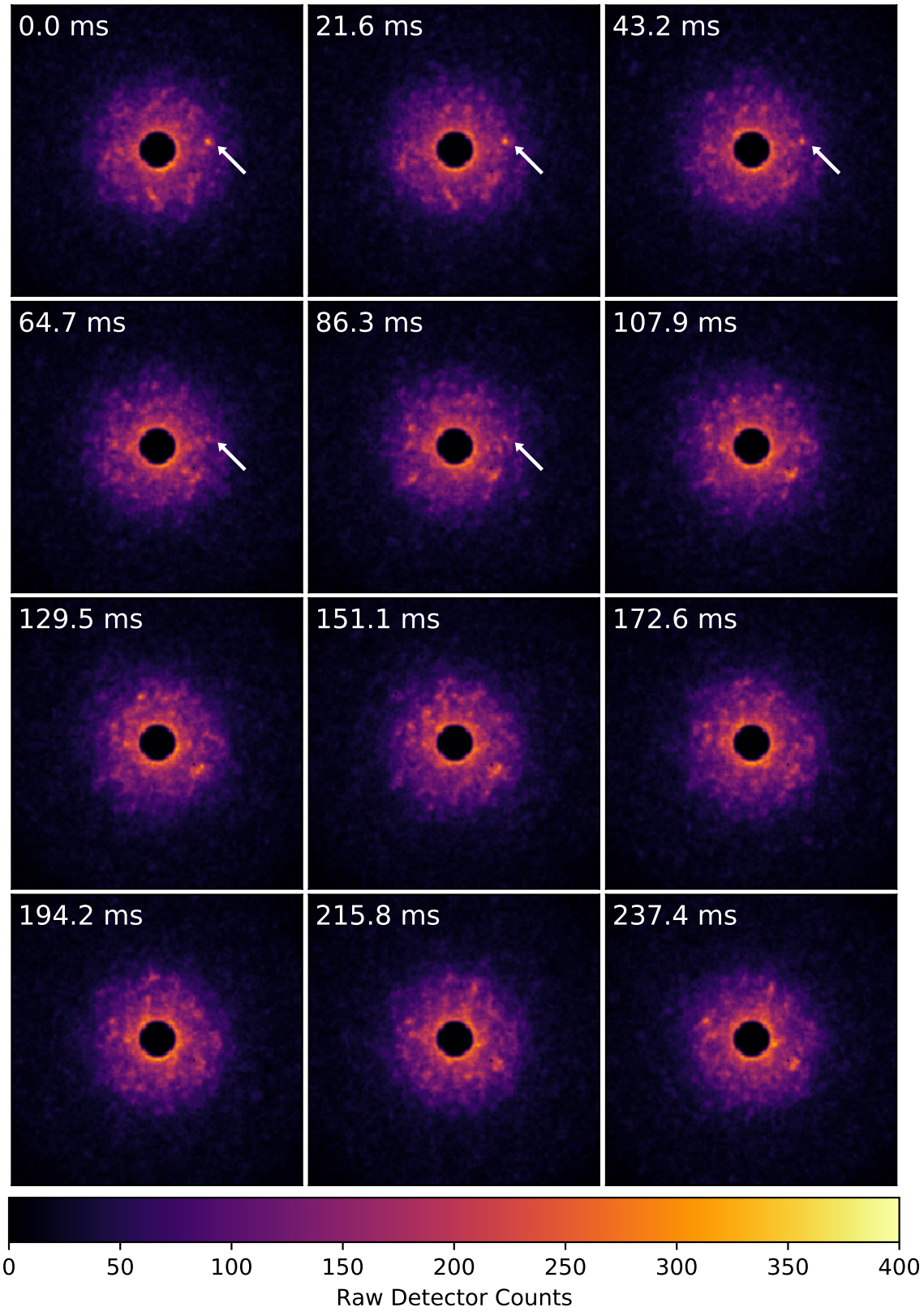

Figure 5.51: DPs obtained from the SiO_2 multilayer film layer using an exposure time of 21.6 ms. This figure shows twelve consecutive patterns taken from the dataset. Arrows are pointing to features of interest.

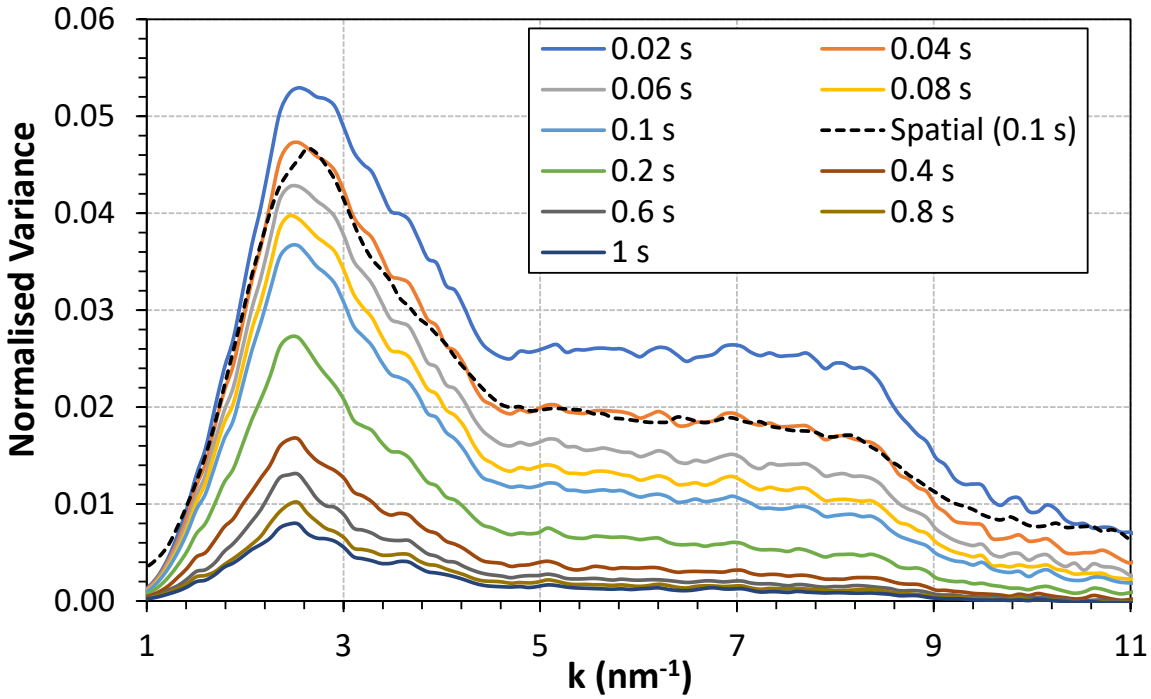

Figure 5.52: Normalised variance obtained from diffraction patterns in the SiO_2 layer using 21.6 ms exposure time. Variance curves from the summed diffraction patterns over ten different timeframes are shown.

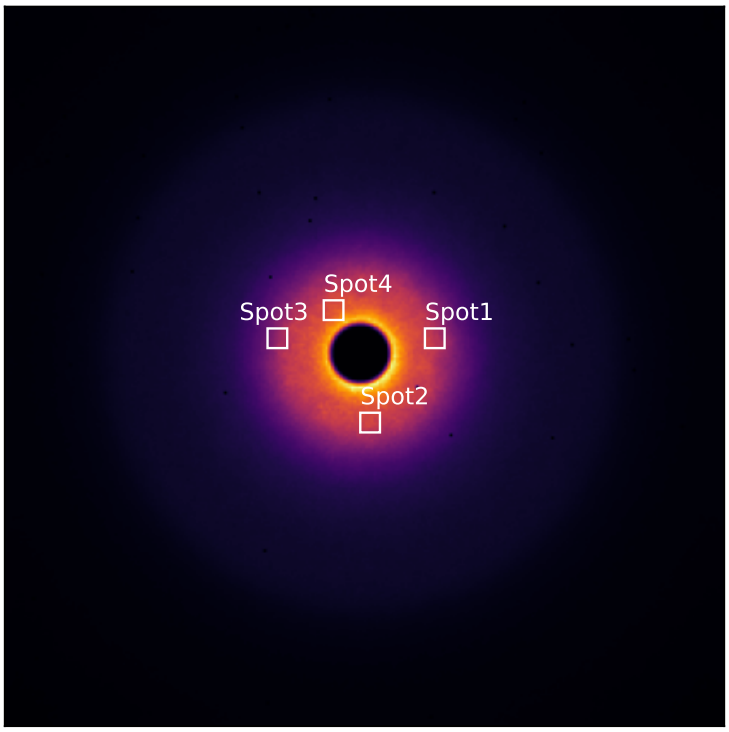

Figure 5.53: Sum of all 500 DPs from the SiO_2 multilayer film layer, showing selected diffraction spots.

The differences between DPs at intervals of 2158 ms are shown in Figure 5.56. Most

Table 5.5: Analysis of the FWHM of intensity peaks from four spots in the DPs obtained from the SiO_2 layer of the Ti:Ta_2O_5/SiO_2 multilayer film using a 21.6 ms exposure time.

Spot	**Number of peaks**	**FWHM (Mean) ms**	**FWHM (σ) ms**
1	4	150.7	23.0
2	5	119.6	9.6
3	8	147.3	34.4
4	5	168.9	34.1

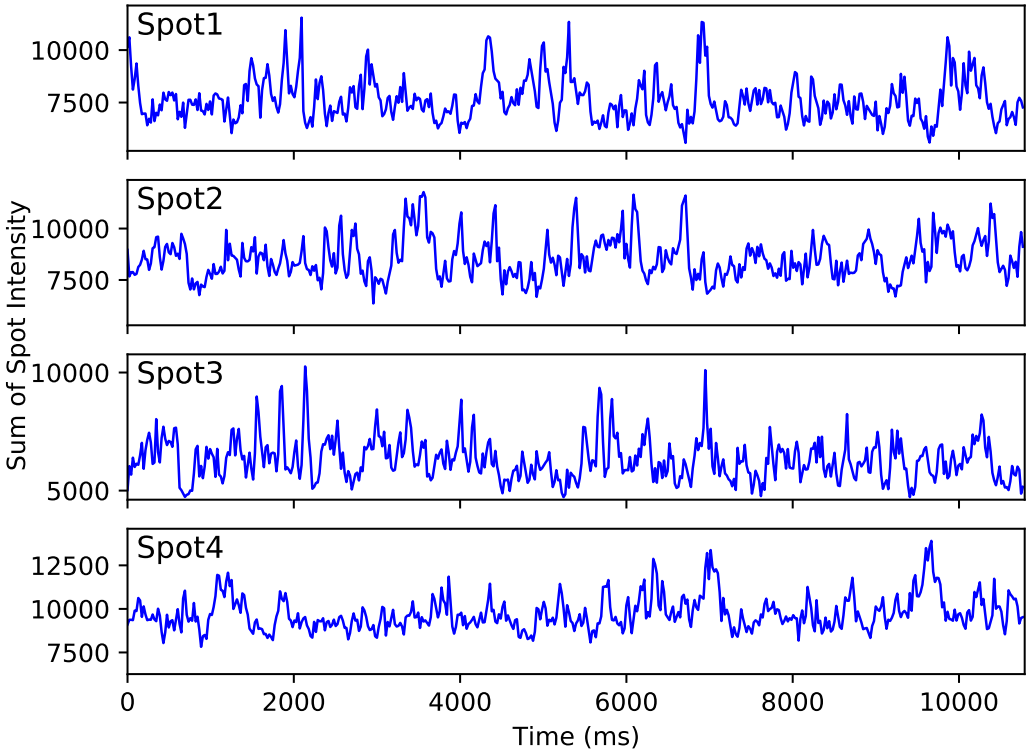

Figure 5.54: Line plots of the summed intensity within each of the four spots as a function of time.

of the differences occur in a ring around the central beam. The images display that each of these DPs bear little resemblance to each other in terms of speckle location. It does not appear that there is a significant increase in total difference as you move further from the reference pattern. Differences between consecutive diffraction patterns are shown in Figure 5.57. These show that the speckle intensity in the DPs changes considerably over 21.6 ms and that a further step of 21.6 ms gives a noticeably greater difference in intensity.

Figure 5.58 shows τ and β calculated from KWW fits to each of the pixels in the masked dataset. As expected τ is much smaller than in the $NbSi_x$ and Ta_2O_5 samples, with most of the pixels calculated to have τ less than 200 ms. Generally β is larger than one and around 1.5 in large areas.

Examples of KWW fits in some of the pixels are shown in Figure 5.59a,b,c these are from

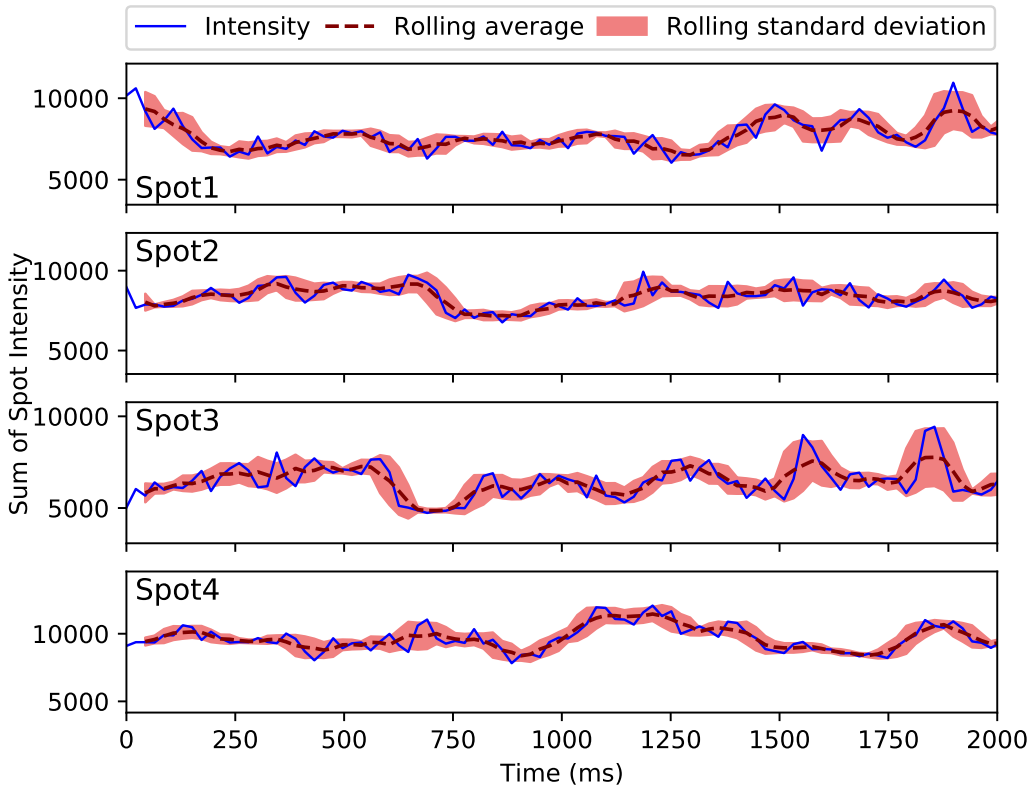

Figure 5.55: Plots of the summed intensity for the first 2000 ms of the dataset within each of the four spots. A rolling average and standard deviation from a window 5 patterns wide are overlaid.

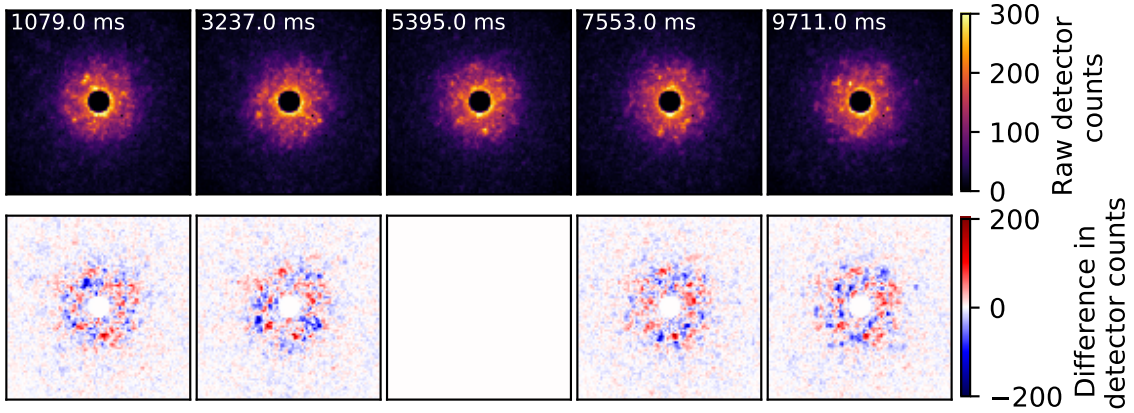

Figure 5.56: This figure shows five DPs obtained with an exposure time of 21.6 ms from the SiO_2 multilayer film layer. These are spread at 2158 ms intervals through the dataset. The top row shows the DPs, while the bottom row shows the absolute difference in intensity (detector counts) between the central DP in the top row and the DP directly above it.

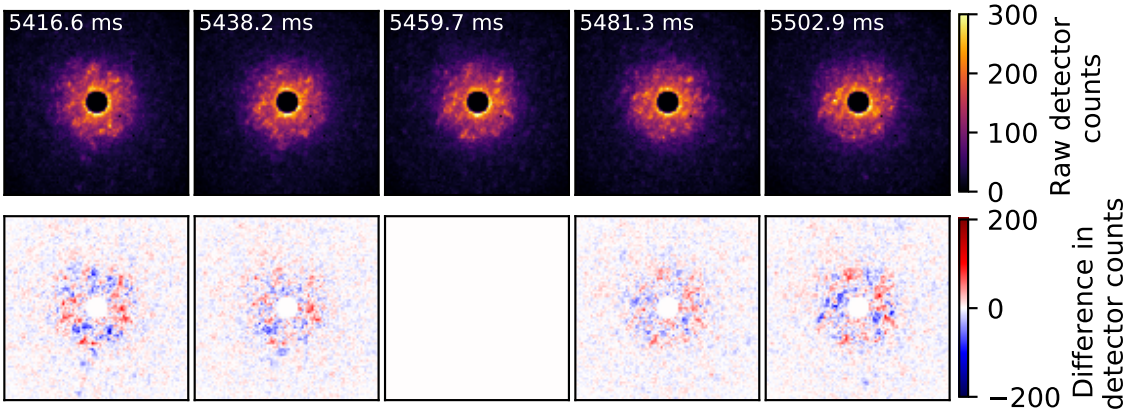

Figure 5.57: This figure shows five consecutive DPs obtained with an exposure time of 21.6 ms from the SiO_2 multilayer film layer. The top row shows the DPs, while the bottom row shows the absolute difference in intensity (detector counts) between the central DP in the top row and the DP directly above it.

some of the larger values of τ within the diffraction pattern, where β is generally lower than in most of the pixels and is close to 1 or below. A histogram of all the calculated values is shown in Figure 5.59d, where there is a smaller spread of τ compared to the $NbSi_x$ and Ta_2O_5 samples, with nearly all the pixels showing τ between 50 and 250 ms.

When $g_2(t)$ is averaged over an annular region positioned over the main diffraction peak, a τ value of 153 ms, with β 1.13 is calculated from a KWW fit, as shown in Figure 5.59e. τ values from pixels contained in this region (Figure 5.59f) are slightly higher than those in the entire masked pattern (Figure 5.59), with a mean value of 150 ms compared to 131 ms. Within the annular region, the mean β value is 1.3, with the distribution skewed towards higher values.

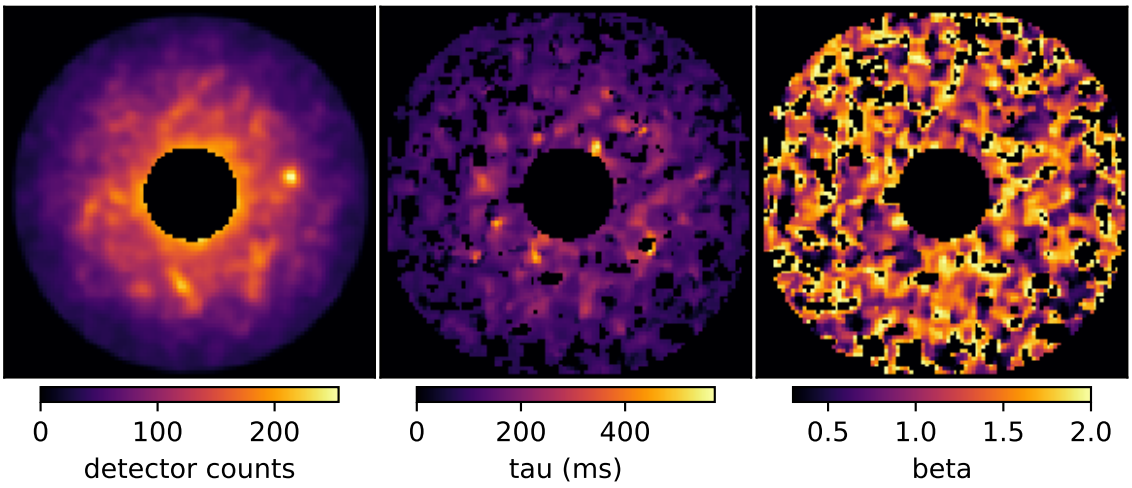

Figure 5.58: This image shows images from the SiO_2 layer of the Ta_2O_5 film, these are the masked version of the first diffraction pattern in the dataset, along with the τ and β values calculated from each pixel.

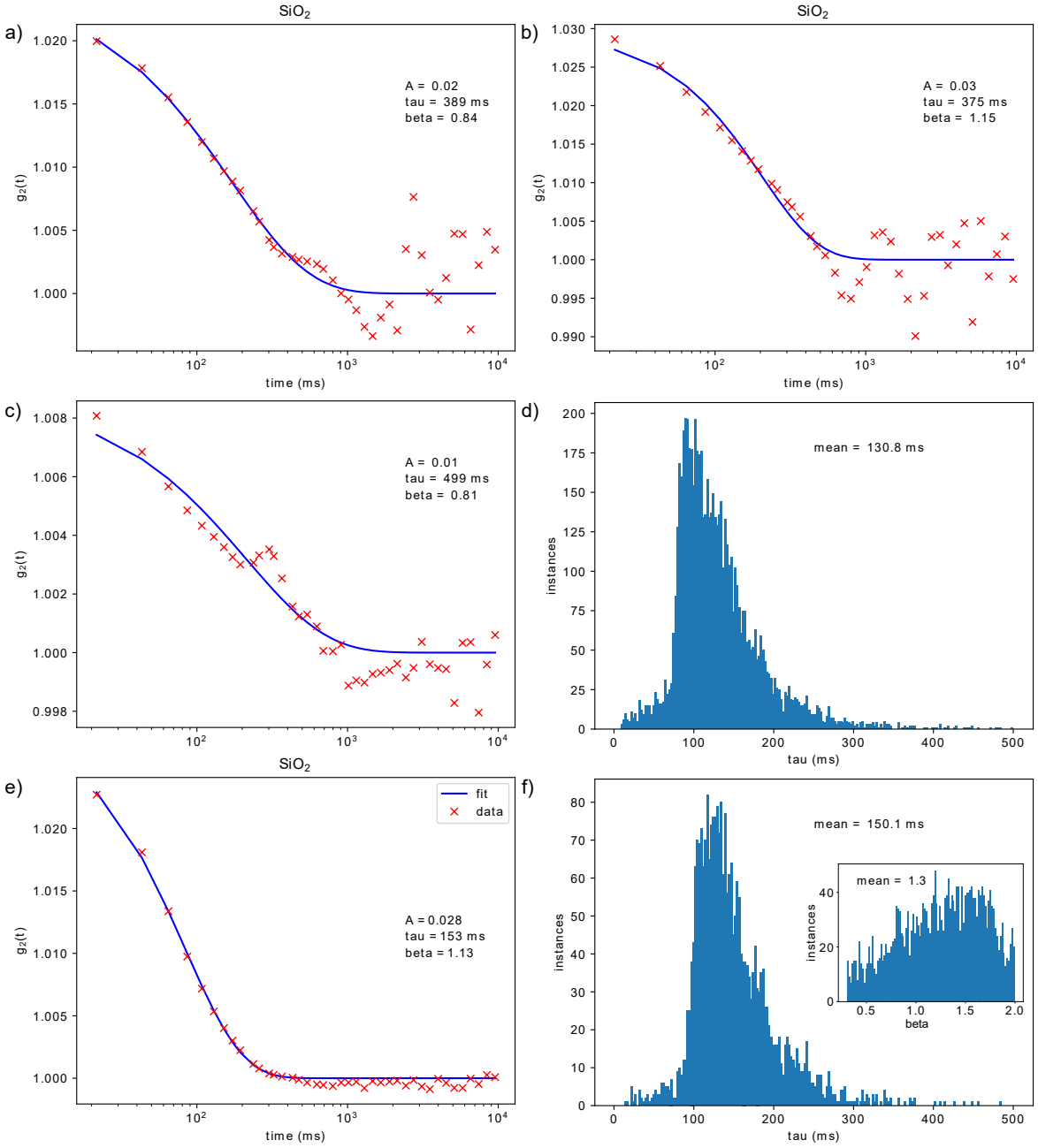

Figure 5.59: a), b) and c) show examples of non-linear least squares KWW fitting to $g_2(t)$ from pixels in the SiO_2 diffraction patterns from the multilayer Ta_2O_5/SiO_2 film. d) shows a histogram of the distribution of τ values calculated from all of the pixels in the masked pattern. Results from the annular masked region are shown with e) a KWW fit to the average $g_2(t)$ of all the pixels and f) histograms of τ and β calculated from each pixel.

5.7 Discussion

Diffraction patterns from each of the samples show some differences in their appearance due to the variation in their composition, as well as the different illumination conditions being used. They each vary with time, gradually becoming less similar to the reference pattern with increasing time, by whatever measure of similarity is used (visual assessment of difference plots, plotting intensity of different spots and $g_2(t)$).

In the glasses containing metals, the diffraction patterns remain more stable as time goes on than in the silica glasses. Diffraction patterns that are 1000 ms apart from the metal containing glasses (Figures 5.1,5.19,5.29) do not show such large differences, whereas those obtained from the silica glasses (Figures 5.9,5.39,5.50) do not share significant structure over a time difference of a few hundred ms.

There was some changes in the intensity of the speckles investigated in the $NbSi_x$ at 1 ms exposure time (Figure 5.5) of up to approximately 30 %, but there were large changes in the SiO_2 film at the same exposure time (Figure 5.13), up to around 75 % of intensity. At the exposure time of 21.6 ms, the changes were larger, the Ti:Ta_2O_5 speckles (Figure 5.33) varied in intensity up to approximately 100 % but remained more consistent than those from $NbSi_x$ where the intensity changes were up to nearly 150 % (Figure 5.23). As expected speckles from both SiO_2 samples were very short lived (Figures 5.44,5.54).

Using 1 ms snapshots does not work well as the timescale is so short that at the beam intensity used, the shot noise is a large component of the differences between diffraction patterns. The 21.6 ms snapshots work far better and show differences in the DP that are much more concentrated on the key radii for diffuse diffraction in each material. Because of this, ECM analysis was not carried out for the datasets with 1 ms exposure time.

Shorter exposure times could be explored, however higher beam currents would have to be used to minimise the effect of shot noise. This would give a higher energy input, more local heating and a greater risk that the beam is driving structural changes, rather than merely observing them.

Electron correlation microscopy was used to calculate the structural relaxation time τ from each dataset with exposure time of 21.6 ms. Time constants resulting from fitting KWW curves to $g_2(t)$ for each dataset are shown in Table 5.6.

Values of τ estimated from $NbSi_x$ and Ti:Ta_2O_5 were much longer than those observed in SiO_2, especially in the case of Ti:Ta_2O_5.

Table 5.6: Structural relaxation times τ from annular region around principal diffraction peak

Dataset	τ **(ms) calculated from mean of** $\mathbf{g_2(t)}$	β	**Electron dose per second** ($\mathbf{nm^{-2}s^{-1}}$)
21.6 ms exposure $\mathbf{NbSi_x}$ **layer**	826	0.73	200,000,000
21.6 ms exposure $\mathbf{Ti:Ta_2O_5}$ **layer**	2366	1.19	3,900,000,000
21.6 ms exposure $\mathbf{SiO_2}$ **substrate**	80	0.75	200,000,000
21.6 ms exposure $\mathbf{SiO_2}$ **layer**	153	1.13	3,900,000,000

Similar experiments have previously been carried out. A $Pd_{40}Ni_{40}P_{20}$ metallic glass at room temperature was found to have τ of 25 ± 2 s.[225] FeNiP nanorods have also been experimented on, with τ values in the range of around 30-50 s depending on the beam current, while it was also discovered that two values of τ existed in Fe rich areas of the nanorod, where the shorter τ had β less than 1 and the longer τ had β larger than one, with each representing different types of ordering that have different lifetimes.[227] The structural relaxation times calculated here are much shorter than any that have been previously observed, indicating that these materials may be intrinsically less stable with time.

In the results presented here, it cannot be excluded that some of the structural changes are driven by the electron beam, whether by direct ionisation and radiolysis, or more generally from local heating. This could be explored further by taking measurements on a single material at a constant probe size over a range of beam currents, adjusting the acquisition time per pattern as necessary to investigate whether there are any issues around dose rate and local heating. It would be interesting in future work to examine the effects of beam current on time constants for structural change across a wider range of glasses.

Changes to the beam energy would be likely to affect the DPs, so datasets taken at lower beam energies may be interesting, especially in the silica glasses. At a lower beam energy, diffracted angles will be higher, but there will be more inelastic scattering as a proportion of the total scattering, so probably more heat deposited in the sample, even if the chances of atom displacement by direct interactions with a beam electron are reduced. Lowering the beam energy could make things worse for this reason.[228]

Variations in the DP as a function of time are known to have a displacement decoher-

ence effect on VDF/FEM experiments where the electron beam changes the structure of the material being investigated.[191] In a dataset that is acquired at 10 ms per pixel, correlations between two neighbouring pixels horizontally should be visible in VDF. If the scan is 30 pixels wide, there is a 300 ms difference in time between two pixels in the vertical direction. Over this timescale, there is guaranteed to be no correlation in SiO_2, and also reduces it somewhat in $NbSi_x$ and Ti:Ta_2O_5, although individual spots have been shown to last longer than the averages quantified using the ECM method.

These results show that the time stability of a material place some boundaries on what can be achieved using FEM and VDF. In a FEM experiment the variance between neighbouring areas in a line is calculated, in this case a shorter time stability is not such a problem. If instead VDF is being applied to create a 2D image then much greater time stability is required, in the order of hundreds of ms. This restricts the types of materials that VDF imaging is useful for. Ultimately, it is necessary to know about the time stability of a material before doing any spatial variance measurements.

Chapter 6

Conclusions

In this thesis, the short and medium range order in amorphous materials have been investigated using fluctuation microscopy in the STEM. Use of a direct electron detector has meant lower noise, so it is possible to produce good results with lower beam dose / faster scans. This applies especially to metal silicides, Ti:Ta_2O_5 and SiO_2. Investigations were carried out to find out about the lengthscale of MRO using VR-FEM and VDF imaging. Time stability of glasses was investigated by the analysis of a sequence of diffraction patterns recorded from a single probe position, then the influence time stability may have on measurements of spatial variance was explored.

6.1 Superconducting Nanowire Single Photon Detectors

Five samples, created from $MoSi_x$ (3 samples), $NbSi_x$ and WSi_x thin film layers with a nominal value of $x = 0.25$ were inspected using both diffraction and EELS techniques. Three of these, the co-sputtered $MoSi_x$ (2 samples) and WSi_x were very thin (approximately 5 nm for both $MoSi_x$ films and 3 nm for WSi_x), meaning that it was not possible to obtain useful diffraction data from them as they are not much larger than the probe sizes available to us for FEM experiments.

Multiple 4D datasets were acquired using two different probe sizes on each sample (except for co-sputtered $MoSi_x$). Both VDF and FEM analysis was carried out on these diffraction datasets.

First, we look at the FEM results obtained from the SNSPD films as a function of exposure time per pixel to determine the effects thereof and the optimal exposure time for this. Using longer exposure times resulted in changes to the FEM curve, as the SNR increased with exposure time over the range sampled (Figure 4.5). This was more apparent in results from the 10 μm aperture compared to those from the 20 μm aperture. Using a 10 ms exposure with the 10 μm aperture resulted in a variance curve that didn't clearly show the majority of the variance peaks apart from the main peak. All of the peaks start becoming clearly visible in the variance curves obtained at exposure times greater than 40 ms. Variance at higher k (above 5 nm^{-1}) reduced with exposure time, due to higher SNR at the longer exposure times. Variance curves obtained using the 20 μm aperture showed a large difference between an exposure time of 10 ms and 20 ms, but differences were much smaller between 20 ms and up to 100 ms. Effects of exposure time were not as large using the larger aperture, likely due to the much higher number of electrons that pass through the larger aperture and thus a higher beam current that produces more signal and better counting statistics.

In general the normalised variance curves for all of these films have a similar shape (Figures 4.7,4.13,4.20,4.27). There is a large variance peak in the k range of 4-5 nm^{-1}, followed by two smaller peaks in the range 6-10 nm^{-1}. The position of the main variance peak obtained from each film corresponded to the position of the largest peak in x-ray diffractogram data from their A15 counterparts, while there was also some similarity to the following smaller variance peaks.[192, 193, 198] These results strongly suggest that there is SRO and MRO in all of these films that is A15-like in its structure.

Since the experiments used in this thesis were carried out, Radic *etal*. published a paper showing how best to setup the microscope to achieve good results in FEM experiments.[197] They made a set of observations, including that changing the probe size by using defocus is not a good approach, as the probe decreases in coherence when defocus is applied, a better approach is to use the condenser lens system to create a set of focused probes using the smallest available aperture.[197]

In the experiments here it was not possible to do generate a range of probe sizes without changing the aperture, due to the lack of flexibility in the two condenser lens system.

VDF images were recorded using two different methods. Firstly, by superimposing virtual ADF detectors onto DPs at k values corresponding to known diffraction peaks in the A15 structures.[192, 193, 198] Secondly, virtual circular apertures were positioned on the DP on the diffraction peaks of interest. A third type of image was created where instead of calculating the sum of intensity within an annular region, the variance in intensity is calculated, creating annular variance images.

As we know the step size that the 4D datasets were obtained with, the extent of brighter areas within the images can give an indication as to the size of ordered regions within the film.

Co-sputtered $MoSi_x$: Brighter spots in the annular VDF/variance images (Figures 4.8,4.9) were mostly found at the edges of the film, especially the lower edge where it connects to the substrate. This could be due to a chemical reaction and the incipient formation of a different structure that is verging on being more crystalline. VDF images from circular apertures (Figure 4.11) showed more detail within the central portion of the film, where bright spots mostly showed a combination of single pixels and small clusters of up to 4 pixels in size. It is not possible from these results to come up with an average size of these regions, however from the images inspected it appears that they could be up to 8 nm in size, suggesting that a small fraction of the film may contain larger ordered regions almost nanocrystalline in size, although the majority of the film has ordered regions more on the length scale of 1-2 nm.

Alloy $MoSi_x$: BF and Annular VDF images (Figure 4.14) did not show very large differences in intensity within the film, it appears that there are some brighter areas of single pixel, as well as some small clusters containing up to three bright pixels. The images that were formed using the circular apertures (Figures 4.16,4.17,4.18) showed a higher contrast between the bright and dark areas, where most of the brightest pixels were solitary, though there were some cases of two or three pixel clusters. Similar results were obtained using annular variance images (Figure 4.15, where there were a lot of bright single pixels, in addition to some clusters of two pixels. There was a higher contrast between bright/dark areas of the film in the annular variance images compared to the VDF images. These figures show that a small minority of ordered regions have longer range ordering of up to 6 nm in size, but the majority are on a lengthscale of less than 1 nm.

Co-sputtered $NbSi_x$: There were generally lighter/darker regions within the film shown in the BF and annular VDF images (Figure 4.21). Images from the 3 nm probe showed less contrast within the film than those obtained using the 2.6 nm and 1.2 nm probe, where there were areas of up to 2 pixels that appeared brighter than their surroundings, as well as solitary pixels. Images formed from the circular apertures (Figures 4.23,4.24,4.25) show mostly single pixel bright areas, although there are some instances where larger clusters appear. Annular variance images (Figure 4.22) showed bright single pixels, as well as some clusters of two pixels in size at the 1.2 nm probe size. Judging from the results here, the size of ordered areas could be up to 8 nm, although most of the areas appear to be much smaller, at around 2 nm.

Co-sputtered WSi_x: It is very difficult to see any brighter/darker areas within this film

Table 6.1: Estimated composition of SNSPD films from EELS-SI analysis.

Film	Composition Ratio (A:B)
Co-sputtered $MoSi_x$ A	76:24 ±2
Co-sputtered $MoSi_x$ B	83:17 ±2
Alloy sputtered $MoSi_x$	80:20 ±2
Co-sputtered $NbSi_x$	85:15 ±3
Co-sputtered WSi_x	NA

using any of the imaging techniques (Figures 4.28,4.29,4.30,4.31,4.32). Most of the brighter areas using all three techniques were found at the edges of the film and may arise from an altered chemistry at the interfaces, that doesn't represent the structure of the central part of the film.

EELS-SI analysis showed that the estimated composition of the films were richer in A (metal) atoms compared to the 3:1 ratio that A15 structures nominally have. Table 6.1 shows the estimated composition of all of the films. All three of the $MoSi_x$ samples were found to have slightly different compositions, although co-sputtered sample A was slightly thinner and there was a smaller region to make an estimate of the composition from. Co-sputtered $NbSi_x$ had a very high ratio of A:B, although A15 structures are known to sometimes have much higher amounts of A atoms.[174–178]

Improvements to the EELS results presented here could be obtained by conducting further experiments, as described below.

Recording EELS-SI datasets from standard samples would provide a better method than used here for a quantitative estimation of the composition of the films. Relevant edges could be collected using EELS-SI from a set of samples consisting of each element contained in the films.

Overall the structure of the films showed A15-like properties. This could be the reason why they work so well as superconductors. A lack of grain boundaries in these films could potentially reduce the scattering of Cooper pairs, which may improve the properties compared to the conventional polycrystalline A15 superconductors.

6.2 Temporal Fluctuations in the Diffraction Pattern

The final major area of investigation was how the glass structures investigated using FEM fluctuate with time. An area of the $NbSi_x$ film and its SiO_2 oxidised substrate, and both the Ti:Ta_2O_5 and SiO_2 layers of the A-LIGO multilayer coating were inspected.

Two different exposure times were used, these were 1 ms and 21.6 ms, 1000 DPs were collected at the 1 ms exposure time and 500 at the 21.6 ms exposure time.

Different techniques were used to analyse the temporal fluctuations in the patterns. The normalised variance of the DPs was calculated, intensity of various diffraction spots were tracked over time, and plots mapping differences in the DP over assorted time periods were calculated, and a statistical measure of overall pattern difference $g_2(t)$ was plotted as a function of time, then analysed and fitted with KWW stretched exponential curves.

Diffraction patterns remained more stable with time in the $NbSi_x$ and Ti:Ta_2O_5 glasses compared to the silica glasses.

In contrast to the metal containing glasses, the DPs obtained from the silica glasses were much less stable with time. After as little as 50 ms (1 ms exposure) the DPs no longer appear to share any significant structure.

Differences in the DP from the 1 ms exposure time were dominated by shot noise, and were not concentrated in the main diffuse scattering rings in the same way as DPs with 21.6 ms exposure time were.

FEM results showed that the DPs in the silica glasses change too quickly to be able to obtain spatial variance results. While the $NbSi_x$ and Ti:Ta_2O_5 glasses are more stable with time, there is still some temporal component to their FEM curve.

As expected from the FEM results, the $NbSi_x$ and Ti:Ta_2O_5 glasses showed a more consistent speckle intensity than the silica glasses. Generally, the Ta_2O_5 speckles were more consistent with time than those found in the $NbSi_x$ film. Intensity peaks from the silica glasses were much sharper, a trace of a speckle area for all patterns would result in a line that hovered around the mean intensity for most of the dataset, but with short sharp peaks in intensity. These peaks lasted longer when a lower beam current was used.

Electron correlation spectroscopy analysis corroborates that changes to the DP occur more slowly in the $NbSi_x$ and Ti:Ta_2O_5 glasses than the silica. Fitting KWW stretched exponential functions to $g_2(t)$ curves allowed the calculation of characteristic decay times τ from each material. Due to the high contribution of shot noise in the datasets acquired at 1 ms exposure time, ECM techniques were not used in those cases.

Estimates of τ and (β) were around 800 ms (0.7) in the $NbSi_x$ film, 2500 ms (1.2) in the Ti:Ta_2O_5, 80 ms (0.75) in the SiO_2 substrate and 153 ms (1.15) in the SiO_2 layer of the LIGO multilayer film. Both τ and β values varied in each dataset with some areas

of the diffraction pattern remaining more stable with time than others. Probe current may have played a part in the τ values in the silica, where a higher probe current was used in the SiO_2 substrate (19.5 pA) than the SiO_2 layer (4.0 pA), τ was shorter in the SiO_2 substrate than in the SiO_2 layer. There could be some effects from the dose rate and local heating of the sample, though this appears to be a minor effect as the change in the time constant is not very large compared to the difference in beam current. This suggests that the time constants are a real effect and a reasonable measurement of the time stability of glasses in the absence of an electron beam.

Spatial measurements, either from FEM or VDF techniques could be affected by the time stability of the material being inspected. For example, if an exposure time of 100 ms per pixel is used to acquire a 50×5 set of DPs, there is a time difference of 100 ms between adjacent points horizontally, but 5000 ms vertically. For a material with a time constant less than 5000 ms, this would mean that DPs from adjacent vertical pixels are no longer correlated.

6.3 Final Conclusions

Conducting scanned diffraction experiments using a direct electron detector works well and allows for shorter exposure times or lower beam currents than with older detectors.

Normalised variances were measured in a range of substances demonstrating clear SRO in accordance with expectations. Estimates of the lengthscale for MRO using VR-FEM were problematic due to restrictions of the microscope setup used for this work, but suggest average lengthscales around 1 nm or less in most cases. VDF imaging is consistent with this, but does reveal that there are occasional ordered regions on the scale of a few nm, suggesting that a minority of volumes may be verging on nanocrystalline.

Studies of glass stability as a function of time found that all the glasses examined in this thesis do change structure with time, but whichever method is used, they have different rates of change with time, where silica is the least stable and Ta_2O_5 is most stable. This may restrict how much information can be determined using spatial variation in FEM, and especially in SiO_2, the structure has so little stability with time that any spatial variances are probably meaningless.

6.4 Future Work

Further FEM experiments on the same silicides and Ti:Ta_2O_5 should focus on creating the most coherent probe possible, by using a very low beam current, the largest spot size and the smallest condenser aperture available. In addition to those parameters, the beam current should be kept constant for all of the probe sizes used and exposure time optimised. For VR-FEM experiments, it would be necessary to use a microscope with a more flexible condenser lens system, enabling the formation of the desired range of probe sizes to get a better idea of lengthscale of MRO.

Better EELS quantification could be carried out on the WSi_x film to estimate its composition. While the W $M_{4,5}$ edges are very close to the Si K edge, it may be possible to collect data from the Si $L_{2,3}$ edge at around 99 eV or W $N_{4,5}$ edge at 250 eV. Harry *et al.* have previously used the Ta $N_{4,5}$ for quantification. [30] A method used by Craven *et al.*, consisting of MLLS fitting could also be used without changing the edges recorded, although the high amount of W in the film would result in large errors.[194]

Additional investigations of time variance across different glasses could be carried out. More systematic studies of dose rate effects could be done to separate natural time variation from beam induced variation from heating. There are possible applications to different variants of the same glass, e.g. different pure SiO_2 and SiO_2 based glasses, or Ta_2O_5 containing varying quantities of TiO_2 or ZrO_2. The latter may be very relevant to the story of mechanical losses and thus thermal noise and loss in application in gravitational wave detection.[229] Utilising a range of different probe parameters including probe size, beam current and beam energy would provide a more rounded understanding on the timescales at which structure of the materials change. Datasets could also be collected over longer timescales for the samples where the DPs are more stable with time, such as in the $NbSi_x$ and Ti:Ta_2O_5 glasses here.

Use of higher convergence angles and VDF imaging could be used to study more explicitly the lengthscale of MRO. This might work in very thin specimens prepared by low energy FIB, with a probe angle set to give about 5 Angstrom resolution. Obviously this technique could only be used in materials that have reasonable time stability, like Ta2O5 blends.

Bibliography

[1] E. Rutherford. "The scattering of α and β particles by matter and the structure of the atom". In: *Philos. Mag.* 21.125 (1911), pp. 669–688.

[2] N. Bohr. "On the constitution of atoms and molecules". In: *Philos. Mag.* 26.151 (1913), pp. 1–25.

[3] W. H. Bragg and W. L. Bragg. "The Reflection of X-rays by Crystals". In: *Proc. R. Soc. A Math. Phys. Eng. Sci.* 88.605 (1913), pp. 428–438.

[4] K. Alberi et al. "The 2019 materials by design roadmap". In: *J. Phys. D. Appl. Phys.* 52.1 (2019).

[5] G. K. H. Madsen. "Automated Search for New Thermoelectric Materials: The Case of LiZnSb". In: *J. Am. Chem. Soc.* 128.37 (2006).

[6] W. S. Yang et al. "Iodide management in formamidinium-lead-halide based perovskite layers for efficient solar cells". In: *Science (80-.).* 356.6345 (2017), pp. 1376–1379.

[7] R. Gómez-Bombarelli et al. "Design of efficient molecular organic light-emitting diodes by a high-throughput virtual screening and experimental approach". In: *Nat. Mater.* 15.10 (2016), pp. 1120–1127.

[8] J. M. Phillips et al. "Research challenges to ultra-efficient inorganic solid-state lighting". In: *Laser Photon. Rev.* 1.4 (2007), pp. 307–333.

[9] J. Dou et al. "Operando chemistry of catalyst surfaces during catalysis". In: *Chem. Soc. Rev.* 46.7 (2017), pp. 2001–2027.

[10] G. Hautier et al. "Novel mixed polyanions lithium-ion battery cathode materials predicted by high-throughput ab initio computations". In: *J. Mater. Chem.* 21.43 (2011), p. 17147.

[11] Y. J. Li et al. "Accelerated atomic-scale exploration of phase evolution in compositionally complex materials". In: *Mater. Horizons* 5.1 (2018), pp. 86–92.

[12] G. Hautier et al. "Identification and design principles of low hole effective mass p-type transparent conducting oxides". In: *Nat. Commun.* 4.1 (2013), p. 2292.

[13] T. Angsten, L. W. Martin, and M. Asta. "Orientation-dependent properties of epitaxially strained perovskite oxide thin films: Insights from first-principles calculations". In: *Phys. Rev. B* 95.17 (2017).

[14] *About the Materials Genome Initiative | Materials Genome Initiative.*

[15] T. Scott et al. *Economic Analysis of National Needs for Technology Infrastructure to Support the Materials Genome Initiative Final Report.* Tech. rep. 2018.

[16] T. D. Lee and A. U. Ebong. "A review of thin film solar cell technologies and challenges". In: *Renew. Sustain. Energy Rev.* 70 (2017).

[17] B. A. Andersson. “Materials availability for large-scale thin-film photovoltaics”. In: *Prog. Photovoltaics Res. Appl.* 8.1 (2000).

[18] T. Söderström et al. “Optimization of amorphous silicon thin film solar cells for flexible photovoltaics”. In: *J. Appl. Phys.* 103 (2008).

[19] R. Tsu et al. “Order-disorder transition in single-crystal silicon induced by pulsed UV laser irradiation”. In: *Phys. Rev. Lett.* 42 (1979).

[20] H. Bartzsch et al. “Properties of SiO2 and Al2O3 films for electrical insulation applications deposited by reactive pulse magnetron sputtering”. In: *Surf. Coatings Technol.* 174-175 (Sept. 2003), pp. 774–778.

[21] D.-T. Lu. “Very low resistance CoSi2 formation by metal vapour vacuum arc implantation into SiO2/Si and Si3N4/Si structures”. In: *Surf. Coatings Technol.* 128-129 (June 2000), pp. 192–198.

[22] V. Dřínek et al. “TEA CO2 pulsed laser deposition of silicon suboxide films”. In: *J. Non. Cryst. Solids* 288.1-3 (Aug. 2001), pp. 30–36.

[23] B. D. Jackson and P. R. Herman. “Vacuum–ultraviolet pulsed-laser deposition of silicon dioxide thin films”. In: *Appl. Surf. Sci.* 127-129 (May 1998), pp. 595–600.

[24] G. Kumar, H. X. Tang, and J. Schroers. “Nanomoulding with amorphous metals”. In: *Nature* 457.7231 (Feb. 2009), pp. 868–872.

[25] H. Liu, R. K. Zheng, and X. X. Zhang. “Observation of large Hall sensitivity in thin Fe–Ge amorphous composite films”. In: *J. Appl. Phys.* 98.8 (Oct. 2005), p. 086105.

[26] M. M. Trexler and N. N. Thadhani. “Mechanical properties of bulk metallic glasses”. In: *Prog. Mater. Sci.* 55.8 (Nov. 2010), pp. 759–839.

[27] T. Miyazaki et al. “Mechanism of bonelike apatite formation on bioactive tantalum metal in a simulated body fluid”. In: *Biomaterials* 23.3 (Feb. 2002), pp. 827–832.

[28] J. Oak, D. V. Louzguine-Luzgin, and A. Inoue. “Fabrication of Ni-free Ti-based bulk-metallic glassy alloy having potential for application as biomaterial, and investigation of its mechanical properties, corrosion, and crystallization behavior”. In: *J. Mater. Res.* 22.5 (May 2007), pp. 1346–1353.

[29] D. Gibson and C. MacGregor. “A Novel Solid State Non-Dispersive Infrared CO2 Gas Sensor Compatible with Wireless and Portable Deployment”. In: *Sensors* 13 (2013).

[30] G. M. Harry et al. “Titania-doped tantala/silica coatings for gravitational-wave detection”. In: *Class. Quantum Gravity* 24.2 (2007), pp. 405–415.

[31] W. H. Zachariasen. “The atomic arrangement in glass”. In: *J. Am. Chem. Soc.* 54 (1932).

[32] W. L. Bragg. “The Structure of Some Crystals as Indicated by Their Diffraction of X-rays”. In: *Proc. R. Soc. A Math. Phys. Eng. Sci.* 89 (1913).

[33] M. L. Rudee. “The Observation of Ordered Domains in Amorphous Ge by Dark-Field Electron Microscopy”. In: *Phys. Status Solidi* 46.1 (July 1971), K1–K3.

[34] M. L. Rudee and A. Howie. “The structure of amorphous Si and Ge”. In: *Philos. Mag.* 25.4 (Apr. 1972), pp. 1001–1007.

[35] P. Chaudhari, J. F. Graczyk, and S. R. Herd. “An Electron Microscope Investigation of the Structure of Some Amorphous Materials”. In: *Phys. Status Solidi* 51.2 (June 1972), pp. 801–820.

[36] A. Howie, O. L. Krivanek, and M. L. Rudee. “Interpretation of electron micrographs and diffraction patterns of amorphous materials”. In: *Philos. Mag.* 27 (1973).

[37] W. Cochran. “Theory of electron micrographs of amorphous materials”. In: *Phys. Rev. B* 8 (1973).

[38] D. Polk and D. Boudreaux. “Tetrahedrally Coordinated Random-Network Structure”. In: *Phys. Rev. Lett.* 31.2 (1973), pp. 92–95.

[39] J. D. Bernal. “A geometrical approach to the structure Of liquids”. In: *Nature* 183 (1959).

[40] J. D. Bernal, J. Mason, and K. R. Knight. “Radial distribution of the random close packing of equal spheres”. In: *Nature* 194 (1962).

[41] G. D. Scott and D. M. Kilgour. “The density of random close packing of spheres”. In: *J. Phys. D. Appl. Phys.* 2 (1969).

[42] T. Sontheimer et al. “Challenges and opportunities of electron beam evaporation in the preparation of poly-Si thin film solar cells”. In: *2010 35th IEEE Photovolt. Spec. Conf.* IEEE, June 2010, pp. 000614–000619.

[43] O. Nilsen et al. “Simulation of growth dynamics in atomic layer deposition. Part I. Amorphous films”. In: *Thin Solid Films* 515.11 (Apr. 2007), pp. 4527–4537.

[44] M. Raible et al. “Amorphous thin-film growth: Theory compared with experiment”. In: *Europhys. Lett.* 50.1 (Apr. 2000), pp. 61–67.

[45] T. Moustakas. “Studies of thin-film growth of sputtered hydrogenated amorphous silicon”. In: *Sol. Energy Mater.* 8.1-3 (Nov. 1982), pp. 187–204.

[46] P. Duwez. “Structure and Properties of Glassy Metals”. In: *Annu. Rev. Mater. Sci.* 6.1 (Aug. 1976), pp. 83–117.

[47] B. Y. Tsaur, Z. L. Liau, and J. W. Mayer. “Ion-beam-induced silicide formation”. In: *Appl. Phys. Lett.* 34.2 (Jan. 1979), pp. 168–170.

[48] J. Keller. “Geometrical theory of diffraction”. In: *J. Opt. Soc. Am.* 52.2 (1962), pp. 116–130.

[49] B. K. Vainshtein. *Structure Analysis by Electron Diffraction*. Pergamon Press, 1964, p. 420.

[50] T. Tietz. “Electron Scattering Cross Section with Relativistic Correction Based on the Thomas-Fermi Theory”. In: *Phys. Rev.* 113.4 (1959), pp. 1056–1057.

[51] D. J. Hughes and R. B. Schwartz. *Neutron cross sections: supplement*. Neutron Cross Sections. Brookhaven National Laboratory, 1958, p. 228.

[52] J. H. Hubbell. “Review and history of photon cross section calculations”. In: *Phys. Med. Biol.* 51.13 (2006).

[53] Z. H. Stachurski. “On structure and Properties of amorphous materials”. In: *Materials (Basel).* 4.9 (2011), pp. 1564–1598.

[54] D. A. Keen. “A comparison of various commonly used correlation functions for describing total scattering”. In: *J. Appl. Crystallogr.* 34.2 (2001), pp. 172–177.

[55] J. J. Rehr. “Theoretical approaches to x-ray absorption fine structure”. In: 72.3 (2000), pp. 621–654.

[56] P. A. Lee et al. “Extended x-ray absorption fine structure - its strengths and limitations as a structural tool”. In: 53.4 (1981), pp. 769–806.

[57] R. Bassiri et al. “Order within disorder: The atomic structure of ion-beam sputtered amorphous tantala (a-Ta2O5)”. In: *APL Mater.* 3.3 (2015), p. 036103.

[58] B. E. Warren. “X-ray diffraction”. In: *Analysis* (1990).

[59] B. Shyam et al. “Measurement and Modeling of Short and Medium Range Order in Amorphous Ta2O5 Thin Films”. In: *Sci. Rep.* 6.1 (2016).

[60] C. Shull. “Early development of neutron scattering”. In: *Rev. Mod. Phys.* 67.4 (1995), pp. 753–757.

[61] *Press release: The 1994 Nobel Prize in Physics.*

[62] R. N. Sinclair et al. “Neutron diffraction studies of amorphous solids”. In: *J. Non. Cryst. Solids* 42.1-3 (Oct. 1980), pp. 107–115.

[63] S. Kugler et al. “Structure of evaporated pure amorphous silicon: Neutron-diffraction and reverse Monte Carlo investigations”. In: *Phys. Rev. B* 48.10 (1993), pp. 7685–7688.

[64] *The Nobel Prize in Physics 1937.*

[65] L. de Broglie. “XXXV. A tentative theory of light quanta”. In: *Philos. Mag. Ser. 6* 47.278 (1924), pp. 446–458.

[66] H. Busch. “Calculation of the channel of the cathode rays in axial symmetric electromagnetic fields”. In: *Ann. Phys.* 81.25 (Dec. 1926), pp. 974–993.

[67] R. Rudenberg. “Origin and Background of the Invention of the Electron Microscope”. In: *Adv. Imaging Electron Phys.* 2010, pp. 171–205.

[68] *The Nobel Prize in Physics 1986.*

[69] A. B. Yankovich et al. “Picometre-precision analysis of scanning transmission electron microscopy images of platinum nanocatalysts”. In: *Nat. Commun.* 5.May (2014), pp. 1–7.

[70] *Electron scattering from an isolated atom.*

[71] E. Takeshi. “Structure of Amorphous Materials”. In: *Pergamon Mater. Ser.* Vol. 16. Pergamon, Jan. 2012, pp. 455–465.

[72] D. B. Williams and C. B. Carter. “Elastic Scattering”. In: *Transm. Electron Microsc.* Boston, MA: Springer US, 2009, pp. 39–51.

[73] D. J. Cockayne. “The Study of Nanovolumes of Amorphous Materials Using Electron Scattering”. In: *Annu. Rev. Mater. Res.* 37.1 (2007), pp. 159–187.

[74] R. Bassiri. “The Atomic Structure and Properties of Mirror Coatings for use in Gravitational Wave Detectors”. PhD Thesis. University of Glasgow, 2011.

[75] K. L. Evans. “Computational Modelling of Amorphous mirror coatings for use in Advanced Gravitational wave detectors”. PhD thesis. University of Glasgow, 2012.

[76] M. J. Hart. “Amorphous Mirror Coatings for Ultra-High Precision Interferometry”. PhD thesis. University of Glasgow, 2017.

[77] C. Ophus. “Four-Dimensional Scanning Transmission Electron Microscopy (4D-STEM): From Scanning Nanodiffraction to Ptychography and Beyond”. In: *Microsc. Microanal.* 25.3 (June 2019), pp. 563–582.

[78] M. Krajnak et al. “Pixelated detectors and improved efficiency for magnetic imaging in STEM differential phase contrast”. In: *Ultramicroscopy* 165 (2016), pp. 42–50.

[79] H. Yang et al. “4D STEM: High efficiency phase contrast imaging using a fast pixelated detector”. In: *J. Phys. Conf. Ser.* 644.1 (2015).

[80] M. M. J. Treacy and J. M. Gibson. “Variable Coherence Microscopy: a Rich Source of Structural Information from Disordered Materials”. In: *Acta Crystallogr. Sect. A Found. Crystallogr.* 52.2 (1996), pp. 212–220.

[81] P. M. Voyles and D. A. Muller. “Fluctuation microscopy in the STEM”. In: *Ultramicroscopy* 93.2 (2002), pp. 147–159.

[82] E. F. Rauch and M. Véron. “Virtual dark-field images reconstructed from electron diffraction patterns”. In: *Eur. Phys. J. Appl. Phys.* 66.1 (2014), p. 10701.

[83] J. Hillier and R. F. Baker. “Microanalysis by means of electrons”. In: *J. Appl. Phys.* 15.9 (1944), pp. 663–675.

[84] I. MacLaren et al. “Performing EELS at higher energy losses at both 80 and 200 kV”. In: *Adv. Imaging Electron Phys.* 210 (Jan. 2019), pp. 299–355.

[85] J. Melngailis. “Focused ion beam technology and applications”. In: *J. Vac. Sci. Technol. B* 5 (1987).

[86] V. E. Krohn and G. R. Ringo. “Ion source of high brightness using liquid metal”. In: *Appl. Phys. Lett.* 27 (1975).

[87] S. Kellogg et al. “High Throughput Sample Preparation and Analysis Using an Inductively Coupled Plasma (ICP) Focused Ion Beam Source”. In: *Microsc. Microanal.* 16 (2010).

[88] R. Kelley et al. “Xe+ FIB Milling and Measurement of Amorphous Silicon Damage”. In: *Microsc. Microanal.* 19 (2013).

[89] L. Giannuzzi and F. Stevie. *Introduction to Focused Ion Beams*. Ed. by L. Giannuzzi and F. Stevie. Springer, 2005.

[90] J. F. Einsle et al. “Hybrid FIB milling strategy for the fabrication of plasmonic nanostructures on semiconductor substrates”. In: *Nanoscale Res. Lett.* 6 (2011), pp. 1–5.

[91] K. Pandey et al. “The impact of focused ion beam induced damage on scanning spreading resistance microscopy measurements”. In: *Sci. Rep.* 10.1 (2020), pp. 1–15.

[92] L. Giannuzzi and N. Smith. “ TEM Specimen Preparation with Plasma FIB Xe + Ions ”. In: *Microsc. Microanal.* 17.S2 (2011), pp. 646–647.

[93] T. L. Burnett et al. “Large volume serial section tomography by Xe Plasma FIB dual beam microscopy.” eng. In: *Ultramicroscopy* 161 (Feb. 2016), pp. 119–129.

[94] T. Hrnčíř et al. *Novel Plasma FIB/SEM for High Speed Failure Analysis and Real Time Imaging of Large Volume Removal*. Nov. 2012.

[95] S. Bals et al. “High-quality sample preparation by low kV FIB thinning for analytical TEM measurements”. In: *Microsc. Microanal.* 14 (2007).

[96] J. P. McCaffrey, M. W. Phaneuf, and L. D. Madsen. “Surface damage formation during ion-beam thinning of samples for transmission electron microscopy”. In: *Ultramicroscopy* 87 (2001).

[97] V. Beck. “Hexapole Spherical-Aberration Corrector”. In: *Optik (Stuttg).* 53.4 (1979), pp. 241–255.

[98] O. L. Krivanek, N. Dellby, and A. R. Lupini. “Towards sub-Å electron beams”. In: *Ultramicroscopy* 78.1-4 (1999), pp. 1–11.

[99] P. W. Hawkes. “Aberration correction past and present”. In: *Philos. Trans. R. Soc. A Math. Phys. Eng. Sci.* 367.1903 (2009), pp. 3637–3664.

[100] R. Leary and R. Brydson. “Chromatic Aberration Correction: The Next Step in Electron Microscopy”. In: *Adv. Imaging Electron Phys.* 165 (2011), pp. 73–130.

[101] A. V. Crewe et al. “Electron Gun Using a Field Emission Source”. In: *Rev. Sci. Instrum.* 39.4 (1968), pp. 576–583.

[102] Y. Rong. *Characterization of Microstructures by Analytical Electron Microscopy (AEM).* Berlin, Heidelberg: Springer Berlin Heidelberg, 2012.

[103] C. Kleint. “Surface diffusion model of adsorption-induced field emission flicker noise. II. Experiments”. In: *Surf. Sci.* 25.2 (1971), pp. 411–434.

[104] K. S. Yeong and J. T. Thong. “Life cycle of a tungsten cold field emitter”. In: *J. Appl. Phys.* 99.10 (2006).

[105] D. Williams and C. Carter. “Lenses, Apertures and Resolution”. In: *Transm. Electron Microsc.* 2009, pp. 91–114.

[106] A. J. Craven et al. “Getting the most out of a post-column EELS spectrometer on a TEM/STEM by optimising the optical coupling”. In: *Ultramicroscopy* 180 (Sept. 2017), pp. 66–80.

[107] I. MacLaren et al. “EELS at very high energy losses”. In: *Microscopy* 67 (2018).

[108] H. H. Rose. “Optics of high-performance electron microscopes”. In: *Sci. Technol. Adv. Mater.* 9.1 (2008).

[109] A. V. Crewe, J. Wall, and J. Lanomore. “Visibility of single atoms”. In: *Science (80-.).* (1970).

[110] S. J. Pennycook and D. E. Jesson. “High-resolution Z-contrast imaging of crystals”. In: *Ultramicroscopy* 37 (1991), pp. 14–38.

[111] D. A. Moncrieff and P. R. Barker. “Secondary electron emission in the scanning electron microscope”. In: *Scanning* 54 (1978).

[112] M. W. Tate et al. “High Dynamic Range Pixel Array Detector for Scanning Transmission Electron Microscopy”. In: *Microsc. Microanal.* 22 (2016).

[113] R. Ritz et al. “Scanning electron diffraction using the pnCCD (S)TEM Camera”. In: *Eur. Microsc. Congr. 2016 Proc.* Weinheim, Germany: Wiley-VCH Verlag GmbH & Co. KGaA, Dec. 2016, pp. 641–642.

[114] H. Ryll et al. “A pnCCD-based, fast direct single electron imaging camera for TEM and STEM”. In: *J. Instrum.* 11.04 (Apr. 2016).

[115] R. Ballabriga et al. “Medipix3 : A 64 k pixel detector readout chip working in single photon counting mode with improved spectrometric performance”. In: *Nucl. Inst. Methods Phys. Res. A* 633 (2011), S15–S18.

[116] G. McMullan et al. “Electron imaging with Medipix2 hybrid pixel detector”. In: *Ultramicroscopy* 107.4-5 (2007), pp. 401–413.

[117] J. A. Mir et al. “Medipix3- Demonstration and understanding of near ideal detector performance for 60 & 80 keV electrons”. In: *Ultramicroscopy* 182.August (2016), pp. 44–53. arXiv: 1608.07586.

[118] J. Scott et al. “Near-simultaneous dual energy range EELS spectrum imaging”. In: *Ultramicroscopy* 108.12 (2008), pp. 1586–1594.

[119] A. Gubbens et al. “The GIF Quantum, a next generation post-column imaging energy filter”. In: *Ultramicroscopy* 110.8 (2010), pp. 962–970.

[120] G. Lucas et al. “Multivariate statistical analysis as a tool for the segmentation of 3D spectral data”. In: *Micron* 52-53 (2013).

[121] J. Spiegelberg and J. Rusz. “Can we use PCA to detect small signals in noisy data?” In: *Ultramicroscopy* 172 (2017).

[122] S. Lichtert and J. Verbeeck. “Statistical consequences of applying a PCA noise filter on EELS spectrum images”. In: *Ultramicroscopy* 125 (2013).

[123] R. F. Egerton. *Electron Energy Loss Spectroscopy in the Electron Microscope*. Third Edit. Springer, 2011, p. 250.

[124] R. D. Leapman, P. Rez, and D. F. Mayers. “K, L, and M shell generalized oscillator strengths and ionization cross sections for fast electron collisions”. In: *J. Chem. Phys.* 72 (1980).

[125] P. Rez. “Cross-sections for energy loss spectrometry”. In: *Ultramicroscopy* 9 (1982).

[126] H. Römer. *Theoretical optics : an introduction*. Wiley-VCH, 2009, p. 372.

[127] H. Köhler. “On Abbe’s theory of image formation in the microscope”. In: *Opt. Acta (Lond).* 28 (1981).

[128] *NanoMEGAS Topspin*.

[129] A. Garner et al. “The microstructure and microtexture of zirconium oxide films studied by transmission electron backscatter diffraction and automated crystal orientation mapping with transmission electron microscopy”. In: *Acta Mater.* 80 (2014), pp. 159–171.

[130] S. N. Bogle et al. “Quantifying nanoscale order in amorphous materials: simulating fluctuation electron microscopy of amorphous silicon”. In: *J. Phys. Condens. Matter* 19.45 (2007), p. 455204.

[131] F. Yi and P. M. Voyles. “Analytical and computational modeling of fluctuation electron microscopy from a nanocrystal/amorphous composite”. In: *Ultramicroscopy* 122 (2012).

[132] J. M. Gibson, M. M. Treacy, and P. M. Voyles. “Atom pair persistence in disordered materials from fluctuation microscopy”. In: *Ultramicroscopy* 83.3-4 (2000), pp. 169–178.

[133] J. M. Gibson and M. M. Treacy. “Diminished medium-range order observed in annealed amorphous germanium”. In: *Phys. Rev. Lett.* 78.6 (1997), pp. 1074–1077.

[134] J. M. Gibson et al. “Structural disorder induced in hydrogenated amorphous silicon by light soaking”. In: *Appl. Phys. Lett.* 73.21 (1998), pp. 3093–3095.

[135] J.-y. Cheng, J. Gibson, and D. Jacobson. “Observations of structural order in ion-implanted amorphous silicon”. In: *J. Mater. Res.* 16.11 (2001), pp. 3030–3033.

[136] P. M. Voyles et al. “Increased medium-range order in amorphous silicon with increased substrate temperature”. In: *J. Non. Cryst. Solids* 295 (2001), pp. 45–52.

[137] L. N. Nittala et al. “Hydrogen-induced modification of the medium-range structural order in amorphous silicon films”. In: *Appl. Phys. Lett.* 87.24 (2005), pp. 1–3.

[138] S. N. Bogle et al. “Size analysis of nanoscale order in amorphous materials by variable-resolution fluctuation electron microscopy”. In: *Ultramicroscopy* 110.10 (2010), pp. 1273–1278.

[139] P. M. Voyles et al. “Absence of an Abrupt Phase Change from Polycrystalline to Amorphous in Silicon with Deposition Temperature”. In: *Phys. Rev. Lett.* 86.24 (2001), pp. 5514–5517.

[140] K. Darmawikarta et al. “Quasi-equilibrium size distribution of subcritical nuclei in amorphous phase change AgIn-Sb2Te”. In: *J. Appl. Phys.* 114.3 (2013).

[141] W. G. Stratton et al. “Aluminum nanoscale order in amorphous Al92 Sm8 measured by fluctuation electron microscopy”. In: *Appl. Phys. Lett.* 86.14 (2005), pp. 1–3.

[142] M. H. Kwon et al. “Nanometer-scale order in amorphous Ge2Sb2Te5 analyzed by fluctuation electron microscopy”. In: *Appl. Phys. Lett.* 90.2 (2007).

[143] B. Lee et al. “Observation of the Role of Subcritical Nuclei in Crystallization of a Glassy Solid”. In: *Science (80-.).* 326.November (2009), pp. 980–985.

[144] J. Hwang and P. M. Voyles. “Variable Resolution Fluctuation Electron Microscopy on Cu-Zr Metallic Glass Using a Wide Range of Coherent STEM Probe Size”. In: *Microsc. Microanal.* 17 (2011), pp. 67–74.

[145] A. Yan et al. “Multi-scale order in amorphous transparent oxide thin films”. In: *J. Appl. Phys.* 112 (2012).

[146] J. M. Gibson et al. “Substantial Crystalline Topology in Amorphous Silicon”. In: *Phys. Rev. Lett.* 105.12 (2010), p. 125504.

[147] T. T. Li, K. Darmawikarta, and J. R. Abelson. “Quantifying nanoscale order in amorphous materials via scattering covariance in fluctuation electron microscopy”. In: *Ultramicroscopy* 133 (2013), pp. 95–100.

[148] R. Bassiri et al. “Investigating the medium range order in amorphous Ta2O5 coatings”. In: *J. Phys. Conf. Ser.* 522 (2014), p. 012043.

[149] M. J. Hart et al. “Medium range structural order in amorphous tantala spatially resolved with changes to atomic structure by thermal annealing”. In: *J. Non. Cryst. Solids* 438 (2016), pp. 10–17.

[150] M. M. J. Treacy et al. “Fluctuation microscopy: a probe of medium range order”. In: *Reports Prog. Phys.* 68.12 (2005), pp. 2899–2944.

[151] J. M. Gibson and M. M. Treacy. “Diminished medium-range order observed in annealed amorphous germanium”. In: *Phys. Rev. Lett.* (1997).

[152] M. Treacy and J. Gibson. “Coherence and multiple scattering in “Z-contrast” images”. In: *Ultramicroscopy* 52.1 (1993), pp. 31–53.

[153] A. Howie. “High resolution electron microscopy of amorphous thin films”. In: *J. Non. Cryst. Solids* 31.1-2 (1978), pp. 41–55.

[154] M. Nord et al. “Towards Mapping Perovskite Oxide 3-D Structure Using Two-Dimensional Pixelated STEM Detector”. In: *Microsc. Microanal.* 22.S3 (2016), pp. 476–477.

[155] O. Kamerlingh. “Communications - Leiden 120b”. In: *Proceeding K. Akad. van Wet. Te Amsterdam* 120b (1911), pp. 1479–1481.

[156] W. Meissner and R. Ochsenfeld. “Ein neuer Effekt bei Eintritt der Supraleitfähigkeit”. In: *Naturwissenschaften* 21.44 (1933), pp. 787–788.

[157] J. Bardeen, L. N. Cooper, and J. R. Schrieffer. “Theory of super conductivity”. In: *Theory Supercond.* (2018), pp. 1–332.

[158] G. N. Gol’tsman et al. “Picosecond superconducting single-photon optical detector Picosecond superconducting single-photon optical detector”. In: *Appl. Phys. Lett.* 79.6 (2001), pp. 705–707.

[159] C. M. Natarajan, M. G. Tanner, and R. H. Hadfield. “Superconducting nanowire single-photon detectors: Physics and applications”. In: *Supercond. Sci. Technol.* 25.6 (2012), p. 063001.

[160] E. A. Dauler et al. “Review of superconducting nanowire single-photon detector system design options and demonstrated performance”. In: *Opt. Eng.* 53.8 (2014).

[161] H. Hartmann, F. Ebert, and O. Bretschneider. “Elektrolysen in Phosphatschmelzen. I. Die Elektrolytische Gewinnung von alpha- und beta-Wolfram”. In: *Z. Anorg. Allg. Chem.* 198.1 (1931), pp. 116–140.

[162] G. F. Hardy and J. K. Hulm. “Superconducting Silicides and Germanides”. In: *Phys. Rev.* 89.4 (Feb. 1953), pp. 884–884.

[163] Y. A. Izyumov and Z. Kurmaev. “Physical properties and electronic structure of superconducting compounds with the β-tungsten structure”. In: *Sov. Phys. Usp.* 17.3 (1974), pp. 356–380.

[164] J. R. Gavaler. “Superconductivity in Nb-Ge films above 22 K”. In: *Appl. Phys. Lett.* 23.8 (1973), pp. 480–482.

[165] B. W. Roberts. “Survey of superconductive materials and critical evaluation of selected properties”. In: *J. Phys. Chem. Ref. Data* 5.3 (1976), pp. 581–822.

[166] H. D. Wiesinger. “Metallkundliche Möglichkeiten zur Erhöhung der Sprungtemperatur zur Supraleitung von A15-Phasen”. In: *Physi. Status Solidi A* 41.2 (1977), pp. 465–479.

[167] J. Muller. “A15-type superconductors”. In: *Rep. Prog. Phys.* 43.3 (1980), pp. 641–687.

[168] H. M. Tütüncü, S. Bağcı, and G. P. Srivastava. “Electronic structure, phonons, and electron-phonon interaction in Mo3Si”. In: *Phys. Rev. B* 82.21 (Dec. 2010), p. 214510.

[169] A. E. Karkin et al. “Specific Heat of Nb3Sn Irradiated by Fast Neutrons”. In: *Phys. Status Solidi (a)* 61 (1980), pp. 117–122.

[170] M. Lehmann et al. “Disordered A15 compounds from the Matthias-Valley: Mo3Ge and Mo3Si”. In: *Physica* 107 (1981), pp. 473–474.

[171] B. A. Aleksashin et al. “Effect of disordering on properties of high-temperature superconductors”. In: *Phys. C* 153 (1988), pp. 339–340.

[172] A. E. Karkin et al. “Superconducting properties of the atomically disordered MgB2 compound”. In: *J. Exp. Theor. Phys. Lett.* 73.10 (May 2001), pp. 570–572.

[173] G. R. Stewart, B. Olinger, and L. R. Newkirk. “Specific Heat of A-15 Nb3Si Produced by Explosive Compression”. In: *Solid State Commun.* 39.i (1981), pp. 5–9.

[174] A. L. Giorgi and B. T. Matthias. “Unusual superconducting behavior of the molybdenum-technetium system”. In: *Phys. Rev. B* 17.5 (Mar. 1978), pp. 2160–2162.

[175] A. Giorgi, B. Matthias, and G. Stewart. “Discovery of a superconducting A-15 phase in the V-Re system”. In: *Solid State Commun.* 27.3 (July 1978), pp. 291–294.

[176] G. R. Stewart, L. R. Newkirk, and F. A. Valencia. “Impurity stabilized A15 Nb3Nb - a new superconductor”. In: *Phys. Rev. B* 21.11 (June 1980), pp. 5055–5064.

[177] M. Aindow et al. “On the origins of ‘forbidden’ 100-type spots in electron diffraction patterns from the A15 compounds Nb3Al, Cr3Si and V3Si”. In: *Philos. Mag. Lett.* 69.1 (1994), pp. 23–30.

[178] A. Junod et al. “Superconductivity, density-of-states models, and specific heat of A15-type compounds V-Ga and V-Si”. In: *J. Low Temp. Phys.* 5.1 (July 1971), pp. 25–43.

[179] V. M. Svechnikov, L. M. Yupko, and Y. O. Kocherzh. “Investigation of Phase Equilibria in Alloys of Silicon With Molybdenum and Titanium”. In: *Lect. Acad. Sci. Ukr. SSR* 6 (1972), p. 570.

[180] J. Jorda, R. Flükiger, and J. Muller. “A New metallurgical investigation of the niobium-aluminium system”. In: *J. Less Common Met.* 75.2 (Nov. 1980), pp. 227–239.

[181] W. Buckel. “Elektronenbeugungs Aufnahmen von dunnen Metallschichten bei tiefen Temperaturen”. In: *Z. Phys.* 138.2 (Apr. 1954), pp. 136–150.

[182] C. C. Tsuei. “Amorphous Superconductors”. In: *Supercond. Mater. Sci. Metall. Fabr. Appl.* Boston, MA: Springer US, 1981, pp. 735–756.

[183] W. L. Johnson and S. J. Poon. “Superconductivity in amorphous and microcrystalline transition-metal alloys”. In: *J. Appl. Phys.* 46.4 (1975), pp. 1787–1792.

[184] G. Bergmann. “Amorphous metals and their superconductivity”. In: *Phys. Rep.* 27.4 (Sept. 1976), pp. 159–185.

[185] E. Havinga. “Bandstructure and superconductivity of non-transition metals”. In: *Phys. Lett. A* 26.6 (Feb. 1968), pp. 244–246.

[186] M. Collver and R. Hammond. “Superconductivity in ”Amorphous” Transition-Metal Alloy Films”. In: *Phys. Rev. Lett.* 30.3 (1973), pp. 92–95.

[187] P. Watson et al. “Superconductivity in 3d series amorphous transition metal alloys”. In: *Mater. Sci. Eng.* 99.1-2 (1988), pp. 175–178.

[188] A. Banerjee et al. “Characterisation of amorphous molybdenum silicide (MoSi) superconducting thin films and nanowires”. In: *Supercond. Sci. Technol.* 30.8 (2017).

[189] *fpd.*

[190] M. M. J. Treacy, J. M. Gibson, and P. J. Keblinski. “Paracrystallites found in evaporated amorphous tetrahedral semiconductors”. In: *J. Non. Cryst. Solids* 231.1-2 (1998), pp. 99–110.

[191] A. Rezikyan et al. “Speckle Suppression by Decoherence in Fluctuation Electron Microscopy.” In: *Microsc. Microanal.* 21.6 (2015), pp. 1455–1474.

[192] A. Norlund Christensen. “Preparation and Characterization of Mo3Si and Mo5Si3”. In: *Acta Chem. Scand.* A37 (1983), pp. 519–522.

[193] W. K. Wang et al. “Crystallization characteristics of an amorphous Nb81Si19 alloy under high pressure and formation of the A15 phase”. In: *J. Mater. Sci.* 17.5 (1982), pp. 1523–1532.

[194] A. J. Craven et al. “Spectrum imaging of complex nanostructures using DualEELS: II. Absolute quantification using standards”. In: *Ultramicroscopy* 186 (2018), pp. 66–81.

[195] F. Yi and P. M. Voyles. “Effect of sample thickness, energy filtering, and probe coherence on fluctuation electron microscopy experiments”. In: *Ultramicroscopy* 111.8 (2011), pp. 1375–1380.

[196] T. T. Li, S. N. Bogle, and J. R. Abelson. “Quantitative fluctuation electron microscopy in the STEM: Methods to identify, avoid, and correct for artifacts”. In: *Microsc. Microanal.* 20.5 (2014), pp. 1605–1618.

[197] D. Radić et al. “Comparison of Experimental STEM Conditions for Fluctuation Electron Microscopy”. In: *Microsc. Microanal.* 26.6 (2020), pp. 1100–1109.

[198] S. Basavaiah and S. R. Pollack. “Superconductivity in beta-tungsten films”. In: *J. Appl. Phys.* 39.12 (1968), pp. 5548–5556.

[199] W. A. Phillips. “Tunneling states in amorphous solids”. In: *J. Low Temp. Phys.* 7 (1972).

[200] P. W. Anderson, B. I. Halperin, and C. M. Varma. “Anomalous low-temperature thermal properties of glasses and spin glasses”. In: *Philos. Mag.* (1972).

[201] K. S. Gilroy and W. A. Phillips. “An asymmetric double-well potential model for structural relaxation processes in amorphous materials”. In: *Philos. Mag. B Phys. Condens. Matter; Stat. Mech. Electron. Opt. Magn. Prop.* 43 (1981).

[202] M. R. Abernathy, X. Liu, and T. H. Metcalf. “An overview of research into low internal friction optical coatings by the gravitational wave detection community”. In: *Mater. Res.* 21 (2018).

[203] J. P. Trinastic et al. “Unified interatomic potential and energy barrier distributions for amorphous oxides”. In: *J. Chem. Phys.* (2013).

[204] R. Hamdan, J. P. Trinastic, and H. P. Cheng. “Molecular dynamics study of the mechanical loss in amorphous pure and doped silica”. In: *J. Chem. Phys.* 141.5 (2014).

[205] J. P. Trinastic et al. “Molecular dynamics modeling of mechanical loss in amorphous tantala and titania-doped tantala”. In: *Phys. Rev. B* 93.014105 (2016).

[206] C. R. Billman et al. “Origin of the second peak in the mechanical loss function of amorphous silica”. In: *Phys. Rev. B* 95.014109 (2017).

[207] N. Jiang. “Electron beam damage in oxides: A review”. In: *Reports Prog. Phys.* 79.1 (2015).

[208] B. P. Abbott et al. “Observation of gravitational waves from a binary black hole merger”. In: *Phys. Rev. Lett.* 116.061102 (2016).

[209] B. P. Abbott et al. “GW151226: Observation of Gravitational Waves from a 22-Solar-Mass Binary Black Hole Coalescence”. In: *Phys. Rev. Lett.* 116.241103 (2016).

[210] B. P. Abbott et al. “GW170104: Observation of a 50-Solar-Mass Binary Black Hole Coalescence at Redshift 0.2”. In: *Phys. Rev. Lett.* 118.221101 (2017). arXiv: 1706.01812.

[211] B. P. Abbott et al. “GW170814: A Three-Detector Observation of Gravitational Waves from a Binary Black Hole Coalescence”. In: *Phys. Rev. Lett.* 119.141101 (2017).

[212] B. P. Abbott et al. “GW170817: Observation of Gravitational Waves from a Binary Neutron Star Inspiral”. In: *Phys. Rev. Lett.* 119.161101 (2017).

[213] B. P. Abbott et al. “GW170608: Observation of a 19 Solar-mass Binary Black Hole Coalescence”. In: *Astrophys. J.* 851.L35 (2017).

[214] B. P. Abbott et al. “GW190425: Observation of a Compact Binary Coalescence with Total Mass 3.4M”. In: *Astrophys. J.* 892.L3 (2020).

[215] R. Abbott et al. “GW190412: Observation of a binary-black-hole coalescence with asymmetric masses”. In: *Phys. Rev. D* 102.043015 (2020).

[216] R. Abbott et al. “GW190521: A Binary Black Hole Merger with a Total Mass of 150 M”. In: *Phys. Rev. Lett.* 125.101102 (2020).

[217] R. Abbott et al. “GW190814: Gravitational Waves from the Coalescence of a 23 Solar Mass Black Hole with a 2.6 Solar Mass Compact Object”. In: *Astrophys. J.* 896.L44 (2020).

[218] A. Einstein. “Die Grundlage der allgemeinen Relativitatstheorie”. In: *Ann. Phys.* 354.7 (1916), p. 769.

[219] P. R. Saulson. *Fundamentals of Interferometric Gravitational Wave Detectors*. World Scientific, 1994.

[220] J. Aasi et al. “Advanced LIGO”. In: *Class. Quantum Gravity* 32.7 (2015). arXiv: 1411.4547.

[221] F. Acernese et al. “Advanced Virgo: A second-generation interferometric gravitational wave detector”. In: *Class. Quantum Gravity* 32.2 (2015), pp. 1–55. arXiv: 1408.3978.

[222] D. R. Crooks et al. “Experimental measurements of mechanical dissipation associated with dielectric coatings formed using SiO2, Ta2O5 and Al2O3”. In: *Class. Quantum Gravity* 23.15 (2006), pp. 4953–4965.

[223] G. M. Harry et al. “Titania-doped tantala/silica coatings for gravitational-wave detection”. In: *Class. Quantum Gravity* 24.2 (2007), pp. 405–415. arXiv: 0610004 [gr-qc].

[224] I. Martin et al. “Measurements of a low-temperature mechanical dissipation peak in a single layer of Ta2O5 doped with TiO2”. In: *Class. Quantum Gravity* 25.5 (2008), pp. 1–8.

[225] L. He et al. “Electron Correlation Microscopy: A New Technique for Studying Local Atom Dynamics Applied to a Supercooled Liquid”. In: *Microsc. Microanal.* 21.4 (2015), pp. 1026–1033.

[226] P. Zhang et al. “Applications and limitations of electron correlation microscopy to study relaxation dynamics in supercooled liquids”. In: *Ultramicroscopy* 178 (2017), pp. 125–130.

[227] K. Spangenberg et al. “Direct View on Non-Equilibrium Heterogeneous Dynamics in Glassy Nanorods”. In: *Adv. Funct. Mater.* 31.38 (2021), pp. 1–11.

[228] R. F. Egerton. “Mechanisms of radiation damage in beam-sensitive specimens, for TEM accelerating voltages between 10 and 300 kV”. In: *Microsc. Res. Tech.* 75.11 (2012), pp. 1550–1556.

[229] M. Granata et al. “Progress in the measurement and reduction of thermal noise in optical coatings for gravitational-wave detectors”. In: *Appl. Opt.* 59.5 (2020). arXiv: 1912.11394.

Appendix A

A.1 Convert APP5 file to HDF5

```
# Import packages

from fpd.fpd_io import topspin_app5_to_hdf5
import h5py

# Convert from app5 to hdf5

output_fn = topspin_app5_to_hdf5('FILENAME.app5')
```

A.2 FEM calculations

```
%%%%%%%%%%%%%%%%%%%%%%%%%%%%%%%%%%%%%%%%%%%%%%%%%%%%%%%%%%%%%%%%%%%%%%%
%% Code for FEM analysis, obtaining normalised variance
%%%%%%%%%%%%%%%%%%%%%%%%%%%%%%%%%%%%%%%%%%%%%%%%%%%%%%%%%%%%%%%%%%%%%%%


%%%%%%%%%%%%%%%%%%%%%%%%%%%%%%%%%%%%%%%%%%%%%%%%%%%%%%%%%%%%%%%%%%%%%%%
%% Importing Data
%%%%%%%%%%%%%%%%%%%%%%%%%%%%%%%%%%%%%%%%%%%%%%%%%%%%%%%%%%%%%%%%%%%%%%%

% Read in diffraction patter010 20um 30ms 1nmns
data = h5read('009 20um 20ms 1nm.hdf5','/fpd_expt/fpd_data/data');
%data = h5read('016 10um 100ms 2nm.hdf5','/fpd_expt/fpd_data/data');
%data = skip_data;
%data = rs100data;
%data = h5read('013_2.hdf5','/dataset_1');

% To reshape into 3D dataset once cropped for averaging
%data = reshape(data,256,256,[]);

dims = size(data);

```

```
% 5D to 4D, remove singleton dimension
data = squeeze(data);
dims = size(data);

% Define dimensions of diffraction patterns and data
ix = dims(1); % diffraction pattern x size
iy = ix; % diffraction pattern y size
dim3 = dims(3); % size of x dimension of dataset
if numel(dims) > 3;
    dim4 = dims(4); % size of y dimension of dataset
else
    dim4 = 1;
end

% Calculate number of diffraction patterns
nimg = dim3*dim4;

%% Permute dataset if necessary so that it is horizontally aligned
% dataP = permute(data, [1 2 4 3]);
% dimsP = size(dataP);
%
%% If dataset is permuted, then data = dataP, dims = dimsP
% data = dataP;
% dims = dimsP;
% dim3 = dims(3); % size of x dimension of dataset
% dim4 = dims(4); % size of y dimension of dataset

% Reshape into a 3D data cube for centering and cropping
data2 = reshape(data,ix,iy,nimg);
data2 = single(data2);
clear data

%%%%%%%%%%%%%%%%%%%%%%%%%%%%%%%%%%%%%%%%%%%%%%%%%%%%%%%%%%%%%%%%%%%%%%%%
%% Probe Current Calculations
%%%%%%%%%%%%%%%%%%%%%%%%%%%%%%%%%%%%%%%%%%%%%%%%%%%%%%%%%%%%%%%%%%%%%%%%

CPE = 4; % Counts per electron
ET = 0.01; % Exposure time
EQ = 1.602*10^-19; % Electron charge

PCs = zeros(nimg,1); % Setup vector for probe current of each DP
for i = 1:nimg;
    DP_im = data2(:,:,i); % DP to calculate probe current
    TC = sum(sum(DP_im)); % Total counts in current DP
    PC = EQ*((TC/CPE)/ET); % Probe current in current DP
    PCs(i) = PC;
end
```

```
69
70 PC_ave = mean(PCs);
71 PC_st_dev = std(PCs);
72 PC_electrons = PC_ave/EQ;
73
74 %%%%%%%%%%%%%%%%%%%%%%%%%%%%%%%%%%%%%%%%%%%%%%%%%%%%%%%%%%%%%%%%%%%%%%%
75 %% Centering Diffraction Patterns
76 %%%%%%%%%%%%%%%%%%%%%%%%%%%%%%%%%%%%%%%%%%%%%%%%%%%%%%%%%%%%%%%%%%%%%%%
77
78 % Sets the range (in pixels) to look for the radius of the central spot
       in the diffraction pattern.
79
80 Rmin = 3;
81 Rmax = 12;
82
83 % creates a matrix called center that initially contains (0, 0)
84
85 center = zeros(1, 2);
86
87 % loop through all of the images, finding the centres of circles in those
       images.
88
89 for i = 1:nimg;
90     Cim = data2(:,:,i);
91     e = edge(Cim,'Canny',[.1 .8]); % Detects edges in Cim, using 'Canny'
          method with [] setting threshold
92     centers = imfindcircles(Cim,[Rmin, Rmax]); % Finds circles with
          radius in set range
93     if size(centers,1) >= 2;
94         %fprintf('detected more than one circle in image %d\n', i);
95     end
96     if size(centers,1) >= 3;
97         %fprintf('detected more than two circles in image %d\n', i);
98     end
99     if size(centers,1) < 1;
100        %fprintf('detected no circles in image %d\n', i);
101    end
102    center = [center; round(centers)]; % Appends central pixel
          coordinates
103 end
104
105 CDPs = mode(center, 1);
106 CDPx = CDPs(1);
107 CDPy = CDPs(2);
108 CDPcrop = min(CDPx - 2, CDPy - 2);
109
110 % New 3D stack with all DPs colinear with respect to optic axis, crop
```

```
111
112 for ii = 1:nimg;
113     A = data2(:,:,ii);
114     A1 = [CDPy+CDPcrop, CDPx+CDPcrop];
115     A2 = max(A1);
116     if A2 > ix;
117         CDPcrop = CDPcrop - (A2 - ix);
118     end
119     cdparray(:,:,ii) = A(CDPy-CDPcrop:CDPy+CDPcrop, CDPx-CDPcrop:CDPx+
        CDPcrop);
120 end
121
122 % Calculate new centre coordinate, x=y
123
124 C = CDPcrop + 1;
125 clear data
126 clear data2
127
128 %%%%%%%%%%%%%%%%%%%%%%%%%%%%%%%%%%%%%%%%%%%%%%%%%%%%%%%%%%%%%%%%%%%%%%%
129 %% Calculating Normalised Variance
130 %%%%%%%%%%%%%%%%%%%%%%%%%%%%%%%%%%%%%%%%%%%%%%%%%%%%%%%%%%%%%%%%%%%%%%%
131
132 cdp_size1 = size(cdparray,1); % Find size of cropped diffraction pattern
133 cdparray1 = reshape(cdparray,cdp_size1,cdp_size1,dim3,[]);
134
135 % Calculate the normalised variance for each pixel in each stack
136 for i = 1:dim4;
137     stack = cdparray1(:,:,:,i);
138     MEAN = mean(stack,3); % Calculates the mean intensity of each pixel
        through the stack
139     %Testing a QE of 1/4 in this code
140     QE = (ones(cdp_size1)); % Creates a matrix containing the detector
        quantum efficiency for each pixel
141     I_SQ = stack.^2; % Calculates the intensity squared of each pixel
        through the stack
142     I_SQ_MEAN = mean(I_SQ,3); % Calculates the mean of the intensity
        squared of each pixel through the stack
143     MEAN_SQ = MEAN.^2;% Calculates the square of the mean intensity of
        each pixel through the stack
144     SHOT = QE./MEAN; % Calculates the shot noise of each pixel through
        the stack
145     VAR = I_SQ_MEAN./MEAN_SQ - 1; %- SHOT; % Calculates the normalised
        variance of each pixel through the stack
146     varstack(:,:,i) = VAR;
147 end
148
149 %% Look at histogram of pixel variance to decide where to set threshold
```

```
    of
% % hot pixels
% for i = 1:cdp_size1;
%     for ii = 1:cdp_size1;
%         cpix = VAR(i,ii);
%         if cpix > thr;
%             varstack(i,ii,:) = 0;
%         end
%     end
% end


% Set threshold so that hot pixels with high variance are not included in
    the variance calculations
thr = 1.0; % Threshold value
thr_ = -0.2;
sz_varstack = size(varstack,3);

for j = 1:sz_varstack;
    c_stack = varstack(:,:,j);
    for i = 1:cdp_size1;
        for ii = 1:cdp_size1;
            cpix = c_stack(i,ii);
            if cpix > thr;
                varstack(i,ii,:) = 0;
            end
            if cpix < thr_;
                varstack(i,ii,:) = 0;
            end
        end
    end
end
B = zeros(cdp_size1*cdp_size1,2,dim4); % Create array to input data
    calculated later on

r3 = C-3; % Set maximum distance (in pixels) from centre of diffraction
    pattern to calculate variance from

% Loop to add the radius from centre and variance for each pixel in each
% stack to the array B
for k = 1:dim4;
    VAR = varstack(:,:,k);
    n = 1;
    for i = 1:cdp_size1;
        for j = 1:cdp_size1;
            B(n,1,k) = sqrt((i-C)^2+(j-C)^2);
            if VAR(j,i) == 0;
```

```
193                     B(n,1,k) = 0;
194                 else B(n,2,k) = VAR(j,i);
195                 end
196                 n = n+1;
197             end
198         end
199     end
200
201     % Loop that sorts the pixels into increasing radius order while setting
202     % NaNs to zero
203     for i = 1:dim4;
204         c_row = B(:,:,i);
205         c_row = sortrows(c_row,1);
206         NaNs = find(isnan(c_row)); % Temporary solution so that NaNs do not
                affect the variance calculation as much
207         c_row(NaNs) = 0;
208         B(:,:,i) = c_row;
209     end
210
211     % Loop that creates an array VQ containing the normalised variance and
            its
212     % standard deviation within the 1 pixel annular radius from the centre of
213     % the diffraction pattern stack
214     for k = 1:dim4;
215         m = 0;
216         i = 0;
217         B1 = B(:,1,k);
218         while m ~= (n-1)
219             if i > r3, break;
220             else;
221                 i = i+1;
222                 first = find(B1>=(i-1),1,'first');
223                 last = find(B1<i,1,'last');
224                 D = B(first:last,2,k);
225                 m = m + size(D,1);
226                 D1 = sum(D)/size(D,1);
227                 D_stdev = std(D);
228                 VQ(i,1,k) = D1;
229                 VQ(i,2,k) = D_stdev;
230             end
231         end
232     end
233
234     % Loop that extracts a variance stack from VQ
235     for i = 1:dim4;
236         VQ_var(:,i) = VQ(:,1,i);
237     end
```

```
238
239 %%%%%%%%%%%%%%%%%%%%%%%%%%%%%%%%%%%%%%%%%%%%%%%%%%%%%%%%%%%%%%%%%%%%%%%
240 %% Creating VDF Images
241 %%%%%%%%%%%%%%%%%%%%%%%%%%%%%%%%%%%%%%%%%%%%%%%%%%%%%%%%%%%%%%%%%%%%%%%
242 %
243 % dimcdparray = size(cdparray,1);
244 % for iii = 1:nimg;
245 %     img = cdparray(:,:,iii);
246 %     for ii = 1:C-1; % Centre-1;
247 %         [x,y]=meshgrid(-(C-1):(dimcdparray-C),-(C-1):(dimcdparray-C));
248 %         c_mask2=uint16((x.^2+y.^2)<=ii^2);
249 %         [x,y]=meshgrid(-(C-1):(dimcdparray-C),-(C-1):(dimcdparray-C));
250 %         c_mask3=uint16((x.^2+y.^2)<=(ii-1)^2);
251 %         DFmask = double(c_mask2 - c_mask3);
252 %         annuli(:,:,ii) = DFmask;
253 %         annDF(iii,ii) = sum(sum(img.*DFmask));
254 %     end
255 % end
256 %
257 %% Reshape annDF dimensions for VDFi
258 % orxdim = dims(3);
259 % for ii = 1:C-1;
260 %     img = reshape(annDF(:,ii),orxdim,[]); %
261 %     img = img';
262 %     DF(:,:,ii) = img;
263 % end
264 %
265 %% Size of a pixel in nm
266 %% dx = 1;
267 %% dy = dx;
268 %% x = dim3.*dx;
269 %% y = dim4.*dy;
270 %
271 % cd VDF_Images
272 %
273 %% Uncomment to plot selected range and save images as bitmap
274 % for ii = 1:C-1;
275 %     figure
276 %     imagesc(DF(:,:,ii))
277 %     %imagesc(x,y,DF(:,:,ii))
278 %     axis image
279 %     colorbar
280 %     %title('VDF')
281 %%      xlabel('nm')
282 %%      ylabel('nm')
283 %     Filename1 = 'DF';
284 %     Filename2 = num2str(ii);
```

```
%     fid = strcat(Filename1,Filename2,'.png');
%     print (gcf, '-dpng', fid);
%%      fid = strcat(Filename1,Filename2,'.bmp');
%%      print (gcf, '-dbmp', fid);
%     close
% end
```

A.3 VDF calculations

```
# Convert APP5 files to HDF5
# Skip if already converted

# Import packages

from fpd.fpd_io import topspin_app5_to_hdf5
import h5py

# Convert from app5 to hdf5

output_fn = topspin_app5_to_hdf5('FILENAME.app5')

# Centre Diffraction Patterns

# Import packages

import fpd.fpd_file as fpdf
import matplotlib.pyplot as plt
from fpd.fpd_file import DataBrowser
from fpd import fpd_processing as fpdp
from fpd import fpd_file as fpdf
from fpd import tem_tools as fpdtt
from fpd.synthetic_data import shift_images
from fpd.synthetic_data import disk_image
import h5py, fpd, math
import pandas as pd
import numpy as np
from matplotlib import ticker
from mpl_toolkits.axes_grid1.anchored_artists import AnchoredSizeBar

# For interactive databrowser

get_ipython().run_line_magic('matplotlib', 'qt')

# Load data from hdf5

hdf5_fn = 'FILENAME_1.hdf5'
```

```
fpd_nt = fpdf.fpd_to_tuple(hdf5_fn, fpd_check=False)
ds = fpd_nt.fpd_data.data

# Check data to see whether it is displayed correctly

b = DataBrowser(hdf5_fn, fpd_check=False)

# Check dimensions of data

ds_shp = ds.shape
ds_d1 = ds_shp[0]
ds_d2 = ds_shp[1]
print(ds.shape)

# Reshape into 3D stack of diffraction patterns, delete 'ds'

ds1 = np.reshape(ds,(ds_d1*ds_d2,256,256))
print(ds1.shape)
del(ds)

# Find central spot

sum_dif = np.sum(ds1, axis=(0))
plot = True
cyx, cr = fpdp.find_circ_centre(sum_dif, 3, (3, 40, 0.5), pct=95, plot=
    plot)

# Print the y,x coordinates and radius of the central spot

print(cyx)
print(cr)

# Make reference image of central spot

im = sum_dif
cy, cx = cyx.astype(int)
p = 8
im_direct = im[cy-(cr+p):cy+(cr+p)+1, cx-(cr+p):cx+(cr+p)+1]
if plot:
    plt.matshow(im_direct)

# Do edge detection on central spot

sigma_wt_avg, sigma_wt_std, sigma_std, (sigma_vals, sigma_stds), (r_vals,
    r_stds) = fpdp.disc_edge_sigma(im_direct, sigma=2, plot=plot)
ref_im = fpdp.make_ref_im(im_direct, 2, plot=plot)
sigma = 1.5
```

```
83
84  # # Generate VDF Images
85  # FIGURE_1=VDF images
86
87  # Generate list of intensity and distance to centre of pattern for every
        pixel in every diffraction pattern in the dataset
88
89  dp_size = ds_shp[2]
90  ndp = ds1.shape[0]
91
92  VDF_lst = np.empty((ndp, 2, dp_size*dp_size))
93  # print(VDF_lst.shape)
94
95  for j in range(ndp):
96      start = 0
97      for i in range(dp_size):
98          y_dim = i
99          for ii in range(dp_size):
100             x_dim = ii
101
102             radius = np.sqrt( (ii - cyx[1])**2 + (i - cyx[0])**2 )
103
104             intensity = ds1[j,i,ii]
105
106             VDF_lst[j, 0, start] = radius
107             VDF_lst[j, 1, start] = intensity
108
109             start = start + 1
110     print(j)
111
112 # Sort pixels by distance from centre of pattern
113
114 for i in range(ndp):
115     cDP_r = VDF_lst[i,0,:]
116     srt = np.argsort(cDP_r, axis=0)
117     VDF_lst[i,0,:] = np.take_along_axis(VDF_lst[i,0,:], srt, axis=0)
118     VDF_lst[i,1,:] = np.take_along_axis(VDF_lst[i,1,:], srt, axis=0)
119
120 # Calculate the sum, average and variance of intensity in each annular
        ring
121
122 max_val = int(np.max(VDF_lst[0,0,:]))
123 rad_sum = np.zeros((ndp,max_val))
124 rad_int = np.zeros((ndp,max_val))
125 rad_var = np.zeros((ndp,max_val))
126
127 for i in range(ndp):
```

```
    strt = 0
    end = 1
    radii = VDF_lst[i,0,:]
    for j in range(max_val):
        rng = (radii>strt)*(radii<end)
        c_rad = np.array(np.where(rng))
        index1 = c_rad[0,0]
        index2 = c_rad[0,-1]
        int_sum = np.sum(VDF_lst[i,1,index1:index2])
        int_av = np.mean(VDF_lst[i,1,index1:index2])
        r_var = np.var(VDF_lst[i,1,index1:index2])
        rad_sum[i,j] = int_sum
        rad_int[i,j] = int_av
        rad_var[i,j] = r_var
        strt = strt + 1
        end = end + 1

# Delete VDF_lst to clear up some memory

del VDF_lst

# Check shape of new data

rad_int.shape

# Reshape new data in preparation for VDF images

VDF_sum = np.reshape(rad_sum,(ds_d1,ds_d2,max_val))
VDF_sum = np.transpose(VDF_sum,(1,0,2)) # transpose if necessary
VDF_ave = np.reshape(rad_int,(ds_d1,ds_d2,max_val))
VDF_ave = np.transpose(VDF_ave,(1,0,2)) # transpose if necessary
Rad_VAR = np.reshape(rad_var,(ds_d1,ds_d2,max_val))
Rad_VAR = np.transpose(Rad_VAR,(1,0,2)) # transpose if necessary

# Generate VDF images and save as pdf

# decide which type of data you want to plot
plt_data = Rad_VAR

# calibration of k per pixel
px = 0.095 # scattering angle range

# set width of annular regions
k1_a = 40 # start of region 1
k1_b = 43 # stop of region 1
k2_a = 50
k2_b = 53
```

```
175 k3_a = 75
176 k3_b = 78
177 k4_a = 100
178 k4_b = 103
179
180 fig, axs = plt.subplots(nrows=1, ncols=5)
181 fc = 0.015 # sets width of colorbar
182
183 fs = 9 # annotation font size
184
185 BF = np.sum(VDF_sum[:,:,:cr],2)
186 im0 = axs[0].matshow(BF, cmap='gist_heat', vmin = np.amin(BF), vmax = np.
        amax(BF))
187 cb0 = fig.colorbar(im0, ax=axs[0], orientation='horizontal', fraction=fc,
         pad=0.01)
188 tick_locator0 = ticker.MaxNLocator(nbins=4)
189 cb0.locator = tick_locator0
190 cb0.update_ticks()
191 scalebar = AnchoredSizeBar(axs[0].transData,10,'20 nm','lower left', pad
        =0.1, color='black', frameon=False, label_top=True, sep=0,
        size_vertical=0.1)
192 axs[0].add_artist(scalebar)
193 axs[0].annotate('BF', xy = [0,3], fontsize =fs, color = 'black')
194
195 vdfk1 = np.sum(plt_data[:,:,k1_a:k1_b],2)
196 im1 = axs[1].matshow(vdfk1, cmap='gist_heat', vmin = np.amin(vdfk1), vmax
         = np.amax(vdfk1))
197 cb1 = fig.colorbar(im1, ax=axs[1], orientation='horizontal', fraction=fc,
         pad=0.01)
198 tick_locator1 = ticker.MaxNLocator(nbins=4)
199 cb1.locator = tick_locator1
200 cb1.update_ticks()
201 ax1_ann = str(np.round(px*(k1_a+1),1)) + '-' + str(np.round(px*(k1_b+1)
        ,1)) + 'nm$^{-1}$'
202 axs[1].annotate(ax1_ann, xy = [0,3], fontsize =fs, color = 'white')
203
204 vdfk2 = np.sum(plt_data[:,:,k2_a:k2_b],2)
205 im2 = axs[2].matshow(vdfk2, cmap='gist_heat', vmin = np.amin(vdfk2), vmax
         = np.amax(vdfk2))
206 cb2 = fig.colorbar(im2, ax=axs[2], orientation='horizontal', fraction=fc,
         pad=0.01)
207 tick_locator2 = ticker.MaxNLocator(nbins=4)
208 cb2.locator = tick_locator2
209 cb2.update_ticks()
210 ax2_ann = str(np.round(px*(k2_a+1),1)) + '-' + str(np.round(px*(k2_b+1)
        ,1)) + 'nm$^{-1}$'
211 axs[2].annotate(ax2_ann, xy = [0,3], fontsize =fs, color = 'white')
```

```
212
213 vdfk3 = np.sum(plt_data[:,:,k3_a:k3_b],2)
214 im3 = axs[3].matshow(vdfk3, cmap='gist_heat', vmin = np.amin(vdfk3), vmax
        = np.amax(vdfk3))
215 cb3 = fig.colorbar(im3, ax=axs[3], orientation='horizontal', fraction=fc,
        pad=0.01)
216 tick_locator3 = ticker.MaxNLocator(nbins=4)
217 cb3.locator = tick_locator3
218 cb3.update_ticks()
219 ax3_ann = str(np.round(px*(k3_a+1),1)) + '-' + str(np.round(px*(k3_b+1)
    ,1)) + 'nm$^{-1}$'
220 axs[3].annotate(ax3_ann, xy = [0,3], fontsize =fs, color = 'white')
221
222 vdfk4 = np.sum(plt_data[:,:,k4_a:k4_b],2)
223 im4 = axs[4].matshow(vdfk4, cmap='gist_heat', vmin = np.amin(vdfk4), vmax
        = np.amax(vdfk4))
224 cb4 = fig.colorbar(im4, ax=axs[4], orientation='horizontal', fraction=fc,
        pad=0.01)
225 tick_locator4 = ticker.MaxNLocator(nbins=4)
226 cb4.locator = tick_locator4
227 cb4.update_ticks()
228 ax4_ann = str(np.round(px*(k4_a+1),1)) + '-' + str(np.round(px*(k4_b+1)
    ,1)) + 'nm$^{-1}$'
229 axs[4].annotate(ax4_ann, xy = [0,3], fontsize =fs, color = 'white')
230
231 for i in range(5):
232     axs[i].get_yaxis().set_visible(False)
233     axs[i].get_xaxis().set_visible(False)
234
235 plt.savefig("FIGURE_1.pdf",bbox_inches='tight', format='pdf')
```

Appendix B

B.1 Convert binary files to HDF5

Skip if files already converted

```
# Import packages

from fpd.fpd_file import MerlinBinary
import h5py

# Load binary file

mb_4D = MerlinBinary(binfns='FILENAME.mib', hdrfn='FILENAME.hdr',
    row_end_skip=0, ds_start_skip=0, scanYalu=(1, 'na', 'na'), scanXalu
    =(500, 'na', 'na'))

# Check shape of dataset

mb_4D.shape

#Write out to hdf5 - only need to do once

mb_4D.write_hdf5(chunks=(1, 50, 256, 256))
```

B.2 Import packages and apply mask to central beam

```
# Import packages

import matplotlib.pyplot as plt
import matplotlib.patches as mpatches
import matplotlib.font_manager as fm
import numpy as np
import fpd.fpd_file as fpdf
```

```
import pandas as pd
import h5py
from scipy import signal
from fpd import fpd_processing as fpdp
from fpd.synthetic_data import disk_image
from fpd.synthetic_data import shift_images
from mpl_toolkits.axes_grid1.anchored_artists import AnchoredSizeBar

# For interactive databrowser

get_ipython().run_line_magic('matplotlib', 'qt')

# Load data from hdf5 file

hdf5_fn = 'FILENAME.hdf5'
fpd_nt = fpdf.fpd_to_tuple(hdf5_fn)
ds = fpd_nt.fpd_data.data

# Print the shape of the dataset 'ds' and set the number of diffraction
    patterns 'ndp'

print(ds.shape)
ndp = ds.shape[1]

# Find central spot

sum_dif = np.sum(ds[0,:,:,:], axis=(0)) # 'sum_dif' is the sum of all
    diffraction patterns
plot = True
cyx, cr = fpdp.find_circ_centre(sum_dif, 3, (3, 40, 1), pct=95, plot=plot
    ) # 'cyx' are [y,x] coordinates of the centre of the spot, 'cr' is
    radius of the spot

# Print y,x coordinates and radius of the central spot

print(cyx)
print(cr)

# Make reference image of central spot

im = sum_dif
cy, cx = cyx.astype(int) # 'cy' is y coordinate of central spot, 'cx' is
    x coordinate
p = 8 # Set how many pixels further than the edge of the spot is included
     in cropped area around central spot
im_direct = im[cy-(cr+p):cy+(cr+p)+1, cx-(cr+p):cx+(cr+p)+1] # Set
    cropped area around central spot
```

```
48 if plot:
49     plt.matshow(im_direct)
50
51 # Do edge detection on central spot
52
53 sigma_wt_avg, sigma_wt_std, sigma_std, (sigma_vals, sigma_stds), (r_vals,
       r_stds) = fpdp.disc_edge_sigma(im_direct, sigma=2, plot=plot)
54 ref_im = fpdp.make_ref_im(im_direct, 2, plot=plot)
55 sigma = 1.5
56
57 # Make an aperture, the radius in line 3 is adjustable
58
59 d_im_pad = cr*3
60 print(d_im_pad)
61 d_im = disk_image(intensity=1, radius=cr+8, sigma=0.25, size=im.shape[0]+
      d_im_pad*2, dtype='float32') # 127.5, 127.5
62 d_im_cyx = np.array(d_im.shape)/2
63 d_im_sum = d_im.sum()
64 print(d_im_cyx)
65
66 # Make a mask for central spot and check on sum_dif image
67
68 dyx = cyx[None] - d_im_cyx[None] + np.array([d_im_pad, d_im_pad])[None]
69 mc = shift_images( dyx[None, :].T, d_im, noise=False, parallel=False)
70 mc = mc[..., d_im_pad:-d_im_pad, d_im_pad:-d_im_pad]
71 mc = mc.sum(0)[0]
72 mc = mc.clip(0, 1)
73 if plot:
74     plt.matshow( (1-mc) * sum_dif)
75
76 # Now look at a few images spread at regular intervals through the
      dataset
77
78 stp = int(ndp/10)
79
80 for i in range(0,ndp,stp):
81     DP = ds[0,i,:,:]
82     plt.matshow(DP*(1-mc), cmap='inferno')
83
84 # Create a new dataset containing all the DPs with a mask applied
85
86 ds_mask = np.zeros((1,ndp,256,256))
87 for i in range(ndp):
88     ds_mask[0,i,:,:] = ds[0,i,:,:]*(1-mc)
89
90 # Set size of cropped DP and check image
91
```

```
DP_cr = 70
ds_mask_cr = ds_mask[0,:,int(cy-DP_cr):int(cy+DP_cr),int(cx-DP_cr):int(cx+DP_cr)] # create new cropped version of masked dataset
plt.matshow(ds_mask_cr[0,:,:])

# Set duration of dataset and create an array containing the timestamps of each pattern

Duration = 10790 # in ms
Increment = Duration/ndp
Time = np.arange(0,Duration-Increment,Increment)
Time = np.round(Time,1)
num = len(Time)
Name_array = [0] * num
for i in range(num):
    Name_array[i] =  f'{i:04}'
```

B.3 Create figures showing diffraction patterns

FIGURE_1=12 patterns spread, FIGURE_2=12 patterns close, FIGURE_3=5 patterns difference

```
#  Twelve diffraction patterns equally spread through the dataset

# Set the index of the starting diffraction pattern and the step size between diffraction patterns for creating a figure containing 12 patterns equally spaced throughout the dataset

start = 0
stop = int(ndp)
step = int(np.floor(ndp/11))

# Print the maximum intensity found in each pattern that will be shown in the figure

for i in range(start,stop,step):
    print(np.amax(ds_mask_cr[i,:,:]))

# Generate figure and save as PDF

rows = 4 # set number of rows in figure
cols = 3 # set number of columns in figure

fig, axs = plt.subplots(nrows=rows, ncols=cols, gridspec_kw = {'wspace':-0.26, 'hspace':0.02})
fig.set_figheight(10)
```

```
21 fig.set_figwidth(8)
22
23 ax = 0
24 ay = 0
25
26 for i in range(start,stop,step):
27     if ay == (rows):
28         break
29     # add arrows in all patterns to show features (doesn't work if arrow
       definitions removed from for loop)
30     arrow = mpatches.Arrow(53+15,105-15,-15,15, width=10.0,facecolor='
       white')
31     arrow1 = mpatches.Arrow(53+15,37+15,-15,-15, width=10.0,facecolor='
       white')
32     arrow2 = mpatches.Arrow(37+15,57+15,-20,0, width=10.0,facecolor='
       white')
33
34     DPc = ds_mask_cr[i,:,:]
35     im = axs[ay,ax].matshow(DPc, vmin=0, vmax=200, cmap='inferno') # '
       vmin','vmax' are the minimum and maximum intensity shown in the
       plot
36     axs[ay,ax].get_yaxis().set_visible(False)
37     axs[ay,ax].get_xaxis().set_visible(False)
38     ax_ann = str(Time[i]) + ' ' + 'ms'
39     axs[ay,ax].annotate(ax_ann, xy = [3,16], fontsize=12, color = 'white'
       )
40     axs[ay,ax].add_patch(arrow)
41     axs[ay,ax].add_patch(arrow1)
42     axs[ay,ax].add_patch(arrow2)
43     if ax == (cols-1):
44         ay = ay + 1
45         ax = 0
46     else:
47         ax = ax + 1
48
49 ## add arrows to selected diffraction patterns to show features
50 # arrow = mpatches.Arrow(88+15,61-15,-15,15, width=10.0,facecolor='white
       ')
51 # arrow1 = mpatches.Arrow(93+15,75+15,-15,-15, width=10.0,facecolor='
       white')
52 # arrow2 = mpatches.Arrow(82+15,40-15,-15,15, width=10.0,facecolor='white
       ')
53 arrow3 = mpatches.Arrow(92+15,95+15,-15,-15, width=10.0,facecolor='white'
       )
54 # arrow4 = mpatches.Arrow(37-15,72+15,15,-15, width=10.0,facecolor='white
       ')
55
```

```
# axs[0,1].add_patch(arrow)
# axs[1,0].add_patch(arrow1)
# axs[1,1].add_patch(arrow2)
axs[1,2].add_patch(arrow3)
# axs[3,0].add_patch(arrow4)

# add a scalebar
cal = 0.095 # calibration (nm^-1 per pixel)
sc_len = 3 # length of scale bar (nm^-1)
sc_size = sc_len/cal # size in pixels of scale bar to display
fontprops = fm.FontProperties(size=9)
scalebar = AnchoredSizeBar(axs[0,0].transData,sc_size, str(sc_len) + ' '
    + 'nm$^{-1}$',loc=3, pad=0.3, color='white', frameon=False, label_top=
    True, sep=0, size_vertical=1, fontproperties=fontprops)
axs[0,0].add_artist(scalebar)

# add a colorbar
fig.colorbar(im, ax=axs.ravel().tolist(), orientation='horizontal',
    fraction=0.036, pad=0.01, label='Raw Detector Counts')

plt.savefig("FIGURE_1.pdf",bbox_inches='tight', format='pdf')

# Twelve consecutive diffraction patterns from the dataset

# Set the index of the starting diffraction pattern and the step size
    between diffraction patterns for creating a figure containing 12
    patterns equally spaced throughout the dataset

start = 0
stop = int(start+12)
step = 1

# Print the maximum intensity found in each pattern that will be shown in
     the figure

for i in range(start,stop,step):
    print(np.amax(ds_mask_cr[i,:,:]))

# Generate figure and save as PDF

fig, axs = plt.subplots(nrows=rows, ncols=cols, gridspec_kw = {'wspace'
    :-0.26, 'hspace':0.02})
fig.set_figheight(10)
fig.set_figwidth(8)
ax = 0
ay = 0

```

```
96  for i in range(start,stop,step):
97      if ay == (rows):
98          break
99      # add arrows in all patterns to show features (doesn't work if arrow
            definitions removed from for loop)
100     arrow = mpatches.Arrow(38-15,75+15,15,-15, width=10.0,facecolor='
            white')
101     arrow1 = mpatches.Arrow(80+15,45-15,-15,15, width=10.0,facecolor='
            white')
102     arrow2 = mpatches.Arrow(98+15,85+15,-15,-15, width=10.0,facecolor='
            white')
103
104     DPc = ds_mask_cr[i,:,:]
105     im = axs[ay,ax].matshow(DPc, vmin=0, vmax=200, cmap='inferno') # '
            vmin','vmax' are the minimum and maximum intensity shown in the
            plot
106     axs[ay,ax].get_yaxis().set_visible(False)
107     axs[ay,ax].get_xaxis().set_visible(False)
108     ax_ann = str(Time[i]) + ' ' + 'ms'
109     axs[ay,ax].annotate(ax_ann, xy = [3,16], fontsize=12, color = 'white'
            )
110     axs[ay,ax].add_patch(arrow)
111     axs[ay,ax].add_patch(arrow1)
112     axs[ay,ax].add_patch(arrow2)
113     if ax == (cols-1):
114         ay = ay + 1
115         ax = 0
116     else:
117         ax = ax + 1
118
119 ## add arrows to selected diffraction patterns to show features
120 # arrow = mpatches.Arrow(38-15,75+15,15,-15, width=10.0,facecolor='white
        ')
121 # arrow1 = mpatches.Arrow(80+15,45-15,-15,15, width=10.0,facecolor='white
        ')
122 # arrow2 = mpatches.Arrow(80+15,98+15,-15,-15, width=10.0,facecolor='
        white')
123 arrow3 = mpatches.Arrow(92+15,92+15,-15,-15, width=10.0,facecolor='white'
        )
124 # arrow4 = mpatches.Arrow(37-15,72+15,15,-15, width=10.0,facecolor='white
        ')
125
126 # axs[0,0].add_patch(arrow)
127 # axs[0,0].add_patch(arrow1)
128 # axs[0,0].add_patch(arrow2)
129 # axs[0,1].add_patch(arrow)
130 # axs[1,1].add_patch(arrow)
```

```
131 # axs[1,1].add_patch(arrow1)
132 # axs[1,1].add_patch(arrow2)
133 axs[3,1].add_patch(arrow3)
134 # axs[3,0].add_patch(arrow4)
135
136 # add a scalebar
137 cal = 0.095 # calibration (nm^-1 per pixel)
138 sc_len = 3 # length of scale bar (nm^-1)
139 sc_size = sc_len/cal # size in pixels of scale bar to display
140 fontprops = fm.FontProperties(size=9)
141 scalebar = AnchoredSizeBar(axs[0,0].transData,sc_size, str(sc_len) + ' '
        + 'nm$^{-1}$',loc=3, pad=0.3, color='white', frameon=False, label_top=
        True, sep=0, size_vertical=1, fontproperties=fontprops)
142 axs[0,0].add_artist(scalebar)
143
144 # add a colorbar
145 fig.colorbar(im, ax=axs.ravel().tolist(), orientation='horizontal',
        fraction=0.036, pad=0.01, label='Raw Detector Counts')
146
147 plt.savefig("FIGURE_2.pdf",bbox_inches='tight', format='pdf')
148
149 # Diffraction patterns shown with absolute and relative difference in
        intensity
150
151 # Set the central diffraction pattern in the figure and the step size
        between patterns
152
153 centre = 432
154 step = 1
155 start = int(centre-2*step)
156 stop = int(centre+3*step)
157
158 Tm = np.arange(start, stop, step)*Increment
159 Tm = np.round(Tm,1)
160 print(Tm)
161
162 # Calculate the difference between diffraction patterns
163
164 ds_shape = ds_mask_cr.shape
165 ds_s = int(ds_shape[2])
166 dp_array = np.zeros((2,5,ds_s,ds_s))
167
168 dp1 = ds_mask_cr[centre-2*step,:,:]
169 dp2 = ds_mask_cr[centre-step,:,:]
170 dp3 = ds_mask_cr[centre,:,:]
171 dp4 = ds_mask_cr[centre+step,:,:]
172 dp5 = ds_mask_cr[centre+2*step,:,:]
```

```
173
174 dp_array[0,0,:,:] = ds_mask_cr[centre-2*step,:,:]
175 dp_array[0,1,:,:] = ds_mask_cr[centre-step,:,:]
176 dp_array[0,2,:,:] = ds_mask_cr[centre,:,:]
177 dp_array[0,3,:,:] = ds_mask_cr[centre+step,:,:]
178 dp_array[0,4,:,:] = ds_mask_cr[centre+2*step,:,:]
179
180 dp_array[1,0,:,:] = dp3 - dp1
181 dp_array[1,1,:,:] = dp3 - dp2
182 #dp_array[1,2,:,:] = dp3 - dp3
183 dp_array[1,3,:,:] = dp3 - dp4
184 dp_array[1,4,:,:] = dp3 - dp5
185
186 # Calculate and print the maximum and minimum differences between
      patterns
187
188 max_df = np.zeros((5,1))
189 min_df = np.zeros((5,1))
190
191 for k in range(5):
192     max_df[k] = np.amax(dp_array[1,k,:,:])
193     min_df[k] = np.amin(dp_array[1,k,:,:])
194
195 print(max_df , min_df)
196
197 # Generate figure and save as PDF
198
199 fig, axes = plt.subplots(nrows=2, ncols=5, gridspec_kw = {'wspace':0.035,
      'hspace':-0.6})
200
201 for j in range(5):
202     C_im1 = dp_array[0,j,:,:]
203     im1 = axes[0,j].matshow(C_im1, cmap='inferno', vmin=0, vmax=200)
204     axes[0,j].get_yaxis().set_visible(False)
205     axes[0,j].get_xaxis().set_visible(False)
206     ax_ann = str(Tm[j]) + ' ' + 'ms'
207     axes[0,j].annotate(ax_ann, xy = [3,16], fontsize=8, color = 'white')
208
209 for j in range(5):
210     C_im2 = dp_array[1,j,:,:]
211     im2 = axes[1,j].matshow(C_im2, cmap='seismic', vmin=-75, vmax=75)
212     axes[1,j].get_yaxis().set_visible(False)
213     axes[1,j].get_xaxis().set_visible(False)
214     #axes[1,j].annotate(Tm[j], xy = [3,30], fontsize=8, color = 'black')
215
216 # add a scalebar
217 cal = 0.095 # calibration (nm^-1 per pixel)
```

```
sc_len = 5 # length of scale bar (nm^-1)
sc_size = sc_len/cal # size in pixels of scale bar to display
fontprops = fm.FontProperties(size=6) # set font size of label
scalebar = AnchoredSizeBar(axes[0,0].transData,sc_size, str(sc_len) + ' '
    + 'nm$^{-1}$',loc=3, pad=0.3, color='white', frameon=False, label_top
    =True, sep=0, size_vertical=1, fontproperties=fontprops)
axes[0,0].add_artist(scalebar)

# add colorbars
fig.colorbar(im1, ax=axes[0,:], location='right', fraction=0.0092, pad
    =0.01, label='Raw detector \n counts')
fig.colorbar(im2, ax=axes[1,:], location='right', fraction=0.0092, pad
    =0.01, label='Difference in \n detector counts')

plt.savefig("FIGURE_3.pdf",bbox_inches='tight', format='pdf')
```

B.4 Tracking intensity of selected spots with time

FIGURE_4=Intensity of four spots as a function of time

```
# View plot of 'sum_dif' or individual diffraction pattern

plt.matshow((sum_dif)*(1-mc))
plt.matshow(ds_mask[0,0,:,:])

# Make an aperture

aprtr = disk_image(intensity=1, radius=7, sigma =0.25, size=256, dtype='
    float32')
plt.matshow(aprtr)

# Set radius, xy coordinates of spots, then create masked datasets

rad = 8

sp1_cyx = np.array([50, 50])
sp2_cyx = np.array([100, 100])
sp3_cyx = np.array([150, 150])
sp4_cyx = np.array([200, 200])

# create aperture
aprtr = disk_image(intensity=1, radius=7, sigma =0.25, size=sum_dif.shape
    [0], dtype='float32')
aprtr_cyx = np.array(aprtr.shape)/2

```

```
# Position apertures
sp1_ = sp1_cyx[None] - aprtr_cyx[None] #+ np.array([d_im_pad, d_im_pad])[None]
aprtr_1 = shift_images(sp1_[None,:].T, aprtr, noise=False, parallel=False)
plt.matshow(aprtr_1[0,0,:,:])

sp2_ = sp2_cyx[None] - aprtr_cyx[None] #+ np.array([d_im_pad, d_im_pad])[None]
aprtr_2 = shift_images(sp2_[None,:].T, aprtr, noise=False, parallel=False)
plt.matshow(aprtr_2[0,0,:,:])

sp3_ = sp3_cyx[None] - aprtr_cyx[None] #+ np.array([d_im_pad, d_im_pad])[None]
aprtr_3 = shift_images(sp3_[None,:].T, aprtr, noise=False, parallel=False)
plt.matshow(aprtr_3[0,0,:,:])

sp4_ = sp4_cyx[None] - aprtr_cyx[None] #+ np.array([d_im_pad, d_im_pad])[None]
aprtr_4 = shift_images(sp4_[None,:].T, aprtr, noise=False, parallel=False)
plt.matshow(aprtr_4[0,0,:,:])

# Apply masks and calculate sum, rolling mean and rolling standard deviation

sp1_msk = ds_mask*(aprtr_1)
sp1_msk_sum = np.zeros(ndp)
sp2_msk = ds_mask*(aprtr_2)
sp2_msk_sum = np.zeros(ndp)
sp3_msk = ds_mask*(aprtr_3)
sp3_msk_sum = np.zeros(ndp)
sp4_msk = ds_mask*(aprtr_4)
sp4_msk_sum = np.zeros(ndp)

for i in range(ndp):
    sp1_msk_sum[i] = np.sum(sp1_msk[0,i,:,:])
    sp2_msk_sum[i] = np.sum(sp2_msk[0,i,:,:])
    sp3_msk_sum[i] = np.sum(sp3_msk[0,i,:,:])
    sp4_msk_sum[i] = np.sum(sp4_msk[0,i,:,:])

N = 5 # rolling window size

# create panda series
sp1_msk_sum_pd = pd.Series(sp1_msk_sum)
```

```
sp2_msk_sum_pd = pd.Series(sp2_msk_sum)
sp3_msk_sum_pd = pd.Series(sp3_msk_sum)
sp4_msk_sum_pd = pd.Series(sp4_msk_sum)

# rolling mean
sp1_rm = sp1_msk_sum_pd.rolling(window=N, center=True).mean()
sp2_rm = sp2_msk_sum_pd.rolling(window=N, center=True).mean()
sp3_rm = sp3_msk_sum_pd.rolling(window=N, center=True).mean()
sp4_rm = sp4_msk_sum_pd.rolling(window=N, center=True).mean()

# rolling standard deviation
sp1_rstd = sp1_msk_sum_pd.rolling(window=N, center=True).std()
sp2_rstd = sp2_msk_sum_pd.rolling(window=N, center=True).std()
sp3_rstd = sp3_msk_sum_pd.rolling(window=N, center=True).std()
sp4_rstd = sp4_msk_sum_pd.rolling(window=N, center=True).std()

# rolling mean +/- standard deviation for fill between
sp1_mn = sp1_rm - sp1_rstd
sp1_mx = sp1_rm + sp1_rstd
sp2_mn = sp2_rm - sp2_rstd
sp2_mx = sp2_rm + sp2_rstd
sp3_mn = sp3_rm - sp3_rstd
sp3_mx = sp3_rm + sp3_rstd
sp4_mn = sp4_rm - sp4_rstd
sp4_mx = sp4_rm + sp4_rstd

# Create figure and save as pdf

fig,ax = plt.subplots(4, sharex=True)

# set potential positions of annotations
xy_h = [0.01,0.8]
xy_l = [0.01,0.05]
xy_rh = [0.9,0.8]

ax[0].plot(Time,sp1_msk_sum_pd, color='b', linewidth=1, label='Intensity'
    )
ax[0].plot(Time,sp1_rm, '--', color='maroon', label='Rolling average')
ax[0].fill_between(Time, sp1_mn, sp1_mx, color='lightcoral', label='
    Rolling standard deviation')
ax[0].annotate('Spot1', xycoords='axes fraction', xy = xy_rh, fontsize
    =10, color = 'black')
# ax[0].set_ylim((,))

ax[1].plot(Time,sp2_msk_sum_pd, color='b', linewidth=1, label='Intensity'
    )
ax[1].plot(Time,sp2_rm, '--', color='maroon', label='Rolling average')
```

```
105 ax[1].fill_between(Time, sp2_mn, sp2_mx, color='lightcoral', label='
    Rolling standard deviation')
106 ax[1].annotate('Spot1', xycoords='axes fraction', xy = xy_h, fontsize=10,
     color = 'black')
107 # ax[1].set_ylim((,))
108
109 ax[2].plot(Time,sp3_msk_sum_pd, color='b', linewidth=1, label='Intensity'
    )
110 ax[2].plot(Time,sp3_rm, '--', color='maroon', label='Rolling average')
111 ax[2].fill_between(Time, sp3_mn, sp3_mx, color='lightcoral', label='
    Rolling standard deviation')
112 ax[2].annotate('Spot1', xycoords='axes fraction', xy = xy_h, fontsize=10,
     color = 'black')
113 # ax[2].set_ylim((,))
114
115 ax[3].plot(Time,sp4_msk_sum_pd, color='b', linewidth=1, label='Intensity'
    )
116 ax[3].plot(Time,sp4_rm, '--', color='maroon', label='Rolling average')
117 ax[3].fill_between(Time, sp4_mn, sp4_mx, color='lightcoral', label='
    Rolling standard deviation')
118 ax[3].annotate('Spot1', xycoords='axes fraction', xy = xy_h, fontsize=10,
     color = 'black')
119 # ax[3].set_ylim((,))
120
121 plt.xlabel('Time (ms)')
122 fig.text(0.02, 0.5, 'Sum of Spot Intensity', va='center', rotation='
    vertical')
123 plt.xlim((0,10790))
124 ax[0].legend(loc=(0,1.1),ncol=3, columnspacing=0.6)
125
126 plt.savefig("FIGURE_4.pdf",bbox_inches='tight', format='pdf')
127
128 ## Optional peak finding calculations
129
130 # import scipy
131
132 ## Finding peaks
133 # sp1_peaks, _ = scipy.signal.find_peaks(sp1_rm,height=20,distance=5,
    prominence=100)
134
135 ## Finding peak width at half height (FWHM)
136 # sp1_FWHM = scipy.signal.peak_widths(sp1_rm, sp1_peaks, rel_height=0.5,
    wlen=30)
137
138 ## Converting to Time x-axis scale
139 # sp1_peaks = sp1_peaks*Increment
140
```

```
## Plotting
# fig = plt.figure()
# ax = fig.subplots()
# ax.plot(Time, sp1_rm, label='Intensity rolling average')
# ax.scatter(sp1_peaks, _['peak_heights'], color ='r', s=15, marker='D',
    label='Maxima')
# ax.hlines(sp1_FWHM[1], sp1_FWHM[2]*Increment, sp1_FWHM[3]*Increment,
    color='C2')
# ax.legend()
# ax.grid()
# plt.xlabel('Time (ms)')
# plt.ylabel('Sum of spot intensity')
# plt.show()

## Optional calculation of FWHM of selected peaks

# indcs = [3,5,6] # Indices of peaks found that you want to include in
    the calculation of average FWHM
# n_in = len(indcs)
# mn_ar = np.zeros(n_in)
# sp1_FWHM_wdth = sp1_FWHM[0]*Increment

# i = 0
# for item in indcs:
#     mn_ar[i] = sp1_FWHM_wdth[item]
#     i = i+1

# sp1_pk_widths_mn = np.mean(mn_ar)
# sp1_pk_widths_std = np.std(mn_ar)

# print(sp1_pk_widths_mn)
# print(sp1_pk_widths_std)
```

B.5 Calculate the similarity of diffraction patterns

FIGURE_5=KWW fit to averaged $g_2(t)$ from the annular region, FIGURE_6=Figure showing images of diffraction pattern, τ and β, FIGURE_7=Plot of KWW fit to individual pixel, FIGURE_8=Histogram of τ values, FIGURE_9=Histogram of β values

```
# Import packages

from fpd.fpd_file import MerlinBinary
from fpd import fpd_processing as fpdp
from fpd.synthetic_data import disk_image
```

```
from fpd.synthetic_data import shift_images
import fpd.fpd_file as fpdf
import h5py
import matplotlib.pyplot as plt
import matplotlib.patches as mpatches
import matplotlib.font_manager as fm
from mpl_toolkits.axes_grid1.anchored_artists import AnchoredSizeBar
import matplotlib.gridspec as gridspec
import matplotlib.colors as colors
import matplotlib.cbook as cbook
from matplotlib import pyplot as plt, cm
from matplotlib.colorbar import Colorbar
import matplotlib.cbook as cbook
from matplotlib import cm
import numpy as np
import pandas as pd
from scipy import signal
from scipy.optimize import curve_fit as cf
from scipy.constants import e, m_p
from skimage.filters import gaussian

# For interactive databrowser
%matplotlib qt

# Set path to find files
path = "//path"

# Set filenames of datasets
ds1_filename = "filename"

# Set description labels for datasets
dataset_1 = 'label'

# Load data from hdf5 file

ds1_hdf5_fn = path+ds1_filename+'.hdf5'
fpd_nt_ds1 = fpdf.fpd_to_tuple(ds1_hdf5_fn)
ds_1 = fpd_nt_ds1.fpd_data.data

#Test plot

plt.matshow(ds_1[0,0,:,:], vmax=400)

# Print the shape of the dataset 'ds' and set the number of diffraction
    patterns 'ndp'

print(ds_1.shape)
```

```
ndp = ds_1.shape[1]

# Set duration of dataset and create an array containing the timestamps
    of each pattern

duration = 10790 # in ms

timestep = duration/ndp
print(str(round(timestep,1))+' ms')

# Create an array containing the timestamps of each pattern
time = np.arange(0,duration-timestep,timestep)

time = np.round(time,1)
num = len(time)
name_array = [0] * num
for i in range(num):
    name_array[i] =  f'{i:04}'

# Calculate detector counts for each diffraction pattern
counts_ds1 = np.sum(ds_1, axis=(0,2,3))
avcounts_ds1 = np.mean(counts_ds1)

# Plot detector counts against time

plt.figure()
plt.plot(time, counts_ds1, label=dataset_1)
plt.xlabel('Time')
plt.ylabel('Detector counts')
plt.legend()

# Function for calculating fluctuations in total intensity

def int_fluc(DP1_int, cDP):
    flc = ((int(DP1_int) - int(np.sum(cDP)))/int(DP1_int)) * (-100)
    return flc

# Calculate fluctuations in detector counts

ds1_int_fluc = np.empty(ndp)

ds1_DP1_cnt = counts_ds1[0]

for i in range(ndp):
    ds1_cdp = ds_1[0,i,:,:]
    ds1_int_fluc[i] = int_fluc(ds1_DP1_cnt, ds1_cdp)

```

```
# Plot fluctuations of detector counts against time

plt.figure()
plt.plot(time, ds1_int_fluc, label=dataset_1)
plt.axhline(y=0, color='k', linestyle='-')
plt.xlabel('Time')
plt.ylabel('Detector count fluctuation (percent)')
plt.legend()

# Calculate beam current for each dataset

current_ds1 = 1e15*(np.mean(counts_ds1)/4)*e/timestep #pA

print('Current in ' + dataset_1 + ' data =', round(current_ds1,2),'pA')

# Find maximum

mx1 = np.max(counts_ds1)

# Setup normalised datasets
ds1_N = np.empty(ds_1[0,:,:,:].shape)

for i in range(ndp):
    ds1_N[i,:,:] = ds_1[0,i,:,:] * (mx1/counts_ds1[i])

## ESTIMATE EFFECT OF BEAM HEATING

# Constants for each material

K_ds1 =1.7
rho_ds1 = 7000

# Define function for calculating dQ/dx
def DQDx(Z, A, E):
    DQDx = 7.8e9*Z/(A*E)*np.log(E/Z/13.5)*e
    return DQDx

# Calculate loss
E = 200000
Z_ds1 = (2*73+5*8)/7
A_ds1 = (2*180.95+5*16)/7
DQDx_ds1 = DQDx(Z_ds1, A_ds1, E)
r_0 = 1e-9 #m
R = 2e-9 #m

print('loss ', dataset_1, DQDx_ds1,'J/kg/m2')
print('loss ', dataset_2, DQDx_ds2,'J/kg/m2')
```

```
145 print('loss ', dataset_3, DQDx_ds3,'J/kg/m2')
146
147 # Define function for calculating delta T under the electron beam
148 def deltaT(I, rho, K, DQDx, r_0, R):
149     deltaT = I*1e-12*rho/(2*np.pi*e*K)*DQDx*np.log(R/r_0)
150     return deltaT
151
152 deltaT_ds1 = deltaT(current_ds1, rho_ds1, K_ds1, DQDx_ds1, r_0, R)
153 print(deltaT_ds1)
154
155 # Find central spot for the dataset
156
157 sum_dif_ds1 = np.sum(ds_1[0,:,:,:], axis=(0)) # 'sum_dif' is the sum of
        all diffraction patterns
158 plot = True
159 cyx_ds1, cr_ds1 = fpdp.find_circ_centre(sum_dif_ds1, 3, (3, 40, 1), pct
        =99, plot=plot)
160 # 'cyx' are [y,x] coordinates of the centre of the spot, 'cr' is radius
        of the spot
161
162 # Print y,x coordinates and radius of the central spot
163
164 print(cyx_ds1)
165 print(cr_ds1)
166
167 # Make an aperture
168 def aperture(R, cyx):
169     ap = disk_image(intensity=1, radius=R, sigma =0, size=256, dtype='
            float32')
170     ap_cyx = np.array(ap.shape)/2
171     sp = cyx[None] - ap_cyx[None] #+ np.array([d_im_pad, d_im_pad])[None]
172     ap_shift = shift_images(sp[None,:].T, ap, noise=False, parallel=False
            ).sum(axis=(0,1))
173     return ap_shift
174
175 # Make an beamstop
176 def stop(R, cyx):
177     st = 1-disk_image(intensity=1, radius=R, sigma =0, size=256, dtype='
            float32')
178     st_cyx = np.array(st.shape)/2
179     sp = cyx[None] - st_cyx[None] #+ np.array([d_im_pad, d_im_pad])[None]
180     st_shift = shift_images(sp[None,:].T, st, noise=False, parallel=False
            ).sum(axis=(0,1))
181     st_shift = np.where(st_shift<0.1,0,1)
182     return st_shift
183
```

```
184 # Set stop and aperture, then look at a few images spread at regular
        intervals through the dataset
185
186 stp_ds1 = int(ndp/5)
187 ds1_st_r = 25
188 ds1_ap_r = 38
189 stop_ds1 = stop(ds1_st_r,cyx_ds1)
190 ap_ds1 = aperture(ds1_ap_r,cyx_ds1)
191 for i in range(0,ndp,stp_ds1):
192     DP = ds_1[0,i,:,:]
193     plt.matshow(DP*stop_ds1*ap_ds1, cmap='inferno')
194
195 # Apply a Gaussian filter to the diffraction patterns and check on an
        image
196
197 ds1_N_G = gaussian(ds1_N, 1)
198
199 plt.matshow(ds1_N_G[0,:,:])
200
201 # Apply annular masks to the dataset
202
203 # Create array for the patterns
204 ds1_ann = np.zeros((ndp,256,256))
205
206 # Apply the annulus to each
207 for i in range(ndp):
208     ds1_ann[i,:,:] = ds1_N_G[i,:,:]*stop_ds1*ap_ds1
209
210 # Crop DPs to exclude unnecessary pixels
211
212 # Set crop size
213 ds1_crop_r = ds1_ap_r + 2
214
215 # Crop
216 ds1_crop = ds1_ann[:,int(cyx_ds1[0]-ds1_crop_r):int(cyx_ds1[0]+ds1_crop_r
        ),int(cyx_ds1[1]-ds1_crop_r):int(cyx_ds1[1]+ds1_crop_r)]
217
218 # Check on plots
219 plt.matshow(ds1_crop[0,:,:])
220
221 # Dimensions of cropped DPs
222
223 ds1_cr_sz = np.shape(ds1_crop)[1]
224
225 ## AUTO-CORRELATION FUNCTION
226
227 ls = ndp#int(ndp/2)
```

```
228
229 # Calculate g2(t) for each pixel in the DP for dataset 1
230
231 g2_ds1 = np.empty((ls,ds1_cr_sz,ds1_cr_sz))
232
233 for i in range(ls):
234     acor1 = ds1_crop[:ls-i]
235     acor2 = ds1_crop[i:i+ls]#[i:i+abc]
236 #     print(i)
237     g2_ds1[i,:,:] = ((ls-i)*(np.sum(acor1*acor2, axis=0))) / ((np.sum(
        acor1, axis=0))*(np.sum(acor2, axis=0)))
238
239 # Calculate intensity variance for each dataset
240
241 ds1_IV = np.mean(ds1_crop[:ls]**2, axis=0)/(np.mean(ds1_crop[:ls],axis=0)
    **2)
242
243 # Plot first terms of g2 and intensity variance of all frames for each
    dataset
244 # If g2 is correctly calculated then the third column should all equal 0
245
246 fig = plt.figure(figsize=(6,6))
247 gs = gridspec.GridSpec(3,3, hspace=0.01, wspace=0.01)
248
249 ax = plt.subplot(gs[0,0])
250 im1 = ax.matshow(g2_ds1[0,:,:])
251 ax = plt.subplot(gs[0,1])
252 im1 = ax.matshow(ds1_IV)
253 ax = plt.subplot(gs[0,2])
254 im1 = ax.matshow(g2_ds1[0,:,:]-ds1_IV,cmap='seismic')
255
256 # ax = plt.subplot(gs[1,0])
257 # im2 = ax.matshow(g2_ds2[0,:,:])
258 # ax = plt.subplot(gs[1,1])
259 # im1 = ax.matshow(ds2_IV)
260 # ax = plt.subplot(gs[1,2])
261 # im1 = ax.matshow(g2_ds2[0,:,:]-ds2_IV,cmap='seismic')
262
263 # ax = plt.subplot(gs[2,0])
264 # im3 = ax.matshow(g2_ds3[0,:,:])
265 # ax = plt.subplot(gs[2,1])
266 # im1 = ax.matshow(ds3_IV)
267 # ax = plt.subplot(gs[2,2])
268 # im1 = ax.matshow(g2_ds3[0,:,:]-ds3_IV,cmap='seismic')
269
270 for i in range(3):
271     for ii in range(3):
```

```
272             ax=plt.subplot(gs[i,ii])
273             ax.get_yaxis().set_visible(False)
274             ax.get_xaxis().set_visible(False)
275
276 # Choose which datapoints to use in the KWW fits (May be better to use
        less points at longer times to avoid domination from those parts)
277
278 log_time = np.round(np.geomspace(1, 500, num=50,endpoint=False))
279
280 for i in range(np.shape(log_time)[0]):
281     log_time[i] = int(log_time[i])
282
283 log_time = np.sort(list(set(log_time)))
284 n_points = np.shape(log_time)[0]
285
286 ds1_log_time = np.empty(n_points)
287 ds1_log_g2 = np.empty((n_points,ds1_cr_sz,ds1_cr_sz))
288
289 for i in range(n_points):
290     pnt = int(log_time[i])
291     ds1_log_time[i] = time[pnt]
292     ds1_log_g2[i,:,:] = g2_ds1[pnt,:,:]
293
294 print(n_points)
295
296 ## FITTING
297
298 from scipy.optimize import least_squares
299
300 def KWW_ls(t,coeffs):
301     return 1 + coeffs[0]*np.exp((-2*(t/coeffs[1])**coeffs[2]))
302
303 def residuals(coeffs, y, t):
304     return y - KWW_ls(t, coeffs)
305
306 # Annular mean of g2 excluding NaNs
307
308 ds1_ann = np.nanmean(ds1_log_g2, axis=(1,2))
309
310 # Plot annular means of g2
311
312 plt.plot(ds1_log_time, ds1_ann, label = dataset_1)
313 plt.legend()
314 plt.xscale('log')
315
316 # Create KWW fit for the annular region
317 # ds1
```

```
318
319 x0 = np.array([0.05, 5000, 1], dtype=float)
320
321 lsqfit_ds1_ann = least_squares(residuals, x0, bounds=((0,0,0)
    ,(2,100000,3)), args=(ds1_ann[3:], ds1_log_time[3:]),max_nfev=10000)
322
323 # Plot data along with the KWW fit of the annular region
324 # ds1
325
326 fig=plt.figure()
327 ax = fig.add_subplot(1, 1, 1)
328 ax.plot(ds1_log_time,KWW_ls(ds1_log_time,lsqfit_ds1_ann.x),'b-',label='
    fit')
329 ax.plot(ds1_log_time,ds1_ann,'rx', label='data')
330 ax.set_xscale('log')
331 ax.set_title(dataset_1)
332 ax.set_xlabel('time (ms)')
333 ax.set_ylabel('g$_2$(t)')
334
335 ax.text(0.75, 0.55, 'A =' + str(round(lsqfit_ds1_ann.x[0],3)),transform=
    ax.transAxes)
336 ax.text(0.75, 0.5, 'tau =' + str(round(lsqfit_ds1_ann.x[1]))+ ' ms',
    transform=ax.transAxes)
337 ax.text(0.75, 0.45, 'beta =' + str(round(lsqfit_ds1_ann.x[2],2)),
    transform=ax.transAxes)
338 ax.legend()
339
340 # plt.savefig("FIGURE_5.pdf",bbox_inches='tight', format='pdf')
341
342 ## FITTING OF EVERY PIXEL IN THE MASKED PATTERN
343
344 # Fit each pixel in the diffraction pattern calculating tau and beta
345 # For ds1
346
347 ds1_A_tau_beta_ = np.empty((4,ds1_cr_sz,ds1_cr_sz))
348 x0 = np.array([0.05, 5000, 1], dtype=float)
349
350 for i in range(ds1_cr_sz):
351     for ii in range(ds1_cr_sz):
352         data = ds1_log_g2[:,i,ii]
353         if np.isnan(data[0]) == False:
354             fit = least_squares(residuals, x0, bounds=((0,0,0.3)
                ,(1,80000,2)), args=(data, ds1_log_time[:]),max_nfev
                =10000)
355             A,tau_1,b,cost = fit.x[0], fit.x[1], fit.x[2],fit.cost
356
357             # Set cost to get rid of bad fits
```

```
358                 if cost <= 0.0005 and 0.3 <= b <= 2:
359                     ds1_A_tau_beta_[0,i,ii] = A
360                     ds1_A_tau_beta_[1,i,ii] = tau_1
361                     ds1_A_tau_beta_[2,i,ii] = b
362                     ds1_A_tau_beta_[3,i,ii] = cost
363                 else:
364                     ds1_A_tau_beta_[0,i,ii] = 0
365                     ds1_A_tau_beta_[1,i,ii] = 0
366                     ds1_A_tau_beta_[2,i,ii] = 0
367                     ds1_A_tau_beta_[3,i,ii] = 0
368             else:
369                 ds1_A_tau_beta_[0,i,ii] = 0
370                 ds1_A_tau_beta_[1,i,ii] = 0
371                 ds1_A_tau_beta_[2,i,ii] = 0
372                 ds1_A_tau_beta_[3,i,ii] = 0
373
374 # Plot ds1: DP, tau, beta
375
376 fig = plt.figure(figsize=(10,3))
377 gs = gridspec.GridSpec(2,4, hspace=0.01, wspace=0.01, height_ratios
        =[1,0.2])
378
379 insets = [0.1, 0.7, 0.8, 0.2]
380
381 cmap='seismic'
382
383 ax = plt.subplot(gs[0,0])
384 im1 = ax.matshow(ds1_crop[0,:,:], cmap='inferno')
385 ax.get_yaxis().set_visible(False)
386 ax.get_xaxis().set_visible(False)
387 ax = plt.subplot(gs[1,0])
388 axins = ax.inset_axes(insets)
389 cb1 = plt.colorbar(im1, cax=axins, orientation='horizontal', label='
        detector counts')
390
391 ax = plt.subplot(gs[0,1])
392 im2 = ax.matshow(ds1_A_tau_beta_[1,:,:],cmap='inferno')
393 ax.get_yaxis().set_visible(False)
394 ax.get_xaxis().set_visible(False)
395 ax = plt.subplot(gs[1,1])
396 axins = ax.inset_axes(insets)
397 cb1 = plt.colorbar(im2, cax=axins,  orientation='horizontal', label='tau
        (ms)')
398
399 ax = plt.subplot(gs[0,2])
400 im3 = ax.matshow(ds1_A_tau_beta_[1,:,:],vmax=3000,cmap='inferno')
401 ax.get_yaxis().set_visible(False)
```

```
402 ax.get_xaxis().set_visible(False)
403 ax = plt.subplot(gs[1,2])
404 axins = ax.inset_axes(insets)
405 cb1 = plt.colorbar(im3, cax=axins, orientation='horizontal', label='tau (
        ms)')
406
407 ax = plt.subplot(gs[0,3])
408 im4 = ax.matshow(ds1_A_tau_beta_[2,:,:],vmin=0.3,vmax=2, cmap='inferno')
409 ax.get_yaxis().set_visible(False)
410 ax.get_xaxis().set_visible(False)
411 ax = plt.subplot(gs[1,3])
412 axins = ax.inset_axes(insets)
413 cb1 = plt.colorbar(im4,cax=axins, ticks=[0.5,1.0,1.5,2], orientation='
        horizontal', label='beta')
414
415 for i in range(4):
416     ax=plt.subplot(gs[1,i])
417     ax.get_yaxis().set_visible(False)
418     ax.get_xaxis().set_visible(False)
419     ax.spines['top'].set_visible(False)
420     ax.spines['bottom'].set_visible(False)
421     ax.spines['left'].set_visible(False)
422     ax.spines['right'].set_visible(False)
423
424 # plt.savefig("FIGURE_6.pdf",bbox_inches='tight', format='pdf')
425
426 # Plot one of the pixels and its fit
427 # ds1
428
429 yp = 0 # y coordinate of pixel
430 xp = 0  # x coordinate of pixel
431 ex_fit_data = ds1_log_g2[:,yp,xp]
432 ex_fit_params = ds1_A_tau_beta_[:,yp,xp]
433
434 fig=plt.figure()
435 ax=fig.add_subplot(1,1,1)
436 ax.plot(ds1_log_time[:],KWW_ls(ds1_log_time[:],ex_fit_params),'b-')
437 ax.plot(ds1_log_time[:],ex_fit_data,'rx')
438 ax.set_xscale('log')
439 ax.set_title(dataset_1)
440 ax.set_xlabel('time (ms)')
441 ax.set_ylabel('g$_2$(t)')
442
443 ax.text(0.75, 0.8, 'A = {:.2f}'.format(ex_fit_params[0]), transform=ax.
        transAxes)
444 ax.text(0.75, 0.75, 'tau = {:.0f} ms'.format(ex_fit_params[1]), transform
        =ax.transAxes)
```

```
445 ax.text(0.75, 0.7, 'beta = {:.2f}'.format(ex_fit_params[2]), transform=ax
        .transAxes)
446
447 # plt.savefig("FIGURE_7.pdf",bbox_inches='tight', format='pdf')
448
449 # Plot histogram of tau
450 # ds1
451
452 fig = plt.figure()
453 ax = fig.add_subplot(1,1,1)
454
455 ax.hist(ds1_A_tau_beta_[1,:,:].flatten(), 200, range=(1,10000))
456 ax.set_xlabel('tau (ms)')
457 ax.set_ylabel('instances')
458
459 ds1___ = ds1_A_tau_beta_[1,:,:].flatten()
460 ds1___[ds1___ == 0] = np.nan
461 ds1_mn = np.nanmean(ds1___)
462 ds1_std = np.nanstd(ds1___)
463
464 ax.text(0.5, 0.85, 'mean = {:.1f} ms'.format(ds1_mn),transform=ax.
        transAxes)
465
466 # plt.savefig("FIGURE_8.pdf",bbox_inches='tight', format='pdf')
467
468 # Plot histogram of beta
469 # ds1
470
471 plt.rcParams.update({'font.size': 23})
472
473 fig = plt.figure()
474 ax = fig.add_subplot(1,1,1)
475
476 ax.hist(ds1_A_tau_beta_[2,:,:].flatten(), 100, range=(0.301,1.999))
477 ax.set_xlabel('beta')
478 ax.set_ylabel('instances')
479
480 ds1___ = ds1_A_tau_beta_[2,:,:].flatten()
481 ds1___[ds1___ == 0] = np.nan
482 ds1_mn = np.nanmean(ds1___)
483 ds1_std = np.nanstd(ds1___)
484
485 ax.text(0.55, 0.85, 'mean = {:.2f}'.format(ds1_mn),transform=ax.transAxes
        )
486
487 # plt.savefig("FIGURE_9.pdf",bbox_inches='tight', format='pdf')
```